Extending the realm of galaxies to the low surface brightness universe

Brisa Mancillas Vaquera

To cite this version:

Brisa Mancillas Vaquera. Extending the realm of galaxies to the low surface brightness universe. Astrophysics [astro-ph]. Université Paris sciences et lettres, 2019. English. NNT : 2019PSLEO013 . tel-02884959

HAL Id: tel-02884959
https://theses.hal.science/tel-02884959

Submitted on 30 Jun 2020

PSL
UNIVERSITÉ PARIS

THÈSE DE DOCTORAT
DE L'UNIVERSITÉ PSL

Préparée à l'Observatoire de Paris

Extending the realm of galaxies to the low surface brightness Universe

Soutenue par

Brisa Llaneth
MANCILLAS VAQUERA
Le 23 Septembre 2019

Ecole doctorale n° 127

Astronomie et Astrophysique
d'Île-de-France

Spécialité

Astronomie et Astrophysique

Composition du jury :

Rosine, LALLEMENT DR CNRS, Observatoire de Paris - GEPI	*Président*
Alessandro, BOSELLI Professor, LAM	*Rapporteur*
Jérôme, PETY Professor, IRAM	*Rapporteur*
Pierre-Alain, DUC DR CNRS, Observatoire Astronomique de Strasbourg	*Examinateur*
Françoise, COMBES-BOTTARO Professeur, Observatoire de Paris - LERMA	*Directeur de thèse*
David, VALLS-GABAUD DR2 CNRS, Observatoire de Paris - LERMA	*Directeur de thèse*

l'Observatoire de Paris | PSL

EXTENDING THE REALM OF GALAXIES TO THE LOW SURFACE BRIGHTNESS UNIVERSE

Brisa Llaneth Mancillas Vaquera

Acknowledgements

This thesis becomes a reality with the kind support and help of my advisors and collaborators. I would like to extend my sincere thanks to all of them.

First of all, I would like to express my deep sense of gratitude to my advisors, Dr. Françoise Combes and Dr. David Valls-Gabaud for their valuable guidance, keen interest, patience and encouragement at various stages of my PhD. I warmly thank to my co-advisors, Dr. Pierre-Alain Duc and Dr. Vladimir Avila-Reese for their guidance and very constructive suggestions on the different topics developed with each one of them.

I thank to the "National Council of Science and Technology (CONACYT)" for providing the financial support to carry out this PhD project.

I am very much thankful to my family for their loving and unconditional support.

I also express my sincere gratitude to my "Parisian family" for their valuable friendship and support, and for all the good times we spent together. I am deeply indebted to David Guerrero Mayorga for his invaluable psychological orientation.

"Nothing in life is to be feared, it is only to be understood.
Now is the time to understand more, so that we may fear less."

— **Marie Curie**

Abstract

The exploration of diffuse light emission and the outskirts of galaxies in the regime of the Low Surface Brightness (LSB) is of utmost importance to understand the formation mechanism of galaxy evolution, and it is essential to constrain the current theoretical models and numerical simulations in the cosmological context. Observational data, both in optical and radio emission, complemented with hydrodynamical cosmological numerical simulations and explored with semi-empirical models, provide us a crucial information about the morphological properties of collisional debris around massive galaxies, as well as the mass distribution, molecular gas content and star formation of Low Surface Brightness (LSB) galaxies such as Ultra Diffuse Galaxies (UDGs).

This thesis presents several analysis addressed to the study of these schemes. From both theoretical and observational perspectives. In first instance, through a semi-empirical approach, we have explored the extension of the powerful statistical galaxy-halo connection method towards the galaxy scaling relations and their internal mass distributions, aimed to be applied to a local galaxy population and a particular subpopulations of galaxies at different environments, such as LSB galaxies and UDGs.

Secondly, motivated in the most recent works about optimized deep imaging surveys observed with the Mega/Cam camera at CFHT Telescope, which have revealed prominent LSB fine structures classified like tidal tails, stellar streams and shells, we have computed statistics of an hydrodynamical numerical simulation in order to interpret observations and make inferences about the past mass assembly of galaxies. We made a census of these substructures and we have computed their survival time. We also studied their dependence with several properties like the projection effects and the surface brightness limits. We found that shells and streams remains visible around 4 Gyr and they are mainly associated to minor and intermediate-mass mergers, and a continuous diffuse gas accretion, while tidal tails have a durability time of around 1 Gyr and are correlated with major merger events. On the other hand, we have performed CO spectroscopy surveys of UDGs observed at IRAM-30m to quantify the molecular gas content. The selected galaxies were conformed by sources from several environments and different properties, including objects like the very red galaxies, Dragonfly 44 and DGSAT I. We have obtained unprecedented upper limits of their CO mass (few $10^6 - 10^7$ $M_\odot$). We also made CO observations at IRAM-30m to detect molecular gas content in a sample of nine selected galaxies that exhibit prominent shell galaxies like the case of NGC 474 and Arp 230. Our goal is to test the phase wrapping formation model proposed in numerical simulations. We detected a molecular mass of $\sim 10^8$ $M_\odot$ in several shells of three galaxies (Arp 10, NGC 3656 and NGC 3934) from our sample and we report the mass upper limits for the other cases.

List of Figures

1.1 Equirectangular projection of all-sky view of the Milky Way Galaxy and neighboring galaxies, i.e., the Magellanic clouds from GAIA Survey. Measurements are based on nearly 1.7 billion stars. The map shows the total brightness and color of stars observed by the ESA satellite in each portion of the sky between July 2014 and May 2016. Credit: ESA/Gaia/DPAC. 2

1.2 A summary of the almost 14 billion year history of the Universe, showing in particular the events that contributed to the Cosmic Microwave Background. *Upper part.* Artistic view of the evolution timeline of the cosmos on large scales. The processes depicted range from inflation, the brief era of accelerated expansion that the Universe underwent when it was a tiny fraction of a second old, to the release of the CMB, the oldest light in our Universe, imprinted on the sky when the cosmos was just 380 000 years old, and from the 'Dark Ages' to the birth of the first stars and galaxies, which reionized the Universe when it was a few hundred million years old, all the way to the present time. *Lower part.* Zoomed-in view on some of the microscopic processes taking place during cosmic history: from the tiny fluctuations generated during inflation, to the dense soup of light and particles that filled the early Universe, from the last scattering of light off electrons, which gave rise to the CMB and its polarization, to the reionization of the Universe, caused by the first stars and galaxies, which induced additional polarization on the CMB. 4

1.3 The Hubble's sequence through the Universe's history (present day, at 4 billion and 11 billion years ago). Hubble tuning-fork diagram describes and separates galaxies according to their morphology into spiral (S), elliptical (E), and lenticular (S0) galaxies. On the left of this diagram are the ellipticals, with lenticulars in the middle, and the spirals branching out on the right side. The spirals on the bottom branch have bars cutting through their centers. The present-day universe shows big, fully formed, and intricate galaxy shapes. As we go further back in time, they become smaller and less mature, as these galaxies are still in the process of forming. Credit: NASA, ESA, M. Kornmesser. 5

1.4 *Left panel*: Schematic "merger-tree" representation of a binary disc merger simulation. Two gas-rich (blue) stellar (yellow) discs with little hot gas (red) merge at z∼1 and form an elliptical galaxy. *Right panel*: Merger tree from a cosmological zoom simulation of the formation of a halo and its galaxy within the concordance cosmology. Black circles indicate the dark matter halo mass at every redshift with the symbol size proportional to the square root of the normalized halo mass at z=0. The yellow stars indicate stellar mass, the blue and red filled circles show the cold and hot gas mass within the virial radius (Naab et al., 2014). It is evident that continuous infall of matter in small and large units is an important characteristic of the assembly of massive galaxies. The galaxy shown has no major merger since z∼3. Others galaxies of similar mass can have up to three major mergers. The mass growth, however, is always accompanied by minor mergers. . 6

1.5 NGC 4038 and 4039, also known as the Antennae galaxies. The long tails of luminous matter formed by the encounter resemble an insect's antennae. A ground-based view of NGC 4038/4039 (left) displays their distinctive antennae. The Hubble Space Telescope image (right) shows more than 1,000 brilliant star clusters at the heart of the collision. 8

1.6 In 1877, French astronomer Édouard Stephan turned a telescope to a spot in the constellation Pegasus and discovered this collection of five large galaxies. Stephan's Quintet, as the group is now known, includes four distant galaxies that are connected to each other through gravity and one galaxy that is much closer to us but just happens to lie in the same direction in the sky. Credits: NASA, ESA, and the Hubble SM4 ERO Team. 9

1.7 A cartoon view of the circumgalactic medium. The galaxy's red central bulge and blue gaseous disk are fed by filamentary accretion from the IGM (blue). Outflows emerge from the disk in pink and orange, while gas that was previously ejected is recycling. The diffuse gas halo in varying tones of purple includes gas that is likely contributed by all these sources and mixed together over time. (Tumlinson et al., 2017) 11

2.1 Accuracy of the M_{dyn}-$M_\star$ relations based on the $S_{0.5}$ parameter. In the top and medium panels we assume that galaxies are rotation or velocity dispersion dominated to estimate the dynamical mass within the effective radius. The red, green, and black stars represent the CALIFA sample, whereas the grey symbols are from the literature compilation. The $S_{0.5}$ dynamical mass estimations perform better than the ones based either only on rotation or dispersion. In the bottom panel we used the $S_{0.5}$ parameter to estimate the dynamical mass and compare them with theoretical predictions based on detailed dynamical models. All the estimated M_{dyn}-$M_\star$ relations are comparable and consistent with observations within the uncertainties. As a reference we also show the semi-empirical predictions of Mancillas et al. (2017) (blue shaded region, see text) which use $\eta = 1$ and are also consistent with our estimations. 20

2.2 The stellar-to-total mass relation (STMR) from Mancillas et al. (2017) for simulated late-type galaxies (LTGs), with the stellar mass M_* and total mass M_{tot} both measured within 2 R_e, is in pink. The SHIVir STMR is shown in blue for LTGs (Irr galaxies are excluded given their highly truncated and/or uncertain RCs), and in red for ETGs. The dashed line is again the 1:1 line. 21

3.1 *Left side:* Comparison of LSB substructures around observed and simulated galaxies. Left panels: Examples of ETGs from MATLAS Survey. From top to bottom, the system NGC 5574/76 (tidal tails emanate from NGC 5576), stellar stream in NGC 4684 and interleaved shells in NGC 3619. Right panels: Examples of mock surface brightness images exhibiting prominent tidal tails, streams and shells at different times of the simulation in random projections. Note the white scale bar indicating 20 kpc: the scales are comparable in observations and simulations. *Right side:* The classification scheme used for the MATLAS deep imaging survey, which is based on the identification of various types of collisional debris. Examples of tails, plumes, shells and streams are illustrated in the insets. The pie chart summarizes the preliminary statistical results for the population of 240 massive Early Type Galaxies (Duc, 2017). 69

4.1 *Left*: The overprocessed negative detail image of Arp 230 Arp (1966) *Right*: NGC 3923 from Malin and Carter (1983). 88

4.2 Images of the individual features found in MegaCam image (Bílek et al., 2016) and in the archival HST image (Sikkema et al., 2006), showing filamentary structure. North is to the top and east is to the left. The abbreviations indicate the following: S_n - shells, F - other tidal features, C_n - probable galactic cirri, H - a hook-like structure. 90
4.3 The phase space and configuration space, time evolution of 5000 test particles falling from rest into an isochrone potential. The number in the top left of each phase plane plot are the time passed in units of the radial period of the most tightly bound particle. The configuration space distribution of the particles at each time is shown directly below the corresponding phase plot. Positions are in units of the isochrone scale length, and velocities are in units of $(GM/10a)^{1/2}$, where M is de total mass and a the scale length. By Quinn (1984). 92
4.4 The sketches of the geometry in space of the shell system surrounding: (a) a prolate elliptical galaxy, and (b) an oblate elliptical galaxy. By Dupraz and Combes (1986). 93
4.5 **a**) A Digitized Sky Survey optical image of CenA with the contours of HI gas (from (Schiminovich et al., 1994)) superimposed in white. The HI contour levels are 1, 4, 7, 10, 15, 30, 35, 40 × 10^{20} cm^{-2}. North is up and east is to the left, while the image scale is shown by the horizontal bar. The positions observed in CO are marked with the red circles whose size corresponds to the SEST 44 beam of CO(1-0). The type of each map (half-beam spacing or simple pointing) is evident by the placement of the circles. The locations of the outer stellar shells are underlined by the yellow solid lines (see also Fig. 1a of (Schiminovich et al., 1994)). The inner 6cm radio continuum lobes (from Clarke et al., 1992) are depicted by the blue contours (contour levels 0.01, 0.05, 0.1 Jy/beam). Note the jet alignment with the location of the CO detections. The outer radio lobes are far more extended. **b**) CO(1-0) and CO(2-1) spectra towards the northern shell S1 with the temperature scale in main beam T_{mb} , smoothed to 18 km s^{-1}. **c**) Same as in b) but for the southern shell S2. 94

5.1 Follow-up small telescope images of DGSAT I (indicated with a red arrow): (top) color image obtained with the FNO TOA-150 refractor; (bottom) luminance filter image obtained with the ROSA 0.4 m telescope. The new dwarf is detected as a small cloud (top left) close to the And II dSph (bottom right), visible only ∼15' to the west. North is top, east is left. The field of view of these cropped images is ∼19' × 11' (Martínez-Delgado et al., 2016). 114
5.2 Deep Gemini g and i images were combined to create a color image of Dragonfly 44 and its immediate surroundings. The galaxy has a remarkable appearance: it is a low surface brightness, spheroidal object that is peppered with faint, compact sources. (van Dokkum et al., 2016). 115
5.3 Stacking of the data for the HI line. 117
5.4 Upper limits for CO(1-0), CO(2-1) and HI-21 cm emission lines for DGSAT-I. . 118
5.5 Upper limits for CO(1-0), CO(2-1) and HI-21 cm emission lines for Dragonfly 44. 119
5.6 Stacking of the data for the CO (1-0) line. 119
5.7 Stacking of the data for the CO (2-1) line 120

List of Tables

5.1 Summary of the properties of the sources. 113

5.2 Summary of the HI line observations using the Nançay telescope. We have calculated the M_{HI} assuming a 3σ upper limit. 117

5.3 Summary of the CO line observations using the IRAM 30-m telescope. We have calculated the M_{H2} assuming a 3σ upper limit. 118

Contents

Abstract . . . v

1 **GENERAL INTRODUCTION** **1**
- 1.1 Overview . . . 1
  - 1.1.1 Cosmological paradigm . . . 2
- 1.2 Taxonomy, morphology and classification . . . 4
  - 1.2.1 Hubble classification . . . 5
- 1.3 Galaxy Mergers . . . 6
  - 1.3.1 Types of galaxy mergers . . . 7
- 1.4 Low surface brightness galaxies . . . 10
  - 1.4.1 Gas content in LSB galaxies . . . 11
  - 1.4.2 Shell galaxies . . . 12
  - 1.4.3 Ultra-Diffuse Galaxies . . . 12
- 1.5 Objectives . . . 12
- 1.6 Methodology . . . 14
- 1.7 Contents . . . 15

2 **Scaling relations and mass distributions in a semi-empirical model of galaxy evolution** **17**
- 2.1 The semi-empirical galaxy-halo connection mapped towards the galaxy scaling relations and their internal mass distributions . . . 18
- 2.2 Early applications of semi-empirical models to observational internal mass distributions . . . 19
- 2.3 Conclusion and perspectives . . . 22
- 2.4 Paper: The galaxy-halo connection . . . 23
- 2.5 Paper: A dynamical mass proxy . . . 51

3 **Low surface brightness shells, streams and tidal tails: the merging history of red early-type galaxies** **67**
- 3.1 Overview . . . 68
- 3.2 Conclusions and perspectives . . . 70
- 3.3 Paper: Probing the merger history with faint substructures . . . 71

4 **The molecular gas content of shell galaxies** **87**
- 4.1 Overview . . . 87
  - 4.1.1 First shell galaxy detection: Examples . . . 87
  - 4.1.2 Incidence of shell galaxies . . . 87
  - 4.1.3 Shell galaxy properties . . . 89
- 4.2 History of the theories of shell galaxy formation . . . 90
- 4.3 Current mechanisms of shell formation . . . 91
  - 4.3.1 Phase-wrapping scenario . . . 91
  - 4.3.2 Space-wrapping scenario . . . 93

4.4 Atomic and molecular gas in shell galaxies 93
4.5 Conclusions and perspectives 94
4.6 Paper: The molecular gas content of shell galaxies 96

5 The molecular gas content of ultra-diffuse galaxies 111
5.1 Overview 111
5.1.1 Incidence of UDGs 111
5.1.2 Origin and formation mechanisms of UDGs 112
5.1.3 The gas mass content 113
5.2 Target Selection: DGSAT I and Dragonfly 44 113
5.3 Observations and data reduction 115
5.3.1 IRAM 30-m observations 115
5.3.2 Nançay observations 116
5.4 Preliminary results 116
5.4.1 Upper limits on the content of atomic and molecular gas 116
5.5 Conclusions and perspectives 120

6 Conclusions 121

Bibliography 123

Appendices 151

A Publications 153
A.1 Refereed publications 153
A.2 Non-refereed publications 153

Chapter 1

GENERAL INTRODUCTION

1.1 Overview

Galaxies are considered the fundamental units that build-up the Universe. By definition, a galaxy is a dynamical gravitationally-bound system consisting of stars, gas, dust and dark matter. By looking inside, a galaxy is a propitious environment where the star cycle occurs, i.e., the birth of a star from a cloud of cold gas, its evolution and collapse inside of the interstellar medium (ISM). A typical example is our own galaxy, the Milky Way, the closest galaxy that we can observe by eye in a clear night sky. We observe our galaxy as a band of light crossing the dark sky, which suggests that its main component is a disk-like structure (see Figure 1.1). The brighter regions displayed in the horizontal structure correspond to dense concentrations of bright stars, meanwhile dark regions correspond to clouds of interstellar gas and dust, which absorb the light of stars hidden behind the clouds. The Milky Way contains a stellar mass of 4×10^{10} stars and a total mass of 10^{12} $M_\odot$ taking into account the dark matter until the virial radius of $\sim$180 kpc, and has a diameter of $\sim$ 30 kpc.

Nonetheless, our galaxy is only one of thousand of billions of galaxies spreading in the whole Universe and located in different environments, such as galaxy groups, galaxy clusters or isolated regions. Studies compute around 2×10^{12} galaxies for a redshift up to z=8 in the observable Universe (Conselice et al., 2016). Galaxies display a wide range of morphologies, structural components, color, luminosities and different ages and shapes. They are observed at several cosmological distances and time scales, becoming primordial tracers of their own large scale structure and the evolution of the Universe.

The observation of this broad set of characteristics has led to the arising of deep questions about their formation mechanism, evolution and distribution in the universe. Some of the key questions are for example: What is the origin of the first generation of galaxies? How have they evolved during more than 13 billion years until our present days? How do they acquire their shape and their different properties? How do they assemble their mass? What are the main physical processes for their formation?

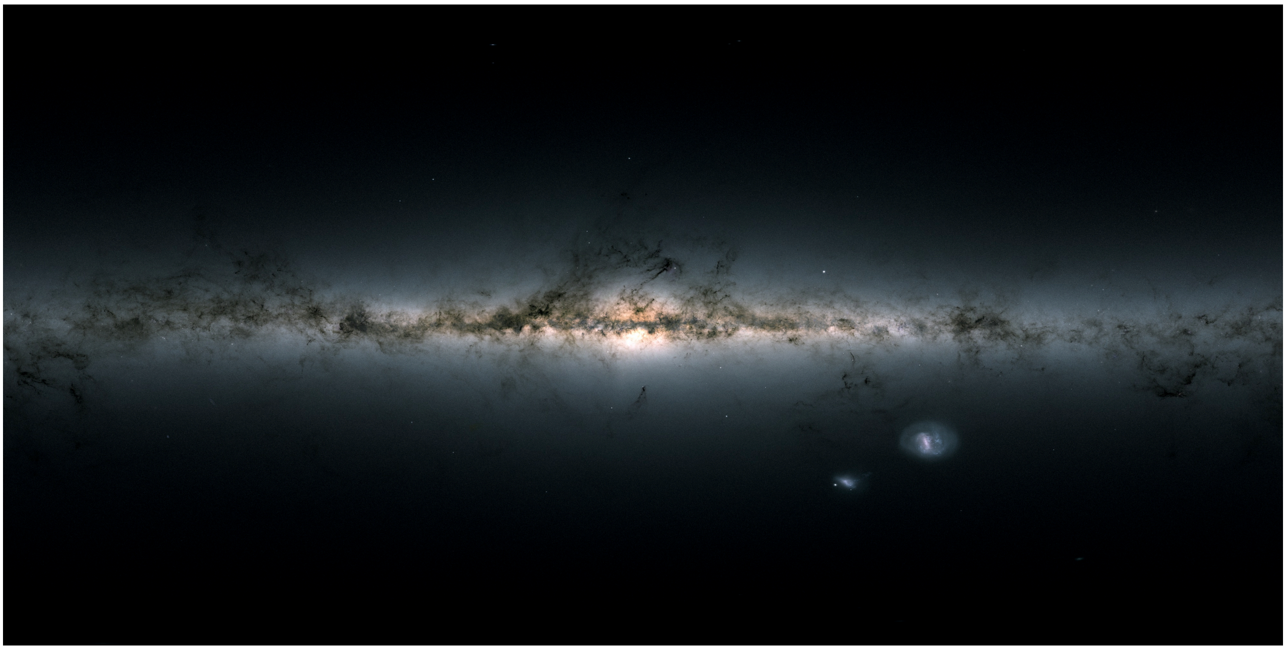

Figure 1.1: Equirectangular projection of all-sky view of the Milky Way Galaxy and neighboring galaxies, i.e., the Magellanic clouds from GAIA Survey. Measurements are based on nearly 1.7 billion stars. The map shows the total brightness and color of stars observed by the ESA satellite in each portion of the sky between July 2014 and May 2016. Credit: ESA/Gaia/DPAC.

1.1.1 Cosmological paradigm

An underlying cosmological framework as well as the initial and physical conditions are needed to describe galaxy formation and evolution. Nowadays, current scenarios of galaxy formation (supported by numerical simulations), provide us with the physical conditions to determine fundamental characteristics of galaxies such as size, mass, and distribution. Although we have to keep in mind the limited knowledge about the details which are important to explore in the internal structure and evolution of galaxies (see e.g., Naab and Ostriker, 2017).

A suitable scenario which confronts cosmological background and astronomical observations and makes them converge, gives as a result a cosmological standard model. Currently, the most accepted theoretical model to describe the galaxy origin and evolution is the so-called Λ-Cold Dark Matter (Λ-CDM), where Λ is the cosmological constant associated with dark energy and CDM is the adopted hypothetical type of dark matter (Planck Collaboration et al., 2018). The model covers several theoretical and observational facts divided in four blocks:

- *Cosmological theories*: Big Bang and Inflation.
- *Physical models*: Beyond the standard model of particles.
- *Astrophysical models*: Gravitational cosmic structure growth, hierarchical clustering, gas physics.
- *Physics*: Cosmic Microwave Background Radiation (CMBR) anisotropies, non-baryonic dark matter, repulsive dark energy, flat geometry, galaxy properties.

Inflationary theory

An inflationary theory is included in the standard model in order to solve the horizon and flatness problems. The model is extended to include quantum processes in order to generate the fluctuations field that produce the density perturbations and leads to the creation of the current observed structures in the Universe (Mukhanov and Chibisov, 1981). Quantum processes occurs during the inflationary epoch, where it is assumed that the Universe is undergoes a fast, accelerated and exponential expansion (Guth, 1981; Linde, 1982).

Λ-CDM model also assumes a gravitational instability framework. According to this this framework, current cosmic structures in the Universe were the outcome of a gravitational evolution in a expanding Universe of a primordial field of tiny density perturbations, which were growing with time. Such perturbations were seeded during the inflationary epoch, when the vacuum quantum fluctuations were causally disconnected to become into perturbations to the space-time metric. As cosmic time passes, these quantum fluctuations evolved and increased their size, and again were causally connected becoming in real density perturbations (density contrast) (see e.g., Avila-Reese, 2007; Mo et al., 2010). These perturbations evolved gravitationally until they separate from the expansion and collapse into self-gravitating structures known as halos.

In the context of the Λ-CDM model, it is proposed that matter is dominated by an invisible component named “dark matter”, which does not interact with radiation but produces gravitational effects. According to cosmological and astronomical tests, dark matter is 5 times more abundant than ordinary (baryonic) matter. Both, dark plus baryonic matter are only 30% of what currently composes the Universe. The remaining 70% belongs to the so-called dark energy, which is a repulsive medium that provokes the accelerated expansion of the Universe. The dynamic of dark energy is well described by the cosmological constant, Λ, although its physical explanation is still a big challenge. The most recent computation of the cosmological parameters are reported in the Planck mission and a combination of several surveys (Planck Collaboration et al., 2018) giving the following values: Hubble constant ($\mathrm{H}_0 = 67.37\pm0.54$ km $\mathrm{s}^{-1}Mpc^{-1}$), physical baryon energy density ($\Omega_b h^2 = 0.0223\pm0.00001$), physical dark matter energy density ($\Omega_c h^2 = 0.1198\pm0.00120$), reionization optical depth ($\tau = 0.0540\pm0.0074$), primordial amplitude of scalar perturbations ($\ln(10^{10})\mathrm{A}_s = 3.043\pm0.01400$) and the spectral index of scalar perturbations ($n_s = 0.9652\pm0.0042$). The resulting parameters for the content of the Universe are: baryon density ($\Omega_b = 0.0486\pm0.0010$), dark matter density ($\Omega_c = 0.265\pm0.0050$) and dark energy density ($\Omega_\Lambda = 0.6889\pm0.0056$), which are parametrized in terms of the dimensionless parameter h, defined by $\mathrm{h} \equiv \mathrm{H}_0/(100$ km $\mathrm{s}^{-1}Mpc^{-1})$. The age of the Universe is $t_0 = 13.799\pm0.0210$ Gyr.

Hierarchical clustering

The hierarchical clustering is a consequence of the inflationary epoch of the Universe. In this scenario, dark matter halos grow following a merger tree. The less massive halos are formed first and they merge to form more massive halos. At each union of branches in the tree, halos are joined to form a larger halo with the resulting mass of the two merging units. A current dark matter halo is made of the merging of several smaller halos throughout cosmic time. Matter flows along the large-scale cosmic structure funneling additional gas to a dark matter halo, transforming a fraction of this gas into stars (Somerville and Davé, 2015; Naab and Ostriker, 2017).

But going into more detail, how a central galaxy is formed inside a dark matter halo? This phenomenon is also described in the context of Λ-CDM model: baryonic gas is gravitationally trapped into the potential wells of dark matter. This gas is radiatively cooled and precipitates towards the center of the dark haloes. Since halos acquire a small angular momentum by the tidal torques, gas which is being dissipated and falls towards the center, partially conserves its angular momentum and infalls down until virial equilibrium is reached.

In summary, we can now date the Big Bang to 13.8 Gyr back in time, and point out several key phases in a chronological way, such as the inflationary universe, the recombination phase, the reionization, and the assembly of matter in large scale structures hosting galaxies of different types, all taking shape along cosmic time (Figure 1.2).

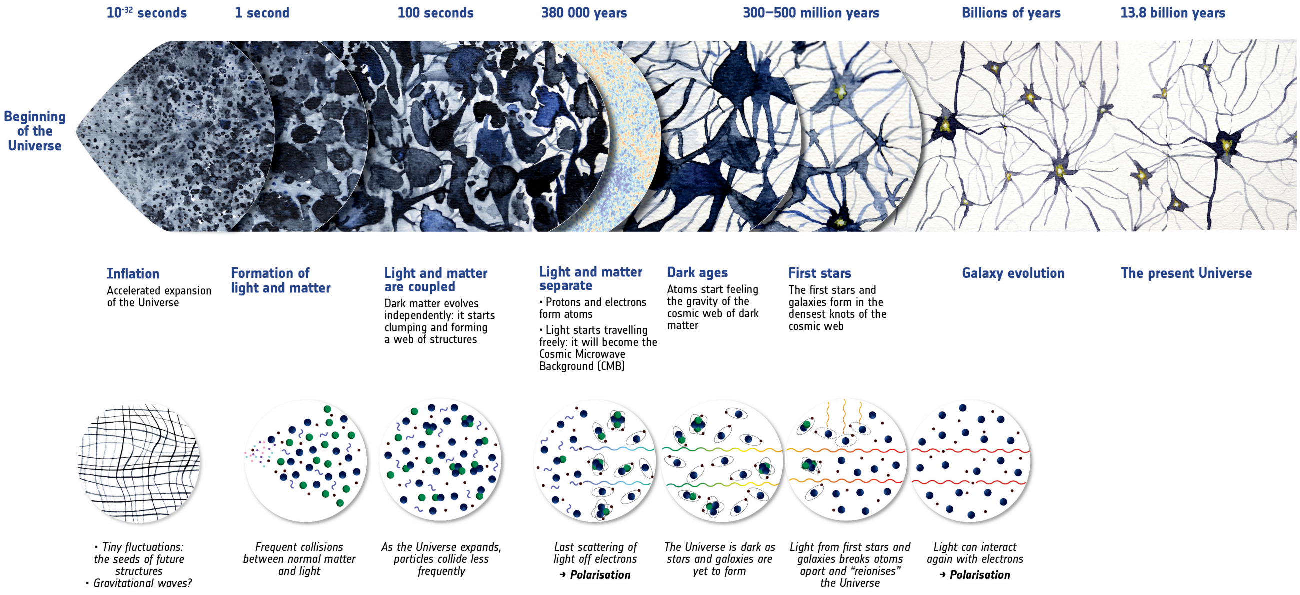

Figure 1.2: A summary of the almost 14 billion year history of the Universe, showing in particular the events that contributed to the Cosmic Microwave Background. *Upper part.* Artistic view of the evolution timeline of the cosmos on large scales. The processes depicted range from inflation, the brief era of accelerated expansion that the Universe underwent when it was a tiny fraction of a second old, to the release of the CMB, the oldest light in our Universe, imprinted on the sky when the cosmos was just 380 000 years old, and from the 'Dark Ages' to the birth of the first stars and galaxies, which reionized the Universe when it was a few hundred million years old, all the way to the present time. *Lower part.* Zoomed-in view on some of the microscopic processes taking place during cosmic history: from the tiny fluctuations generated during inflation, to the dense soup of light and particles that filled the early Universe, from the last scattering of light off electrons, which gave rise to the CMB and its polarization, to the reionization of the Universe, caused by the first stars and galaxies, which induced additional polarization on the CMB.

1.2 Taxonomy, morphology and classification

The Universe is composed by two main galaxy morphologies: spiral (disk) and ellipticals (spheroidal). Nonetheless, this definition is not completely absolute, since disk galaxies can contain spheroidal components in their centers and spheroidal galaxies may have embedded discs. The spheroidal component in a disk galaxy is called bulge, while a spheroidal system which contains a disk, generally is called disky elliptical.

1.2.1 Hubble classification

Hubble sequence is the most used classification scheme for galaxies introduced by Edwin Hubble in 1926. It is also known as the Hubble tuning-fork diagram due to the shape of its morphological classification arrangement, which consists of a combination of disk and spheroidal or ellipsoidal components present in a galaxy. (see figure 1.3)

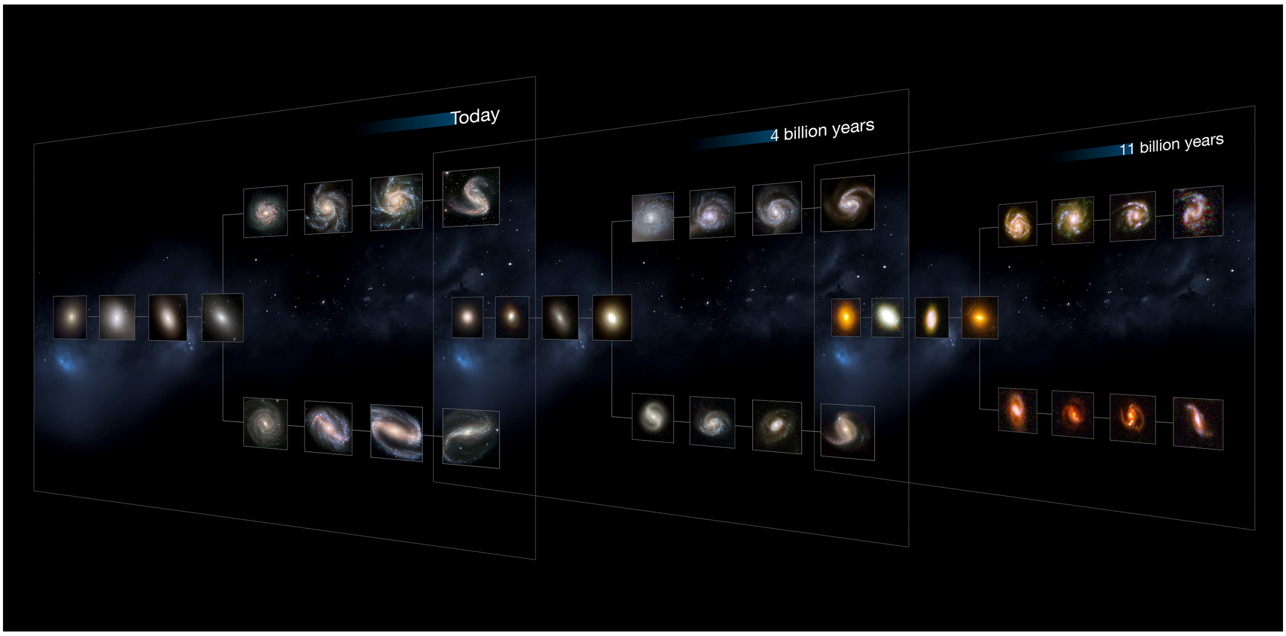

Figure 1.3: The Hubble's sequence through the Universe's history (present day, at 4 billion and 11 billion years ago). Hubble tuning-fork diagram describes and separates galaxies according to their morphology into spiral (S), elliptical (E), and lenticular (S0) galaxies. On the left of this diagram are the ellipticals, with lenticulars in the middle, and the spirals branching out on the right side. The spirals on the bottom branch have bars cutting through their centers. The present-day universe shows big, fully formed, and intricate galaxy shapes. As we go further back in time, they become smaller and less mature, as these galaxies are still in the process of forming. Credit: NASA, ESA, M. Kornmesser.

Disk galaxies

Spiral galaxies, are thin disk-shaped systems mainly supported by rotation. They exhibit spiral patterns composed by gas and stars. They have a blue, young stellar population. Their mechanism formation is through a secular evolution.

Spheroidal galaxies

Elliptical galaxies are spheroidal, ellipsoidal systems which are mainly supported by the random motions of their stars. They have a red, old stellar population. Their mechanism formation is through violent interactions between disk galaxies and mergers. They are known as early-type galaxies because the first astronomers, who made the classification, thought that the evolution of galaxies were from the simpler systems (ellipticals) to the more complex (spirals). Early and late was a time sequence. Today, we know that it is in fact the opposite: galaxies begin their life under a spiral shape (late-type) and then through interactions and mergers, become ellipticals (early-type).

1.3 Galaxy Mergers

In the hierarchical framework of galaxy formation, the role that mergers play in the assembly of galaxies and dark matter is of utmost important. A *galaxy merger* happens when two (or even more) galaxies collide forming a new system characterized with very different properties which are coming from its progenitors (referring to the halos). Several effects are produced as a result of these gravitational interactions between galaxies, which depend on factors such as their mass ratio (size), components (gas and stars) and interaction angles. Inside of the Λ-CDM model, dark matter halos grow hierarchically, i.e., larger halos are formed by the coalescence of smaller progenitors. The formation history of a dark matter halo can be described by a "merger-tree" that traces all its progenitors (see e.g. Figure 1.4). The growth of a massive halo is given by a consecutive accumulation of a large number of very small halos, considered as smooth accretion. The merging of two dark matter halos of similar mass leads to a violent relaxation that rapidly transforms the orbital energy of the progenitors into the internal binding energy of the quasi-equilibrium remnant. If such halos host central galaxies, galaxies also merge as part of the violent relaxation process and producing a new central galaxy in the final halo+galaxy system. When the interacting galaxies have a high cold gas content, the merger produce a strong star formation or even triggers an AGN activity, but if the two merging halos have very different mass, the dynamical processes are less violent. The smaller companion orbits the main galaxy during a long period of time leaving traces or collisional debris of such interaction.

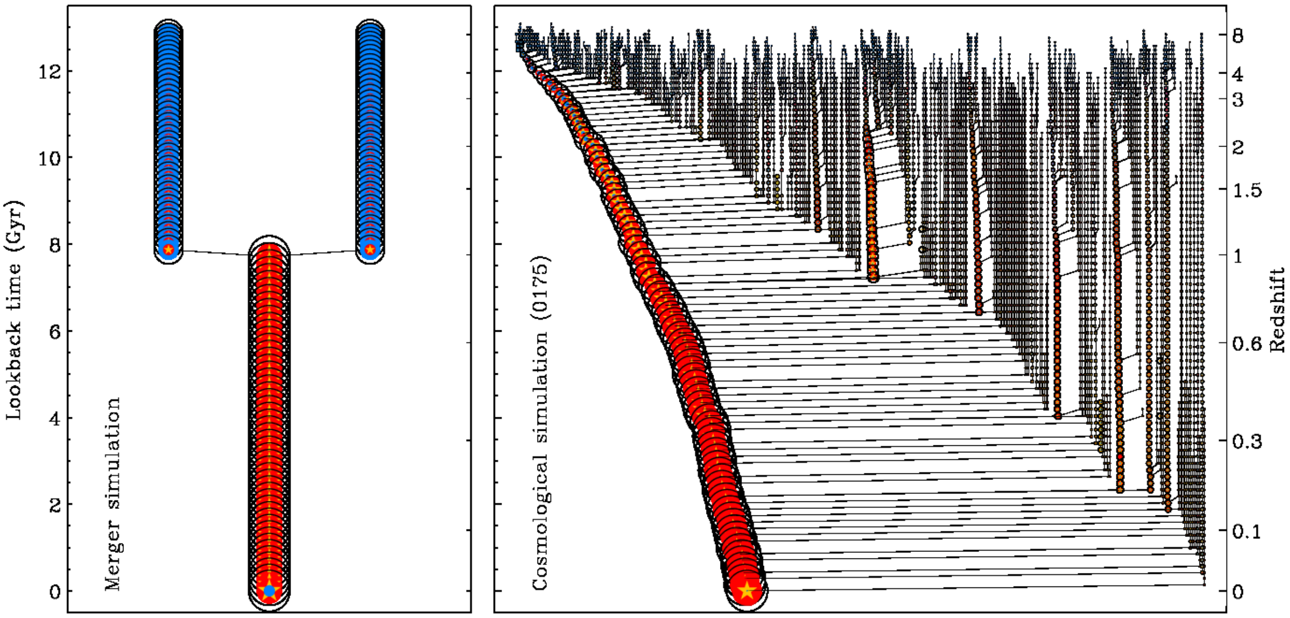

Figure 1.4: *Left panel*: Schematic "merger-tree" representation of a binary disc merger simulation. Two gas-rich (blue) stellar (yellow) discs with little hot gas (red) merge at z∼1 and form an elliptical galaxy. *Right panel*: Merger tree from a cosmological zoom simulation of the formation of a halo and its galaxy within the concordance cosmology. Black circles indicate the dark matter halo mass at every redshift with the symbol size proportional to the square root of the normalized halo mass at z=0. The yellow stars indicate stellar mass, the blue and red filled circles show the cold and hot gas mass within the virial radius (Naab et al., 2014). It is evident that continuous infall of matter in small and large units is an important characteristic of the assembly of massive galaxies. The galaxy shown has no major merger since z∼3. Others galaxies of similar mass can have up to three major mergers. The mass growth, however, is always accompanied by minor mergers.

By means of *dynamical friction*, the small companion or satellite transfers energy from its orbit to the main halo, while tidal effects remove mass from its external regions until it is dissolved. N-body numerical simulations have shown that the merger of two galaxies of equal mass (either spiral or elliptical) forms an elliptical galaxy (see e.g. Toomre, 1977). Current hierarchical models of galaxy formation assume that most elliptical galaxies are merger remnants. Nonetheless, if gas cools into this merger remnant with significant amount of angular momentum, a new disk may form, producing a disk-bulge system like that in an early-type spiral galaxy.

1.3.1 Types of galaxy mergers

Galaxy mergers can be phenomenologically classified into three main groups according to the properties and the nature of the encounters involved in the galaxy interaction. These categories are the number of members in the interaction, the progenitors mass ratio and the gas content.

Number of members in the interaction

- Binary merger. A binary merger is produced when only two galaxies participate in the interaction process (see e.g. 1.5).
- Multiple merger. This kind of interaction takes place when more than two members are involved in the merger process (see e.g. 1.6).

The progenitors mass ratio

This category concerns the comparison between the masses of the main and the companion progenitors of the interacting system. Usually, in the literature this classification is given in terms of the *mass ratio*, defined as q $\equiv M_1/\mathrm{M}_2$ (see definitions in high-resolution numerical simulations, Boylan-Kolchin et al., 2005; Bournaud et al., 2005, 2007; Cox et al., 2006).

- Major merger. A major merger occurs when two galaxies have similar masses, and has a mass ratio equal or larger than 1:4. In a major merger event, violent relaxation plays an important role during the relaxation of the merger remnant, where the remnant ends with a little resemblance to its progenitors. The resulting system shows multiple vestiges, such as tidal tails and/or shells.
- Minor merger. A Minor merger takes place when the secondary progenitor is significantly less massive than the main progenitor. Its mass ratio is smaller than 1:4 but larger or equal to 1:10. Mergers with values below the mass ratio 1:10 are considered to produce imperceptible effects on the main galaxy. During the phase mixing of a minor merger event, a damping process dominates and the merger is less destructive, so that, the remnant of a minor merger often resembles its most massive progenitor. The resulting system displays signatures such as stellar streams and plums which trace the orbit of the small companion around the main galaxy.

Gas content

This classification refers to the role that gas dynamics plays in a merger process. Gas responds to pressure forces and gravity in a different way than stars and dark matter particles, since gas can lose energy through radiative cooling. Additionally, gas clouds generate collisions, whilst streams of stars can freely interpenetrate.

- Wet merger. Mergers between gas-rich progenitors are known as "wet" mergers. Wet mergers produce an increase in the star formation rate, giving place to the production of globular clusters. When a blue late-type galaxy is transformed into a red early-type galaxy a quasar activity can be triggered (Lin et al., 2008).

- Dry merger. Mergers between gas-poor progenitors are called "dry" mergers. The star formation rate does not show important changes.

- Damp merger. A damp merger is the outcome of the interaction between a wet and a dry mergers. In this case there is a moderate amount of gas that can produce a significant star formation rate, but not the generation of globular clusters .

- Mixed merger. It is the product of the interaction between gas-rich and gas poor galaxies, e.g, between a blue late-type and a red early-type galaxy.

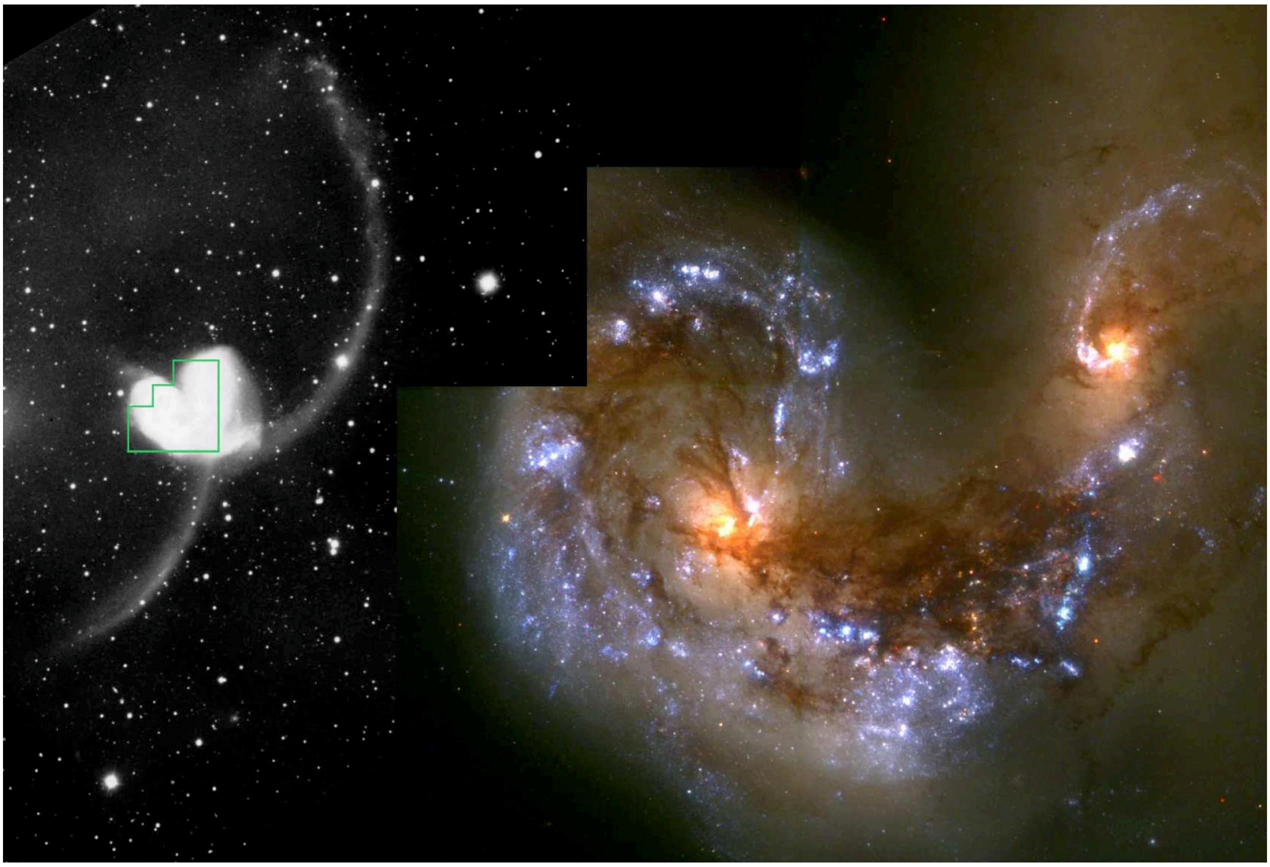

Figure 1.5: NGC 4038 and 4039, also known as the Antennae galaxies. The long tails of luminous matter formed by the encounter resemble an insect's antennae. A ground-based view of NGC 4038/4039 (left) displays their distinctive antennae. The Hubble Space Telescope image (right) shows more than 1,000 brilliant star clusters at the heart of the collision.

Figure 1.6: In 1877, French astronomer Édouard Stephan turned a telescope to a spot in the constellation Pegasus and discovered this collection of five large galaxies. Stephan's Quintet, as the group is now known, includes four distant galaxies that are connected to each other through gravity and one galaxy that is much closer to us but just happens to lie in the same direction in the sky. Credits: NASA, ESA, and the Hubble SM4 ERO Team.

1.4 Low surface brightness galaxies

The conception about the surface brightness universe has changed since 1970. One of the pioneering work was presented in Disney (1976), where it was exposed the problem on the bias by selection effects due to the sky background that limits our knowledge of galaxies. Concernings were based on the idea of a “hidden galaxy” population to be found, and the *announcement* to search for a new observing techniques in order to identify and quantify such a hidden galaxies. Sandage (1976) reported an analysis of extended regions of faint nebulosity, nowadays called “cirri”, which is a diffuse emission at very low surface brightness (LSB) levels produced by the scattering of stellar light due to interstellar dust grains. This emission was shown to extend over the entire sky, and was detected in wide-field photographic plates using fast-optics telescopes. The problematic raised about the surface brightness bias exposed in these studies, led to the prediction of the existence of low surface brightness galaxies whose observations were not available due to the instrumental limitations of that time.

A low surface brightness (LSB) galaxy usually has a surface brightness limit $> \mu_B \sim 23.8$ mag arcsec^{-2}. This common characteristic can be present in several types of galaxies with different properties and contents. For example, dwarf galaxies, ultra-faint dwarf spheroidal (dSphs), gas-rich irregulars with low star formation. Also galaxies with larger sizes including the recently discovered extended Ultra-Diffuse Galaxies (UDGs) and massive giant disk galaxies like Malin 1, which was the first identified LSB galaxy discovered by David Malin in 1986. This galaxy is a giant barred spiral galaxy located at 369 Mpc away in the Virgo cluster.

1.4.1 Gas content in LSB galaxies

Some of the theoretical challenges that might be implemented in the galaxy formation models in more detail, is how galaxies accrete gas. Gas accretion is a fundamental process to describe galaxy formation. In the numerical studies it is unclear whether the gas accreted onto the galaxies is from cold filaments (Kereš et al., 2005; Dekel et al., 2009) or whether the filaments dissolve in the halos and the accretion is smoother (Nelson et al., 2013). The gas surrounding galaxies outside their disks or the interstellar medium (ISM) and inside their virial radius is known as the "circumgalactic medium" (CGM). This CGM is a source for the star-foming fuel of a galaxy, the place in which galactic feedback and recycling process occurs, as well as the key regulator of the galactic gas supply (see Figure 1.7, Tumlinson et al., 2017).

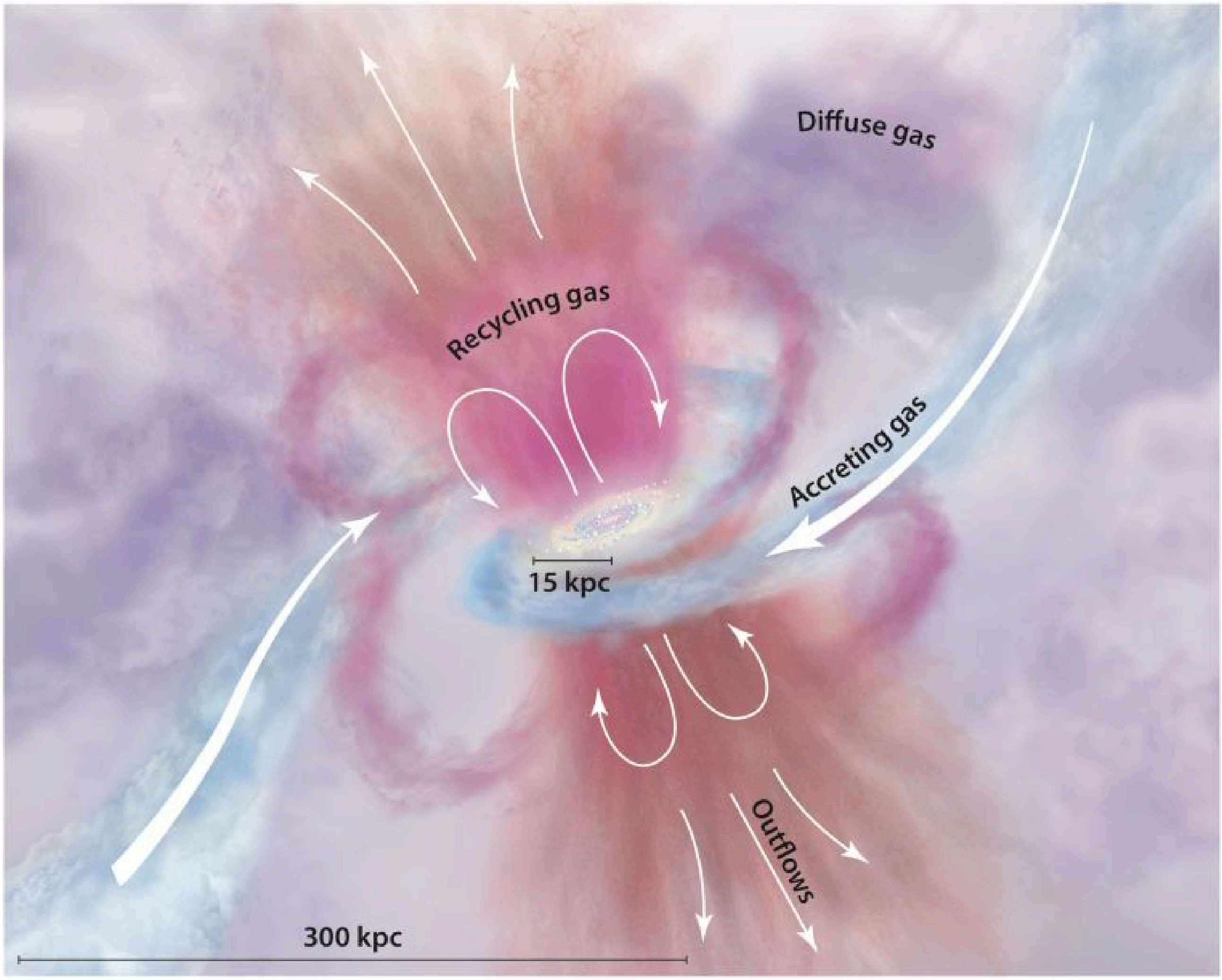

Figure 1.7: A cartoon view of the circumgalactic medium. The galaxy's red central bulge and blue gaseous disk are fed by filamentary accretion from the IGM (blue). Outflows emerge from the disk in pink and orange, while gas that was previously ejected is recycling. The diffuse gas halo in varying tones of purple includes gas that is likely contributed by all these sources and mixed together over time. (Tumlinson et al., 2017)

1.4.2 Shell galaxies

After the publications of the largest catalog of shell galaxies by Malin and Carter (1983), which presents 137 galaxies displaying shell structures at large distances from the central galaxy, several studies have been focused on this topic and describe different scenarios for the mechanism of shell formation. In a first hypothesis, Fabian et al. (1980) suggested that the shells are regions of star formation in a shocked galactic wind in elliptical galaxies, which are preceded by a subsequent star formation under specific conditions. Williams and Christiansen (1985) proposed that visible stellar shells at larger distances from the center of isolated elliptical galaxies were generated by a blast wave expelled during an active nucleus phase in the early stages of the galaxy, sweeping the interstellar medium out of the galaxy into an expanding gaseous shell which radiatively cools behind its leading shock front. On the other hand, the simulations of Quinn (1984) showed that shell formation in normal ellipticals were produced by a disruption of a small companion (disk) induced by a big elliptical galaxy of 10 to 100 times more massive than the companion. Quinn (1984) and Dupraz and Combes (1986) tested the Schweizer's model (Schweizer, 1980), where is assumed that shells are the result of mergers or accretions involving disk systems. The simple N-body models developed by Quinn (1984) turned out to be consistent with structures formed as a result of collision between an elliptical and a disk galaxy. Concretely, it was shown that shells arises from a *phase wrapping* of the dynamical cold disk in the fixed potential well of the elliptical galaxy. The dynamics of the shells traced by test particles, as well as the large range in radius that they cover, allowed them to develop an impression of the detailed shape of potential wells in elliptical galaxies.

1.4.3 Ultra-Diffuse Galaxies

Ultra-Diffuse Galaxies (UDGs) are objects which have very extended morphology, sizes of $R_{eff} \sim 1.5$ - 5 kpc and faint central surface brightness of $\mu_{0,V} \geq 24$ mag arcsec^{-2}. The estimation of their stellar mass is some few 10^7 $M_\odot$ and their luminosities of $\sim 10^8$ $L_\odot$. Typically, they have a high dark matter content (Amorisco and Loeb, 2016). Most UDGs are discovered in high-density environments such as galaxy clusters and groups, which populate mainly the red sequence. Some are found in low density environments. Those detected in the field, are mainly gas-rich, bluer. The diffuse morphology and faint surface brightness make them difficult to distinguish from the sky background.

1.5 Objectives

The present work is focused on several goals carried out under the regime of the low surface brightness Universe. The method used is based in observational and theoretical tools in order to achieve a wide and comprehensive analysis on the formation mechanism of the low surface brightness galaxies traced mainly by the properties of their external regions.

Particularly, from a theoretical perspective, a hydrodynamical numerical simulation is analyzed in order to *test the merger history of an early-type galaxy traced by their faint stellar substructures*. Additionally, by using semi-empirical models, a series of experiments and calibrations were performed in a semi-empirical galaxy-halo connection mapped into the scaling relations previously developed in the Master's thesis of Mancillas 2015, with the idea of applying this approach to LSB galaxies and UDG galaxies in a future work.

On the other hand, from the observational point of view, we make use of radio observations of the ^{12}CO molecule to search for *molecular gas content in shell galaxies and Ultra-Diffuse*

Galaxies in order to investigate the gas dynamics and thus make inferences on their origin and formation mechanism. Below it is described the most relevant specific objectives of this project.

- Statistically infer the spin parameter of the baryonic matter from which the observed disk galaxies were formed and examine how much it is deviated from the halo spin parameter according to their mass and environment. Apply the method also to a sample of observed galaxies from CALIFA and MaNGA surveys.

- Predict the distributions of the effective radius, R_e, and (stellar and gaseous) surface densities of galaxies based on their mass.

- Mapping the global stellar-to-halo mass relations, M_*-M_h, for both late- and early-type galaxies over local relations such as stellar-to-dynamical mass, M_*-M_{dyn}, and baryonic-to-dynamical mass, M_{bar}-M_{dyn}, within 0.5, 1, 1.5 and 2 R_e as a function of the mass. Use these results as restrictions on the models and simulations of galaxy evolution. Compare these results with observations from MaNGA and CALIFA surveys, and explore consistencies and possible difficulties.

- Explore and resolve the potential inconsistency that has been reported in semi-analytical models and simulations between the galaxy stellar mass function and the zero point of Tully-Fisher relations. Explore related issues such as assembly bias.

- Analyze a hydrodynamical cosmological simulation to build a comprehensive interpretation of the properties of fine structures and estimate their visibility time-scale in order to reconstruct the past merger history of galaxies. Additionally, examine the dependence on several properties such as the surface brightness limit and projection effects.

- Make a census of several types of LSB fine structures by visual inspection of individual snapshots at several time-scales.

- Characterize the shape of the faint stellar structures in the outskirts of the main central galaxy to make a census of the number of these structures and classify them into tidal tails, streams and shells.

- Make interpretations on the shape and frequency of fine structures observed in deep images in terms of mass assembly from the estimation of the survival time of collisional debris.

- Search for molecular gas by means of the ^{12}CO molecule in a sample of nine selected shell galaxies with the available radio telescopes such as the IRAM-30m telescope, in order to examine its distribution and association with shells structures.

- Test the mechanism of shell formation through phase wrapping (or space wrapping if it is the case) during a radial minor mergers proposed in the numerical simulation models.

- Determine the shell velocity from its molecular gas, as optical redshifts from the stellar component are difficult to get. Indeed, getting stellar velocity is costly and requires the use of spectrographs with IFU capabilities on large telescopes. The HI maps suffer from low spatial resolution, so molecular gas might be one of the best ways to determine shell kinematics.

- Derive the amount of molecular gas in shells and in the center for those cases where it was possible the detection of ^{12}CO molecule. Quantify the amount of molecular gas found in each pointing, relying on the empirically established proportionality between the CO(1-0) luminosity and H_2 mass, for a large number of Milky-Way like galaxies.

- Examine the expected association between the stellar and gaseous (HI or CO) shells, and discuss the various scenarios, taking into account the predictions from N-body numerical simulations.

- Search for molecular and atomic gas in several samples of selected UDG galaxies with the available radio telescopes such as the IRAM-30m telescope and Nançay Radio-Telescope, in order to analyze the gas distribution in this type of galaxies.

- Estimate the upper mass limit on the content of atomic and molecular gas for DGSAT-I and Dragonfly 44, which have a measured redshift.

1.6 Methodology

To achieve the particular goals of this thesis described in the previous section, we have used a method based in both theoretical and observational perspectives.

In first instance, to obtain a global semi-empirical galaxy-halo connection, we generate a volume-complete synthetic catalogues for spatially-resolved disc-bulge-halo galactic systems, which consists mainly of two parts: a) the application of a semi-empirical approach on a given simulated cosmological N-bodies box, and b) the use of halo properties and their respective stellar and gaseous mass fractions as initial conditions for the static models that produce the resolved galaxies.

The synthetic catalogue is generated using the Bolshoi-Planck (BolshoiP), Small Multi Dark-Planck (SMDPL) and MultiDark-Planck (MDPL) simulations described in Klypin et al. (2016) and analyzed in Rodríguez-Puebla et al. (2016). By means of statistical methods, each mock galaxy in our catalogue has individual information of its stellar mass and color. Once these two values are known, we assign the gas fraction inferred in (Calette et al., 2018). In summary, in our synthetic catalogue of the Local Universe, each mock galaxy is identified by these properties: color (g-r), stellar mass (M_*), atomic and molecular gas mass (M_{gas}), as well as the halo properties that host it, such as the halo mass (M_h), concentration (C) and halo spin parameter (λ_h). Once our synthetic catalogue is generated, for each individual mock galaxy is applied a "static" model previously developed in Master's thesis of Mancillas 2015 (see also Mancillas et al., 2017). The dynamic models developed in this project are mainly based on the approach introduced in Mo et al. (1998) and its extension in Dutton et al. (2007).

Secondly, to perform the analysis on the identification and classification of low surface brightness (LSB) features observed in a host halo, we have used the hydrodynamical numerical simulations previously presented in Martig et al. (2009) and Martig et al. (2012) in order to follow galaxy evolution in the Λ-CDM cosmological context. The technique used in these simulations consists of two steps: first a Λ-CDM cosmological simulation is run, with only dark matter, while the merger and accretion history for a given halo is extracted. In the second step, the mass assembly history is re-simulated at higher resolution, replacing each halo by a realistic galaxy, containing gas, stars and dark matter.

Consequently, a mock image catalogue of surface brightness maps composed by 105 images (35 snapshots in three different 3 projections) was built. For each image, we prepare two g-band maps, one with a cut at 33 mag arcsec^{-2} (value corresponding to the surface brightness limit in Valls-Gabaud and MESSIER Collaboration, 2017) and one at 29 mag arcsec^{-2} (value corresponding to the surface brightness limit in the MATLAS survey, Duc, 2017). The first snapshot start at 3.5 Gyr and the last one finish at 13.7 Gyr (plus an extra simulation which evolved until 15.7 Gyr), with a time interval of 0.3 Gyr. After, we proceed to give a phenomenological description of collisional debris through a via visual identification in a similar way than in some previous observational surveys (see e.g. Atkinson et al., 2013; Duc et al., 2015; Duc, 2017). We were a team of five professional astronomers who made a visual inspection in each mock image. We identified and classified the observed fine structures (tidal tails, stellar streams and shells) and made a census of them for both surface brightness cuts.

On the other side, as a part of this PhD project, a search for molecular gas was made, addressed to investigate the properties and dynamics of gas present in shell galaxies and ultra-diffuse galaxies. For this task, we performed observations of the ^{12}CO(1-0) and ^{12}CO(2-1) line emission for several samples of selected shell galaxies and UDGs, carried out at IRAM 30-m telescope at Pico Veleta, Spain. We choose shell galaxies observable from the northern hemisphere, which were previously observed in HI-21cm and in CO in the millimeter domain. Observations were made during July and September 2017 (Arp 230, NGC 474 and NGC 3934). Additionally, we included the data reduction and analysis for another set of shells galaxies previously observed during September, October and November 2000 (Arp 10, NGC 3032, NGC 3656, NGC 5018, NGC 7600 and Arp 295N).

In the case of the ultra-diffuse galaxies we choose targets with measured redshift. DGSAT-I and Dragonfly 44, observations were made during two seasons (December 2016 and March 2017) at IRAM-30m, and also were observed in HI line at 1420.4 MHz at Nançay radio telescope. Besides, we also carried out more UDG observations, including five blue selected UDGs (DDO 99, UGC 2162, UDG-B, UDG-B3 and UDG-B5) and four HI-selected blue UDGs (AGC 114882, AGC 219533, AGC 238636, AGC 229110), which will be analyzed in detail in a future work.

The data reduction was done with the CLASS program of the GILDAS software package (`http://www.iram.fr/IRAMFR/GILDAS`). To quantify the amount of molecular gas found in each pointing, we rely on the empirically established proportionality between the CO(1-0) luminosity and H_2 mass, for a large number of Milky-Way like galaxies (e.g. Bolatto et al., 2013). The derived M(H_2) was determined assuming the standard CO-to-H_2 conversion factor of $X_{CO} = 2\times10^{20}$ cm^2(K km/s)$^{-1}$, applicable to Milky Way-like galaxies.

1.7 Contents

In addition to the present chapter on a general introduction, this manuscript contains four chapters more corresponding to four independent blocks plus a global conclusion, which is organized as follows: Chapter 2 describes the semi-empirical galaxy-halo connection projected towards the scaling relations. In Chapter 3, I present the analysis on the hydrodynamical numerical simulation to test the merger history of an early-type galaxy traced by their low surface brightness stellar substructures. Observations on molecular gas content for shell galaxies and ultra-diffuse galaxies, the selected galaxy samples and derived results are presented in Chapter 4 and Chapter 5, respectively. Chapter 6 summarizes the conclusions.

Chapter 2

Scaling relations and mass distributions in a semi-empirical model of galaxy evolution

This Chapter presents a semi-empirical galaxy-halo connection mapped towards the galaxy scaling relations and their internal mass distributions. We generate a mock catalog of local galaxy population using cosmological numerical simulations and the HI and H_2 mass fractions. For each mock galaxy, we apply a "static" model previously developed in Master's thesis of Mancillas 2015 (see also, Mancillas et al., 2017) and enhanced to include input parameters directly from N-body cosmological simulation boxes described in Rodríguez-Puebla et al. (2016), and thus obtain a volume complete galaxy population up to the limit in M_* of $\sim 10^{8.5}$ $M_\odot$. I also present early applications of our semi-empirical models to the observational internal mass distributions for the galaxies of CALIFA survey and for the Virgo cluster galaxies in the SHIVir survey.

2.1 The semi-empirical galaxy-halo connection mapped towards the galaxy scaling relations and their internal mass distributions

By means of a semi-empirical approach, we explore the projection of the global statistical galaxy-halo connection towards the structural-dynamic properties of galaxies, separated in both early- and late-type galaxies.

We generate a volume-complete synthetic catalog for a spatially-resolved disco-bulge-halo galactic systems into boxes of the Bolshoi-Planck, Small MultiDark-Planck and MultiDark-Planck ΛCDM numerical simulations presented in Klypin et al. (2016) and analyzed in Rodríguez-Puebla et al. (2016), which reproduce the luminosity, stellar mass and two-point correlation functions (Rodríguez-Puebla et al., 2015), as well as the color distributions and HI and H_2 mass fractions, recently computed in Calette et al. (2018). In our synthetic catalog, each mock galaxy is identified by the following properties: color (g-r), stellar mass (M_*), atomic and molecular mass (M_{gas}), as well as the halo properties, such as halo mass (M_h), concentration (C) and halo spin parameter (λ_h). Then, the galaxy distribution is divided in red and blue populations using a cut in the stellar mass-color ratio. This paper is focused mainly on late-type galaxies for which a spatially resolved galactic system is modeled and previously developed in the Master's thesis of Mancillas 2015 (see also Mancillas et al., 2017). Nonetheless, we also propose a simple model for galaxies dominated by spheroids. The dynamical “static” models developed are mainly based on the approach introduced in Mo et al. (1998) and its extension by Dutton et al. (2007).

We use an heuristic approach and include a merger fraction in order to calibrate the underlying parameters which reproduce the observational correlations of the size-mass ($R_e - M_*$) and the bulge-to-total mass ratio vs mass (B/T-M_*) at high masses, where the merger effects are highly significant. As a result, our method is used as a sophisticated tool to estimate the *initial spin parameter of the baryons from which disc galaxies form*, λ_{bar}. Up to $\log(M_h/M_\odot)\sim 11.5$, λ_{bar} and its dispersion are the same than those of dark matter halos, but at larger masses λ_{bar} decreases with M_h (and hence M_*). The predicted stellar and baryonic Tully-Fisher relations agree with observations.

We explore the effects of the global M_{bar}-M_h relation and its dispersion on the internal mass distributions of our mock galaxies. We found that the disk-to-total velocity ratio at 2.2 scale radii is always a submaximal type. The “luminous” mass fraction evaluated at one effective radius (1 R_e) has its maximum (about 0.5 on average) for galaxies with Vmax ≈200 km/s, Σ_e ≈500 $M_\odot/pc^2$, and $M_* \approx 5 \times 10^{10}$ $M_\odot$. For lower values than B/T⩽0.5, disk galaxies are more and more dominated by dark matter at 1 R_e, but for larger values, a clear print of the M_{bar}-M_h relation shape is shown.

2.2 Early applications of semi-empirical models to observational internal mass distributions

Semi-empirical models have been used to compare with observational internal mass distributions. In paper II, is presented the study of ionized gas and stellar kinematics for 667 spatially resolved galaxies of the CALIFA Survey (Sánchez et al., 2012), aimed to study kinematic scaling relations, such as the Tully & Fisher (Tully and Fisher, 1977) and the Faber & Jackson (Faber and Jackson, 1976) relations, as well as combination of them through the S_K parameter defined as $S_K^2 = K\ V_{rot}^2 + \sigma^2$ (with $K = 0.5$). In this work is analyzed the distribution of the dynamical-to-stellar mass relation within 1 R_e, based in the S_K^2 parameter, and it is compared with predictions from numerical simulations and semi-empirical modelling approaches. Specifically, for the latter theoretical predictions, it was generated a population of galaxies with bulge-to-disc mass ratios lower than ~ 0.7, modeled by loading the bulge-disc systems into Λ-CDM halos, taking into account the adiabatic contraction of the inner halo by the baryons (see Figure 2.2, Aquino-Ortíz et al., 2018). The predicted stellar-to-dynamical masses within 1 R_e, inherit partially the shape of the stellar-to-halo ($M_\star$-M_h) mass relation which bends to lower $M_\star/M_h$ ratios both at lower and higher masses. Observational inferences based on the $S_{0.5}$ parameter in agreement with semi-empirical predictions, show the possibility to attain a connection between the inner galaxy dynamics of the local galaxy population and the properties of the cosmological dark matter haloes.

On the other side, following our semi-empirical approach, we generated the stellar-to-total mass relation (STMR) measured within 2 R_e and we compared with the observational internal mass distributions from the Virgo cluster galaxies in the “Spectroscopy and H-band Imaging of the Virgo cluster” (SHIVir) survey (Roediger and Courteau, 2015) (see Figure 2.2, Ouellette et al., 2017). As a result of this comparison, it was found that our STMR match well the SHIVir LTG sample below $M_{tot} < 10^{10}\ M_\odot$, with slopes being nearly identical.

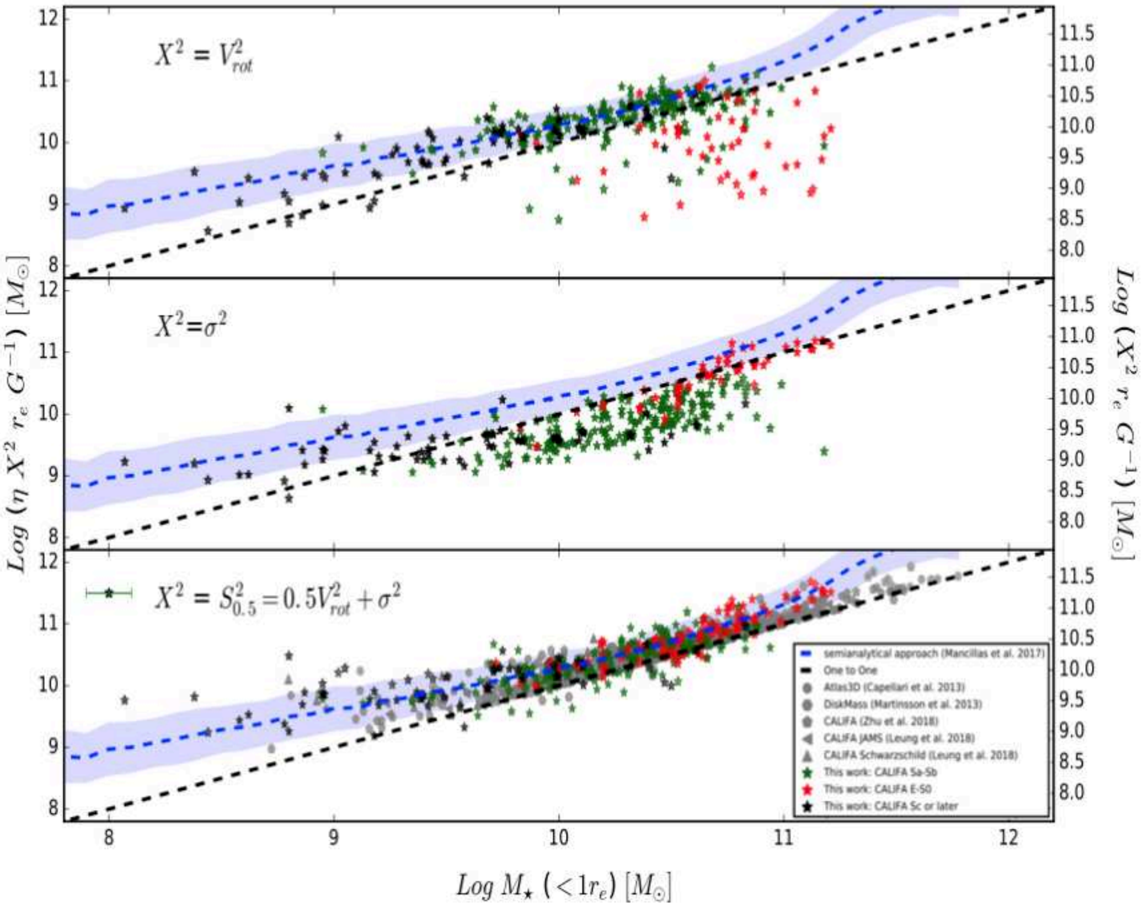

Figure 2.1: Accuracy of the M_{dyn}-$M_\star$ relations based on the $S_{0.5}$ parameter. In the top and medium panels we assume that galaxies are rotation or velocity dispersion dominated to estimate the dynamical mass within the effective radius. The red, green, and black stars represent the CALIFA sample, whereas the grey symbols are from the literature compilation. The $S_{0.5}$ dynamical mass estimations perform better than the ones based either only on rotation or dispersion. In the bottom panel we used the $S_{0.5}$ parameter to estimate the dynamical mass and compare them with theoretical predictions based on detailed dynamical models. All the estimated M_{dyn}-$M_\star$ relations are comparable and consistent with observations within the uncertainties. As a reference we also show the semi-empirical predictions of Mancillas et al. (2017) (blue shaded region, see text) which use $\eta = 1$ and are also consistent with our estimations.

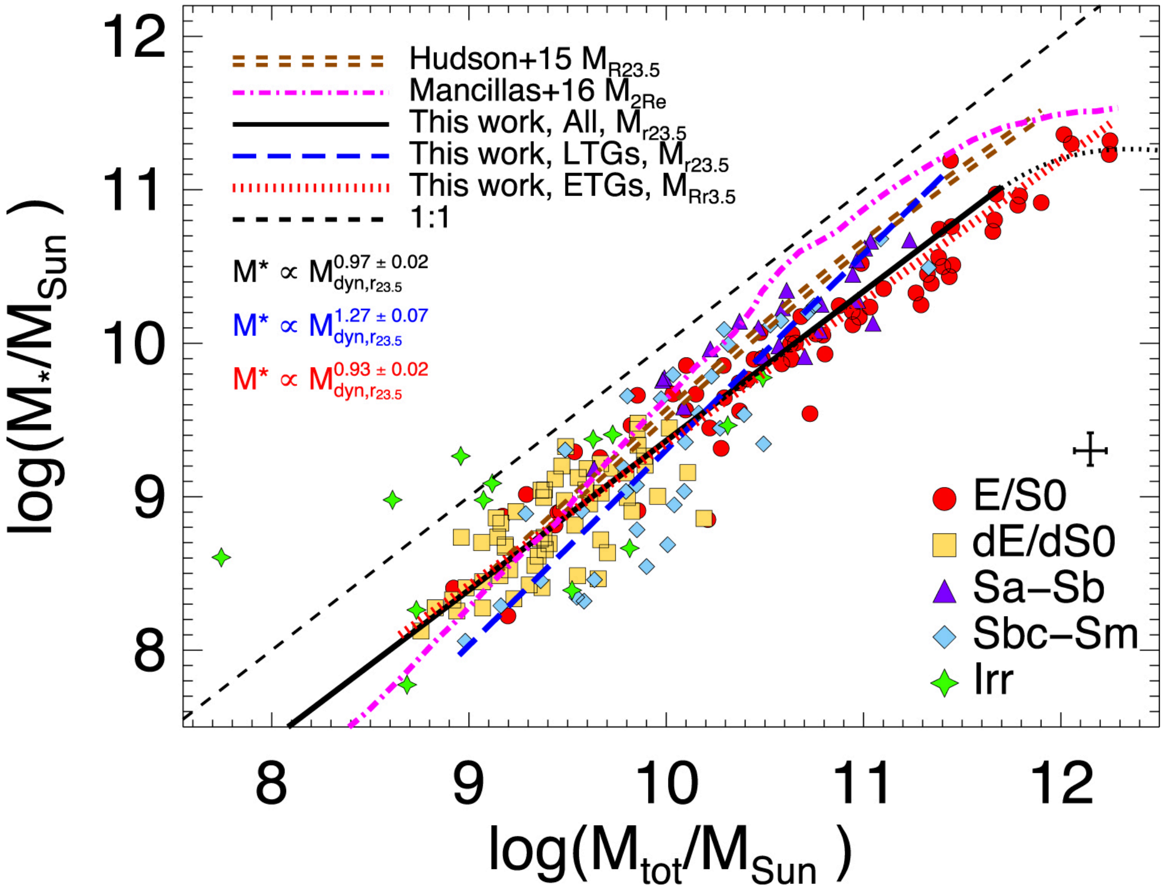

Figure 2.2: The stellar-to-total mass relation (STMR) from Mancillas et al. (2017) for simulated late-type galaxies (LTGs), with the stellar mass M_* and total mass M_{tot} both measured within 2 R_e, is in pink. The SHIVir STMR is shown in blue for LTGs (Irr galaxies are excluded given their highly truncated and/or uncertain RCs), and in red for ETGs. The dashed line is again the 1:1 line.

2.3 Conclusion and perspectives

The cosmological scenario Λ-CDM provides the most suitable context for interpret the nature, origin and evolution of galaxies, particularly those of the Local Universe. In this paper, we have explored the consistency of this scenario for the main observational correlations of a local galaxy population, taking into account the semi-empirical inferences of the baryonic fraction, $f_{bar} = \mathrm{M}_{bar}/\mathrm{M}_h$ or the stellar-to-halo mass (M_*-M_h) relation. The relations stellar-to-halo mass (M_*/M_h–M_h), gas-to-halo mass (M_{gas}/M_h–M_h) and consequently baryonic-to-halo mass (M_{bar}/M_h–M_h), including their intrinsic scatter, were computed separately for both local late- and early-type galaxies in Rodríguez-Puebla et al. (2015) and Calette et al. (2018). A "static" (non-evolutionary) model was implemented as a tool in each galaxy of a synthetic catalog of a local galaxy population in the Master's Thesis of Mancillas 2015 (see also Mancillas et al., 2017). Following the semi-empirical approach, we found a good agreement between our models and the observational scaling relations, such as the size-mass (R_e-M_*) relation, and the bulge-to-total mass vs M_* (B/T-M_*) and gas mass vs M_* (M_{gas}-M_*) ratios. As a remarkable result, our method may be understood as a sophisticated semi-empirical way to determine the *initial spin parameter from which the observed disk galaxies were formed*, λ_{bar}, as a function of M_* and M_h, and be applied to masses up to $M_* \approx 3 - 5 \times 10^{10}$ $\mathrm{M}_\odot$.

In addition to the application of semi-empirical approaches to scaling relations of early- and late-type galaxy population, we will include particular subpopulations of galaxies at different environments, such as Low Surface Brightness Galaxies (LSBGs) and Ultra Diffuse Galaxies (UDGs) in a second paper.

2.4 Paper: The galaxy-halo connection: demography, scaling relations and radial distributions of the luminous and dark matter

MNRAS **000**, 1–27 (2019) Preprint 29 December 2019 Compiled using MNRAS LATEX style file v3.0

The galaxy-halo connection: demography, scaling relations and radial distributions of the luminous and dark matter

Brisa Mancillas[1★], Vladimir Avila-Reese[2], Aldo Rodríguez-Puebla[2] and David Valls-Gabaud[1,3]
[1] *Sorbonne Université, Observatoire de Paris, Université PSL Univ., CNRS, LERMA, 61 Avenue de l'Observatoire, 75014 Paris, France*
[2] *Instituto de Astronomía, Universidad Nacional Autónoma de México, A.P. 70-264, 04510 CDMX, Mexico*
[3] *Institute of Astronomy, Madingley Road, Cambridge CB3 0HA, UK*

Accepted XXX. Received YYY; in original form ZZZ

ABSTRACT
Through a semi-empirical approach, we extend the powerful statistical galaxy-halo connection method towards the galaxy scaling relations and their internal mass distributions. We have performed a demographic description of the global galaxy-halo connection. Our results make restrictions to the models and N-body simulations of galaxy evolution and allow us to constrain the key astrophysical processes as a function of the mass (and environment). By using these restrictions for both early- and late-type galaxies, we have mapped different correlations for galactic disk-bulge-halo systems, as well as for the luminous-to-dynamical mass ratios (including dark matter) evaluated at different effective radius. We have made comparisons between predictions of the semi-empirical approach with the structural-dynamic correlations of observed galaxies, and the internal dynamic as well. We generate a mock catalog of a volume-complete local galaxy population into boxes of the Bolshoi-Planck, Small MultiDark-Planck and MultiDark-Planck ΛCDM numerical simulations, which reproduce the luminosity, stellar mass and two-point correlation functions, as well as the color distributions and HI and H_2 mass fractions. For each mock galaxy seeded in its respective halo, we apply a static model, where a disk-bulge is loaded inside the halo (taking into account the adiabatic contraction) in order to generate a disk-bulge-halo in centrifugal equilibrium, computing its stellar and gas radial distributions.

We use an heuristic approach and include a merger fraction in order to tuning the underlying parameters which reproduce the observational correlations of radius-mass (radius-M_*) and bulge-to-total mass ratio (B/T–M_*) at high masses. Thus, our method becomes a sophisticated tool to estimate the *initial spin parameter of the baryons from which disk galaxies form*, $\lambda_{\rm bar}$. Up to $\log(M_h/{\rm M}_\odot)\sim 11.5$, $\lambda_{\rm bar}$ and its dispersion are the same than those of dark matter halos, but at larger masses $\lambda_{\rm bar}$ decreases with the halo mass, M_h (and hence with the stellar mass, M_*). The predicted stellar and baryonic Tully & Fisher (TF) relations agree with observations. There is no problem with the zero point, since by construction our models are in agreement with the observed baryonic (and stellar) mass function. We also explore the effects of the global baryonic-to-halo mass ($M_{\rm bar}$–M_h) relation and its dispersion on the internal mass distributions of our mock galaxies. We found that the disk-to-total velocity ratio at 2.2 scale radius is always a submaximal type. The "luminous" mass fraction evaluated at one effective radius (1 R_e) has its maximum (about 0.5 on average) for galaxies with a maximal circular velocity, $V_{\rm max}\approx 200$ km/s, effective surface density, $\Sigma_{\rm e}\approx 500\ {\rm M}_\odot/{\rm pc}^2$, and a stellar mass, $M_*\approx 5\times10^{10}\ {\rm M}_\odot$. For lower values than B/T≤ 0.5, disk galaxies are more and more dominated by dark matter at 1 R_e, but for larger values, a clear print of the $M_{\rm bar}$–M_h relation shape is shown.

Key words: galaxies:halo – galaxies:spiral – galaxies:connection

---

★ E-mail: brisa.mancillas@obspm.fr

1 INTRODUCTION

Disk galaxies are the most common morphological type in the Local Universe and observational studies suggest that they were more abundant in the past (Bruce et al. 2012; Buitrago et al. 2013; Mortlock et al. 2013; Avila-Reese et al. 2014). Observational evidence suggests that disc formation is a generic process of galaxy assembly through a secular evolution, while spheroidal components are generated from violent interactions between disk galaxies (Toomre 1977).

According to the Lambda Cold Dark Matter (ΛCDM) cosmological model (see e.g. Planck Collaboration et al. 2018), the formation of large-scale structure is dominated by the gravitational dynamics of dark matter. This process occurs in a hierarchical way and culminates with the assembly of dark matter halos. Since dark matter halos are structures in virial equilibrium, they attract and incorporate a fraction of the baryonic gas into their central regions leading to the formation of a galaxy. Halos are defined by a set of several properties, such as their mass, concentration and angular momentum, which determine in the first instance the amount of gas and its distribution of angular momentum. On the other hand, from an astrophysical point of view, the properties of formed galaxies are established through the processes of star formation and their feedback with the interstellar medium, secular evolution, mergers, the formation of supermassive black holes and their respective feedback with the interstellar medium during AGN phases (see e.g., Somerville & Davé 2015).

One of the main key questions in extragalactic astronomy is to understand how the galaxy properties are correlated with the cosmological properties of their corresponding dark matter halos. Thus, there has been an open discussion in the scientific community on the determination and understanding of a galaxy-halo connection, which is represented in the form of the stellar-to-halo mass relation (SHMR) (Behroozi et al. 2010; Moster et al. 2010; Yang et al. 2012; Behroozi et al. 2013; Moster et al. 2013), and the derived galaxy scaling relations separated in both late- and early-type galaxies. The scaling relations are given by the several galactic parameters such as the stellar mass (M_*), rotation velocity (V_{rot}) or velocity dispersion (σ) and the effective radius (R_e) (Avila-Reese et al. 2008).

The galaxy-halo connection can be determined through three different methods. Two of them based in semi-analytic models of galaxy formation and numerical hydrodynamical simulations (Somerville & Davé 2015), and a third one based in a semi-empirical approach (see e.g. Mo et al. 1998, 2010), in which this work is based. The semi-empirical galaxy-halo connection is established mainly in a demographic level by using an abundance matching technique (AMT), which consist in correlating in a statistical way the dark halo/subhalo population from numerical simulations of large volumes with the observed galaxy population of large surveys. The model uses a mass distribution function and a two-point correlation function and also assumes that the average galactic stellar mass growth follows the average halo mass accretion (see e.g., Wechsler & Tinker 2018).

A semi-empirical approach has allowed to constrain relevant properties of the galaxy-halo connection such as the halo occupation distribution (Berlind & Weinberg 2002; Zheng et al. 2005), the stellar-to-halo/subhalo mass relation (M_*–M_h relation) (Behroozi et al. 2010; Moster et al. 2010; Rodríguez-Puebla et al. 2013) and the relation between the physical processes of the galaxy formation as a function of the scale and environment. In the M_*–M_h relation has been shown that it exists a color/type segregation of galaxies (More et al. 2011; Rodríguez-Puebla et al. 2015; Mandelbaum et al. 2016). In addition, by using the method called Multi-Abundance matching Technique Constraints in Halos (MATCH), it has been possible to include the gaseous component of galaxies in the galaxy-halo connection and hence, constrain the baryonic-to-halo mass relation (M_{bar}-M_h) (Baldry et al. 2008; Calette et al. 2018).

In the present work, we extend the semi-empirical approach towards the scaling relations of galaxies and the radial distributions of dynamic and luminous mass, i.e., *we project the global galaxy-halo connection towards the structural-dynamic properties of galaxies, separated into their two large families.* Thus, we make a complete demographic and structural-dynamic description of observed galaxies and their corresponding dark halos.

In recent years, the new generation of galaxy surveys have provided us with uniform and precise measures of properties for a large number of galaxies, complete in magnitude or volume. Photometric and Integral Field Spectroscopy (IFS) surveys of local galaxies, have allowed us to determine in a homogeneous way the scaling relations and the internal dynamics of galaxies. These surveys include the sample of 260 early-type galaxies from ATLAS^{3D} (Cappellari et al. 2011), the 660 galaxies of CALIFA survey (Sánchez et al. 2012), the $\sim$ 10000 galaxies from MaNGA/SDSS-IV (Bundy et al. 2015) and the $\sim$ 3400 galaxies from SAMI Survey (Allen et al. 2015). For example, in Cortese et al. (2016) and Aquino-Ortíz et al. (2018) are reported the Tully & Fisher (TF) and the Faber & Jackson (FJ) relations of galaxies from SAMI and CALIFA surveys, respectively, as well as the relation of the S_K parameter (defined by $(KV_{rot} + \sigma)^{1/2}$ with K=0.5) versus the total stellar mass. In addition, in Aquino-Ortíz et al. (2018) and Ouellette et al. (2017), it has been examined the dynamic-to-luminous mass ratios evaluated at one scale length as a function of the stellar mass and the morphological type. Simultaneously, the impressive progress made in cosmological N-body simulations has allowed us to have precise predictions for the evolution, properties, and distributions of the ΛCDM halos (see a recent review, Knebe et al. 2013). Thus, having available observational data plus advanced numerical simulations it is possible to achieve an empirical description of galaxies not only at a global level, but also a local one.

In order to extend the galaxy-halo connection we use "static" models introduced in Mo et al. (1998), since this modeling offers us remarkable advantages, such as its simplicity and its proximity with observables. The approach consists into building a disk in centrifugal equilibrium inside of cosmological dark matter halos, taking into account the adiabatic contraction that the baryonic disk induces in the halo during its formation. The model has the following initial conditions: the virial mass (and radius) of the halo, M_h, the concentration, C, the spin parameter, λ, and the baryonic fraction, f_{bar}=M_{bar}/(M_{bar}+M_h). As a result, the model predicts several galactic properties, such as the scale radius, R_D, central surface density, $\Sigma_{*,0}$ of the exponential disc, as well as the rotation curves and their decomposition.

Our static model does not follow the complex evolutive process of galaxies, but set a connection between halo properties and galaxies at a given epoch (z=0 for this case). The model is based in simple assumptions making it a powerful tool to extend the semi-empirical approach. Several studies have developed some modifications on the original models of Mo et al. (1998) in order to introduce a bulge component in the disk, and also the addition of the role that stars versus gas plays on the galaxy formation (e.g., Dutton et al. 2007; Gnedin et al. 2007). In Mancillas 2015, it was applied the modifications mentioned above in order to extend the semi-empirical approach to the properties and the internal correlations of galaxies composed of a disk and a bulge components.

In this paper, we use and improve the tools implemented in Mancillas 2015 (see also Mancillas et al. 2017) in order to generate semi-empirical synthetic mock catalogs directly from N-body cosmological simulation boxes (Rodríguez-Puebla et al. 2016). In this way, we obtain a volume complete galaxy population up to the limit in M_* of $\sim 10^{8.5}$ $M_\odot$. Such populations reproduce by construction the luminosity, the stellar mass and the spatial two-point correlation functions, as well as the color distribution and the HI and H_2 fractions as a function of the mass. We operate on the angular momentum of gas (spin parameter) and the secular/merger effects in order to reproduce the radial distributions of stellar, gaseous and dark masses. We will apply this approach to spatial abundances of particular subpopulations of galaxies at different environments, such as Low Surface Brightness Galaxies (LSBGs) and Ultra-Diffuse Galaxies (UDGs) in a future paper.

Several works have already used the static model of Mo et al. (1998). However, most of them have applied this approach in a deductive sense, i.e, just to predict the galaxy properties out of cosmological initial conditions printed in the simulated halos. This study is addressed to use this kind of models to achieve a semi-empirical description of galaxies based on N-body cosmological simulation boxes, where it can be explored the spatial distributions and different environments of individual simulated halos in order to obtain a synthetic galaxy population in agreement with statistical observed distributions. Each object of this population contains information of the halo properties and multiple properties of disk-bulge-halo system, including radial mass distributions and rotation/dispersion velocities. In previous works it has been explored the projection of the baryonic fraction parameter (f_{bar}) on the scaling relations and internal distributions of modeled galaxies (Dutton et al. 2011; Dutton 2012). However, the baryonic fractions used at that time were obsolete, since the most recent computations of f_{bar} determined from a semi-empirical approach, resulted in a more sophisticated way to obtain it.

This paper is organized as follows. In Section 2, we describe the followed strategy to the mock catalog generation. This section describes the semi-empirical galaxy-halo connection, the “static” model and the procedure to generate each synthetic galaxy of the catalog. In Section 3 we present the main results of this work. We show the scaling relations, such as the radius-M_*, the B/T–M_* and the gas ratio vs. M_*, and we discuss the implications of their corresponding scatter. We also present the predicted stellar and baryonic Tully-Fisher relations and their scatter. We infer the dependence of the initial spin parameter of gas out of which disk galaxies form, as a function of the M_h and M_*. Section 4 introduces the spatial internal mass distributions of the mock galaxies. The luminous and total masses at different radius are studied as a function of M_*, $V_{\rm max}$ and effective stellar surface density of galaxies, $\Sigma_{*,e}$. We also present several velocity ratios evaluated at $2.2R_D$ or at their maximum radius as a function of the global properties, in order to compare them with the available observational correlations. Additionally, we present the dependence of the external slope of the rotation curves as a function of global properties. Finally, in Section 5, we discuss the main results and conclusions.

2 MOCK CATALOG GENERATION

The generation of volume-complete synthetic catalogs for spatially-resolved disco-bulge-halo galactic systems consists mainly of two parts: a) the application of a semi-empirical approach on a given simulated cosmological N-bodies box, and b) the use of halo properties and their respective stellar and gaseous mass fractions as initial conditions for the static models that produce the resolved galaxies. Below is described the methodology followed for the two steps.

2.1 The semi-empirical galaxy-halo connection

We generate a synthetic catalog using the Bolshoi-Planck (BolshoiP), Small Multi Dark-Planck (SMDPL) and MultiDark-Planck (MDPL) simulations described in Klypin et al. (2016) and analyzed in Rodríguez-Puebla et al. (2016). In particular, we use the semi-empirical models under which it is built the fraction of halos hosting blue/red central galaxies and the occupation statistics of blue and red satellites as a function of halo mass (Rodríguez-Puebla et al. 2015). This model takes into account that the stellar-to-halo mass relation (SHMR) is separated in both local blue and red central galaxies. By using statistical methods, the semi-empirical model is generalized in order to constrain the individual colors of synthetic galaxies seeded in dark matter halos, i.e., each mock galaxy in our catalog has individual information of its stellar mass and color. Once these two values are known, we assign the atomic and molecular gas fractions (whence M_{gas}) inferred in Calette et al. (2018), where was done a homogeneous compilation of radio observations. In summary, in our synthetic catalog of Local Universe, each mock galaxy is identified by these properties: color (g-r), stellar mass (M_*, atomic and molecular mass (M_{gas}), as well as the halo properties that host it, such as the halo mass (M_h, concentration (C) and halo spin parameter (λ_h). By construction, our catalog reproduce the stellar mass and luminosity function, color mass distribution, HI and H_2 fractions, the two-point correlation function and the galaxy abundances of groups and clusters.

2.2 The "static" model

Once our synthetic catalog is generated, we divide the galaxy distribution into red and blue populations using a cut in the stellar mass-color ratio. Afterwards, we associate red galaxies like those galaxies dominated by spheroid or early-type morphology, while the blue ones are associated to galaxies dominated by disk or late-type morphology. In the present project, we focus mainly on late-type galaxies for which a spatially resolved galactic system is modeled and previously developed in Mancillas (2015) (see also Mancillas et al. 2017). Nonetheless, we also propose a simple model for galaxies dominated by spheroids. We describe in greater detail the procedure followed below:

The dynamic models developed in this project are mainly based on the approach introduced in Mo et al. (1998) and its extension in Dutton et al. (2007). We call this model "static" in order to differentiate it from those where the evolution of the galaxy is followed (e.g., Firmani & Avila-Reese 2000; Avila-Reese & Firmani 2000; van den Bosch 2000; Dutton & van den Bosch 2009).

2.2.1 *Disk galaxy modeling*

The model assumes that an exponential disk is loaded instantaneously into the gravitational potential of a ΛCDM halo, and the dynamics is solved in order the disk settles into centrifugal equilibrium. It is assumed that the disk has conserved the angular momentum of the dark matter halo, which is parameterized through the spin parameter λ_h, and that the mass distribution of the dark matter halo has taken into account the *adiabatic* formation of the disk. Initially, we have assumed that the halo mass distribution follows a Navarro, Frenk & White (NFW) profile, defined from the total halo mass, M_h, and its concentration, C. The parameters λ_h, M_h and C are obtained from direct measurements of the BolshoiP, SMDPL and MDPL simulations. In addition, we have extended the basic model of Mo et al. (1998) including a pseudo-bulge and bulge component.

The total stellar bulge mass is determined by the accumulated mass through mergers. We use the semi-empirical results from Rodríguez-Puebla et al. (2017), where is reported the average fraction of cumulative mass merger based on the total stellar mass of galaxies. In the case of (classic) bulges, we assume that they have a superficial mass distribution that follows a Sérsic profile with index n = 4.

The stellar mass of the pseudo-bulge is computed by determining the radius from which the exponential disk is unstable. All the stellar mass evaluated at this radius is assumed to be part of the pseudo-bulge. Consequently, the new disk has a smaller total mass in proportion to the stars assigned to the pseudo-bulge. Additionally, we assume that the disk instabilities provoke a redistribution of the angular momentum, so that this case we follow in detail the model described in Dutton et al. (2007), where the bulge mass assignment is performed by setting a critical instability parameter according to the numerical simulations of Christodoulou et al. (1995) (all details in Appendix A2). Using the new disk, we follow an iterative process in order to find dynamic instabilities in the disk. At each step we assign stellar mass to the pseudo-bulge and we redistribute the disk angular momentum. The process ends up when the disk-bulge system is dynamically stable. In the case of pseudo-bulges, we assume that they have a superficial mass distribution that follows a Sérsic profile with index n = 2.

As a result, a bulge + pseudo-bulge + disk + halo system in equilibrium is obtained. The rotation curves are calculated for each of these components and we determine the maximum of the total rotation curve. The stellar and gas baryonic profiles are also decomposed under empirical criteria dependent on the disk structure. Additionally, several derived quantities are directly compared with observations such as: effective radius, dynamic and luminous mass at different radius, central densities at 1 kpc, the rotation curve slope at different radius, etc.

2.2.2 *Spheroid galaxy modeling*

In the case of galaxies dominated by a spheroidal component (ellipticals), we introduce a variant of the method described above. Instead of following the adiabatic contraction and the mentioned iterations, observational conditions and certain dynamic assumptions are imposed in order to model the spheroid-halo system. We assume that elliptical galaxies follow the Sérsic profile with index $n = 4$ and the observed effective radius and stellar mass ratio of local early galaxies (Mosleh et al. 2013). Finally, we assume that these galaxies are supported by a stellar velocity dispersion (without rotation) so that we compute their velocity dispersion profiles.

2.3 The procedure

In this Section, we describe the steps to generate a mock catalog of a local galaxy population. We set up the parameters described in the previous section, which are the initial conditions to generate the mock catalog. The halo mass, M_h, halo spin parameter, λ_h and concentration, C, are sampled from the SMDPL simulation Rodríguez-Puebla et al. (2016), while M_* and M_{gas} are reported in Calette et al. (2018).

2.3.1 *Halo parameters*

For each halo mass bin of 0.1 dex, we assign the input parameters randomly sampled from their corresponding distributions, as shown below:

- The halo spin parameter is described by a Schechter-like distribution:

$$P(\log \lambda) = A f(\lambda), \tag{1}$$

where

$$f(\lambda) = \left(\frac{\lambda}{\lambda_0}\right)^{-\alpha} \exp\left[-\left(\frac{\lambda}{\lambda_0}\right)^{\beta}\right], \tag{2}$$

$$A = \left[\int_{-\infty}^{\infty} f(\lambda) d\lambda\right]^{-1}, \tag{3}$$

where the best-fitting parameters measured in BolshoiP, SMDPL and MDPL simulations for $z = 0$ are $\log\lambda_0 = -2.919$ $\alpha = 4.124$ and $\beta = 0.610$.

- The NFW concentration parameter, C, is taken from a lognormal distribution,

$$\log_{10} C = a(z)\log_{10}(M_h/[h^{-1}M_\odot]) + b(z), \tag{4}$$

where $a(z=0) = -0.116$ and $b(z=0) = 2.409$ are the coefficients for a redshift zero. For the dispersion we adopt $\sigma_{\log C} = 0.25$ dex.

2.3.2 Galaxy parameters

- The stellar mass is obtained from the M_*–M_h relation for blue/late-type galaxies, where the fitting is provided in Behroozi et al. (2013):

$$\log_{10}(M_*) = \log_{10}(M_1) + \log_{10}(\epsilon) + f_x - f_0, \tag{5}$$

where

$$f_x = -\log_{10}(10^{-\alpha x}+1) + \frac{\delta[\log_{10}(1+\exp(x))]^{\gamma}}{1+\exp(10^{-x})}, \tag{6}$$

and $x = \log_{10}(M_h) - \log_{10}(M_1)$. The best fitting parameters for a Behroozi function reported in Calette et al. (2018) are: $\log_{10} M_1 = 11.77$, $\epsilon = 0.03$, $\alpha = 1.96$, $\delta = 3.05$ and $\gamma = 0.83$.

- Gas mass is obtained from the gas-to-stellar mass ratio vs. stellar mass.

The determination of the gas fractions for large samples of galaxies is not an easy task since it requires dedicated campaigns of observations in radio, for both the atomic HI and molecular H_2 gas contents. For the latter, a tracer of H_2 should be used for massive studies, for example the CO emission lines. Besides, in order to infer the gas fractions or the gas-to-stellar mass ratios, observations in the optic that provide the data to infer M_* are necessary.

A recent compilation and homogenization of data from the literature of local galaxy samples that contain information on M_*, morphology and $M_{\rm HI}$ and/or $M_{\rm H_2}$ is presented in Calette et al. (2018). The total cold gas mass is calculated as $M_g = (M_{HI} + M_{H_2}) + M_{(He+Z)} = 1.4(M_{HI} + M_{H_2})$, where the factor 1.4 accounts for helium and metals. In Calette et al. (2018), blue/late-type and red/early-type galaxies were treated separately since the gas fractions in both populations are quite different. The author determined the $M_{\rm HI}$-M_* and $M_{\rm H_2}$–M_* correlations, and from them inferred the M_g–M_* correlation, separated for blue/late-type and red/early-type galaxies.

For each set of initial conditions taken from the distributions mentioned above, we apply the static model of disk galaxies in centrifugal equilibrium inside ΛCDM halos described in Section A1 and in Appendix A, and generate the global properties and internal mass distributions of the given galaxy. The dynamical criterion for bulge formation, as well as the Toomre criterion for disk star formation are described in appendices §§A2 and §§A3. In both cases, the criteria are given by one parameter, β_{crit} and Q, respectively. The values we assume for these parameters are $\beta_{crit} = 0.62$ and $Q = 2.5$.

For each halo mass bin, we perform 1000 random extractions from the distribution set for M_h, λ, C, M_* and M_g presented above. We have checked that 1000 extractions are enough to sample well each one of these distributions. Since we cover the halo mass range from 10^{10} to 10^{14} $M_\odot$ in bins of 0.1 dex, we have 40 mass bins. For each bin, we perform 1000 realizations of the five parameters for a total of 40000 models.

3 A SEMI-EMPIRICAL PICTURE OF LOCAL DISK GALAXY CORRELATIONS

Since the static model is not an evolutionary approach, we are not in position to follow the merger history of the halo-galaxy systems and, consequently, to estimate the merger-driven bulge growth and star formation, as well as the merger-driven angular momentum transport processes. Instead, in the case of massive galaxies, the bulge mass is assigned through the average accreted mass fraction of mergers recently determined in Rodríguez-Puebla et al. (2017). According with this fraction, galaxies seeded in more massive halos accreted up to ∼ 40 % of their mass from mergers, while in halos of $\sim 10^{12} M_\odot$ the fraction is of 2 - 3 % at z=0. Then, the bulge components in our models, which are assumed to be composed only of stars, have both accreted and formed in-situ stellar mass contributions. On the other hand, we also attempt to emulate the effects of mergers, yet within our scheme, by artificially lowering the instability parameter β_{crit} and the spin parameter λ. In order to constrain the change of these parameters with M_h, we may proceed in a heuristic way, looking for reproducing the observed scaling correlations at high masses that mostly depend on these parameters, as we will show below. The size–mass relation depends strongly on the spin parameter λ, since the scale radius correlate directly with the angular momentum and the virial radius (R_{vir}) of the halo. Similarly, the B/T–M_* correlation, depends mostly on the β_{crit} parameter, since this factor determines the dynamical instability on the disk that assigns the mass bulge. For low masses, we leave the models to be generated in our mock catalog with the initial conditions, while for larger masses, the parameters are varied as a function of M_h, in such a way that these observational correlations are reproduced at high masses (at lower masses our model already reproduced them). We introduce dependences of the parameters λ and and β_{crit} with the halo mass from $\log(M_h/M_\odot) \approx 3-5\times10^{11}$ $M_\odot$ by using first a subset of models with the mean parameter values in λ, C and $f_{\rm bar}$. From these experiments, we establish the functionalities that describe how the parameters λ and β_{crit} should depend on M_h in order to improve the model predictions in the size–mass and B/T–M_* correlations at high masses. Then, we calibrate with better accuracy the parameters of these functionalities in order that the complete generated mock catalog reproduce the high-mass ends of the observational correlations. At this point, it should be said that our approach turned on to be less deductive (ab initio) and more heuristic or semi-empirical. The approach is aimed to generate ΛCDM-based models that are consistent with several observational scaling correlations of disk galaxies. This allows us then:

- To predict other global correlations of disk galaxies and compare them with observations in order to test the overall consistency of the model, as well as of the underlying cosmological background.
- To probe the effects of the recently determined $M_{\rm bar}$–M_h and M_*–M_h relations (galaxy-halo connection) on the structural/dynamical properties of galaxies accessible to direct observations.
- To explore and constrain how much the initial parameters (e.g., the spin parameter) and the key assumptions (e.g., adiabatic invariant halo contraction) of the model should be modified in order to generate a disk galaxy population in agreement with observations.
- To use these constraints to speculate about the physical and evolutionary processes relevant to disk galaxy evolution at different scales, for example the role of mergers.
- To explore the inner structure and dynamics of the generated bulge-disk-halo systems as a function of global properties.

Below, we present the results obtained from our mock catalog generated as described in Section 2.3, including a modification in some parameters for halos more massive than 3−5×10^{11} M$_\odot$, following the strategy mentioned above.

3.1 Disk galaxy correlations

3.1.1 The size–mass relation and inference of the spin parameter of galaxies

In Fig. 1 we plot the R_e–M_* and $R_{e,bar}$–$M_{\rm bar}$ relations (left and right upper panels, respectively), as well as the $R_{e,D}$–M_* and $R_{\rm bar}$–$M_{\rm bar}$ relations (left and right lower panel). While the first two radii are calculated for the whole (disk + bulge) stellar or baryonic galaxy, the latter radii refer only to the disk stellar or baryonic component. The black solid lines and gray shaded areas are the mean and standard deviations in bins of 0.1 dex in M_* for galaxies with B/T≤ 0.5. The means and standard deviations for the few galaxies with B/T> 0.5, are plotted with green dots and error bars, respectively. In Fig. 1, the blue dashed line and the dotted lines are the mean and the 1σ scatter from observations corresponding to Shen et al. (2003), while the pink and red dots connected by long-dashed lines correspond to the studies by Mosleh et al. (2013) and Bernardi et al. (2012), respectively.

For masses lower than $M_* \approx 3\times10^{10}$ M$_\odot$, the model results in good agreement with observations, while for higher masses, as the radius increases with M_*, the models are higher and are slightly deviated from the mean value of the observations, although they are still in agreement with them. The agreement is good also at the level of the scatters around the size–mass relations, even at large masses. In Fig. 2, we compare the one sigma scatter of the R_e-M_* and $R_{e,D}$-M_* relations (showed in Fig. 1) from our models (black solid lines) with those of the corresponding observations (blue dashed lines). As seen both scatters are similar, in special for the $R_{e,D}$-M_* relation.

The spin parameter λ, is the parameter that most affects the size–mass relations. The semi-empirical models presented in Fig. 1 are carried out with a "initial cosmological" mean λ distribution, but with the mean of λ decreasing with the halo mass from $M_h = 3\times10^{11}$ M$_\odot$ as:

$$\lambda_0 \rightarrow \lambda_{0,bar} = 0.145 - 0.0095\times\log(M_h/{\rm M}_\odot). \quad (7)$$

Therefore, our static model of disk galaxies in centrifugal equilibrium inside ΛCDM halo, allows us to probe the initial spin parameter of baryons out of which disk galaxies formed. Different observational size–mass relations and their scatters are well reproduced if this spin parameter is log-normally distributed following the results from N-body cosmological simulations (see eq. 1), with a dispersion of $\sigma_\lambda = 0.22$ dex and an average value which is equal to the one in the simulations up to $M_h = 3\times10^{11}$ M$_\odot$ ($\lambda_{0,bar} = 0.037$), as well as for larger masses with an average value decreasing with M_h as it is given in eq. (7).

Our results show that the ratio of the mean initial spin parameter of the baryons out of which the galaxy is assembled to the spin parameter of halos $\ell \equiv \lambda_{0,bar}/\lambda_0$, is equal to one for halos smaller than M_h = 3×10^{11} M$_\odot$, and it decreases with M_h from this mass as:

$$\ell = 3.955 - 0.257\times\log(M_h/{\rm M}_\odot), \qquad M_h > 3\times10^{11}{\rm M}_\odot. \quad (8)$$

For instance, $\ell = 0.5$ for halo masses of $\log(M_h/{\rm M}_\odot)$ =13.44. An implication of this result is that galaxies formed in halos less massive than $M_h \approx 3\times10^{11}$ M$_\odot$, on average, conserve in detail the angular momentum acquired by the ΛCDM halo, while in more massive halos, the baryons out of which galaxies form transported a fraction of their angular momentum to substructures and dark matter (see e.g., Zavala et al. 2008). This process is more efficient in more massive halos (eq. 8), which is consistent with the fact that more massive halos assemble larger fractions of their masses in major mergers than the less massive ones.

In the literature, there were some observational attempts to infer the spin parameters of the baryons out of which galaxies formed (e.g., Cervantes-Sodi et al. 2008; Berta et al. 2008). These inferences were done for SDSS galaxies by using very simplified approaches to estimate λ_{bar} from only the optical information. It is interesting that these studies agree in the fact that λ_{bar} decreases on average with the luminosity or stellar mass of galaxies, having little dependence on environment. In comparison with these studies, our models based on disk galaxies in centrifugal equilibrium inside of ΛCDM halos offer a sophisticated way to constrain λ_{bar} and its scatter, even taking into account the effect of the halo contraction. The mock galaxy catalog that we use reproduces several observational correlations of galaxies and it is also agrees with the Galactic Stellar Mass Function (GSMF) by means of the $f_{\rm bar}$–M_h relation. Therefore, *the λ_{bar} values of the disk galaxy models are expected to reflect well the $\lambda_{\rm bar}$ values that real galaxies should have if they were formed in ΛCDM halos.* The galaxies in our mock catalog have on average $\lambda_{0,bar} \approx \lambda_0 = 0.037$ up to $M_* \approx 3\times10^{10}$ M$_\odot$ and for larger masses it decreases down to $\lambda \approx 0.02$ at $M_* = 5\times10^{11}$ M$_\odot$ (see the upper left panel of Fig. 6 to be presented below). The scatter is basically equal to the scatter of the halo spin parameter used as input in the model, $\sigma_\lambda = 0.22$ dex (compare both shaded areas in the upper panels of Fig. 6). It is interesting to notice that the

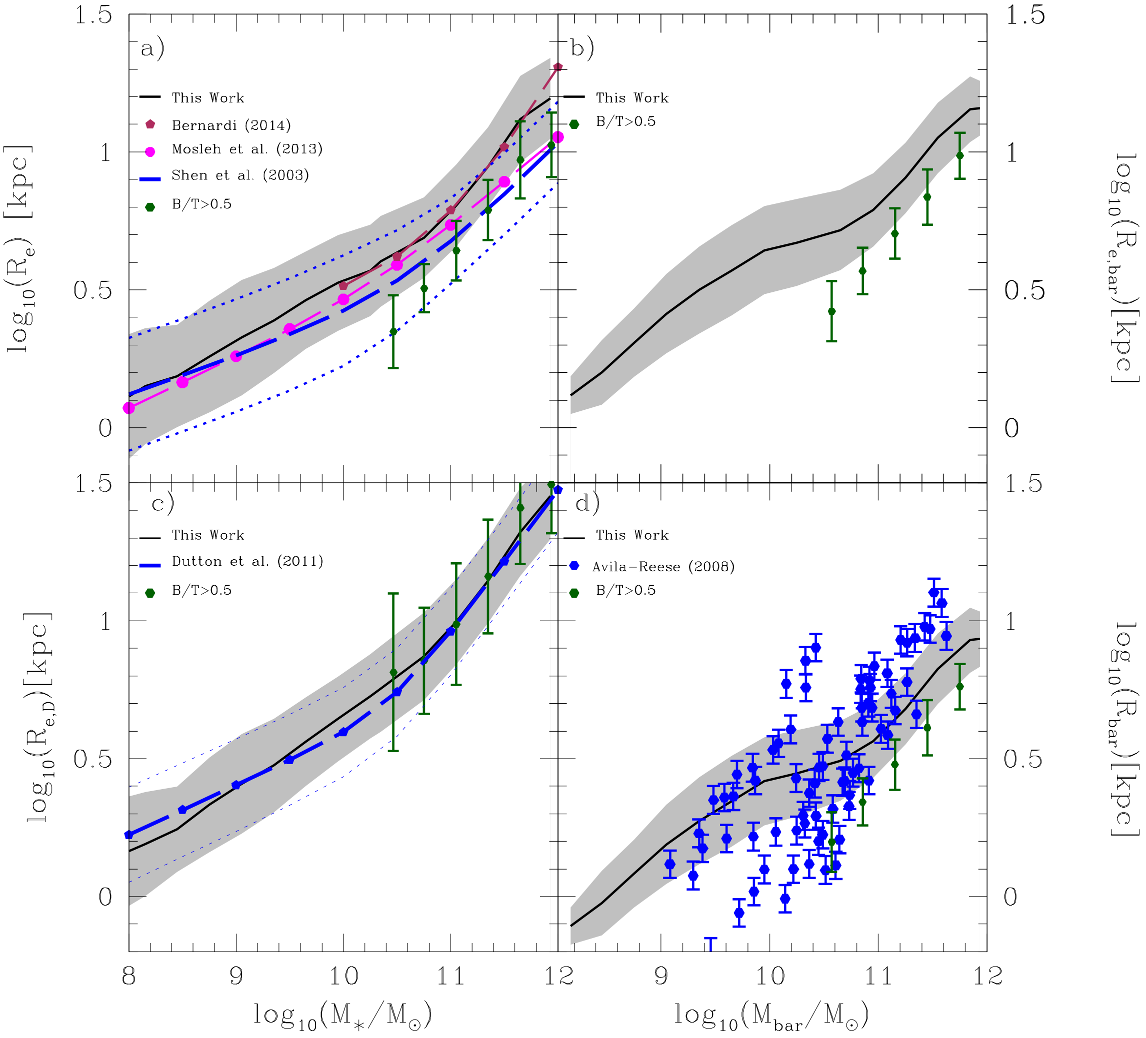

Figure 1. Different radius–mass relations from the semi-empirical models compared to some observational determinations (indicated inside the panels). The black solid lines and the shaded areas are the model means and standard deviations (B/T≤ 0.5) obtained in small M_* bins. The green dots with error bars are the means and standard deviations for models with B/T> 0.5. *Upper left panel:* Stellar effective radius vs. M_*. *Upper left lower panel:* Disk stellar effective radius vs. M_*. Note that the observational correlation by Dutton et al. (2011) is actually for the exponential disk scale length; for this case, $R_{e,D}$=1.68R_D. *Upper right panel:* Baryonic stellar effective radius vs. $M_{\rm bar}$. *Lower right panel:* Disk baryonic scale radius vs. $M_{\rm bar}$.

scatter around both the observed R_e–M_* and $R_{e,D}$–M_* relations follows a similar trend than the “cosmological” scatter in λ_{bar}, as shown in Fig. 2. Therefore, *the dispersion in the spin parameter values of the relaxed* Λ*CDM halos explains the dispersion in the size–mass relations of observed local disk galaxies.*

3.1.2 The B/T–M_*, R_{gas}–M_* and $\Sigma_{\rm e}$–M_* correlations

We calibrated the parameters related to the bulge formation (β_{crit}), at large masses in order to take into account the effects of the mergers. We perform this calibration by making that the predicted B/T–M_* and R_{gas}–M_* correlations were in agreement with the observations. The upper panels of Fig.

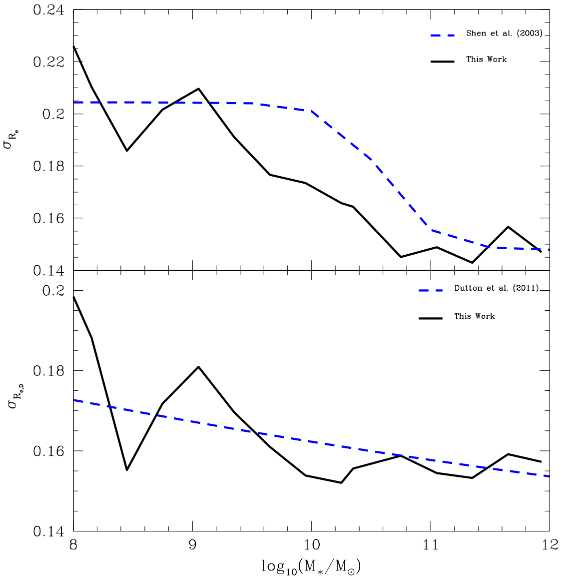

Figure 2. Intrinsic scatters of the $\boldsymbol{R_e}$-$\boldsymbol{M_*}$ (upper panel) and $\boldsymbol{R_{e,D}}$-$\boldsymbol{M_*}$ (lower panel) relations showed in Figure 1. Solid black and dashed blue lines are for the models and the observations, respectively.

3 show the B/T– and R_{gas}–M_* correlations from the models which include a correction in the instability parameters β_{crit} at large masses; the correction to λ as a function of M_h discussed in the previous subsection remains the same. The green solid circles with error bars correspond to the galaxies with B/T> 0.5. The sample of Weinzirl et al. (2009) includes only spiral galaxies; this is why their average B/T ratios are small and the statistics at large masses is poor (most of massive galaxies are early-type). In the case of models, galaxies that likely would be classified as S0 are actually taken into account. Therefore, we should compare the curve of our models between the data from Weinzirl et al. (2009) and Cibinel et al. (2013). The corrections introduced in β_{crit} and λ for halos larger than $M_h = 3\times10^{11}$ M$_\odot$, are addressed to improve the comparison of models with observations at stellar masses larger than $M_* \approx 3 - 5\times10^{10}M_\odot$.

- The B/T ratio increases on average with M_*. The increasing is slight for masses up to $M_* \approx 10^{10}$M$_\odot$ and stronger for larger masses; most of the low-mass galaxies are actually bulgeless (B/T< 0.1).
- Mock galaxies with B/T> 0.5 are massive galaxies. The fraction of them increases with M_*Ḟor $M_* > 10^{11}$M$_\odot$ the percentage is 10.6. If we add to this fraction, those models that did not converge (1.8%, they are mostly too unstable), the fraction is then 12.4%. This can be considered as the fraction of early-type galaxies predicted by our semi-empirical approach.
- The (cold) gas-to-stellar mass ratio, R_{gas}=M_g/M_*, is on average 10 for $M_* \approx 10^8$M$_\odot$ (or 91% in fraction, $M_g/(M_g$+M_*)) and it decreases with M_*. For a Milky Way-sized galaxy, $R_{gas} \approx 0.15$ (0.13 in fraction). At larger masses, the mean R_{gas} decreases faster.
- The 1σ scatter around the R_{gas}–M_* relation increases slightly with M_* decreasing. In general, the intrinsic scatter of the model R_{gas}–M_* relation is slightly larger than that one of the observational inference, but it should be taken into account that the latter is very uncertain because the sample selection effects, observational errors, and non-detections. It is better be said that at low masses the fraction of pure gaseous galaxies is significant (for M_*< 10^9M$_\odot$, this fraction is 17.8%.

In order to attain a good agreement with observations of the B/T ratios at large masses, we have artificially lowered the value of β_{crit} in the criterion of bulge formation (see subsection A2 and eq. A39 therein) for $\log(M_h/\mathrm{M}_\odot) > 11.5$. The fact to decrease β_{crit} implies that the disk is more unstable and hence larger bulges are formed. The source of instability is not already intrinsic, but external, i.e., it is produced by mergers. This parameter was lowered as:

$$\beta_{crit} = -0.0217\left[log_{10}\frac{M_h}{M_\odot}\right]^2 + 0.4319\cdot log_{10}\left[\frac{M_h}{M_\odot}\right] - 1.4932, \tag{9}$$

for $\log(M_h/\mathrm{M}_\odot) > 11.5$. In our scheme, we are assuming that the bulge is all the time formed of stars from the disk, which means that as larger is the formed bulge, the lower is the surface density of the disk. This might not be the case when there are major mergers, since in this case most of the stars in the bulge will come from the accreted galaxy rather from the disk. This implies that the disk remains the same or even more dense due to the merger-induced instabilities. This is why our scheme is valid only for galaxies with non-dominant bulges, i.e., B/T$\lesssim$ 0.5.

Finally, the lower panel of Fig. 3 shows the effective stellar surface density, Σ_e, vs. M_* for those models with B/T$\leq$ 0.5 (solid line surrounded by the gray area). This effective surface density refers to the surface density evaluated at half mass of the sum of both bulge and disk components. The semi-empirical disk galaxies show a significant correlation between Σ_e and M_*. Up to $\sim 2\times10^{10}$M$_\odot$, the slope of the correlation is $\sim$ 0.6 and for larger masses it systematically flattened. The flattening of the Σ_e–M_* correlation at large masses is associated to the steepening seen in the R_e–M_* correlation at these masses (Fig. 1).

Regarding the Σ_e–M_* or (R_e–M_*) correlations, our results show that the shape of the semi-empirical f_bar–M_h relation has an imprint on this correlations. As previous authors have already shown, for pure disks and assuming that the stellar mass is equal to the disk mass, M_*=M_d, then Σ_e scales as ${M_*}^{1/3}$ when f_bar and λ are constant (e.g., Mo et al. 1998; Avila-Reese et al. 1998, this dependence is indicated with a thin blue solid line in the bottom panel of Fig. 1). This is evident from the following dependences in exponential disks:

$$\Sigma_\mathrm{e} = \frac{(M_*/2)}{2\pi(1.68R_D)^2} \propto \frac{f_\mathrm{bar}M_h}{(\lambda R_h)^2} \propto \frac{f_\mathrm{bar}^{2/3}{M_*}^{1/3}}{\lambda^2}, \tag{10}$$

where we have used $R_D = g(C)f_\mathrm{bar}M_h\lambda$, and $R_h \propto {M_h}^{1/3}$ for the CDM halos. So, if f_bar and λ do not depend on the mass,

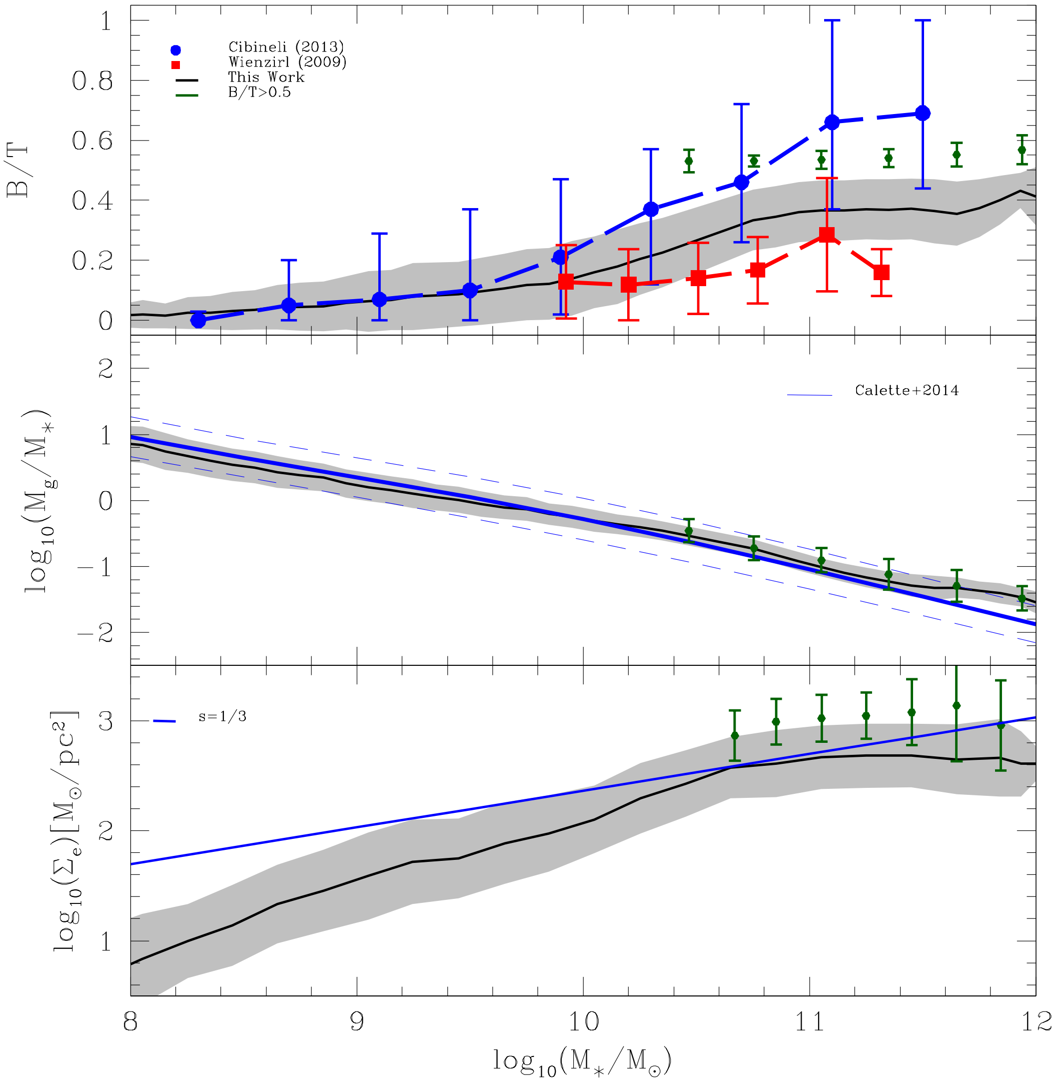

Figure 3. *Upper panel:* Bulge-to-total mass ratio vs. M_* for the semi-empirical models (black solid line surrounded by a gray area) compared to some observational determinations (indicated inside the panels). The gray area and the error bars are the standard deviations at each M_* bin. The semi-empirical models and the observations by Weinzirl et al. refer to disk galaxies (B/T$\leq$ 0.5). The green solid circles with error bars are the averages and standard deviations corresponding to the models with B/T> 0.5. *Medium panel:* Gas-to-stellar mass ratio vs. M_* for the semi-empirical models (black solid line surrounded by a gray area) compared to the empirical correlation inferred in Calette et al. (2014; blue solid line surrounded by the blue dashed lines).The green solid circles with error bars are the averages and standard deviations corresponding to the models with B/T> 0.5. *Lower panel:* Effective stellar surface density, Σ_e, vs. M_* for the disk (B/T$\leq$ 0.5) semi-empirical models. The blue line indicates a slope of 1/3 predicted for disk galaxies when f_{bar} and λ are constant.

$\Sigma_e \propto {M_*}^{1/3}$. However, our semi-empirical galaxies were constructed with a baryon fraction and a spin parameter that depend on the mass. At low masses, roughly $f_{\rm bar} \propto {M_h}^{0.4}$, and since $M_h{=}M_*/f_{\rm bar}$, then $f_{\rm bar} \propto {M_*}^{0.4/1.4} = {M_*}^{0.29}$, then λ does not depend on M_h. Therefore, using eq. (10) we obtain that for the low-mass end $\Sigma_e \propto {M_*}^{0.53}$, which is close to the slope seen in the lower panel of Fig. 3.

At the high-mass end, roughly $f_{\rm bar} \propto {M_h}^{-0.56}$, then $f_{\rm bar} \propto {M_*}^{-0.56/0.44} = {M_*}^{-1.27}$, and using eq. (10), $\Sigma_e \propto {M_*}^{-0.53}$. However, at high masses, λ decreases with M_h according to our semi-empirical approach: very roughly $\lambda \propto {M_h}^{-0.22}$ or $\propto {M_*}^{-0.28}$. Therefore, according to eq. (10), $\Sigma_e \propto {M_*}^{0.03}$, which means that the flattening of the Σ_e–M_* correlation is in agreement with the one observed in Fig. 3. Note that these approximate calculations refer to an exponential stellar disk (no bulge, no gas). The results presented in Fig. 3 are for a disk that can contain gas and is not perfectly exponential, as well as a stellar bulge. In any case, this approximation and our results are in a good agreement.

We conclude that the Σ_e–M_* correlation of disk galaxies results with a slope steeper than 1/3 for low masses because the baryonic fraction that decreases as M_h (or M_*) is smaller, while for larger masses the slope is flattened because the baryonic fraction that decreases as M_h (or M_*), is larger. The slope of the Σ_e–M_* relation can be even negative for higher masses if λ keeps constant. However, our semi-empirical model shows that the spin parameter out of which massive galaxies form, should decrease with the mass. This decreasing provokes a compensation on the effect of low values of $f_{\rm bar}$ and make the slope of the Σ_e–M_* relation almost flat at higher masses. A large survey of galaxies with measured Σ_e values and stellar masses would provide valuable information in the light of the predictions of our semi-empirical approach. The surface density of galaxies is remarkable affected by the astrophysical processes that coin the $f_{\rm bar}$–M_h and $\lambda_{\rm bar} - M_h$ relations.

3.1.3 *The Tully-Fisher relations*

The predicted stellar and baryonic TF relations from our semi-empirical mock catalog are plotted in Fig. 4 (black dashed line surrounded by a gray area). Comparing both figures, we observe a steepening on the TF relations at high masses. We attribute this effect to the formation of large bulges at high masses, which leads a whole baryonic mass distribution to be strongly concentrated towards the center of the galaxy. The peak of the baryonic circular velocity component is shifted to the very inner radius as a result. Since the total circular velocity is the sum in quadratures of the halo and the baryonic contributions, at the radius where the baryon component has now its maximum, the halo contribution is low in such a way that the quadratic sum is also low. The maximum velocity, $V_{\rm max}$, is attained at larger radius, where the disk component dominates more than the bulge, but since the disk is now less massive and more extended, $V_{\rm max}$ results lower than the one when the bulge was smaller. The net result is that the $V_{\rm max}$–$M_{\rm bar}$ and $V_{\rm max}$–M_* relations becomes flatten at large masses. In the case of the $V_{\rm max}$–M_* relation, it is important to notice that M_* also increases slightly as larger is the mass, this is because massive galaxies are more efficient in transforming gas into stars.

It is quite encouraging that the predicted TF relations are in good agreement with the observations. This fact confirms that the ΛCDM cosmology offers a natural explanation on the origin of these relations (see extensive discussions in Avila-Reese et al. 1998, 2008, and more references therein). Note that there is not a problem in the zero-point of both the stellar and baryonic TF relations, as it was suggested in the literature[1] (e.g., Dutton et al. 2007). Thus, by construction the initial conditions used in our models, are in agreement with the galaxy stellar and baryonic mass functions. Recall that the $f_{\rm bar}$–M_h relation used as input here, was constrained by using the observed baryonic mass function. In Fig. 5, we plot the $f_{\rm bar}$–M_h relation and its scatter from our semi-empirical models and compare them with the semi-empirical $f_{\rm bar}$–M_h relation taken from Calette et al. (2018); the latter relation has been actually used as input to generate our mock catalog. Therefore, this plot is just to show that we have sampled well the input $f_{\rm bar}$–M_h relation. In Fig. 5, it is also plotted the f_s-M_h relation ($f_s \equiv M_*/M_h$) and its scatter from our models, and it is compared with the semi-empirical inference of this relation for blue galaxies given in Calette et al. (2018); this relation is the one that maps the ΛCDM halo mass function to the GSMF of blue galaxies. The overall agreement between our prediction and the semi-empirical inference *implies that our semi-empirical model would map well the observed GSMF.*[2]

The bending is less pronounced for the baryonic TF relation than for the stellar one, in good agreement with observations. Regarding the bending at high masses, it is difficult to say whether observations exhibit also such a systematic bending since very massive disk galaxies are rare, and the fit to observations is just an extrapolation at the largest masses. *It would be interesting to have more observations of massive disk galaxies in order to test this prediction.*

3.1.4 *The intrinsic scatter around the TF relations*

The standard deviations in mass bins of our semi-empirical models in the TF relations (associated to the 1σ intrinsic scatter of these relations), are in general larger than the intrinsic scatter estimated from the observations.[3] The lower panels of Fig. 4 shows the logarithmic standard deviations of

---

[1] The problem was originally enunciated for the semi-analytic models: if the input parameters are tuned to fit the observed GSMF, then the modeled galaxies might have too large $V_{\rm max}$ for their masses (or luminosities) in comparison with observations.

[2] However, according to Fig. 5, at low halo masses, our galaxies have systematically slightly higher f_s values than those in Calette et al. (2018); and the scatter around the f_s-M_h relation significantly increases. This is because in halos smaller than 10^{11} M$_\odot$, a fraction of the disk galaxy models are quite stable to the Toomre criterion for gas transformation into stars and form small amounts of stars or not form stars at all. The fraction of purely gaseous galaxies increases as M_h decrease. Some fraction of these pure-gas model galaxies should actually have small stellar masses, which would contribute to lower the average values of f_s at these masses.

[3] In Avila-Reese et al. (2008), the compiled and homogenized galaxy sample was not pruned to minimize the scatter as other samples do it (the main goal of these samples was to use them for calibrating the TF relation as distance indicator). Avila-Reese et al. (2008) have also subtracted the observational errors in order to estimate the *intrinsic* scatter of the TF relations.

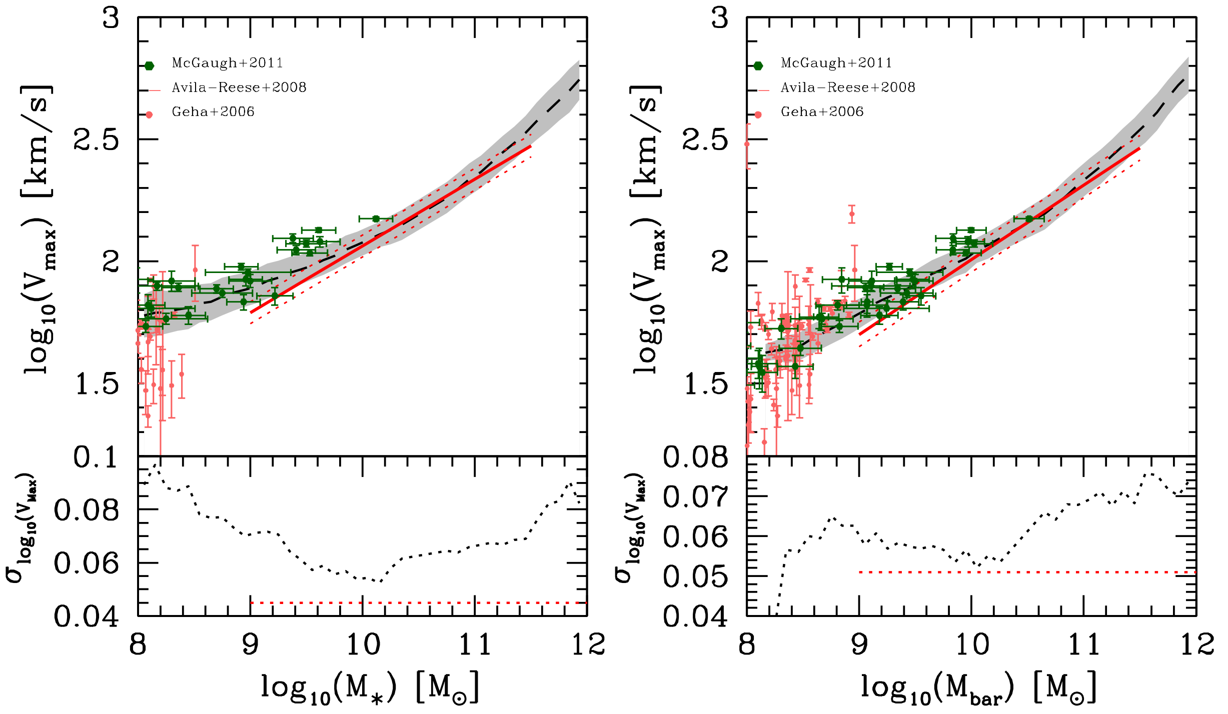

Figure 4. Stellar and baryonic TF relations from our (semi-empirical) mock catalog compared with observations (indicated inside the panels). The dashed line and the gray area are the means and standard deviations calculated in small M_* bins. Only galaxies with B/T$\leq$ 0.5 are considered.

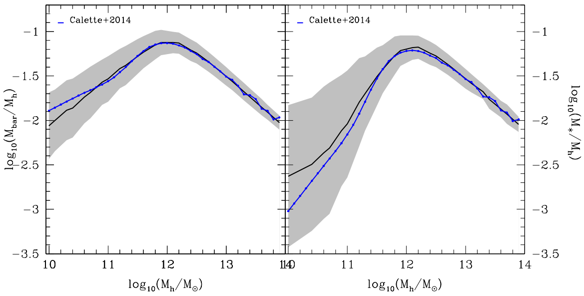

Figure 5. Galaxy baryonic and stellar mass fractions as a function of M_h from the (semi-empirical) mock catalog. The means and standard deviations are plotted with solid lines and shaded areas, respectively. The blue lines are the means from the semi-empirical inferences by Calette et al. (2018) for blue/late-type galaxies. Our catalog was generated actually by using as input the $f_{\rm bar}$–M_h from these authors.Only galaxies with B/T$\leq$ 0.5 are considered.

the $\mathrm{V_{max}}$–M_* and $\mathrm{V_{max}}$–$M_{\rm bar}$ relations as a function of mass. The semi-empirical models show a minimal scatter at stellar and baryonic masses in between approximately 5×10^9 and 1.5×10^{10} $\mathrm{M_\odot}$. At lower and larger masses, the scatter increases, specially for the stellar TF relation. Even in the mentioned mass range, the model scatter is larger than the estimated from the observations. The dashed horizontal lines in both panels of Fig. 4 show the intrinsic scatters inferred from the observations in Avila-Reese et al. (2008). The scatter around the TF relation is a long standing problem of the models in the context of the CDM cosmologies stated originally in Eisenstein & Loeb (1996) and Avila-Reese et al. (1998).

In the next subsection, we will explore the role that the initial parameters play on the scatter of the scaling TF and size–mass relations. We will see that in the case of the TF relations, the scatter is mainly produced by the dispersion in the halo concentration parameter C. At this point, we should mention that the mock catalog was generated by sampling the distributions of the parameters C, $\lambda_{\rm bar}$ and $f_{\rm bar}$ in the assumption that *they are independent among them.* If these parameters are correlated among them, then the scatter in the TF relations could reduce (or it could increase). We leave for a future work the exploration in detail of these possibilities.

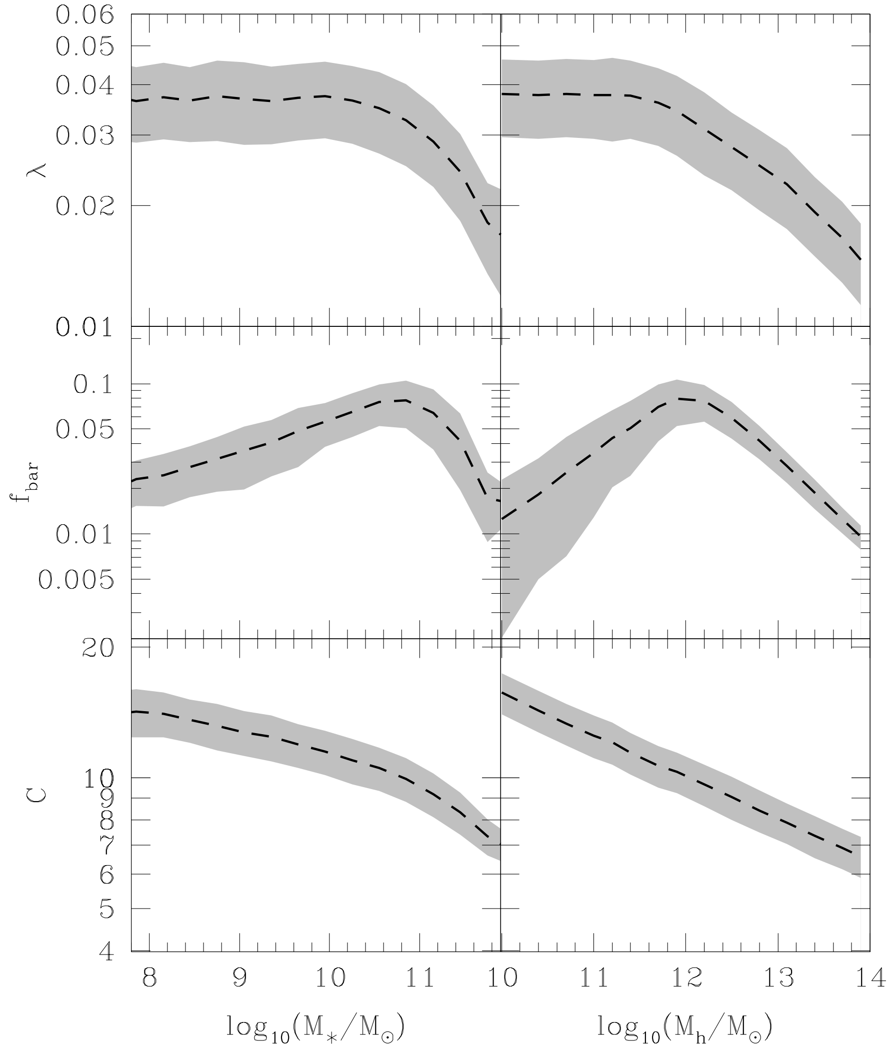

Figure 6. Correlations of the model input parameters $\lambda_{\rm bar}$, $f_{\rm bar}$, and C with M_* (left panels) and M_h (right panels) from our (semi-empirical) mock catalog. The dashed lines are the means and the gray shaded areas represent the standard deviations. The correlations of these parameters with M_h are actually a sampling of the *assumed* input relations and their scatters. Only galaxies with B/T$\leq$ 0.5 are considered.

3.2 The source of scatter in the disk scaling relations

The predicted size–mass relations have a large scatter, while the TF relations are much tighter, i.e., they have smaller scatters. We explore further which parameters from the initial conditions are related to the scatters around these disk galaxy (B/T$\leq$ 0.5) scaling relations. First, we present how the initial condition parameters, λ_{bar}, $f_{\rm bar}$, and C, correlate with M_* (left panels of Fig. 6). The correlations are actually a result of the input dependences of λ_{bar}, $f_{\rm bar}$, and C on M_h, shown for completeness in the right panels of Fig. 6. However, since our semi-empirical model results agree very well with several of the observed scaling correlations, we can say also that *our models constrain in an empirical fashion the values and how the* λ_{bar}, $f_{\rm bar}$, *and C parameters correlate with* M_* *or* M_h. This was discussed already for the case of the spin parameter in §§3.1.1.

In Fig. 7, we plot the residuals of the R_e–M_* and V$_{\rm max}$–M_* scaling relations vs. the residuals of the dependences of

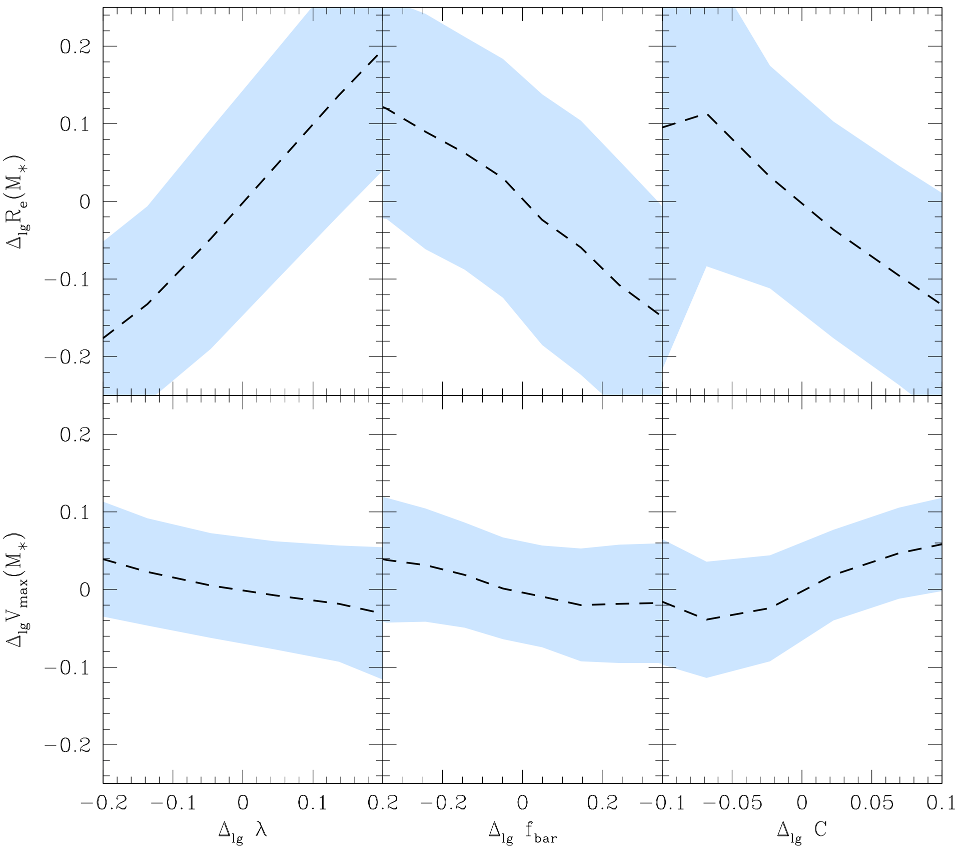

Figure 7. Residuals of the stellar TF and R_e–M_* relations vs. the residuals of the λ_{bar}–, C–, and $f_{\rm bar}$–M_* correlations. The correlations among these residuals show how much the origin of the scatters around the scaling relations depend on the "initial" parameters. Only galaxies with B/T≤ 0.5 are considered.

$\lambda_{\rm bar}$, C, and $f_{\rm bar}$ on M_* (see Fig. 6). This plot shows us how much the "input" parameters affect the intrinsic scatter of the scaling relations of disk galaxies (B/T≤ 0.5). The dispersion around the R_e–M_* relation is large and it is produced actually by the three parameters (the residuals of these relations correlate with the residuals of the three parameters). The main source of scatter, at a given M_*, is $\lambda_{\rm bar}$: the larger the $\lambda_{\rm bar}$, the larger is the galaxy size; the slope of the correlation $\Delta_{\rm lg} R_e$ vs. $\Delta_{\rm lg}\lambda_{bar}$ is higher than 1. The second source of scatter is $f_{\rm bar}$; the higher the $f_{\rm bar}$, the smaller is the galaxy size, with a correlation slope around 1. The residuals of the R_e–M_* relation correlate only weakly with the residuals of the $C - M_*$ relation (the scatter is large in the right upper panel of Figure 7), in the sense that, for a given M_*, more concentrated halos tend to produce galaxies with smaller R_e, i.e., more concentrated in their stellar mass distributions.

The dispersion around the $V_{\rm max}$–M_* relation, which is small, is produced mainly by the C parameter. For a given M_*, the higher the halo concentration C, the larger is the galaxy $V_{\rm max}$. The correlation among the residuals is tight with a slope around 1. The $\Delta_{\rm lg} V_{\rm max}$ residuals anticorrelate weakly with the $\Delta_{\rm lg}\lambda_{bar}$ and $\Delta_{\rm lg} f_{\rm bar}$ residuals (slopes are negative for both parameters). Thus, *the scatter around the TF relation is small because its source is practically only the scatter of the C parameter.*

We have also studied the correlations among the residuals of the baryonic size–mass and TF relations and the residuals of the $\lambda_{\rm bar}$–$M_{\rm bar}$, C–$M_{\rm bar}$, and $f_{\rm bar}$–$M_{\rm bar}$ relations. They are actually similar to those of the stellar case discussed above, though more scattered in the case of the size-mass relation and less scattered in the case of the TF relation.

3.3 Correlations among the residuals of the TF relations vs residuals of radius-mass relations

In Fig. 8, the correlation among the residuals of the R_e–M_* and $V_{\rm max}$–M_* relations (left panel), and among the residuals of the $R_{e,bar}$–$M_{\rm bar}$ and $V_{\rm max}$–$M_{\rm bar}$ relations (right panel) are shown. The dashed lines and shaded blue areas correspond to the means and standard deviations. For exponential disks

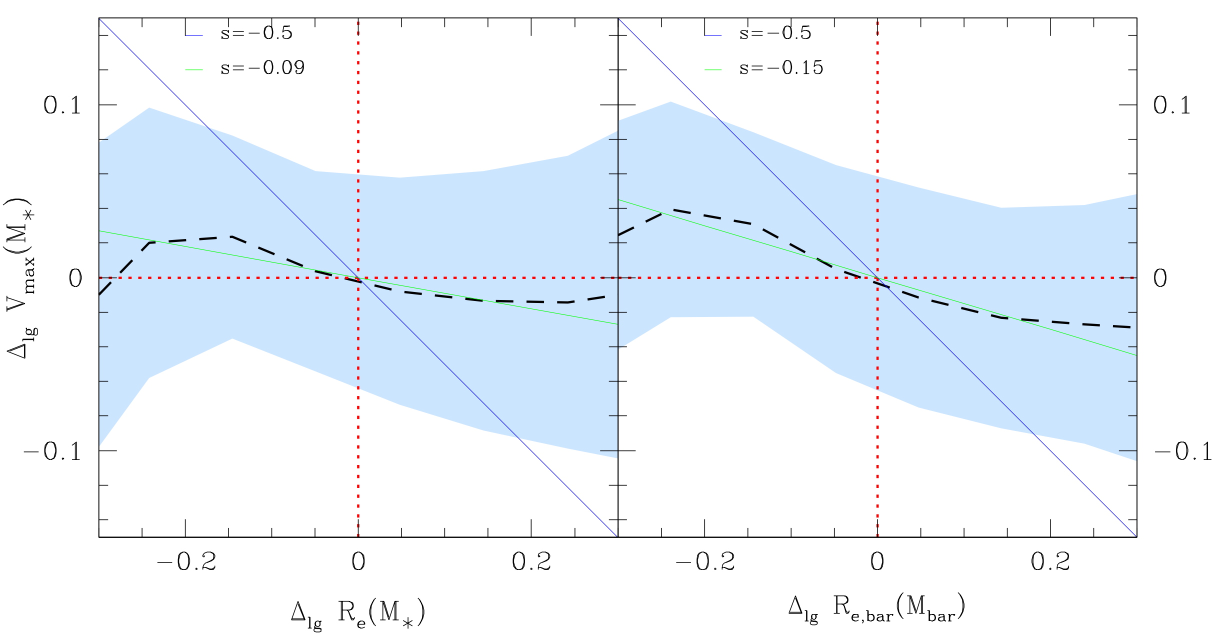

Figure 8. Residuals of the stellar and baryonic TF relations vs. the residuals of the respective stellar and baryonic effective radius–mass relations. The residuals are in dex. The blue lines correspond to a slope of −0.5, valid for exponential disk galaxies without dark halo and bulge. The absence of correlation is indicative of dark matter dominion at radii where V_{max} is attained. The green lines are the orthogonal linear fits to the observations presented in Avila-Reese et al. (2008). Their slopes are indicated inside the panels.

without dark matter, the logarithmic residuals of the radius–mass and V_{max}–mass relations anti-correlate with a slope of −0.5 (Courteau & Rix 1999, blue line in the panels). This is because for a given mass, the smaller the disk scale radius (the more compact the disk), the higher is V_{max} (the more peaked is the circular velocity rotation). The presence of a dark matter halo, softens this dependence and in the case of dark halo dominion, the dependence may completely disappear: V_{max} is determined by the halo internal mass distribution and it does not depend on the disk component. Our results show that there is a weak and scattered anti-correlation among the residuals both for the baryonic and stellar scaling relations, implying that the semi-empirical disk galaxies are mostly dark matter dominated already at radii around the one where V_{max} is attained. However, a weak anti-correlation is seen, meaning that there is a little trend: those galaxies that at a given mass deviate to larger V_{max} values tend to have smaller effective radii.

The weak anti-correlations among the residuals of the scaling relations of model galaxies are similar to those inferred from observational samples (e.g., Dutton et al. 2007; Courteau et al. 2007; Avila-Reese et al. 2008). If any, the latter authors have found that the correlation in the baryonic case is slightly stronger and steeper than in the stellar case. These authors interpreted this difference as a compensation effect in the TF and size–mass relations when passing from the baryonic to the stellar quantities (see Firmani & Avila-Reese 2000). Our results are surprisingly similar to these empirical inferences; the green lines in Fig. 8 are the orthogonal linear fits to their data presented in Avila-Reese et al. (2008).

4 THE INNER MASS DISTRIBUTIONS OF THE SEMI-EMPIRICAL DISK GALAXIES

We have found in the previous section a weak and shallow anti-correlation among the residuals of the baryonic and stellar scaling relations, which suggests nearly dark matter dominion at radii where the maximum circular velocity is achieved (see Fig. 8). Our goal in this section is to study in more detail the inner mass distributions and dynamics of the galaxy disk-bulge-halo systems build up inside ΛCDM halos. The $f_{\rm bar}$–M_h relation used as the "astrophysical" input in our model, and the closely related stellar fraction, f_s–M_h relation (Fig. 5, recall that $f_s \equiv M_*/M_h$) summarize the key aspects of galaxy formation and evolution of galaxies within the ΛCDM halos. We will explore now *how these relations do project into the inner mass distributions of the disk galaxy systems, within optical radii of the galaxies instead of the hypothetical virial radius.*

4.1 The inner baryon and dark matter mass fractions

In Fig. 9, we present the *direct* measures of the baryon (bulge+disk) mass fraction (i.e., the amount of baryon matter with respect to the total one) in the semi-empirical galaxies as a function of $\rm V_{max}$, $\Sigma_{\rm e}$ and M_*. The solid lines and shaded areas are the means and standard deviations of this fraction, $M_{\rm bar}/M_{\rm tot}$, measured up to one stellar effective radius, R_e, for our disk (B/T≤ 0.5) nongaseous galaxies. The green dots and error bars correspond to the galaxies with B/T> 0.5. The dashed lines are the means of the measured mass fractions at 0.5, 1.5 and $2.0R_e$, from top to bottom, respectively. Note that the corresponding *dark matter mass fractions* are $1 - M_{\rm bar}/M_{\rm tot}$. From Fig. 9, we learn that:

- The baryon mass fraction at $1R_e$ has a maximum on average for galaxies with $\rm V_{max} \approx 200$ km/s, $\Sigma_{\rm e} \approx 500\ \rm M_\odot/pc^2$, and $M_* \approx 5\times10^{10}\ \rm M_\odot$. These maximal baryon fractions are slightly above 0.5, i.e. the above mentioned galaxies have a slight domination of baryon matter over dark matter at $1R_e$. At values lower and higher than these, the mass ratios decrease. The decreasing is more pronounced for the dependence on M_*. Such a behavior of the inner baryon mass fraction is partially a consequence of the global $f_{\rm bar}$–M_h relation of disk galaxies used as input in our stationary model. This implies that *the $f_{\rm bar}$–M_h relation (or the closely related f_s–M_h relation) has a clear imprint in the inner galaxy and halo mass distributions.*
- As expected, the baryon (dark matter) mass fraction increases (decreases) as the radius is smaller, but for small, low-density galaxies, the differences between 0.5 and $2.0R_e$ are on average very small (the galaxies are already dark matter dominated since $\sim 0.5R_e$), while for larger, higher-density galaxies, the differences are more notorious, being many giant galaxies baryon-matter dominated at $0.5R_e$ but dark-matter dominated already at $2R_e$. It is interesting that for Milky-Way sized galaxies, contain on average 50% of baryons and 50% of dark matter at $1R_e$, while for $2R_e$, the proportion change on average to 40% of baryons and 60% of dark matter.
- The baryon mass fraction at $1R_e$ depends more tightly on $\Sigma_{\rm e}$ than on M_* and $\rm V_{max}$. This can be seen from the small scatter in the medium panel with respect to the left and right ones. The inner baryon mass fraction in the ΛCDM-based semi-empirical galaxies is determined by both the galaxy surface density (concentration) and the mass, but it dominates the first one.
- For the subsample of bulge-dominated semi-empirical galaxies (green dots with error bars), which are mostly high-$\rm V_{max}$, massive galaxies, the baryon mass fractions at $1R_e$ are high, being most of them actually baryon matter-dominated at this radius.

Our results clearly show how are expected to be the "luminous" and dark matter distributions in disk galaxies formed in ΛCDM halos. An interesting prediction is that very massive, high-surface density galaxies become dark matter dominated already at $1R_e$. The trend of increasing the baryon matter domination as galaxies are more massive and of higher surface density is broken, and the reason is that the halo baryon fraction, $f_{\rm bar}$, decreases significantly with M_h for massive halos. Note that massive galaxies could be even more dark matter dominated than we show in Fig. 9 if the halo spin parameter λ would have remained the same for the baryons (detailed angular momentum conservation). After have explored a decreasing of the initial spin parameter out of which galaxies form as M_h is larger, the galaxies are more concentrated and hence, increase their contribution to the total mass in the inner regions. But not enough as to dominate over dark matter at radii $\sim 1R_e$.

4.2 Galaxy-to-total maximum velocity ratios

The ratio of disk (or disk + bulge) to total circular velocity is a quantity related to the "luminous"-to-dark matter ratio. The velocities can be defined (and measured) at a given radius or estimated at their respective maxima (the total one, $\rm V_{max}$, comes directly from observations while the disk or disk+bulge ones are inferred from the observed luminosity mass distributions or from vertical disk dynamics studies).

In Fig. 10, we plot three circular velocity ratios vs. some global properties: $\rm V_{max}$, the effective stellar (bulge + disk) surface density $\Sigma_{\rm e}$, and M_*. The model results for the disk galaxies (B/T≤ 0.5) are shown as the averages and standard deviations calculated in small bins of these properties (dashed lines and shaded areas, respectively). We also show the corresponding means and standard deviations for the "early-type" subsample, i.e. those models with B/T> 0.5 (green dots with error bars, respectively). Recall that a significant fraction of the low-mass model galaxies are gaseous, so they can not be plotted in the panels where stellar quantities appear (central and right columns). However, in the first column, they can be included and are plotted with red dots and error bars. The upper panels are for the ratio of disk circular velocity to total circular velocity at $2.2R_D$, where R_D is the baryonic disk scale length (exponential by definition). The medium panels are for the ratio of the maximum circular velocity of the disk component, $\rm V_{D,max}$, to $\rm V_{max}$ while the lower panels are for the ratio of the baryonic (bulge +

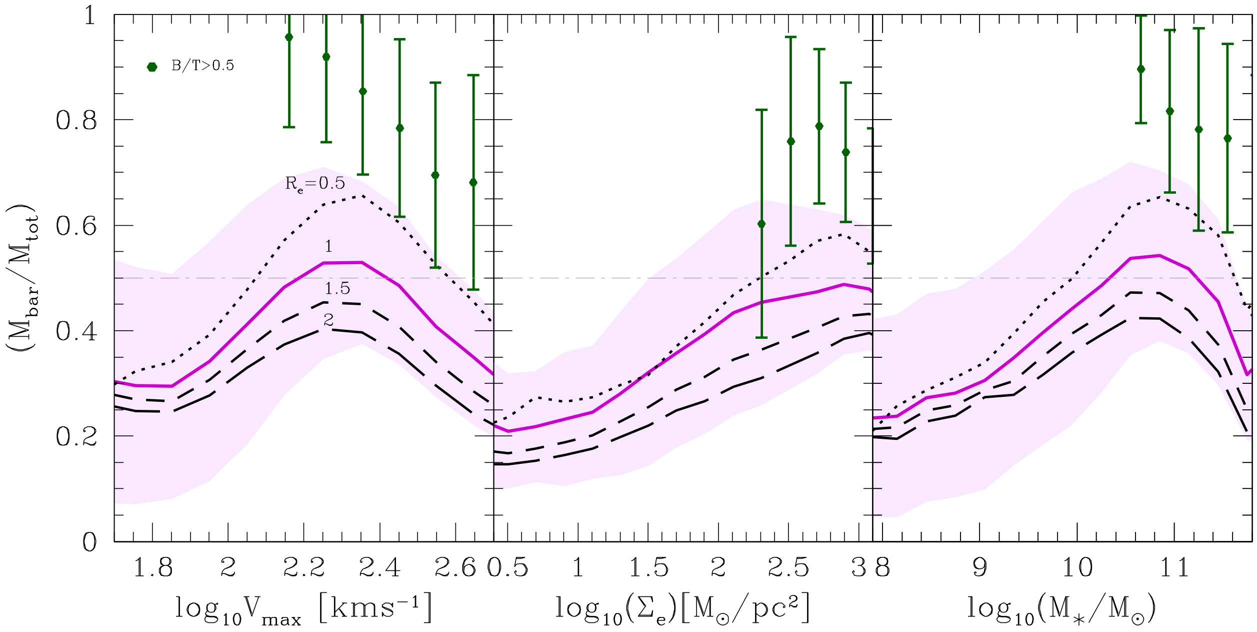

Figure 9. Baryon-to-total mass ratio at a given radius, $M_{\rm bar}/M_{\rm tot}$, of the semi-empirical galaxies as a function of V$_{\rm max}$, $\Sigma_{\rm e}$, and M_*. The solid lines and shaded areas are for measures of this ratio at 1 R_e (the means and standard deviations, respectively). The dashed lines, from top to bottom, are the means of the $M_{\rm bar}/M_{\rm tot}$ ratio measured at 0.5, 1.5, and 2.0 R_e, respectively. The green dots with error bars are the means and standard deviations of this ratio at 1 R_e for the sample of B/T> 0.5 galaxies.

disk) maximum circular velocity, V$_{\rm bar}$ to V$_{\rm max}$ note that the disk or disk+bulge maximum circular velocity may occur at radii different to the one where the total circular velocity has its maximum.

The $V_{D,2.2}/V_{2.2}$ and V$_{\rm D,max}$/V$_{\rm max}$ ratios of the semi-empirical model galaxies are almost always lower than 0.6, far from the disk-dominated case which has values of 0.75–0.85 (Sackett 1997) (not taking into account a bulge). At low V$_{\rm max}$, $\Sigma_{\rm e}$, and M_* the ratios slightly decrease as lower are these quantities. At V$_{\rm max}$ ≈ 150 km/s, $\Sigma_{\rm e} \approx 200$ M$_\odot/pc^2$, and $M_* \approx 2{\times}10^{10}$ M$_\odot$, these ratios have a shallow maximum, and for larger values the ratios decrease. Determinations of the $V_{D,2.2}/V_{2.2}$ ratio (which is close to the V$_{\rm D,max}$/V$_{\rm max}$ ratio for small-bulge galaxies) with vertical-disk dynamics studies using spectroscopical data were carried out by Bershady et al. (2011). For the small sample these authors present, they infer a correlation of the $V_{D,2.2}/V_{2.2}$ with V$_{\rm max}$, which we reproduce with a solid line (the dotted lines show the scatter of their correlation). The low-velocity semi-empirical model galaxies have larger velocity ratios than those of the small observational sample by Bershady et al. (2011). If we include the significant fraction of gaseous model galaxies (red dots and error bars), then the agreement would be better. It is likely that our algorithm for gas transformation into stars based on a simple Toomre instability criterion underpredicts the amount of stars formed at our lowest halo masses Bershady et al. (2011) velocity ratios seem to be too low; previous studies with similar techniques showed higher ratios, around 0.6 (e.g., Bottema 1993). The sample of this author was small, only 12 galaxies, and he did not find a dependence of $V_{D,2.2}/V_{2.2}$ on luminosity or V$_{\rm max}$. At maximum velocities around 200 km/s, the velocity ratios of the Bershady et al. (2011) and (Bottema 1993) observations are of the order of our predictions. However, for the observational sample from the former authors, it seems that the $V_{D,2.2}/V_{2.2}$ ratio continues increasing with V$_{\rm max}$, while in our mock sample, the ratio at these values decreases with V$_{\rm max}$. Unfortunately, there are not dynamical observational determinations for galaxies with V$_{\rm max}$ values larger than ~ 250 km/s.

Zavala et al. (2003) provided estimates of the V$_{\rm D,max}$/V$_{\rm max}$ ratio for 79 disk galaxies, whose properties were compiled from the literature (it is the same sample used in Avila-Reese et al. 2008). Their data are plotted in Fig. 10 (color dots). The data do not show a significant correlation with V$_{\rm max}$ nor with M_*, but a trend of increasing V$_{\rm D,max}$/V$_{\rm max}$ with $\Sigma_{\rm e}$ is seen. At low values of V$_{\rm max}$, $\Sigma_{\rm e}$, and M_* the semi-empirical galaxies are in rough agreement with the observational inferences, but at large values of these quantities, the semi-empirical galaxies decrease their V$_{\rm D,max}$/V$_{\rm max}$ ratios with respect to the observational inferences. Recall that the disk velocity contribution in the massive models becomes smaller in favor of a bulge component that increases the total maximum circular velocity, V$_{\rm max}$. So, it could be that when the bulge is significant, too much

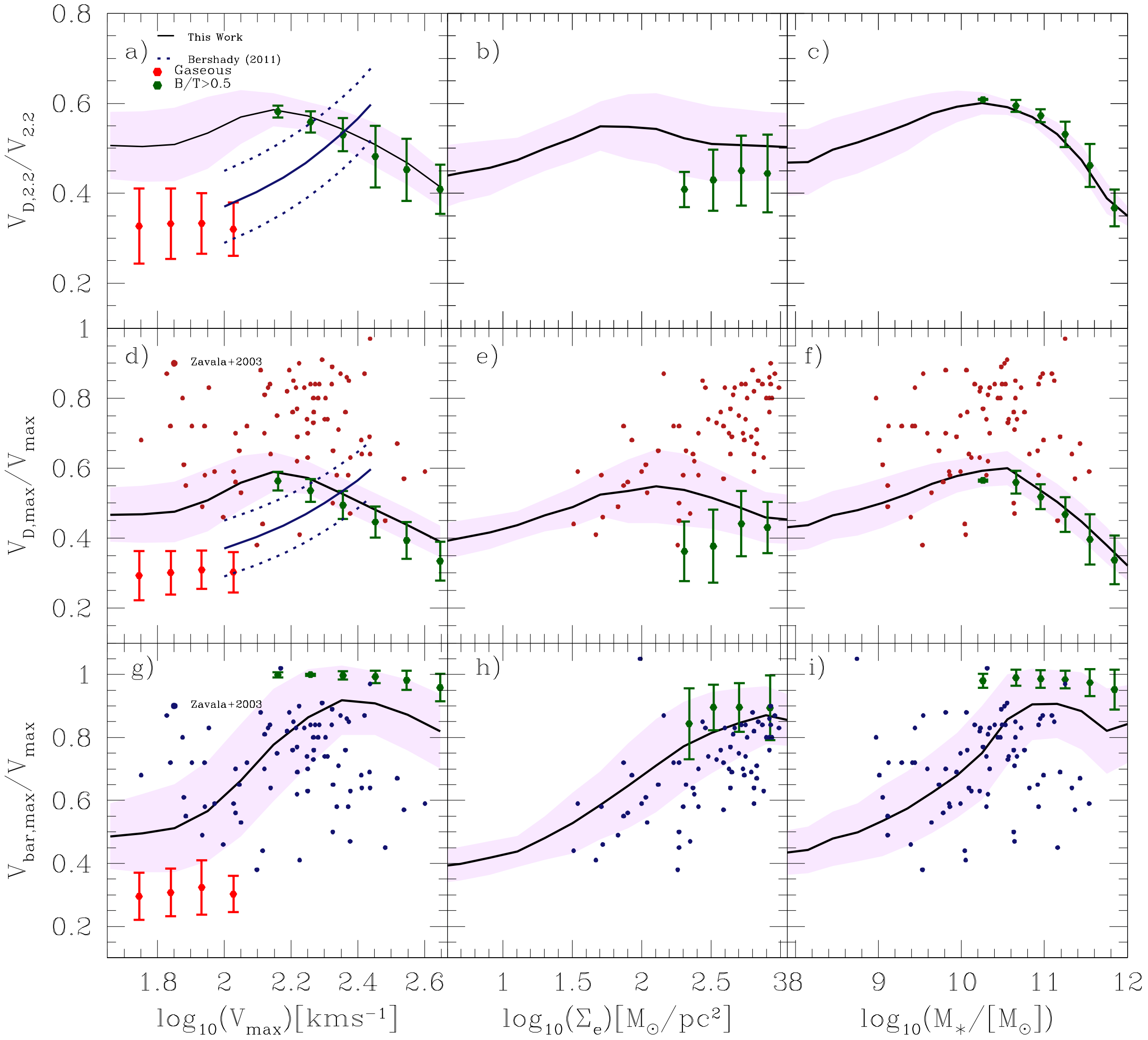

Figure 10. Different "luminous"-to-total velocity ratios as a function of V_{max}, Σ_e and M_* for the semi-empirical mock disk galaxy catalog (B/T$\leq$ 0.5); the dashed lines and shaded areas are the means and standard deviations, respectively. Green dots with error bars correspond to the sample of galaxies with B/T> 0.5. The red dots with error bars correspond to the sample of purely gas disk galaxies; they can not be plotted in the medium and right panels because they do not have stars. *Upper panels:* Disk-to-total velocity ratio measured at 2.2 scale radii of the baryonic disk. *Medium panels:* Maximum disk-to-maximum total velocity ratio. *Lower panels:* Maximum disk+bulge-to-total velocity ratio.

of the inner disk has been reduced. On the other hand, it should be said that the observational inferences could be contaminated partially by a bulge component at the time of estimating $V_{D,max}$.

In the lower panels of Fig. 10, the disk+bulge velocity component is used. As expected, this component is now higher than in the only disk case, specially for the larger and higher surface density model galaxies. From our results, we see that in general the inclusion of the bulge increases significantly the maximum circular velocities ratios; this is even more notorious for the B/T> 0.5 galaxies (green dots with error bars). The circular velocity decompositions into bulge, disk and halo from observations are actually not trivial. On the other hand, the total velocity maxima can be at very different radii than those where the disk or disk+bulge maxima are attained. Therefore, these ratios are not reflecting already the luminous-to-dark matter contents at a given radius, specially for the bulge-dominated or dark-matter dominated galaxies.

Unfortunately, observational samples with structural and dynamical information are scarce and do not allow for a full disk-bulge-halo decomposition in such a way that we can get the maximum circular velocities for each component and compare with our predictions.

For all the maximum velocity ratios presented in Fig. 10, there is a general trend: these ratios as a function of $V_{\rm max}$, $\Sigma_{\rm e}$ and M_* follow a bell-shaped dependence; after a maximum, they decrease as smaller/less dense and larger/more dense are the galaxies. The latter behavior could seem unexpected, but, as we will see below, its related to the dependence of $f_{\rm bar}$ on M_h used as an input in our static model of disk galaxies.

4.3 The outer slope of the circular velocity curves

A debated question in the literature is the one related to the rotation velocity shape of disk galaxies (e.g., Persic & Salucci 1997; Catinella et al. 2006). Are the rotation curves described by an universal profile? Do the parameters of this profile depend more on luminosity (or M_*) or in surface brightness or any other galaxy property? The answers to these questions are tightly related to how are distributed the luminous and dark matter mass components.

Here, we focus only on the outer slope of the circular velocity profiles. By outer we understand galaxy radii further away the radius where the luminous (bulge + disk) component attained its maximum. For example, in the case of an exponential disk-dominated system, where the maximum is attained at $\approx 2.2R_D$, or equivalently, $\approx 1.3R_e$, the outer slope could be measured let say at $\sim 3R_D$. Because of our galaxies are composed of bulge, disk and halo, it is not so obvious where is the maximum. If the halo dominates, then the maximum happens typically at radii larger than the one of the disk component. The opposite happens if the bulge dominates. In order to assure a region far away the maximum of the bulge+disk component, we measure the slope of the circular velocity profile in between 3.0 and $3.5R_D$, $\alpha_{\rm out}$. This can be considered as an outer radius in the sense of the luminous galaxy. We could measure the slope at even outer radii, but in the hope to compare in the future our results with observational determinations, it is better to keep the measure not too further away. The observational measures of the rotation velocities do not extend typically to much outer radii.

In Fig. 11, we plot the dependence of the outer slope of the total circular velocity curves ($\alpha_{\rm out}$) of our semi-empirical disk galaxies as as function of $V_{\rm max}$, $\Sigma_{\rm e}$, and M_*. According to the figure, $\alpha_{\rm out}$ correlates with these three galaxy properties, but more with $\Sigma_{\rm e}$ (the tightest correlation is with this property), implying that outer shape of the circular velocity is mainly determined by the galaxy surface density. In the case of this correlation, we have actually obtained the means and standard deviations for the mock galaxies smaller than $M_* = 5 \times 10^{10}$ $M_\odot$ separate from those larger than this mass. Recall that an important result from our semi-empirical mock galaxy catalog is that the $\Sigma_{\rm e}$–M_* correlation flattens at the high-mass end (see subsection 3.1.1 in the previous section) in such a way that increasing M_*, $\Sigma_{\rm e}$ almost already does not increase. This behavior in combination with that α strongly increases with M_* at high masses, make that in the $\alpha_{\rm out}$–$\Sigma_{\rm e}$ plane appeared a clear bimodality driven by mass. In order to take into account such a bimodality at the time of obtaining means and standard deviations, we have separated our mock sample into two groups by the mass criterion mentioned above.

Small, low-surface density galaxies have rising circular velocities ($\alpha_{\rm out} > 0$) at 3–$3.5R_D$, but as the surface density and galaxy size increase, the slope becomes flatter and even decreasing ($\alpha_{\rm out} < 0$). However, for $M_* \gtrsim 5 \times 10^{10}$ $M_\odot$ ($V_{\rm max} \gtrsim 200$ km/s) the slope again increases on average; the velocity profiles are rising for the largest disk galaxies. In other words, the baryonic component is sub-dominant for these galaxies and the total circular velocity curve is mainly the one of the dark matter halo at these radii. This is in agreement with the above reported luminous-to-total mass contents at 1.5 and $2R_e$, see Fig. 9. The circular velocity profiles of large galaxies are rising at large radii mainly because these galaxies become dark matter dominated, as the low-mass ones.

What about the dependence of $\alpha_{\rm out}$ on $\Sigma_{\rm e}$ for high-surface density galaxies? According to Fig. 11, on average $\alpha_{\rm out}$ would continue decreasing up to the largest possible values of $\Sigma_{\rm e}$. When separated by mass, many of the most massive galaxies can have lower values of $\Sigma_{\rm e}$ and positive values of $\alpha_{\rm out}$. A clear bimodality in the $\alpha_{\rm out}$–$\Sigma_{\rm e}$ plane appears. This is why we plot the means and standard deviations in this plane separated by mass.

Our results show that a way to probe the luminous-to-total content of galaxies yet within optical radii, is by the outer shape of the rotation curves. With the advent of large galaxy surveys, large samples of galaxies with rotation curves measured up to 3–$3.5R_D$ (1.5-$2R_e$) will be available, and it will be possible then to test whether their outer slopes have the dependences that we have found in our ΛCDM-based semi-empirical disk galaxies. The secondary sample of the MaNGA/SDSS-IV survey (Bundy et al. 2015) is designed to attain $2.5R_e$. Therefore, we will have optical rotation curves at least up to this radius for ~ 1500 galaxies, for which most of the optical properties will be also available.

5 SUMMARY AND CONCLUSIONS

The cosmological ΛCDM scenario provides the most suitable context to interpret the nature, origin and evolution of galaxies, in particular those which are more common in the local Universe: disk galaxies (see e.g. Mo et al. 1998; Avila-Reese et al. 1998; Avila-Reese & Firmani 2000; Avila-Reese et al. 2008; Firmani & Avila-Reese 2000; Gnedin et al. 2007; Dutton et al. 2007). In the present work, we explored the consistency of this scenario with the main observational correlations of a local disk galaxy population, taking into account the recent semi-empirical inferences of the baryonic fraction, $f_{\rm bar}$=$M_{\rm bar}/M_h$, as a function of the halo mass, M_h. The $f_{\rm bar}$–M_h (or $M_{\rm bar}$–M_h) relations contains the information of the main astrophysical processes that operate in the evolution of galaxies as a function of the mass, such as the falling and cooling of the gas towards the halos and galaxies, the star formation, the feedback of this process towards

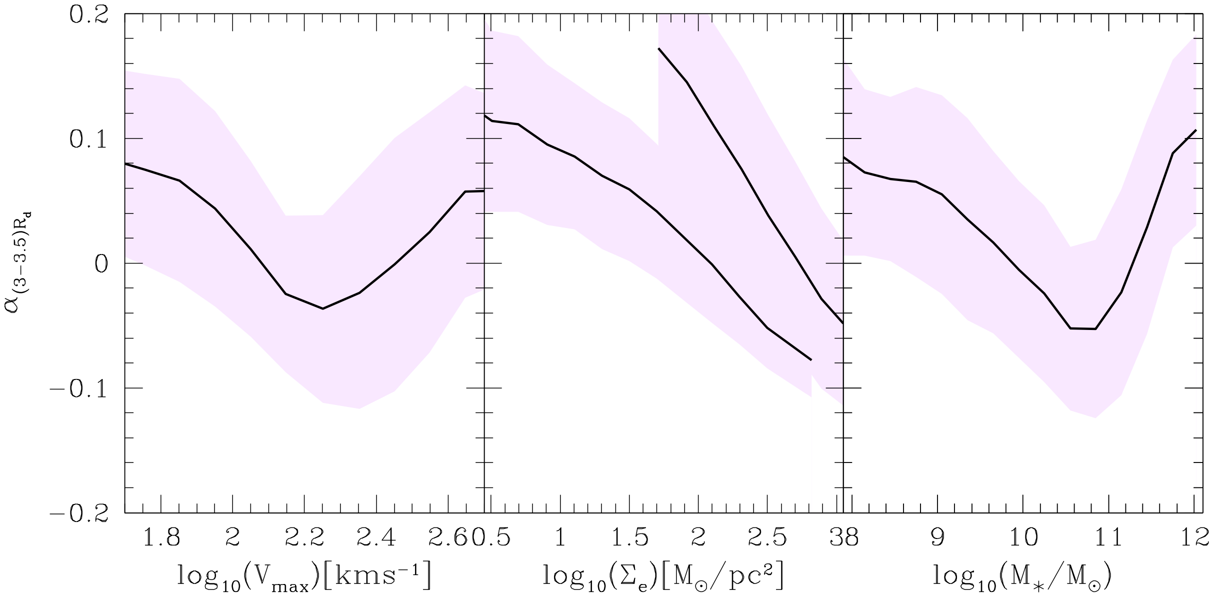

Figure 11. Outer slope of the circular velocity of our semi-empirical galaxies as a function of V_{max}, Σ_e, and M_*. The solid lines and shaded areas are the means and standard deviations. In the case of Σ_e (medium panel), we have calculated these means and standard deviations separated into galaxies smaller and larger than $M_* = 5 \times 10^{10} M_\odot$ because a strong bimodality driven by mass appears in the α_{out}–Σ_e plane.

the interstellar medium, as well as active galactic nuclei, etc. The M_*/M_h–M_h, M_g/M_h–M_h relations and consequently M_{bar}/M_h–M_h (including their intrinsic scatter) were inferred for the first time for both local late- and early-type galaxies (Rodríguez-Puebla et al. 2015; Calette et al. 2018). We used such corresponding inferences for blue/late galaxies.

A "static" (non-evolutionary) model of a disk galaxy population was implemented as a tool, which consisted of loading discs in a centrifugal equilibrium in ΛCDM halos, taking into account the adiabatic contraction exerted by the halo internally due to the galaxy formation effects (Mo et al. 1998). The model was extended to include the formation of bulges by following the formalism applied in Dutton et al. (2007). The initial conditions used in the static model were those from the "cosmological" halo properties (M_h, λ_h and C), as well as those from observational correlations inferred in Calette et al. (2018), such as M_*–M_h M_g–M_h and hence f_{bar}–M_h relations, which summarizes the astrophysical processes of the incorporation and loss of baryons in the galaxies. All parameters where taken from statistical distributions.

Once established a semi-empirical approach, we proceeded to generate a synthetic catalog of 40,000 local disk galaxies covering a range of halo mass of 10^{10} to 10^{14} $M_\odot$. In order to be consistent with observations, we take into account only disk galaxies with the B/T ratio less than or equal to 0.5. The fraction of galaxies with B/T > 0.5 is low (≈ 11%) and applies only to massive galaxies. Below we describe the main conclusions related with the galactic global scaling relations:

- We have operated on the parameters which control disk instabilities in order to make them "artificially" more unstable while more massive are their halos because of the merger effects. We have decreased the spin parameter of gas out of which galaxy forms, and we achieve that the most massive galaxies were in agreement with the mass-size relation, as well as the observed correlations B/T–M_* and M_g-M_*. Thus, our method might be understood at this point as a sophisticated semi-empirical form to determine the initial spin parameter from which the observed disk galaxies were formed, λ_{bar} as a function of M_* and M_h, and applied to masses up to $M_* \approx 3-5 \times 10^{10}$ $M_\odot$.

  This parameter is similar in magnitude and distribution (Schechter-like function) to the halos ΛCDM (λ average of 0.037 without a dependency with M_h), but at larger masses, decreases with M_h like a $\lambda_{bar} \propto -0.0095 \log M_h$ or, as a function of M_*, like $\lambda_{bar} \propto -0.0126 \log M_*$, meaning that, there is a loss of angular momentum at higher masses. The dispersion of the original "cosmological " distribution is maintained, in a such a way that it was possible to reproduce the dispersion observed in the radius-mass relations.
- The R_e–M_* and $R_{e,D}$–M_* relations have a considerable dispersion, which increases for less massive galaxies. These dispersions are similar to those inferred in the observations. *A parity of* M_* , dispersion has its main source in the dispersion of λ_{bar}: as λ_{bar} increases, the radius also increases.

However, we found that $f_{\rm bar}$ is also a source of dispersion and a to much lesser degree, the concentration parameter C.

- Once radius-mass, B/T– M_* and M_g/M_*–M_* relations were reproduced, the predicted stellar and baryonic TF relations are in excellent agreement with the observations. In particular, we do not find any problem with zero points, since by construction our models are in agreement with the baryonic (and stellar) mass function inferred from observations. For lower masses, the stelar TF relation suffers a bending which apparently also shows the dwarf galaxies. At a level of baryonic TF this bending is much less noticeable. At very high masses, semi-empirical models also show a bending that will be interesting to check whether observations are given or not.
- The dispersion in the predicted TF relations is moderate and is produced mainly by the dispersion on the concentration, C. The λ_{bar} and $f_{\rm bar}$ parameters do not seem to be a source of dispersion and hence the stellar and baryonic TF relations are very robust to variations for these parameters. However, the intrinsic dispersion in the TF relations of the semi-empirical models are larger than the observations presented. This result could be a potential problem, although we note that the catalog was constructed under the assumption that the dispersions in λ_{bar}, C and $f_{\rm bar}$ are independent. In case that there was a certain correlation between C and the other two parameters, the dispersion in the TF could decrease (or even increase!).
- The residuals of R_e–M_* and $\rm V_{max}$–M_* relations anti-correlate very weakly with a slope much smaller than −0.5 and according to certain observational inferences. Something similar occurs with residuals of the baryonic scaling relations, showing a slightly larger anti-correlation. The anti-correlation between the residuals and a low slope is an evidence that the disk + bulge component in the rotational speed is less dominant, i.e., the dark halo component is more predominant.

In Section 5 we studied in more detail the contributions of the circular velocity by the disk and the disk + pseudo-bulge + bulge system, as well as the internal mass distributions in disk galaxies. Main results are presented below:

- The "luminous" mass fraction increases towards more central radius, although for small galaxies with low surface density, the increasing is minimal. For example at 0.5 R_e, these galaxies are already dominated by dark matter. Our results show that a galaxy similar to Milky Way contains on average 50 % of baryons and 50 % of dark matter at 1 R_e; The ratio changes on average to 40 % and 60 % respectively.
- The disc to total velocities ratios at $2.2R_D$ and $2.2R_D$, $V_{D,2.2}/V_{2.2}$, is almost less than 0.6 far from the case of "maximum disk" (0.75-0.85). For semi-empirical galaxies, this ratio decreases on average with $\rm V_{max}$, $\Sigma_{\rm e}$ and M_* on the side of low values of the global galaxy properties. The peak reaches a soft maximum (about 0.6) to $\rm V_{max} \approx 150$ km/s, $\Sigma_{\rm e} \approx 200$ $\rm M_\odot/pc^2$, and $M_* \approx 2\times10^{10}$ $\rm M_\odot$, and for larger values, the $V_{D,2.2}/V_{2.2}$ ratio decreases again. Compared with vertical dynamics spectroscopic studies in disc galaxies that infer these ratios for very small samples, our results are very consistent within the uncertainties.
- The $\rm V_{D,max}/V_{max}$ velocities ratio (where the maximum can vary at different radius) shows a behavior with $\rm V_{max}$, $\Sigma_{\rm e}$ and M_* similar to the one mentioned above: the ratio grows as these properties increase in value, reaching a given maximum, and for the case of larger and dense galaxies, this ratio decreases again. This behavior is a footprint of the $f_{\rm bar}$–M_h relation used as the initial condition in semi-empirical models. When the maximum velocity of the disk + bulge is used, the $\rm V_{B+D,max}/V_{max}$ ratio, increases, especially for the most massive and high surface densities galaxies. Unfortunately, there are not many observational data of this type to confront predictions.
- An amount that could be obtained observationally for galaxy surveys and which is related to the "luminous" to dark mass ratio, is the external slope (between 3 and 3.5 R_D) of the rotation curve, $\alpha_{\rm out}$. We calculate $\alpha_{\rm out}$ for our semi-empirical galaxies and found that the slope correlates with $\rm V_{max}$, $\Sigma_{\rm e}$ and M_*, but more with $\Sigma_{\rm e}$, implying that it is the surface density the one that affect more to the external shape of the rotation curves.

ACKNOWLEDGEMENTS

B. Mancillas-Vaquera was supported in part by CONACYT grant, CVU 420397.

REFERENCES

Allen, J. T., Croom, S. M., Konstantopoulos, I. S., et al. 2015, MNRAS, 446, 1567

Aquino-Ortíz, E., Valenzuela, O., Sánchez, S. F., et al. 2018, MNRAS, 479, 2133

Avila-Reese, V., Firmani, C., & Hernández, X. 1998, ApJ, 505, 37

Avila-Reese, V., & Firmani, C. 2000, Rev. Mex. Astron. Astrofis., 36, 23

Avila-Reese, V. 2007, Astrophysics and Space Science Proceedings, 2, 115

Avila-Reese, V., Zavala, J., Firmani, C., & Hernández-Toledo, H. M. 2008, AJ, 136, 1340

Avila-Reese, V., Colín, P., González-Samaniego, A., et al. 2011, ApJ, 736, 134

Avila-Reese, V., Zavala, J., & Lacerna, I. 2014, MNRAS, 441, 417

Baldry, I. K., Glazebrook, K., & Driver, S. P. 2008, MNRAS, 388, 945

Behroozi, P. S., Conroy, C., & Wechsler, R. H. 2010, ApJ, 717, 379

Behroozi, P. S., Wechsler, R. H., & Conroy, C. 2013, ApJ, 770, 57

Bell, E. F., & de Jong, R. S. 2001, ApJ, 550, 212

Bell, E. F., McIntosh, D. H., Katz, N., & Weinberg, M. D. 2003, ApJS, 149, 289

Bell, E. F., McIntosh, D. H., Katz, N., & Weinberg, M. D. 2003, ApJ, 585, L117

Berg, T. A. M., Simard, L., Mendel Trevor, J., & Ellison, S. L. 2014, MNRAS, 440, L66

Berlind, A. A., & Weinberg, D. H. 2002, ApJ, 575, 587

Bernardi, M., Shankar, F., Hyde, J. B., et al. 2010, MNRAS, 404, 2087

Bernardi, M., Meert, A., Vikram, V., et al. 2012, arXiv:1211.6122

Bernardi, M., Meert, A., Sheth, R. K., et al. 2013, MNRAS, 436, 697

Bernardi, M., Meert, A., Vikram, V., et al. 2014, MNRAS, 443, 874

Bershady, M. A., Martinsson, T. P. K., Verheijen, M. A. W., et al. 2011, ApJ, 739, L47

Berta, Z. K., Jimenez, R., Heavens, A. F., & Panter, B. 2008, MNRAS, 391, 197
Bett, P., Eke, V., Frenk, C. S., et al. 2007, MNRAS, 376, 215 s
Blanton, M. R., & Moustakas, J. 2009, ARA&A, 47, 159
Blanton, M. R., Schlegel, D. J., Strauss, M. A., et al. 2005, AJ, 129, 2562
Blanton, M. R., Eisenstein, D., Hogg, D. W., Schlegel, D. J., & Brinkmann, J. 2005, ApJ, 629, 143
Blanton, M. R., & Roweis, S. 2007, AJ, 133, 734
Blanton, M. R., Geha, M., & West, A. A. 2008, ApJ, 682, 861-873
Blumenthal, G. R., Faber, S. M., Flores, R., & Primack, J. R. 1986, ApJ, 301, 27
Bottema, R. 1993, A&A, 275, 16
Bruce, V. A., Dunlop, J. S., Cirasuolo, M., et al. 2012, MNRAS, 427, 1666
Bruzual, G., & Charlot, S. 2003, MNRAS, 344, 1000
Buitrago, F., Trujillo, I., Conselice, C. J., et al. 2008, ApJ, 687, L61
Buitrago, F., Trujillo, I., Conselice, C. J., & Häußler, B. 2013, MNRAS, 428, 1460
Bundy, K., Ellis, R. S., Conselice, C. J., et al. 2006, ApJ, 651, 120
Bundy, K., Bershady, M. A., Law, D. R., et al. 2015, ApJ, 798, 7
Calette, A. R., Avila-Reese, V., Rodríguez-Puebla, A., Hernández-Toledo, H., & Papastergis, E. 2018, Rev. Mex. Astron. Astrofis., 54, 443
Cappellari, M., Emsellem, E., Krajnović, D., et al. 2011, MNRAS, 413, 813
Carollo, C. M., Cibinel, A., Lilly, S. J., et al. 2013, ApJ, 776, 71
Catinella, B., Giovanelli, R., & Haynes, M. P. 2006, ApJ, 640, 751
Cattaneo, A., Salucci, P., & Papastergis, E. 2014, ApJ, 783, 66
Cebrián, M., & Trujillo, I. 2014, MNRAS, 444, 682
Cervantes-Cota, J. L., Rodríguez-Meza, M. A., & Nuñez, D. 2007, Journal of Physics Conference Series, 91, 012007
Cervantes-Sodi, B., Hernandez, X., Park, C., & Kim, J. 2008, MNRAS, 388, 863
Chabrier, G. 2003, PASP, 115, 763
Chakrabarty, D., & Jackson, B. 2009, A&A, 498, 615
Cibinel, A., Carollo, C. M., Lilly, S. J., et al. 2013, ApJ, 776, 72
Ciotti, L. 1991, A&A, 249, 99
Christodoulou, D. M., Shlosman, I., & Tohline, J. E. 1995, ApJ, 443, 551
Colless, M., Dalton, G., Maddox, S., et al. 2001, MNRAS, 328, 1039
Cortese, L., Fogarty, L. M. R., Bekki, K., et al. 2016, MNRAS, 463, 170
Courteau, S., & Rix, H.-W. 1999, ApJ, 513, 561
Courteau, S., Dutton, A. A., van den Bosch, F. C., et al. 2007, ApJ, 671, 203
Davis, M., Faber, S. M., Newman, J., et al. 2003, Proc. SPIE, 4834, 161
Dekel, A., & Birnboim, Y. 2008, MNRAS, 383, 119
De Rijcke, S., Zeilinger, W. W., Hau, G. K. T., Prugniel, P., & Dejonghe, H. 2007, ApJ, 659, 1172
Desmond, H. 2012, arXiv:1204.1497
de Souza, R. E., Gadotti, D. A., & dos Anjos, S. 2004, ApJS, 153, 411
Dutton, A. A., van den Bosch, F. C., Dekel, A., & Courteau, S. 2007, ApJ, 654, 27
Dutton, A. A., & van den Bosch, F. C. 2009, MNRAS, 396, 141
Dutton, A. A., Conroy, C., van den Bosch, F. C., Prada, F., & More, S. 2010, MNRAS, 407, 2
Dutton, A. A., van den Bosch, F. C., Faber, S. M., et al. 2011, MNRAS, 410, 1660
Dutton, A. A. 2012, MNRAS, 424, 3123
Dutton, A. A., Treu, T., Brewer, B. J., et al. 2013, MNRAS, 428, 3183
Dutton, A. A., Macciò, A. V., Mendel, J. T., & Simard, L. 2013, MNRAS, 432, 2496
Dutton, A. A., & Macciò, A. V. 2014, MNRAS, 441, 3359
Eisenstein, D. J., & Loeb, A. 1996, ApJ, 459, 432
Eke, V. R., Baugh, C. M., Cole, S., et al. 2004, MNRAS, 348, 866
Elmegreen, B. G. 2011, ApJ, 737, 10
Eskridge, P. B., Frogel, J. A., Pogge, R. W., et al. 2002, ApJS, 143, 73
Fall, S. M., & Romanowsky, A. J. 2013, ApJ, 769, L26
Firmani, C., & Avila-Reese, V. 2000, MNRAS, 315, 457
Fisher, D. B., & Drory, N. 2008, AJ, 136, 773
Fisher, D. B., Drory, N., & Fabricius, M. H. 2009, ApJ, 697, 630
Fisher, D. B., & Drory, N. 2010, ApJ, 716, 942
Fisher, D. B., & Drory, N. 2011, ApJ, 733, L47
Freeman, K. C. 1970, ApJ, 160, 811
Frenk, C. S., & White, S. D. M. 2012, Annalen der Physik, 524, 507
Gadotti, D. A. 2009, MNRAS, 393, 1531
Geha, M., Blanton, M. R., Masjedi, M., & West, A. A. 2006, ApJ, 653, 240
Ghosh, S., & Jog, C. J. 2014, MNRAS, 439, 929
Gnedin, O. Y., Kravtsov, A. V., Klypin, A. A., & Nagai, D. 2004, ApJ, 616, 16
Gnedin, O. Y., Weinberg, D. H., Pizagno, J., Prada, F., & Rix, H.-W. 2007, ApJ, 671, 1115
González-Samaniego, A., Colín, P., Avila-Reese, V., Rodríguez-Puebla, A., & Valenzuela, O. 2014, ApJ, 785, 58
Gonzalez, A. H., Williams, K. A., Bullock, J. S., Kolatt, T. S., & Primack, J. R. 2000, ApJ, 528, 145
Gottlöber, S., Klypin, A., & Kravtsov, A. V. 2001, ApJ, 546, 223
Graham, A. W., & Driver, S. P. 2005, Publ. Astron. Soc. Australia, 22, 118
Hernquist, L. 1990, ApJ, 356, 359
Hoffmann, V., & Romeo, A. B. 2012, MNRAS, 425, 1511
Hopkins, P. F., Bundy, K., Croton, D., et al. 2010, ApJ, 715, 202
Katz, H., McGaugh, S. S., Sellwood, J. A., & de Blok, W. J. G. 2014, MNRAS, 439, 1897
Kauffmann, G., Heckman, T. M., White, S. D. M., et al. 2003, MNRAS, 341, 54
Kauffmann, G., Heckman, T. M., White, S. D. M., et al. 2003, MNRAS, 341, 54
Kelvin, L. S., Driver, S. P., Robotham, A. S. G., et al. 2012, MNRAS, 421, 1007
Klypin, A., Yepes, G., Gottlöber, S., Prada, F., & Heß, S. 2016, MNRAS, 457, 4340
Kennicutt, R. C., Jr., Lee, J. C., Funes, J. G., et al. 2008, ApJS, 178, 247-279
Knebe, A., Pearce, F. R., Lux, H., et al. 2013, MNRAS, 435, 1618
Kormendy, J. 2013, Secular Evolution of Galaxies, 1
Kormendy, J., & Kennicutt, R. C., Jr. 2004, ARA&A, 42, 603
Kormendy, J., Fisher, D. B., Cornell, M. E., & Bender, R. 2009, ApJS, 182, 216
Kravtsov, A., Vikhlinin, A., & Meshscheryakov, A. 2014, arXiv:1401.7329
Kroupa, P., Tout, C. A., & Gilmore, G. 1993, MNRAS, 262, 545
Lange, R., Driver, S. P., Robotham, A. S. G., et al. 2015, MNRAS, 447, 2603
Łokas, E. L., & Mamon, G. A. 2001, MNRAS, 321, 155
Macciò, A. V., Dutton, A. A., van den Bosch, F. C., et al. 2007, MNRAS, 378, 55
Macciò, A. V., Dutton, A. A., & van den Bosch, F. C. 2008, MNRAS, 391, 1940
Maller, A. H., Berlind, A. A., Blanton, M. R., & Hogg, D. W. 2009, ApJ, 691, 394
Mancillas, B., Ávila-Reese, V., Rodríguez-Puebla, A., & Valls-Gabaud, D. 2017, Galaxy Evolution Across Time, Proceedings of a conference held 12-16 June, 2017 in Paris. Online at <A href="https://galaxiesinparis.sciencesconf.org/"> https://galaxiesinparis.sciencesconf.org/</A>, id. 92, 92

Mandelbaum, R., Wang, W., Zu, Y., et al. 2016, MNRAS, 457, 3200

Marleau, F. R., & Simard, L. 1998, ApJ, 507, 585

Masters, K. L., Mosleh, M., Romer, A. K., et al. 2010, MNRAS, 405, 783

McGaugh, S. S. 2011, Physical Review Letters, 106, 121303

McGaugh, S. S., & Schombert, J. M. 2015, ApJ, 802, 18

Merritt, D., Navarro, J. F., Ludlow, A., & Jenkins, A. 2005, ApJ, 624, L85

Mo, H. J., Mao, S., & White, S. D. M. 1998, MNRAS, 295, 319

Mo, H., van den Bosch, F. C., & White, S. 2010, Galaxy Formation and Evolution, by Houjun Mo , Frank van den Bosch , Simon White, Cambridge, UK: Cambridge University Press, 2010,

More, S., van den Bosch, F. C., Cacciato, M., et al. 2009, MNRAS, 392, 801

More, S., van den Bosch, F. C., Cacciato, M., et al. 2011, MNRAS, 410, 210

Mortlock, A., Conselice, C. J., Hartley, W. G., et al. 2013, MNRAS, 433, 1185

Mosleh, M., Williams, R. J., & Franx, M. 2013, ApJ, 777, 117

Moster, B. P., Somerville, R. S., Maulbetsch, C., et al. 2010, ApJ, 710, 903

Moster, B. P., Naab, T., & White, S. D. M. 2013, MNRAS, 428, 3121

Muñoz-Cuartas, J. C., Macciò, A. V., Gottlöber, S., & Dutton, A. A. 2011, MNRAS, 411, 584

Navarro, J. F., Frenk, C. S., & White, S. D. M. 1997, ApJ, 490, 493

Neto, A. F., Gao, L., Bett, P., et al. 2007, MNRAS, 381, 1450

Noordermeer, E. 2008, MNRAS, 385, 1359

Ouellette, N. N.-Q., Courteau, S., Holtzman, J. A., et al. 2017, ApJ, 843, 74

Peng, C. Y., Ho, L. C., Impey, C. D., & Rix, H.-W. 2002, AJ, 124, 266

Perez, J., Valenzuela, O., Tissera, P. B., & Michel-Dansac, L. 2013, MNRAS, 436, 259

Persic, M., & Salucci, P. 1997, VizieR Online Data Catalog, 209,

Petric, A. O., & Rupen, M. P. 2007, AJ, 134, 1952

Planck Collaboration, Aghanim, N., Akrami, Y., et al. 2018, arXiv:1807.06209

Reyes, R., Mandelbaum, R., Gunn, J. E., Pizagno, J., & Lackner, C. N. 2011, MNRAS, 417, 2347

Rodríguez-Puebla, A., Avila-Reese, V., Firmani, C., & Colín, P. 2011, Rev. Mex. Astron. Astrofis., 47, 235

Rodríguez-Puebla, A., Avila-Reese, V., Firmani, C., & Colín, P. 2011, Revista Mexicana de Astronomia y Astrofisica Conference Series, 40, 84

Rodríguez-Puebla, A., Avila-Reese, V., & Drory, N. 2013, ApJ, 767, 92

Rodríguez-Puebla, A., Avila-Reese, V., Yang, X., et al. 2015, ApJ, 799, 130

Rodríguez-Puebla, A., Behroozi, P., Primack, J., et al. 2016, MNRAS, 462, 893

Rodríguez-Puebla, A., Primack, J. R., Avila-Reese, V., & Faber, S. M. 2017, MNRAS, 470, 651

Romeo, A. B., & Falstad, N. 2013, MNRAS, 433, 1389

Romeo, A. B., & Wiegert, J. 2011, MNRAS, 416, 1191

Sackett, P. D. 1997, ApJ, 483, 103

Salim, S., Rich, R. M., Charlot, S., et al. 2007, ApJS, 173, 267

Sánchez, S. F., Kennicutt, R. C., Gil de Paz, A., et al. 2012, A&A, 538, A8

Schawinski, K., Lintott, C., Thomas, D., et al. 2009, MNRAS, 396, 818

Schaye, J., Crain, R. A., Bower, R. G., et al. 2015, MNRAS, 446, 521

Sérsic, J. L. 1963, Boletin de la Asociacion Argentina de Astronomia La Plata Argentina, 6, 41

Sersic, J. L. 1968, Cordoba, Argentina: Observatorio Astronomico, 1968

Shadmehri, M., & Khajenabi, F. 2012, MNRAS, 421, 841

Shen, Y., & Lou, Y.-Q. 2003, MNRAS, 345, 1340

Shen, S., Mo, H. J., White, S. D. M., et al. 2003, MNRAS, 343, 978

Sheth, R. K., & Tormen, G. 1999, MNRAS, 308, 119

Sheth, R. K., Mo, H. J., & Tormen, G. 2001, MNRAS, 323, 1

Simard, L., Willmer, C. N. A., Vogt, N. P., et al. 2002, ApJS, 142, 1

Sommer-Larsen, J., & Dolgov, A. 2001, ApJ, 551, 608

Somerville, R. S., & Davé, R. 2015, ARA&A, 53, 51

Tamburro, D., Rix, H.-W., Leroy, A. K., et al. 2009, AJ, 137, 4424

Terzić, B., & Graham, A. W. 2005, MNRAS, 362, 197

Tinker, J., Kravtsov, A. V., Klypin, A., et al. 2008, ApJ, 688, 709-728

Toomre, A. 1964, ApJ, 139, 1217

Toomre, A. 1977, Evolution of Galaxies and Stellar Populations, 401

Trujillo, I., Erwin, P., Asensio Ramos, A., & Graham, A. W. 2004, AJ, 127, 1917

Trujillo, I., Conselice, C. J., Bundy, K., et al. 2007, MNRAS, 382, 109

Tully, R. B., & Fisher, J. R. 1977, A&A, 54, 661

van den Bosch, F. C. 2000, ApJ, 530, 177

van den Bosch, F. C., Abel, T., Croft, R. A. C., Hernquist, L., & White, S. D. M. 2002, ApJ, 576, 21

van Zee, L., & Bryant, J. 1999, AJ, 118, 2172

Vikram, V., Wadadekar, Y., Kembhavi, A. K., & Vijayagovindan, G. V. 2010, MNRAS, 409, 1379

Weinzirl, T., Jogee, S., Khochfar, S., Burkert, A., & Kormendy, J. 2009, ApJ, 696, 411

Wechsler, R. H., & Tinker, J. L. 2018, ARA&A, 56, 435

Wyse, R. F. G., Gilmore, G., & Franx, M. 1997, ARA&A, 35, 637

York, D. G., Adelman, J., Anderson, J. E., Jr., et al. 2000, AJ, 120, 1579

Zaritsky, D., Courtois, H., Muñoz-Mateos, J.-C., et al. 2014, AJ, 147, 134

Zavala, J., Avila-Reese, V., Hernández-Toledo, H., & Firmani, C. 2003, A&A, 412, 633

Zavala, J., Okamoto, T., & Frenk, C. S. 2008, MNRAS, 387, 364

Zavala, J., Avila-Reese, V., Firmani, C., & Boylan-Kolchin, M. 2012, MNRAS, 427, 1503

Zheng, Z., Berlind, A. A., Weinberg, D. H., et al. 2005, ApJ, 633, 791

Yang, X., Mo, H. J., van den Bosch, F. C., Zhang, Y., & Han, J. 2012, ApJ, 752, 41

APPENDIX A: THE STATIC MODEL

A1 A disk-halo model

The halo is assumed to be spherical and with an initial NFW density profile (Navarro et al. 1997):

$$\rho = \frac{4\rho_s}{(r/r_s)(1+r/r_s)^2}, \tag{A1}$$

where r_s is the characteristic radius at which the logarithmic slope of the density distribution $dln\rho/dlnr = -2$ and $\rho_s = \rho(r_s)$. We define the virial radius, R_{vir}, as the radius that encloses a mean density equal to Δ_{vir} times the mean density of the universe, where Δ_{vir} is obtained from the spherical top-hat collapse model. The halo mass profile obtained by integrating equation (A1) is:

$$M(r) = 8\pi\rho_s r_s^3 \left[\frac{1}{1+Cx} - 1 + ln(1+Cx)\right], \tag{A2}$$

where $x \equiv r/R_{vir}$ and

$$C = \frac{R_{vir}}{r_s} \tag{A3}$$

is the NFW concentration parameter. We also define the virial velocity V_{vir} as the circular velocity at the virial radius, $V_{vir}^2 = GM_{vir}/R_{vir}$, where G is the gravitational constant, M_{vir} is the virial mass and R_{vir} is the virial radius.

The angular momentum of the halo is expressed through the so-called spin parameter λ:

$$\lambda = \frac{J_{vir}\,|E|^{\frac{1}{2}}}{GM_{vir}^{\frac{5}{2}}} = \frac{J_{vir}/M_{vir}}{\sqrt{2}R_{vir}V_{vir}} f_C^{\frac{1}{2}}, \tag{A4}$$

where J_{vir} is the total angular momentum at the virial radius, E is the halo energy and

$$f_C = \frac{C}{2}\frac{1-1/(1+C)^2 - 2ln(1+C)/(1+C)}{[C/(1+C) - ln(1+C)]^2}, \tag{A5}$$

which measures the deviation of E from a singular isothermal sphere with the same mass (see MMW98). The spin parameter is a measure of the centrifugal rotational support of a structure against the potential energy. For $\lambda = 1$, the structure is fully supported by rotation, while for $\lambda << 1$, rotation is not important for the virial equilibrium.

Due to the gravitational effects produced by forming galaxies, the halo contracts its inner regions. This happens when baryons cool and concentrate in the center of the spheroid, modifying the shape of the gravitational potential. Since this process is slow with respect to the dynamical time of the system, the halo contracts to conserve its adiabatic invariants taking into account that its spherical symmetry remains. In this way, the angular momentum of individual dark matter particles, which moves on circular orbits, is conserved during contraction. Therefore, a particle that is initially (before the formation of the disk) at radius r_i, ends up at radius r_f, where

$$GM_f(r_f)r_f = GM_i(r_i)r_i. \tag{A6}$$

Here $M_i(r_i)$ is given by equation (A2) (NFW profile) and $M_f(r_f)$ is the total final mass within r_f. The final mass is the sum of the dark matter mass inside the initial radius r_i and the mass of an exponential disk (Blumenthal et al. (1986)):

$$M_f(r_f) = M_d(r_f) + M_{h,f}(r_f) = M_d(r_f) + (1 - f_{\rm bar})M_i(r_i), \tag{A7}$$

where $f_{\rm bar}$ is the fraction of the total mass locked in the baryonic disk of mass M_d, that is, $f_{\rm bar} \equiv M_d/M_h$, and

$$M_d(r) = M_d\left[1 - \left(1 + \frac{r}{R_D}\right)e^{-r/R_D}\right]. \tag{A8}$$

Thus, from equations (A6) and (A7), we can find iteratively a contraction factor $\Gamma(r_i) \equiv \frac{r_f}{r_i}$, which allows us to calculate the mass distribution of the contracted dark matter halo. The relation between r_i and r_f can be generalized as

$$r_f = \Gamma^{\nu} r_i, \tag{A9}$$

where ν is a free parameter and varies according the type of contraction. For example, $\nu = 1$ is the standard contraction for radial orbits from Blumenthal et al. (1986), $\nu = 0$ is for non contraction, and $\nu < 0$ corresponds to models of expansion of the inner dark matter halo instead of contraction. In Dutton et al. (2007) it was proposed that most of halos actually should expand due to galaxy formation, because of the strong effects of SN-driven outflows. In a more standard context, based on numerical cosmological hydrodynamical simulations, Gnedin et al. (2004) have found that the Blumenthal et al. (1986) adiabatic contraction formalism should be slightly corrected (the particle orbits deviate from the pure circular motion). The corrections suggested by their results is such that instead of the standard value $\nu = 1$, one should use $\nu = 0.8$. This is the value that we will use in our model.

In the static model of disk galaxies in centrifugal equilibrium loaded inside ΛCDM halos, it is assumed that the baryons initially had the same density profile and angular momentum distribution as the dark matter. Therefore, if we assume detailed angular momentum conservation (i.e., the specific angular momentum of the disk, J_{gal}/M_d remains the same as that one of the halo, J_{vir}/M_h), then the spin parameter of the baryons that will form the disk is the same than the halo one, $\lambda_{bar} = \lambda_h$. If this assumption is relaxed, then

$$\lambda_{bar} \equiv \left(\frac{j_{gal}}{f_{\rm bar}}\right)\lambda_h, \tag{A10}$$

where

$$j_{gal} = J_{gal}/J_{vir}. \tag{A11}$$

The total angular momentum for a disk with a surface density distribution $\Sigma(R)$ and a circular velocity profile $V(R)$ is

$$J_{gal} = 2\pi\int_0^{R_{vir}} \Sigma(R)RV_{\rm T}(R)RdR. \tag{A12}$$

We assume that the disk has an exponential surface density distribution $\Sigma(R) = \Sigma_0\exp(-R/R_D)$, so that

$$J_{gal} = M_d R_D V_{vir} f_V, \tag{A13}$$

where

$$f_V = \frac{1}{2}\int_0^{R_{vir}/R_D} e^{-u}u^2\frac{V(uR_D)}{V_{vir}}du, \tag{A14}$$

a factor that takes into account the gravitational effects of the disk. Assuming that the angular momentum of the disk is a fraction of the total angular momentum of the halo (i.e. $J_{gal} = j_{gal}J_{vir}$), we can combine equations (A4) and (A12) to obtain:

$$R_D = \frac{1}{\sqrt{2}}\left(\frac{j_{gal}}{f_{\rm bar}}\right)\lambda_{bar}R_{vir}f_c^{-1/2}f_V^{-1}, \tag{A15}$$

with λ_{bar}=λ_h when detailed angular momentum conservation is assumed.

Once calculated the scale radius R_D, we can calculate the (total) circular velocity $\mathrm{V_T(R)}$, which is the sum in quadrature of contributions from disk and halo:

$$\mathrm{V_T}^2(R) = \mathrm{V_D}^2(R) + \mathrm{V_H}^2(R), \tag{A16}$$

where

$$\mathrm{V_H}^2(R) = G[M_f(R) - M_d(R)]/R, \tag{A17}$$

and

$$\mathrm{V_D}^2(R) = \frac{GM_d}{R_D} 2y^2 \; [I_0(y)K_0(y) - I_1(y)K_1(y)] \tag{A18}$$

is the circular velocity produced by an exponential disk, where $y = r/(2R_D)$, and I_n and K_n are modified Bessel functions (Freeman 1970). However, in order to define R_D, according to eq. (A15), we should know the total circular velocity profile (see eq. A14). This circularity leads us to use an iterative approach in order to calculate the final disk scale radius R_D of the disk in centrifugal equilibrium with the potential of the cosmological halo contracted on its own by this disk.

A2 A disk-bulge-halo model

In this Section, we describe the inclusion of a bulge proposed to be formed by internal instabilities of the disk, following Dutton et al. (2007, hereafter D+2007). The baryonic mass of the galaxy is now the sum of a disk and a bulge:

$$M_{\rm bar} \equiv f_{\rm bar} M_{vir} = M_d + M_{\rm B}. \tag{A19}$$

The bulge-to-disk mass ratio is defined as:

$$\theta \equiv \frac{M_{\rm B}}{M_d} \tag{A20}$$

and the disk mass and the bulge mass are given in terms of this ratio, so that

$$M_d = \frac{1}{1+\theta} f_{\rm bar} M_{vir}, \tag{A21}$$

and

$$M_{\rm B} = \frac{\theta}{1+\theta} f_{\rm bar} M_{vir}. \tag{A22}$$

According to eq. (A11), the fractional angular momentum of the baryons is given by $j_{gal} = J_{gal}/J_{vir}$. Let $J_b = j_b J_{vir}$ be the original angular momentum of the baryonic material out of which the bulge forms. However, during the bulge formation process this angular momentum is transferred to the disk plus the halo, and therefore the final angular momentum of the bulge is zero (D+2007). If f_t is the fraction of J_b that is transferred to the disk, then the final angular momentum of the disk is

$$J_{gal} = [j_{gal} - (1-f_t) j_b] J_{vir}, \tag{A23}$$

and the specific angular momentum of the final disk is

$$\frac{J_{gal}}{M_d} = (1+\theta)(1-f_{lost}) \left(\frac{j_{gal}}{m_{gal}}\right) \frac{J_{vir}}{M_{vir}}, \tag{A24}$$

where the parameter f_{lost} is the fraction of the total angular momentum of the material out of which the bulge plus disk forms and which has been lost to the halo:

$$f_{lost} = (1-f_t)\left(\frac{j_b}{j_{gal}}\right). \tag{A25}$$

We define other important parameter:

$$f_x \equiv f_{lost}\left(\frac{1+\theta}{\theta}\right) = (1-f_t)\left(\frac{J_b/M_B}{J_{gal}/M_{gal}}\right), \tag{A26}$$

which expresses the ratio of specific angular momentum that has been lost to the halo due to bulge formation to the total specific angular momentum of the material out of which the disk and bulge have formed. This parameter should be less than unity if the bulge is formed out of material with low specific angular momentum (van den Bosch et al. 2002).

We can obtain a new relation for the scale length of the disk after a bulge formed from the disk by dynamical instabilities by combining equations (A4), (A12), (A11). One obtains:

$$R_D = \frac{1}{f_V\sqrt{2f_c}} \left[1 + (1-f_x)\theta\right] \lambda_{bar} R_{vir}, \tag{A27}$$

where λ_{bar} is now the effective initial spin parameter of the material out of which the bulge and disk form, and it is given by

$$\lambda_{bar} \equiv \left(\frac{j_{gal}}{f_{bar}}\right)\lambda, \tag{A28}$$

where $f_{\rm bar}$ is the baryonic fraction. As we can see in equation (A25), the bulge formation affects the final scale length of the disk through the parameters θ and f_x. Following D+2007, it is assumed that the material that forms the bulge has the same specific angular momentum as the disk. Here, we assume $f_x = 0.5$ (see Shen et al. 2003).

The new total circular velocity $V(R)$ is given by the equation:

$$V_T^2(R) = V_D^2(R) + V_B^2(R) + V_H^2(R), \tag{A29}$$

the component V_B is the circular velocity of the bulge, which is derived from the mass distribution of the bulge. In principle, the instabilities are instrinsic (isolated disk), giving rise to secular evolution that ends in a pseudo-bulge (see e.g. Kormendy 2013). Observations show that pseudo-bulges are well described by a Sérsic surface brightness (surface density) profile with index n between 0.5 and 3. A Sérsic surface density profile (Sérsic 1963; Sersic 1968), is given by

$$I(R) = I_{e,B} exp\left\{-b_n\left[\left(\frac{R}{R_{e,B}}\right)^{1/n} - 1\right]\right\}. \tag{A30}$$

where $I_{e,B}$ is the surface brightness at the effective radius $R_{e,B}$, which is defined as the projected radius that encloses one half of the total luminosity (mass), by adjusting the value of b_n. The conditions to sets the value of b_n is (see Graham & Driver 2005; Ciotti 1991):

$$\Gamma(2n) = 2\gamma(2n, b_n), \tag{A31}$$

where Γ and γ are the Gamma and lower Incomplete Gamma Functions, respectively. Capaccioli (1989) introduced the following approximation for b_n, valid for $0.5 < n < 10$:

$$b_n \approx 2n - (1/3). \tag{A32}$$

Assuming a spherical density distribution, the surface density profile given by equation (A30) can be translated into a volumetric density distribution. According to the formation mechanism, the mass distribution of bulges are expected to be different. Bulges formed by secular evolution of the disk (our starting scenario) have typically the properties of pseudo-bulges (e.g., Kormendy & Kennicutt 2004; **?**), with Sérsic profiles shallower than a de Vacouleours profile, that is with Sérsic index $n < 4$. Here, we assume an average value of $n = 2$ for the secular bulges (see e.g., Gadotti 2009), in which case the mass profile is

$$\nu(R) = M_B \left\{ 1 - exp(-\sqrt{\alpha^2\eta}) \left[1 + \sqrt{\alpha^2\eta} + \frac{(\alpha^2\eta)}{2} + \frac{(\alpha^2\eta)^{3/2}}{6} + \frac{(\alpha^2\eta)^2}{24} + \frac{(\alpha^2\eta)^{5/2}}{120} \right] \right\}, \tag{A33}$$

where M_B is the total mass bulge, $\alpha = 5.67$ and $\eta \equiv R/R_{e,B}$. The corresponding circular velocity profile is

$$V_B(R) = \sqrt{\frac{G\nu}{R}}, \tag{A34}$$

where G is the gravitational constant.

As it will be discussed below, in the case of massive galaxies, interactions and mergers are actually common. Therefore, the massive disks are expected to undergo strong induced instabilities that end commonly with the formation of large bulges with a de Vacouleours profile or $n = 4$ Sérsic profile. The corresponding density profile in this case is given by the Hernquist function (Hernquist 1990):

$$\rho_b = \frac{M_B}{2\pi} \frac{r_b}{R(R + R_b)^3}, \tag{A35}$$

where $R_b = R_{e,B}/1.815$ is a scale length. The corresponding circular velocity is:

$$V_B(R) = \frac{\sqrt{GM_B R}}{(R + R_{e,B})}. \tag{A36}$$

Thus, for galaxies smaller than a given mass, we will assume Sérsic distribution with $n = 2$, while for massive galaxies, $n = 4$. The corresponding circular velocities are given by equations (A34) and (A36). In both cases, the relevant parameters are M_B and $R_{e,b}$. Since our model is not evolutionary, we are not in conditions of calculating $R_{e,B}$ for our bulges. Instead, we use an empirical relation between $R_{e,B}$ and M_B, as given in Gadotti (2009):

$$\log \frac{R_{e,B}}{\mathrm{kpc}} = \begin{cases} -2.062 + 0.2\log(M_B/M_\odot), & \log(M_B/M_\odot) < 10 \\ -3.057 + 0.3\log(M_B/M_\odot), & \log(M_B/M_\odot) > 10 \end{cases} \tag{A37}$$

Finally, we include the bulge component to the final mass budget and Eq. A7 is then rewritten as

$$\begin{aligned} M_f(r_f) &= M_d(r_f) + M_B(r_f) + M_{DM,f}(r_f) \\ &= M_d(r_f) + M_B(r_f) + (1 - f_{bar})M_i(r_i)\,. \end{aligned} \tag{A38}$$

Thus, we calculate the adiabatic invariant dark matter halo contraction by using this new mass distribution.

Bulge mass assignment

Let us first consider the case of internal dynamical instabilities produced by the secular evolution of a self-gravitating disk. For this, the critical instability parameter let be $\beta(R) = V_D(R)/V_T(R)$. According to the numerical simulations of Christodoulou et al. (1995) the disk is stable as long as $\beta(R) < \beta_{crit}$, where the value of the parameter β_{crit} falls roughly in the range $0.52 \leq \beta_{crit} \leq 0.70$. Following D+2007, we calculate the mass of the disk contained within the radius where $\beta(R)$ attains a maximum and check if $\beta_{max} > \beta_{crit}$:

$$\beta_{max} = \max_{0 \leq R \leq R_{vir}} \beta(R) < \beta_{crit}. \tag{A39}$$

If this is the case, then all this mass is assigned to a bulge. We use $\beta_{crit} = 0.62$ for the case of an isolated disk.

However, the secular bulge formation mechanism is not suitable in the case of galaxy interactions and mergers. The mergers transfer the secondary galaxy to the bulge of the primary, and induce disk instabilities in the primary (Hopkins et al. 2010, see more references therein),. In order to take into account these effects, yet within our scheme of β_{max}, we propose that the bulge formation by mergers can be emulated by lowering the value of β_{crit}. It is well known that mergers become important in the mass assembly of only massive galaxies ($M_* \geq 2-3\times10^{10} M_\odot$, $M_h \geq 3-5\times10^{11} M_\odot$), being more frequent as more massive they are (see e.g., Gottlöber et al. 2001; Zavala et al. 2012). Therefore, one expects that β_{crit} will decrease on average with M_h. This dependence will be fixed in order our model could reproduce the observational trend of the bulge-to-disk ratio with M_*.

Note that in our scheme the bulge is formed only from stars of the primary disk. This might not be the case when the mergers are majors because in this case most of the stars in the bulge come from the accreted secondary galaxy rather from the disk. This is why our scheme becomes somewhat uncertain for galaxies dominated by bulges.

A3 Stellar and gas fractions

So far in our static model of disk galaxies in centrifugal equilibrium loaded inside ΛCDM halos, we did not make any difference between stellar and gas components in the galaxies. Since the static model is not an evolutionary model, we can not follow a star formation history as well as we can not follow the secular or major merger processes. However, as was done in the case of bulge formation, the structural and dynamical internal distributions of our "instantaneous" galaxies can be used for estimating when the conditions of large-scale star formation due to disk instabilities are fulfilled. The simple Toomre criterion (Toomre 1964) will be used for this purpose.

First, we consider that if a fraction of the disk is converted into bulge, according to the criterion described in the previous subsection, then the bulge is composed only by stars. Second, for the remaining baryonic disk, we estimate the fraction of it that could have been transformed into stars. According to the Toomre criterion, instabilities in a gaseous disk able to drive star formation happen when

$\Sigma_{crit}(R) < \Sigma_d(r)$, where

$$\Sigma_{crit}(R) = \frac{\sigma_{gas}(R)\kappa(R)}{3.36QG}. \tag{A40}$$

Here, $\Sigma_d(r)$ is the baryonic (assumed gaseous initially) disk surface density profile, $\kappa(R)$ and σ_{gas} are the epicycle frequency and velocity dispersion radial distributions, and Q is the Toomre stability parameter. The two first distributions are given by the solution of our static model. Regarding σ_{gas}, observational studies of neutral, atomic (H_I) gas for spiral galaxies, including our galaxy, show that it lies in a range of $5-15$ km/s (Tamburro et al. 2009; Petric & Rupen 2007; van Zee & Bryant 1999) without any clear trend with radius. We will assume a constant value of $\sigma_{gas} = 7$ km/s.

The Q stability parameter originally given in Toomre (1964) for an infinitesimal thin disk has the value of 1. However, in numerical simulations of more realistic disks, the value found for Q is typically $1.5-2.5$. In the early stays of the gaseous disk, the formation of massive clumps make the disk more unstable and the value of Q can be larger (Dekel & Birnboim 2008; Perez et al. 2013). Besides, the Toomre criterion changes a little when taking into account the coexistence of two fluids, stars and gas (Shen et al. 2003)). The value of Q is affected by other factors, such as the presence of a bulge; a bulge provides more dynamical support against instabilities, making the Q parameter larger. Other factors affecting Q are the height of disk, which is derived from vertical equilibrium, as well as the gas dissipation which extends the instability to small scales, producing infinitesimally thin disks unstable for all Toomre-Q values and reasonable thick disks stable at high Q, primarily because of thickness effects (Elmegreen 2011; Romeo & Wiegert 2011). The turbulences of gas also change Q; the perturbations in the molecular and atomic gas have a significant effect on both the inner and outer regions of the disk. This can drive the inner gas disk to a regime of transition between two stability phases such that the outer disk is more prone to star-dominated instabilities (Hoffmann & Romeo 2012; Shadmehri & Khajenabi 2012).

There are also observational studies that attempted to constrain the value of Q along the disks of local galaxies. For example, Bottema (1993) conclude that Q along the disks of their analyzed spiral galaxies is around 2 and 2.5.

We will take a constant value of $Q = 2.5$ for the "secular" disks, i.e. those that are not expected to have suffered mergers. This applies on average for low-mass galaxies, let say those smaller than $M_* \approx 3 \times 10^{10}$ M$_\odot$ ($M_h \approx 5 \times 10^{11}$ M$_\odot$. However, as already discussed in the previous subsection, for galaxies formed in more massive halos, the major mergers become more frequent in such a way that the central galaxy likely suffers also mergers and interactions, which trigger strong disk instabilities able to produce bursts of star formation. Since our model is not evolutionary, we are not able to calculate these processes, but if we keep ourselves in the scheme of the Toomre instability criterion, such an enhanced star formation can be estimated someway by increasing artificially the value of Q. As in the case of bulge formation in massive galaxies, we again will proceed empirically. The "artificial" value of Q as a function of M_h for the massive halos will be set in such a way that the gas fraction, R_{gas}, vs stellar mass empirical relation is reproduced. The observations show that as larger are the galaxies, the smaller gas fractions have (or larger stellar fractions have). In the next Section, it is described in more detail our procedure.

Following the Toomre instability criterion, the stellar mass contained up to the radius r along the disk is calculated as:

$$M_{d,*}(r) = 2\pi \int_0^r [\Sigma_s(r)] r' dr' \tag{A41}$$

where $\Sigma_s(r) = \Sigma_{bar}(r) - \Sigma_{crit}(r)$ is the stellar surface mass density in the regions where the local criterion for instability is fulfilled. $M_{d,*}(r)$ is computed up to the radius where $\Sigma_b(r) = \Sigma_{crit}(r)$. The total baryonic surface density is then $\Sigma_{bar}(r) = \Sigma_d(r) + \Sigma_g(r)$. Since by construction $\Sigma_{bar}(r)$ is an exponential function, the stellar surface mass density is expected then to be deviate from an exponential distribution.

A4 Summary

The main equations solved in the iterations are (A38), (A8), (A20), (A27) and (A29). Following MMW98 and D+2007, we start with a guess for R_D by setting $f_V = 1$ in equation (A27). Then, we obtain M_d from equation (A8) and M_B from equation (A20); by replacing this into equation (A38) and using equation (A6), we find r_i as a function of r to obtain M_f from equation (A38). Thus, we have $V_T^2(R)$ and the bulge mass M_B for the given R_D, and we can calculate the bulge circular velocity and the new disk circular velocity from equations (A17) and (A29). Replacing this into eq. (A14) and using (A27), finally we obtain a new value for R_D and M_B and check for convergence.

APPENDIX A: THE EMPIRICAL HI-TO-M_* AND H$_2$-TO-M_* CORRELATIONS FOR LOCAL LATE- AND EARLY-TYPE GALAXIES

Calette et al. (2018) have compiled and homogenized from the literature several samples of local galaxies with reported measures of stellar mass, HI and H$_2$ masses, as well as morphology type and/or color. By defining the mass ratios $R_{HI} \equiv M_{HI}/M_*$ and $R_{H_2} \equiv M_{H_2}/M_*$, in this work, it is found that the R_{HI}–M_* and R_{H_2}–M_* correlations for blue/late-type (LTG) and red/early-type (ETG) galaxies are better described by a double-power law.

The double power law proposed to fit the R_{HI} vs M_* correlations is:

$$\log_{10}\left(R_{\rm H_I}\right) = \log_{10}(B) - \log_{10}\left[\left(\frac{M_*}{M^s}\right)^{\xi} + \left(\frac{M_*}{M^s}\right)^{\rho}\right], \tag{A1}$$

where B is the normalization, ξ and ρ are the slopes of the function and M^s is the breakdown mass. In Table A1, the values of these parameters for both LTGs and ETGs are given.
For the scatter around the determined R_{HI}-M_* correlations, they assume that it is log-normal distributed in agreement with several previous studies (see Calette et al. (2018) for the references). The lognormal intrinsic scatter is proposed to slightly depend on M_* as:

$$\sigma_{\log_{10} R_{\rm H_I}} = A + \varphi \log_{10}\left(\frac{M_*}{M^s}\right). \tag{A2}$$

Galaxy population	Parameters.			
ETG	$\log_{10}(B)$	ξ	ρ	$\log_{10}(M^S)$
	-0.82	0.20	1.86	9.50
LTG	$\log_{10}(B)$	ξ	ρ	$\log_{10}(M^S)$
	0.06	0.20	0.85	9.50

Table A1. Parameters of the R_{HI}–M_* two-power law relations

Galaxy population	Parameters	
ETG	A	φ
	0.70	0.00
LTG	A	φ
	0.41	-0.04

Table A2. Parameters for the scatters around the R_{HI}–M_* relations

Galaxy population.	Parameters.			
ETG	$\log_{10}(C)$	β	γ	$\log_{10}(M^S)$
	-1.52	0.0	1.50	9.50
LTG	$\log_{10}(C)$	β	γ	$\log_{10}(M^S)$
	-0.5	0.34	0.78	9.50

Table A3. Parameters of the R_{H_2}–M_* double power-law correlations

In Table A2, the values of A and φ for the two galaxy populations are reported.

The double-power law proposed to fit the R_{H_2} vs M_* correlations is:

$$\log_{10}\left(R_{\mathrm{H}_2}\right) = \log_{10}(C) - \log_{10}\left[\left(\frac{M_*}{M^S}\right)^{\beta} + \left(\frac{M_*}{M^S}\right)^{\gamma}\right], \tag{A3}$$

where C is the normalization, β and γ are the slopes of the function and M^S is the breakdown mass. In Table A3 are given the values of these parameters.

Regarding the intrinsic scatter around the R_{H_2}–M_* relations, again, Calette et al. (2018) assumes that it is log-normally distributed. The width of this distribution, in the case of LTGs, which are mostly star-forming objects, is expected to be close to the width of the specific star formation rate (sSFR) vs. M_* relation, the so-called "main sequence"[4]. The observations of local galaxies show that the scatter around this relation is 0.3 – 0.5 dex, increasing slightly to lower masses (e.g., Salim et al. 2007). Based on this reasoning as well as on the scatter that observations show in the largest compiled samples in Calette (2015), he finds that a good description for the intrinsic scatter of LTGs is:

$$\sigma_{\log_{10} R_{\mathrm{H}_2}} = A' + \varphi' \log_{10}\left(\frac{M_*}{M^S}\right). \tag{A4}$$

with $A' = 0.37$ and $\varphi' = -0.01$.

In the case of ETGs, the intrinsic scatter seems to be larger than for LTGs. The former are in general passive, devoid of gas reservoirs, but probably a fraction of them can acquire some gas and trigger star formation during interactions and mergers. Then, the amount of H_2 depends on the kind of merger and on the conditions to transform the atomic gas to molecular one. The range of possibilities is huge, hence, the scatter around the R_{H_2}–M_* relation should be large. Calette et al. (2018) assumes the width of the log-normal distribution to be $\sigma_{\log_{10} R_{\mathrm{H}_2}} = 0.7$ dex and constant with mass.

This paper has been typeset from a TEX/LATEX file prepared by the author.

---

[4] The sSFR is a measure of the efficiency of current SFR of a galaxy with respect to its past average efficiency. Since star formation proceeds in molecular clouds, the fraction of H_2 in a galaxy with respect to its size (M_*), is expected to correlate with the sSFR

2.5 Paper: Kinematic scaling relations of CALIFA galaxies: A dynamical mass proxy for galaxies across the Hubble sequence

Monthly Notices
of the
ROYAL ASTRONOMICAL SOCIETY

MNRAS **479,** 2133–2146 (2018) doi:10.1093/mnras/sty1522
Advance Access publication 2018 June 11

Kinematic scaling relations of CALIFA galaxies: A dynamical mass proxy for galaxies across the Hubble sequence

E. Aquino-Ortíz,[1★] O. Valenzuela,[1] S. F. Sánchez,[1] H. Hernández-Toledo,[1] V. Ávila-Reese,[1] G. van de Ven,[2,3] A. Rodríguez-Puebla,[1] L. Zhu,[2] B. Mancillas,[4] M. Cano-Díaz[1] and R. García-Benito[5]

[1] *Instituto de Astronomía, Universidad Nacional Autónoma de México, A.P. 70-264, 04510 CDMX, Mexico*
[2] *Max Planck Institute for Astronomy, Konigstuhl 17, D-69117 Heidelberg, Germany*
[3] *European Southern Observatory, Karl-Schwarzschild-Str. 2, D-85748 Garching b. Munchen, Germany*
[4] *LERMA, CNRS UMR 8112, Observatoire de Paris, 61 Avenue de l'Observatoire, F-75014 Paris, France*
[5] *Instituto de Astrofísica de Andalucía (CSIC), PO Box 3004, E-18080 Granada, Spain*

Accepted 2018 June 6. Received 2018 May 26; in original form 2018 April 25

ABSTRACT

We used ionized gas and stellar kinematics for 667 spatially resolved galaxies publicly available from the Calar Alto Legacy Integral Field Area survey (CALIFA) third Data Release with the aim of studying kinematic scaling relations as the Tully & Fisher (TF) relation using rotation velocity, V_{rot}, the Faber & Jackson (FJ) relation using velocity dispersion, σ, and also a combination of V_{rot} and σ through the S_K parameter defined as $S_K^2 = KV_{rot}^2 + \sigma^2$ with constant K. Late-type and early-type galaxies reproduce the TF and FJ relations. Some early-type galaxies also follow the TF relation and some late-type galaxies the FJ relation, but always with larger scatter. On the contrary, when we use the S_K parameter, all galaxies, regardless of the morphological type, lie on the same scaling relation, showing a tight correlation with the total stellar mass, $M_\star$. Indeed, we find that the scatter in this relation is smaller or equal to that of the TF and FJ relations. We explore different values of the K parameter without significant differences (slope and scatter) in our final results with respect to the case $K = 0.5$ besides a small change in the zero-point. We calibrate the kinematic S_K^2 dynamical mass proxy in order to make it consistent with sophisticated published dynamical models within 0.15 dex. We show that the S_K proxy is able to reproduce the relation between the dynamical mass and the stellar mass in the inner regions of galaxies. Our result may be useful in order to produce fast estimations of the central dynamical mass in galaxies and to study correlations in large galaxy surveys.

Key words: galaxies: evolution – galaxies: fundamental parameters – galaxies: kinematics and dynamics.

1 INTRODUCTION

Galaxy scaling relations describe trends that are observed between different properties of galaxies. They are assumed to be the consequence of their formation and evolution. Probably the kinematic scaling relation most widely studied for spiral galaxies is the Tully–Fisher relation (hereafter TF) – a correlation between luminosity and rotational velocity, first reported by Tully & Fisher (1977). It was originally established as a tool to measure distances to spiral galaxies (Giovanelli et al. 1997). It has been suggested that the slope, zero-point, and tightness may have a cosmological origin helping us to understand the formation and evolution of galaxies (Cole et al. 1994; Eisenstein & Loeb 1996; Avila-Reese, Firmani & Hernández 1998; Mo, Mao & White 1998; Courteau & Rix 1999; Firmani & Avila-Reese 2000; Navarro & Steinmetz 2000). In the local universe the TF relation is very tight (Verheijen 2001; Bekeraité et al. 2016; Ponomareva et al. 2017), locating galaxies with rising rotation curves on the low-velocity end and galaxies with declining rotation curve on the high-velocity end (Persic, Salucci & Stel 1996). The luminosity-based TF is more directly accessible, however, the amount of light measured from the stellar population is a function of passband, and therefore different TF relations emerge when observing galaxies at different wavelengths. A physically more fundamental approach instead of luminosity is based on stellar mass, $M_\star$. The resulting TF relation is well approximated

---

★ E-mail: eaquino@astro.unam.mx

Published by Oxford University Press on behalf of the Royal Astronomical Society

by a single power law with small scatter at least for disc galaxies more massive than $\sim 10^{9.5} M_{\odot}$ (McGaugh et al. 2000; Bell & de Jong 2001; Avila-Reese et al. 2008). A similar correlation between the luminosity (or the stellar mass) of elliptical galaxies and the velocity dispersion in their central regions was established by Faber & Jackson (1976) (hereafter FJ). The shape and scatter of the FJ relation has been less frequently studied because its large residuals show a significant correlation with galaxy size, i.e. a third parameter within the so called fundamental plane (Djorgovski & Davis 1987; Dressler et al. 1987; Cappellari et al. 2013; Desmond & Wechsler 2017).

It is presumed that galaxy internal kinematics as tracer of the gravitational potential provide the dynamical mass. If spiral and elliptical galaxies were completely dominated by rotation velocity and velocity dispersion, respectively, the TF and FJ relations would provide insights into the connection between galaxies and their dark matter content. However, structural properties, environmental effects, or internal physical processes perturb the kinematics of late-type galaxies producing non-circular motions that under/overestimates the circular velocity (Valenzuela et al. 2007; Holmes et al. 2015; Randriamampandry et al. 2015). On the other hand, elliptical galaxies, although dominated by velocity dispersion, often present some degree of rotation (Lorenzi, Debattista & Gerhard 2006; Emsellem et al. 2007; Cappellari et al. 2011; Emsellem et al. 2011; Rong et al. 2018). Non-circular motions on disc galaxies and rotation on ellipticals may contribute to miss a fraction of the gravitational potential, modifying the scaling relations and precluding them from being directly comparable to theoretical predictions.

Weiner et al. (2006) introduced a new kinematic parameter involving a combination of rotation velocity and velocity dispersion in order to study high-redshift galaxies, where in some cases random motions were not negligible. Weiner et al. (2006) showed that such parameter provides a better proxy to the integrated line-width of galaxies emission lines than rotation velocity or velocity dispersion alone, regardless of the galaxy morphology. The parameter is defined as:

$$S_K^2 = K V_{rot}^2 + \sigma^2, \quad (1)$$

where V_{rot} is the rotation velocity, σ is the velocity dispersion, and K a constant that could be extremely complicated function of the formation history, dynamic state, and environment of galaxies. Kassin et al. (2007) found that by adopting a value of $K = 0.5$, the $S_{0.5}$ parameter presents a tight correlation with the stellar mass for a sample of galaxies at redshift $z \leq 1.2$ extracted from the All Wavelength Extended Groth Strip International Survey and the Deep Extragalactic Evolutionary Probe 2. This correlation seems to be independent of the morphological type. Other analyses, focused on the evolution of the TF relation at high redshift ($z \sim 2$), explored the $M_{\star}$–$S_{0.5}$ relation confirming that turbulent motions might play an important dynamical role (Cresci et al. 2009; Gnerucci et al. 2011; Vergani et al. 2012; Price et al. 2016; Christensen & Hjorth 2017). Zaritsky, Zabludoff & Gonzalez (2008) provided a possible explanation of the $M_{\star}$–$S_{0.5}$ relation as a virial one, including all galaxy evolution, geometrical and dynamical complications into the K coefficient.

Cortese et al. (2014) (hereafter C14) performed the only systematic study of this relation at low redshift ($z \leq 0.095$). They used the stellar and ionized gas kinematics integrated within one effective radius, r_e, for galaxies observed with the Sydney-AAO Multi-object Integral Field survey (SAMI, Croom et al. 2012). C14 confirmed that all galaxies, regardless of the morphological type, lie on the same kinematic scaling relation $M_{\star}$–$S_{0.5}$ with a significant improvement compared with the TF and FJ relations. Although the result is encouraging, the spatial covering of the observations ($1 r_e$) and the coarse spatial resolution of the data may contribute to the uncertainties in a similar way as they do it in HI line-width TF estimations (Ponomareva et al. 2017). Therefore, it is needed to repeat this analysis using data with better spatial resolutions and coverage.

The aim of this paper is to explore and calibrate the TF, FJ, and S_K scaling relations in the local universe for galaxies from the Calar Alto Legacy Integral Field Area survey (CALIFA, Sánchez et al. 2012). These data present a larger spatial coverage and better physical resolution (Sánchez et al. 2016c).[1] In a recent study, Gilhuly et al. (in preparation), presented an exploratory study of these relations for a limited sample of galaxies. They perform a systematic and detailed analysis of the limitations of the kinematics parameters, and in particular the velocity dispersion in the CALIFA data set. The current study would explore a larger sample, being focused on the nature of these scaling relations.

The structure of this article is as follows. In Section 2 we briefly describe the CALIFA sample, including a summary of the delivered data sets. Details of the analysis performed over the data are presented in Section 3.1. In Section 3.2 we estimate the kinematics parameters within $1 r_e$, following the same methodology as C14. In Section 3.3 we perform a detailed modelling of the 2D spatially resolved velocity maps for a subsample of good quality data sets. With this modelling we estimate the possible effects of aperture and non-circular motions in disc galaxies and obtain a more precise derivation of the maximum rotational velocity, V_{max}. In Section 4, we present the main results of this study. In Section 5, we discuss the results and their physical implications and finally we summarize the main conclusions in Section 6.

2 DATA SAMPLE

We use the data provided by the CALIFA survey (Sánchez et al. 2012) that has delivered publicly available integral field spectroscopy data for 667 galaxies (Sánchez et al. 2016c), although the current samples comprises more than 700 galaxies (Sánchez et al. 2017). Details of the observational strategy and data reduction are explained in these two articles. All galaxies were observed using *PMAS* (Roth et al. 2005) in the PPaK configuration (Kelz et al. 2006), covering a hexagonal field of view (FoV) of 74 arcsec × 64 arcsec that is sufficient to map the full optical extension of most of the galaxies up to two to three effective radii. This is possible due to the diameter selection of the CALIFA sample (Walcher et al. 2014). The final observed sample comprises galaxies of any morphological type (See Fig. 1). It covers, with a good sampling, the colour–magnitude diagram and the stellar mass distributions of the Local Universe in a representative and statistically significant way for galaxies more massive than $10^{9.5}$ M$_{\odot}$ (Walcher et al. 2014; Sánchez et al. 2016c).

The observing strategy guarantees a complete coverage of the FoV, with a final spatial resolution of Full Width at Half Maximum (FWHM) $\sim$2.5 arcsec, corresponding to $\sim$1 kpc at the average redshift of the survey (García-Benito et al. 2015; Sánchez et al. 2016c). CALIFA observed the galaxies in two configurations: (i) the V500 setup, a low-resolution mode that covers a wavelength range between 3745 and 7500 Å, with a resolution of $\lambda/\Delta\lambda \sim 850$

---

[1] Both surveys present a similar projected PSF FWHM of $\sim$2.5 arcsec. However CALIFA sample galaxies observed in a considerable lower redshift and narrower redshift range.

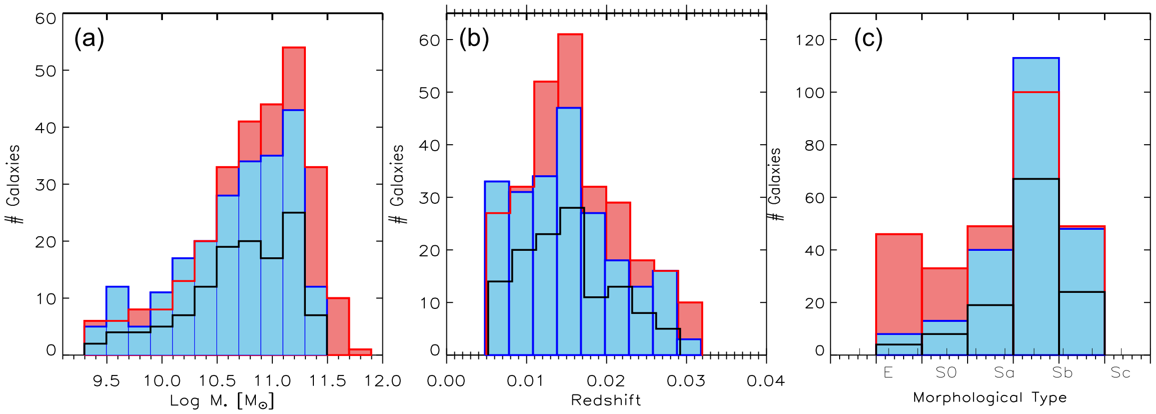

Figure 1. Galaxy Sample distributions in (a) total stellar masses, (b) redshift, and (c) morphological type. The blue and red histograms indicate galaxies with ionized gas and stellar kinematics, respectively, whereas the unfilled black histogram indicate galaxies with both, ionized gas and stellar kinematics.

(FWHM ∼6 Å), and (ii) the V1200 setup, an intermediate resolution mode, that covers the wavelength range between 3700 and 4800 Å, with a resolution of $\lambda/\Delta\lambda$ ∼1650 (FWHM ∼2.7 Å). The delivered data set was reduced using version 2.2 of the CALIFA pipeline, whose modifications with respect to the previous ones (Sánchez et al. 2012; Husemann et al. 2013; García-Benito et al. 2015) are described in Sánchez et al. (2016c). The final data-product of the reduction is a data-cube comprising the spatial information in the x- and y-axis, and the spectral one in the z one. For further details of the adopted data format and the quality of the data consult Sánchez et al. (2016c).

3 ANALYSIS

We describe here the analysis performed to estimate the stellar mass distribution and the kinematics parameters for the different galaxies included in the current data set.

3.1 Spectroscopic analysis

In this paper, we use the data-products (ionized gas kinematic maps) derived for the CALIFA V500 setup data set by Pipe3D pipeline (Sánchez et al. 2016b) based on the Fit3D fitting tool (Sánchez et al. 2016a), together with the stellar line-of-sight velocity and intrinsic dispersion maps for the V1200 setup performed using pPXF by Falcón-Barroso et al. (2017).

Pipe3D models the stellar continuum adopting a multi Single Stellar Population (SSP) template library, taking into account the velocity, dispersion, and dust attenuation of the stellar populations. Then, it estimates the main properties of the nebular emission lines. The current implementation of Pipe3D adopted the GSD156 (Cid Fernandes et al. 2013) template library for the analysis of the stellar population properties. This library comprises 156 templates covering 39 stellar ages (from 1 Myr to 13 Gyr), and four metallicities ($Z/Z_\odot$ = 0.2, 0.4, 1, and 1.5). A spatial binning for the stellar population analysis was applied to reach a homogeneous signal-to-noise (S/N) of 50 across the FoV. The stellar population fitting was applied to the coadded spectra within each spatial bin. Finally, following the procedures described in Cid Fernandes et al. (2013) and Sánchez et al. (2016a), the stellar-population model was estimated for each spaxel by rescaling the best-fitting model within each spatial bin to the continuum flux intensity in the corresponding spaxel. The stellar-population model spectra are then subtracted from the original data-cube to create a gas-pure cube comprising only the ionized gas emission lines. For this pure-gas cube, the stronger emission lines were then fitted spaxel by spaxel using single Gaussian models for each emission line in each individual spectrum to derive the corresponding flux intensity and line-of-sight kinematics. In addition, the spatial distribution of the stellar mass densities and the integrated stellar masses at different apertures are recovered from the Pipe3D analysis by taking into account the decomposition in SSPs, the Mass-to-Light ratio of each of them, and the integrated light at each spaxel within the FoV. For this derivation was assumed the Salpeter Initial Mass Function (Salpeter 1955). More details of the fitting procedure, adopted dust attenuation curve, and uncertainties of the process are given in Sánchez et al. (2016a, b).

Falcón-Barroso et al. (2017) performed a detailed analysis to extract the stellar kinematics for the intermediate resolution CALIFA data (V1200 setup). The data-cubes were spatially binned with the Voronoi 2D binning method of Cappellari & Copin (2003) to achieve an approximately constant S/N of 20 per spaxel taking into account the correlation in the error spectrum of nearby spaxels (see Husemann et al. 2013 for details). This S/N value conserves a good spatial resolution while still being able to reliably estimate the line-of-sight velocity distribution. The stellar kinematics was estimated using the PPXF code of Cappellari & Emsellem (2004). The stellar templates were taken from the Indo-US spectral library (Valdes et al. 2004) with ∼330 selected stars. The stellar rotation velocity, the velocity dispersion, and corresponding error were estimated by χ^2 minimization in pixel space as the biweight mean and standard deviations of a set of 100 Monte Carlo realizations of the fitting.

3.2 Integrated kinematics

The original data set comprises 734 galaxies for the V500 data set observed within the framework of the CALIFA survey (Sánchez et al. 2017), and the 300 galaxies for the V1200 data set described by Falcón-Barroso et al. (2017). From this data set we perform a selection of the optimal data for the proposed analysis following the methodology described by C14. First, spaxels are discarded if the error in velocities is greater than 20 km s^{-1} and 50 km s^{-1} for gaseous and stellar kinematics, respectively. This conventional cut corresponds to one third of the spectral FWHM

(∼6 Å, i.e. ∼150 km s^{-1}) of V500 CALIFA data. Secondly, we selected only those galaxies for which at least 80 per cent of the spaxels within an ellipse of semimajor axis equal to $1r_e$ fulfill this quality criterion. This criterion guarantee that we are tracing well the kinematics parameters up to $1r_e$. Finally, galaxies under merging and clear traces of interactions are discarded based on morphological distortions and the abundance of galaxy neighbors with a comparable size. Following this procedure our final sample comprise 223 galaxies with ionized gas kinematics (V500 setup), 278 with stellar kinematics (V1200 setup), and 123 with both of them.

3.2.1 *Velocity dispersion: σ*

Stellar velocity dispersions were estimated as the linear average of the velocity dispersion of all spaxels within the ellipse mentioned in the previous section using the velocity dispersion maps from the V1200 data set without correction for inclination. Following C14 we use linear instead of luminosity-weighted averages to be consistent with our velocity width measurements which are not luminosity-weighted. Ionized gas velocity dispersions were estimated fitting the integrated spectrum within a diameter of 5 arcsec with Pipe3D for the V500 data set using the template library described above. Regarding the determination of the stellar and gaseous velocity dispersions (up to $1r_e$), which dominate in early-type galaxies, we rely on the detailed kinematic analysis presented in Zhu et al. (2018a, b).

3.2.2 *Rotation velocity:* V$_{\rm rot}$

Once more, we followed C14, to derive the stellar (V1200 data set) and gaseous (V500 data set) rotation velocities. They adopted the same classical procedure developed to analyse the integrated HI emission profiles in galaxies, i.e. through the width parameter, *W* (Mathewson, Ford & Buchhorn 1992; Vogt et al. 2004). First, a histogram is derived of the velocities estimated for all the good spaxels within the r_e. Then, it is calculated the difference between the 10th and 90th percentile points of this velocity histogram, defined as the width: $W = V_{90} - V_{10}$ (Catinella, Haynes & Giovanelli 2005). Finally, the rotation velocity is defined as:

$$V_{rot} = \frac{W}{2(1+z)sin(i)}, \tag{2}$$

where z is the redshift and i is the galaxy inclination determined from the observed ellipticity ϵ as:

$$cos(i) = \sqrt{\frac{(1-\varepsilon)^2 - q_0^2}{1-q_0^2}}, \tag{3}$$

with q_0 being the intrinsic axial ratio of edge-on galaxies. Following Catinella et al. (2012) and C14, we adopted $q_0 = 0.2$ for all galaxies and set the inclination to 90° edge-on if $\epsilon \geq 0.8$.

Integrated rotation velocity estimated by equation (2) is a good representation of the maximum rotation velocity, V_{max}, if the kinematics of the galaxy is axisymmetric (i.e. without non-circular motions). However, this is not always the case. Some galaxies show deviations from a pure rotational pattern due to warps, lopsidedness, arms, bars, outflows, inflows, nuclear activity, etc. (Bosma 1978; Schoenmakers, Franx & de Zeeuw 1997; Verheijen 2001; Holmes et al. 2015; Kalinova et al. 2017; Sánchez-Menguiano et al. 2017), producing non-circular motions and distorting the velocity profile (i.e. velocity histogram). In the next subsection, we try to quantify these effects in the derivation of V_{max} by performing a more detailed analysis on a limited sample of galaxies and comparing the results.

3.3 Spatially resolved kinematics: V_{max}

Kinematic maps of spiral galaxies are often treated as being consistent with a purely circular flow pattern. This means that the kinematics of a galactic disc at a certain galactocentric radius can be described by a single tilted ring model defined by three parameters: the rotation velocity and two parameters that describe the local disc orientation with respect to some reference system (Rogstad, Lockhart & Wright 1974). Several routines exist to fit kinematic maps based on this method. The most extensively used is the ROTCUR routine (Begeman 1989), which fits a set of inclined rings to a velocity field. However, as we mentioned above, the kinematics could be affected by the presence of non-circular motions and in some cases the tilted-ring model is an oversimplification. A more precise kinematic analysis requires tools that consider non-circular motions.

Spekkens & Sellwood (2007) and Sellwood & Sánchez (2010) developed the VELFIT code specifically to characterize the non-circular motions in the kinematics of spiral galaxies expressed in a Fourier series. We used this code with some improvements (E. Aquino-Ortíz in preparation) to derive the properties of the velocity maps. This fit provides an estimate of the rotation curve, the kinematic inclination, and position angle of the galaxy, together with the amplitude of the non-circular motions as a function of radius. A bootstrap procedure is adopted to estimate the uncertainties on the derived parameters.

The current procedure is not performed over the full data set, since in many cases the kinematics present clear deviations due to external perturbations or is strongly affected by random motions. We discarded those cases whose kinematics appeared highly disturbed by the presence of large nearby companions or clear indications of being in a merging process. Therefore, we select a control sample, with good quality spatially resolved kinematics, comprising those isolated galaxies with low velocity dispersion, and inclinations in the range $30° < i < 70°$. This sample of galaxies, that are the best suited for modelling their velocity maps, comprises 42 galaxies for ionized gas kinematics (V500) and 92 galaxies for stellar kinematics (V1200).

The estimated rotation curves for all these galaxies present a great diversity, in agreement with previous results (Kalinova et al. 2017). For a limited fraction of galaxies (∼ 10 per cent) the spatial coverage was insufficient to measure the maximum velocity, V_{max}. In order to still estimate V_{max} we follow Bekeraité et al. (2016) and parametrize the rotation curve using the formula proposed by Bertola et al. (1991):

$$v(r) = v_0 + \frac{v_c r}{(r^2 + k^2)^{\frac{\gamma}{2}}}, \tag{4}$$

where v_0 is the systemic velocity of the galaxy, v_c is a parameter governing the amplitude of the rotation curve and k describes its sharpness, and finally γ allows modelling rising or falling curves, with $\gamma = 1$ for a flat rotation curve.

4 RESULTS

Fig. 2 shows the analysed kinematic scaling relations using the total stellar mass (unless noted otherwise) and the integrated kinematics, segregated by stellar and ionized gas kinematics (upper panels) and by morphology (lower panels), respectively. In each panel is

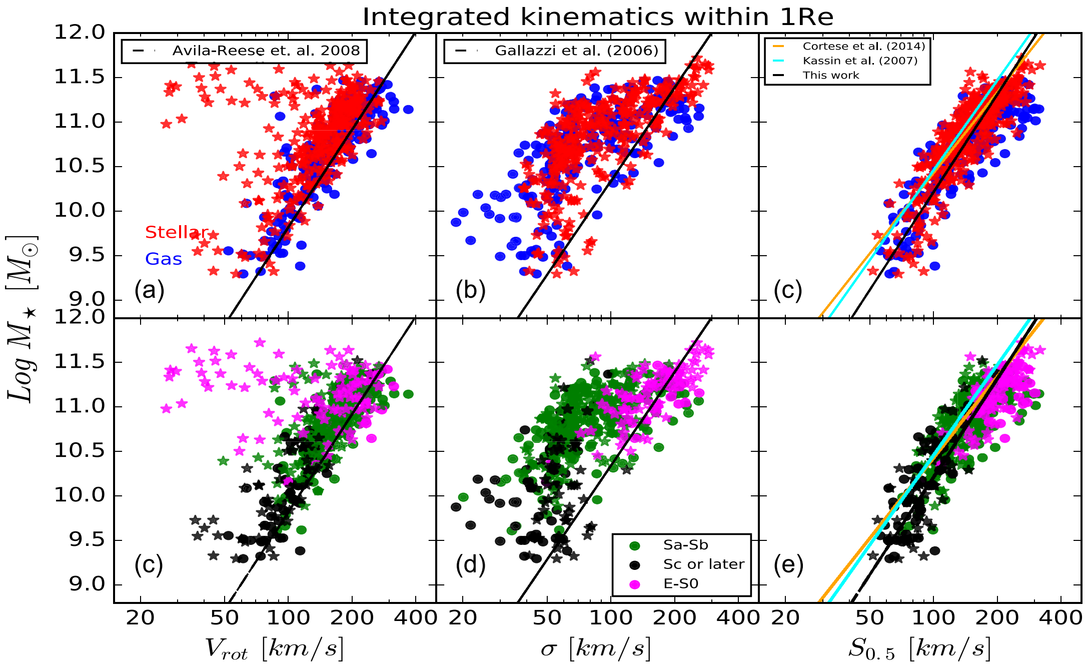

Figure 2. Kinematic scaling relations with integrated kinematics. Left-hand panel: TF relation with the black line representing the orthogonal best-fitting TF relation from Avila-Reese et al. (2008). Middle panel: FJ relation with the black line the best-fitting FJ relation from Gallazzi et al. (2006). Right-hand panel: The $M_\star - S_{0.5}$ relation, cyan and yellow lines indicate the best-fitting $M_\star - S_{0.5}$ relation from Kassin et al. (2007) and Cortese et al. (2014), respectively, whereas the black line represent our best-fit. *Top panels:* The red stars and blue circles represent galaxies with stellar and ionized gas kinematics. *Bottom panels:* Galaxies with different morphological types; the magenta stars indicate elliptical and lenticular galaxies, the green stars are Sa and Sb galaxies, and the black circles are Sc galaxies.

included some reference relations found by previous results, and the best-fitting relations for the $M_\star - S_{0.5}$ distribution. Fig. 3 shows the same distributions for the resolved kinematics.

Table 1 summarizes the results of an orthogonal linear fit along the horizontal axis, considering the total stellar mass on the vertical axis as the independent variable, using the routines presented by Akritas & Bershady (1996), for each of the kinematic scaling relations and data set. It includes the zero-points and slopes, together with the scatter around the best-fitting relations estimated from the 'error-in-variable' of the corresponding fit as the standard deviation of residuals. In addition, there are listed the reference results for the TF, FJ, and $S_{0.5}$ scaling relations extracted from the literature shown in Figs 2 and 3.

4.1 TF relation

The TF relation including early type galaxies based on the integrated analysis are shown in the left-hand panels of Fig. 2. These relations show a large scatter, 0.084 dex in log V_{rot} for ionized gas kinematics and 0.20 dex for stellar kinematics. The value for ionized gas kinematics is in agreement with the one reported for the luminosity TF relation estimated by Bekeraité et al. (2016), ∼0.09 dex, despite the fact that their study was based on a detailed analysis of the rotation velocity of a subsample of the CALIFA galaxies. In that study they analysed their velocity within a radius containing 83 per cent of all light, V_{opt}. On the other hand, our scatter for stellar kinematics is lower than the one reported by C14 for SAMI (∼0.25 dex). The difference with this later study is not surprising because the SAMI sample is dominated by Sc low-mass galaxies, where the rotation curves are still rising at $1r_e$, being far from V_{max}, whereas our sample is dominated by Sa and Sb galaxies (see lower panels of Fig. 2).

The left-hand panel of Fig. 3 shows the TF relation also including early-type galaxies based on the spatially resolved analysis (i.e. using V_{max}). The parameters of the best-fitting relation to these data are listed in Table 1. When adopting this improved estimation of the velocity, the scatter decreases to ∼0.07 dex for the ionized gas kinematics, but it increases to ∼0.24 dex for the stellar one. This later value agrees with the one reported by C14. The scatter for our stellar kinematics TF relation increases due to that late-type galaxies move to higher velocities and also for the inclusion of early-type galaxies in the relation. Such galaxies are undetected in the gas component, being the analysed sample limited to mostly late-type galaxies.

As a reference we include in Figs 2 and 3 the derivation of the stellar TF relation as presented in Avila-Reese et al. (2008).[2] We use their orthogonal linear fit considering the stellar mass as the independent variable. As expected, there is an offset between this classical derivation and our results for the integrated kinematics. However, for the resolved kinematics, which determines V_{max}, the offset tends to disappear, at least for the spiral galaxies.

4.2 FJ relation

Central panels of Figs 2 and 3 show the FJ distributions including late-type galaxies using the integrated kinematics sample and

---

[2] We have increased the stellar mass in Avila-Reese et al. (2008) by 0.15 dex in order to convert from diet-Salpeter to Salpeter IMF.

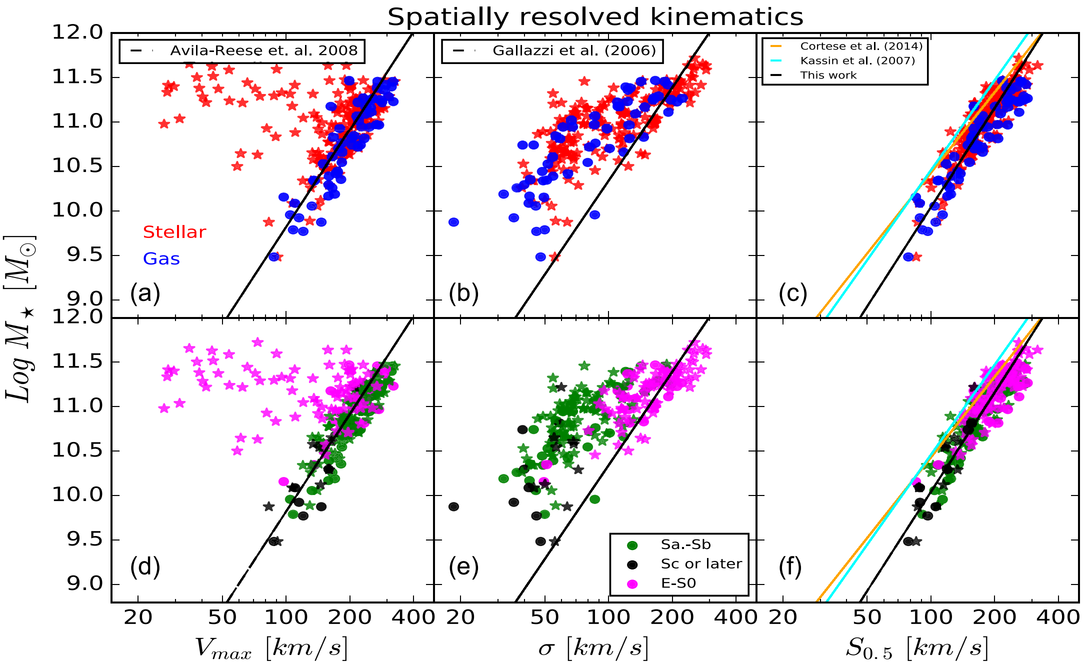

Figure 3. Kinematic scaling relations for our control sample with spatially resolved kinematics. Left-hand panel: TF with the black line as the stellar mass TF from Avila-Reese et al. (2008). Middle panel: FJ with the black line as the Gallazzi et al. (2006). Right-hand panel: The $M_\star$–$S_{0.5}$ relation, cyan and yellow lines are the best-fits of Kassin et al. (2007) and Cortese et al. (2014), respectively, whereas the black line represents our best-fit. *Top panels:* The red stars and blue circles represent galaxies with stellar and gas kinematics. *Bottom panels:* The colour-code represents different morphologies.

Table 1. Orthogonal linear fit parameters to scaling relations.

Relation		Tully–Fisher			Faber–Jackson			$S_{0.5}$		
	Galaxies	scatter	slope	zero-point	scatter	slope	zero-point	scatter	slope	zero-point
Integrated kinematics at R_e										
Gas	223	0.084	0.27 ± 0.01	− 0.65 ± 0.12	0.171	0.36 ± 0.02	− 2.03 ± 0.27	0.087	0.29 ± 0.01	− 1.03 ± 0.12
Stellar	278	0.200	0.16 ± 0.02	0.32 ± 0.30	0.160	0.31 ± 0.03	− 1.37 ± 0.25	0.075	0.26 ± 0.01	− 0.67 ± 0.10
Total	501	0.171	0.20 ± 0.01	− 0.01 ± 0.18	0.165	0.34 ± 0.02	− 1.71 ± 0.18	0.082	0.27 ± 0.01	− 0.79 ± 0.07
Cortese et al. (2014)		0.26	–	–	0.16	–	–	0.10	0.33 ± 0.01	− 1.41 ± 0.08
Kassin et al. (2007)		–	–	–	–	–	–	0.10	0.34 ± 0.05	1.89 ± 0.03
Resolved kinematics, V_{max}										
Gas	59	0.07	0.25 ± 0.02	− 0.41 ± 0.17	0.10	0.31 ± 0.01	− 1.47 ± 0.19	0.053	0.29 ± 0.01	− 0.92 ± 0.13
Stellar	167	0.24	− 0.10 ± 0.09	3.34 ± 1.07	0.14	0.53 ± 0.03	− 3.88 ± 0.34	0.052	0.27 ± 0.01	− 0.72 ± 0.12
Total	226	0.22	0.08 ± 0.04	1.37 ± 0.48	0.13	0.44 ± 0.02	− 2.79 ± 0.22	0.054	0.27 ± 0.01	− 0.71 ± 0.11
Only spiral galaxies, V_{max}										
Gas	42	0.043	0.27 ± 0.01	− 0.63 ± 0.15	0.076	0.35 ± 0.02	− 1.84 ± 0.21	0.043	0.29 ± 0.01	− 0.88 ± 0.13
Stellar	92	0.053	0.30 ± 0.02	− 1.00 ± 0.02	0.091	0.35 ± 0.03	− 1.94 ± 0.34	0.052	0.28 ± 0.02	− 0.92 ± 0.21
Total	134	0.052	0.28 ± 0.01	− 0.73 ± 0.13	0.098	0.33 ± 0.02	− 1.69 ± 0.22	0.051	0.27 ± 0.01	− 0.80 ± 0.13
Avila-Reese et al. (2008)		0.045	0.27 ± 0.01	− 0.69 ± 0.12	–	–	–	–	–	–

Note. All scatters are estimated from the linear fit as the standard deviation of all residuals, we consider stellar mass, $M_\star$, as independent variable. $log(V, \sigma, S_{0.5}) = a + blog(M_\star)$. V, σ, and $S_{0.5}$ are given in $[\mathrm{km\,s^{-1}}]$, $M_\star$ in $\mathrm{M_\odot}$.

the spatially resolved one, respectively. A reference FJ relation, derived by Gallazzi et al. (2006), has been included for comparison. Our stellar FJ relations show a scatter of ~0.16 dex (~0.14 dex) and ~0.17 dex (~0.10 dex) for gaseous and stellar kinematics, respectively, for the integrated (spatially resolved) subsamples. These dispersions are similar to the ones found by C14 (~0.16 dex), but larger than the one reported by Gallazzi et al. (2006) (~0.07 dex).

On a parallel situation as the one found for the TF relation, the stellar velocity dispersions and those derived for early-type ones are more in agreement with the FJ relation than the gaseous dispersions and/or those derived for late-type galaxies.

4.3 $M_\star$–S_K relation

The right-hand panels of Fig. 2 show the $M_\star$–$S_{0.5}$ distribution for the integrated kinematics segregated by gas and stellar kinematics (upper panel) and by morphology (lower panel). As a reference the $S_{0.5}$ relations, derived by C14 and Kassin et al. (2007), have been included together with the best-fitting relation derived with our own data. As in the previous cases, the best-fitting parameters for the linear regression have been included in Table 1. The distribution is clearly tighter than those of the FJ relations, with scatter very similar or lower to the one found for the TF relation (∼0.08 dex).

The right-hand panels of Fig. 3 show the same distributions for the resolved kinematics subsample. For this control sample, the scatter decreases significantly to 0.053 dex and 0.052 dex for both the ionized gas and stellar kinematics, respectively. As we mentioned above, the slope, zero-point, and scatter of the TF and FJ relations could depend on several factors including (i) the morphology of the galaxies, (ii) the adopted shape for the rotational curve, and even (iii) the methodology used to measure both the rotational velocity and/or the velocity dispersion (see Colleen et al., for an example of the effects of the uncertainties). For the $S_{0.5}$ parameter, the dependence on morphology and the described offsets between gaseous and stellar kinematics eventually disappear. Thus, galaxies of any morphology lie on the same scaling relation in agreement with previous studies.

C14 found a good agreement in the slope of the $S_{0.5}$ relation derived using integrated kinematics up to $1r_e$ for the SAMI data set with that derived by Kassin et al. (2007) for a sample of star-forming galaxies, using the maximum rotational velocities. However, they found larger differences in the zero-point of their relations. In our analysis the behaviour is similar. The slope remains unchanged between both the integrated and resolved kinematics, with small differences compared with the ones derived by Cortese et al. (2014) and Kassin et al. (2007). However, our best-fit for the total sample (gas + stars) presents a scatter clearly lower than the one found by previous studies, being ∼0.082 dex for the integrated kinematics and ∼0.054 dex for the spatially resolved one. The reduction in the scatter combining rotation velocity and velocity dispersion in a single parameter, indicate that together they trace the gravitational potential than each one separately. Actually, this latter value is in agreement with the physical interpretation of Zaritsky et al. (2008).

5 DISCUSSION

We discuss here the implications of the results listed in the previous section, trying to understand how the uncertainties may affect them and the physical nature of the described relations.

5.1 Narrowing down the uncertainties

A critical challenge giving a physical interpretation to galaxy scaling relations are the uncertainties because they can potentially modify or erase the dependence between the analysed properties. We have tried to narrow down their effects by performing the analysis twice. Once using the integrated kinematics, following C14, and then, we improved the accuracy using a spatially resolved kinematic analysis. This second analysis is performed at the expenses of the statistics. We consider that this second data set is best suited to derive a more accurate $S_{0.5}$ relation.

Table 1 shows there is a clear improvement in the TF and $S_{0.5}$ relations (in most of the cases) when adopting the spatially resolved kinematics. On the other hand, there is only a mild improvement in the FJ relation (since this relation does not involve rotation velocities). To verify the scatter we tried to reproduce the 'classical' TF relation using the spatially resolved kinematics. For doing so, we select only the spiral galaxies and compare their distribution in the $M_\star - V_{max}$ diagram with that of a well-established comparison sample: the compilation and homogenization presented in Avila-Reese et al. (2008). The left-hand panel of Fig. 4 shows this comparison. The parameters derived for the TF relation for both subsamples match pretty well, with very good agreement, in particular for the gas kinematics, as shown in Table 1. Therefore, the spatially resolved kinematic sample seems to be the best one to characterize the scaling relations involving rotation velocities.

Using this new subsample we derive the most precise estimation of the $M_\star - S$ relation, shown in the right-hand panel of Fig. $4_{0.5}$. The parameters of this relation are listed in Table 1. The first result emerging from this analysis is that the scatter is of the order of the $S_{0.5}$ relation found for the completely resolved kinematics (∼0.05 dex). Therefore, to select a better subsample in terms of the TF relation does not seem to affect the result. In other words, the inclusion of early-type galaxies affects the TF relation, but it does not affect the $S_{0.5}$ one. Another interesting result is that the scatter in this relation is very similar to that of the TF relation for the same subsample. Therefore, the inclusion of the effects of random motions does not increase the scatter, even for galaxies clearly supported by rotation.

Finally, the slope and zero-point of the $S_{0.5}$ relations found for (i) this particular subsample of galaxies that reproduces the better TF relation, (ii) the completely resolved kinematics sample, and (iii) the integrated kinematics sample, when considering both the gaseous and stellar kinematics, agree with each other. Thus, only the precision is increased by performing a detailed resolved kinematics for a TF-compatible subsample, but the general trends are the same. The result of this test suggests that our analysis is not dominated by velocity uncertainties and the early tight correlation presented by C14 and in this paper is real and not the result of the poorly constrained in velocity for dispersion-dominated systems.

5.2 S_K as a proxy of the dynamical mass

The observed kinematics of a galaxy is often used to infer the total (dynamical) mass enclosed at different radii (Persic & Salucci 1988; Zavala et al. 2003; Courteau et al. 2014; Ouellette et al. 2017). Assuming that the $M_\star - S_{0.5}$ scaling relation is a consequence of a more physical relation between the dynamical mass and the stellar mass in the inner regions, we suppose that the $S_{0.5}$ parameter traces the dynamical mass as follow:

$$M_{dyn} \propto S_{0.5}^2 \Rightarrow M_{dyn} = \eta \frac{r_r S_{0.5}^2}{G} = \eta \frac{r_r (0.5 V_{rot}^2 + \sigma^2)}{G}, \qquad (5)$$

where r_r is a characteristic radius of the galaxy, G the gravitational constant, and η is a structural coefficient which encapsulate information of the shape of the galaxy, projection effects, dynamical structure, etc., in fact it can be included into the K coefficient of the $S_{0.5}^2$ parameter, however it is useful to introduce η in order to compare with former studies. Dynamical models such as Jeans Anisotropic Models (JAMs, Cappellari 2008) or Schwarzschild (Schwarzschild 1979) are considered the state-of-the-art inferences of galaxies mass distribution including dynamical enclosed mass. Cappellari et al. (2006) calibrated equation (5) for a sample of early-type galaxies from the SAURON project (Bacon et al. 2001) using the velocity dispersion instead of the $S_{0.5}$ parameter in combination with

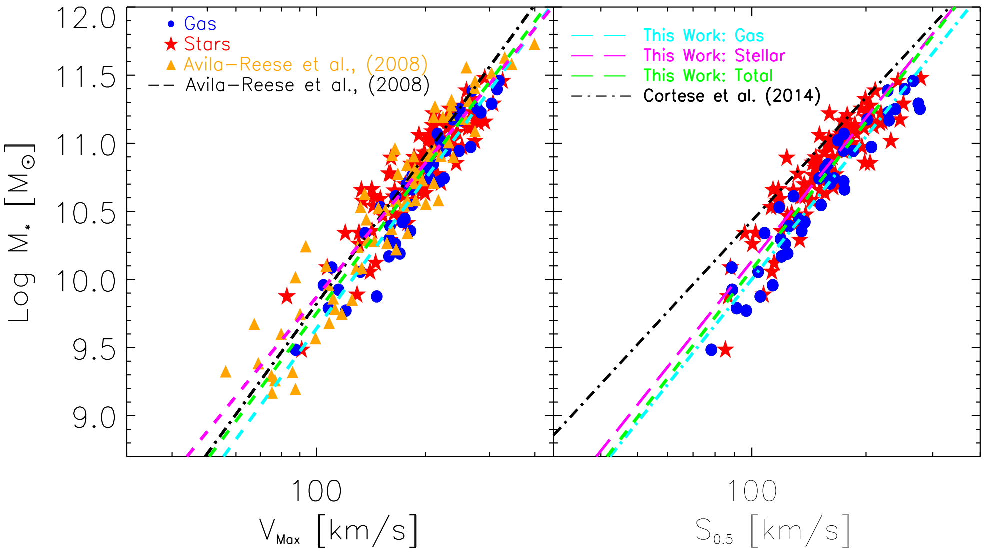

Figure 4. Scaling relations for our control subsample. The left-hand and right-hand panels show the TF and $S_{0.5}$ scaling relations, respectively. The blue and red symbols represent gaseous and stellar kinematics for galaxies with inclinations in the range $30^\circ < i < 70^\circ$. The Cyan, magenta, and green lines are the best-fits for gas, stellar, and total (gas + stellar). In the TF relation we recover in great detail the result of the data compilation from Avila-Reese et al. (2008); their masses were corrected to convert to a Salpeter IMF. It is clear that in galaxies where the random motions are negligible, the $S_{0.5}$ relation tends to be the TF.

Schwarzschild dynamical models. They found that the dynamical mass within the effective radius can be robustly recovered using a coefficient $\eta \approx 2.5$, which varies little from galaxy to galaxy.

Leung et al. (2018) performed a detailed comparison of JAMs and Schwarzschild models for 54 of the CALIFA galaxies included here. We use these dynamical masses, M_{dyn}^{JAMs}, to calibrate the equation (5) based on the $S_{0.5}$ parameter. We found that the enclosed dynamical mass within the effective radius [i.e. using r_e as the characteristic radius in equation (5)] can be robustly recovered using a single coefficient $\eta \approx 1.8$ for all the galaxies, with a narrow dispersion of 0.15 dex. To validate that calibration we compare the estimated dynamical masses by the equation (5) with those derived using dynamical models for a sample of 300 galaxies analysed by Zhu et al. (2018a, b), together with the ones by Leung et al. (2018). Fig. 5 shows the comparison between the different estimations of the dynamical masses. As expected, the agreement between the values derived using JAMs and Schwarzschild dynamical models for the galaxies studied by Leung et al. (2018) agree with each other with a low scatter of 0.08 dex. Interestingly, we still find a very good agreement using $\eta = 1.8$ between our $S_{0.5}$ derived dynamical masses and sophisticated dynamical mass estimations, with a scatter of ~0.15 dex. We may wonder why is the $S_{0.5}$ parameter such a good mass tracer. This is remarkable in view that, we do not systematically study IMF effects (Martín-Navarro et al. 2015) and kinematic anisotropy (Zhu et al. 2018a). The enclosed mass within r_e is an integrated quantity weakly sensitive to the specific mass and shape density profile, a similar discussion has been presented by Wolf et al. (2010) for dwarf spheroidal galaxies, only on such grounds the $S_{0.5}$ is a competitive M_{dyn} proxy.

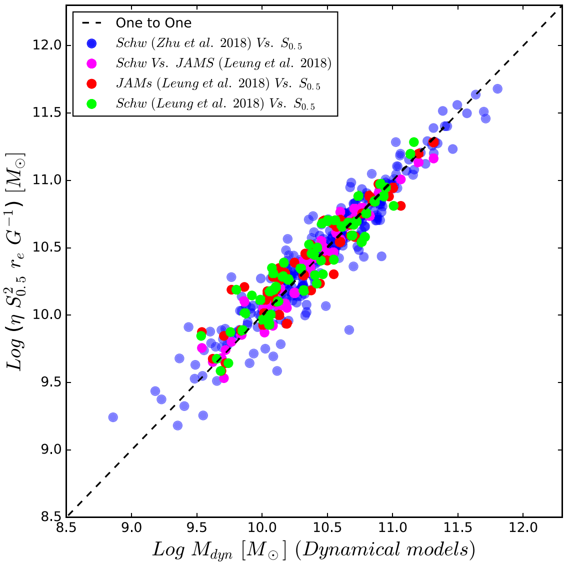

Figure 5. One-to-one relation between dynamical masses inferred from dynamical models and kinematic parameter $S_{0.5}$. The blue symbols are the comparison between the Schwarzschild models by Zhu et al. (2018a) with our estimations. The red and green symbols are the comparison between JAMs and Schwarzschild models by Leung et al. (2018) with our estimations, respectively. Both comparisons show a scatter of ~0.15 dex. The magenta symbols are the comparison between Schwarzschild and JAMs estimations with a scatter of 0.08 dex.

5.3 The Dynamical-to-stellar mass relation

We explore the literature in order to compile the most recent state-of-the-art derivations of the dynamical mass in the central regions of galaxies using dynamical models. Cappellari et al. (2013) estimated the dynamical mass within the effective radius for 258 early-type galaxies from the $ATLAS^{3D}$ project (Cappellari et al. 2011) using the JAMs dynamical models and compared it with the stellar masses. Martinsson et al. (2013) performed a similar study for 24 late-type galaxies extracted from the Disc Mass survey (Bershady

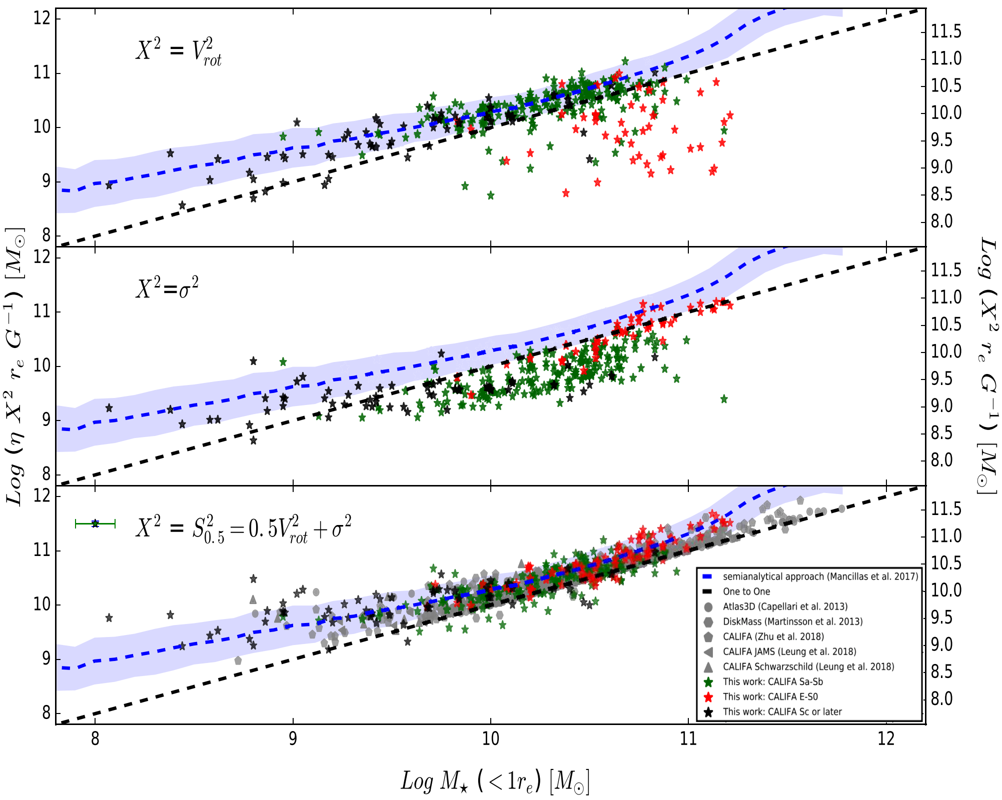

Figure 6. Accuracy of the M$_{dyn}$–M$_\star$ relations based on the $S_{0.5}$ parameter. In the top and medium panels we assume that galaxies are rotation or velocity dispersion dominated to estimate the dynamical mass within the effective radius. The red, green, and black stars represent our CALIFA sample, whereas the grey symbols are from the literature compilation. The $S_{0.5}$ dynamical mass estimations perform better than the ones based either only on rotation or dispersion. In the bottom panel we used the $S_{0.5}$ parameter to estimate the dynamical mass using equation (5) and compare them with theoretical predictions based on detailed dynamical models. All the estimated M$_{dyn}$–M$_\star$ relations are comparable and consistent with observations within the uncertainties. As a reference we also show the semi-empirical predictions of Mancillas et al. (2017) (blue shaded region; see text) which use $\eta = 1$ and are also consistent with our estimations.

et al. 2010). Zhu et al. (2018a, b) constructed orbit-superposition Schwarzschild models at different radii that simultaneously fit the observed surface brightness and stellar kinematics for 300 galaxies included in the CALIFA-V1200 resolution subsample studied here. In Zhu et al. (2018b) they constrained the stellar orbit distribution and found that a fraction of stars are within a plane with unperturbed orbits tracing the rotation velocity, while others are out of the plane with perturbed orbits tracing the velocity dispersion. This result implies that the kinematics in galaxies is more complex that just rotation or velocity dispersion: both components are present in all types of galaxies and should be considered to trace the potential. The bottom panel of Fig. 6 presents the comparison between the distributions of dynamical masses along the stellar ones between this compilation of data extracted from the literature and the ones derived using the equation (5) within the effective radius, based on the $S_{0.5}$ parameter with $\eta = 1.8$. In addition, we present the dynamical masses derived if we consider only the rotational velocities or the velocity dispersions.[3] All these dynamical masses, derived at r_e are listed in Table A1. We observe a clear offset and a large scatter between our dynamical masses and those derived using detailed models when we use only rotation velocity (mostly for ellipticals) or velocity dispersion (mostly for spirals). However, when we use the dynamical mass proxy based on the $S_{0.5}$ parameter, the distribution along the stellar mass is in agreement with the results extracted from the literature. Thus, it seems that the $S_{0.5}$ parameter is indeed a good proxy for calculating the dynamical mass.

Our distribution of M_{dyn}–$M_\star$ follows a linear and nearly one-to-one relation for masses in the range $3 \times 10^9 \lesssim M_\star\,[M_\odot] \lesssim 5 \times 10^{10}$. The fact that for some galaxies (both from our sample and from other works), the stellar mass seems to be higher than the dynamical one shows the presence of several systematical uncertainties both in the stellar and dynamical mass determinations. Within these uncertainties, what we learn from Fig. 6 is that in the above-mentioned mass range luminous matter strongly dominates within $1r_e$. Below $\sim 3 \times 10^9$M$_\odot$ there is a clear deviation, with galaxies showing larger dynamical masses than their stellar masses, which indicates that in the low-mass regime galaxies are more dark matter dominated as less massive they are, even within the effective radius. In the high-mass end, there is some weak evidence of a deviation, with the few E/S0 galaxies at these masses showing again larger dynamical masses than their stellar masses. This difference could be due to more bottom-heavy IMF (Lyubenova et al. 2016) and/or due to the contribution of dark matter.

---

[3] Corrections for different adopted values for the effective radius and IMFs offset have been considered when required.

Both our data and literature collected ones show similar trends. Indeed, this result is predicted by different theoretical studies, including hydrodynamical cosmological simulations (Oman et al. 2015) from the Evolution and Assembly of GaLaxies and their Environments project (Crain et al. 2015; Schaye et al. 2015), and semi-empirical modelling approaches (Mancillas et al. 2017). We include the latter theoretical predictions for comparison in Fig. 6. In Mancillas et al. (2017), a population of galaxies with bulge-to-disc mass ratios lower than ~0.7 was generated by loading the bulge/disc systems into Lambda cold dark matter haloes, taking into account the adiabatic contraction of the inner halo by the baryons. The modelled population reproduces well the TF relation, radius-mass, *B*/*T*-mass, and gas-to-stellar mass relations, and by construction follows the stellar-to-halo ($M_\star - M_{vir}$) relation constrained from a semi-empirical approach for blue galaxies (Rodríguez-Puebla et al. 2015). The predicted inner mass distributions, in particular the stellar-to-dynamical masses within $1r_e$, inherit partially the shape of the latter relation, which bends to lower $M_\star/M_{vir}$ ratios both at lower and higher masses. This explains the bends seen for the predictions in Fig. 6 (dashed blue line and shadow region around it). It is encouraging that our observational inferences based on the $S_{0.5}$ parameter agree with these predictions, showing the possibility to attain a connection between the inner galaxy dynamics of the local galaxy population and the properties of the cosmological dark matter haloes.

6 CONCLUSIONS

Originally the S_K parameter was introduced as a tool to deal with galaxies difficult to classify or with high amount of velocity dispersion like clumpy high-redshift galaxies. The remarkable reduction of scatter in the $S_{0.5}$ relationship compared with TF and FJ relations found by previous studies (Cortese et al. 2014) and confirmed with higher accuracy by our study, points towards a more complex internal kinematics in galaxies even in the local Universe: non-circular motions in disc galaxies and some amount of rotation in elliptical galaxies.

In summary, we demonstrate that (i) the $M_\star - S_{0.5}$ is a tighter correlation than the TF relation or the FJ relation when galaxies of all morphological types are considered, and (ii) this relation is a consequence of $S_{0.5}$ being a proxy of the dynamical mass and the relation between this later parameter with the stellar mass. Finally, we propose a simple but competitive procedure to estimate the dynamical mass in galaxies, easier to apply to massive surveys than more detailed analysis, although with lower precision.

ACKNOWLEDGEMENTS

We thank the support by CONACYT grant CB-285080. OV and EA acknowledge support from the PAPIIT grant IN112518. S.F.S. thank PAPIIT-DGAPA-IA101217 (UNAM) project. We would like to thank Damian Mast for his valuable job observing the CALIFA galaxies. Many thanks to Gigi Y. C. Leung from the Max Planck Institute for Astronomy for providing us the stellar and dynamical masses from dynamical models for the 54 galaxies from her study. GvdV acknowledges funding from the European Research Council (ERC) under the European Union's Horizon 2020 research and innovation programme under grant agreement No 724857 (Consolidator Grant ArcheoDyn).

This study uses data provided by the CALIFA survey (http://califa.caha.es/).

CALIFA is the first legacy survey performed at Calar Alto. The CALIFA collaboration would like to thank the IAA-CSIC and MPIA-MPG as major partners of the observatory, and CAHA itself, for the unique access to telescope time and support in manpower and infrastructures. The CALIFA collaboration also thanks the CAHA staff for the dedication to this project.

Based on observations collected at the Centro Astronómico Hispano Alemán (CAHA) at Calar Alto, operated jointly by the Max-Planck-Institut für Astronomie and the Instituto de Astrofísica de Andalucía (CSIC).

REFERENCES

Akritas M. G., Bershady M. A., 1996, ApJ, 470, 706
Avila-Reese V., Firmani C., Hernández X., 1998, ApJ, 505, 37
Avila-Reese V., Zavala J., Firmani C., Hernández-Toledo H. M., 2008, AJ, 136, 1340
Bacon R. et al., 2001, MNRAS, 326, 23
Begeman K. G., 1989, A&A, 223, 47
Bekeraité S. et al., 2016, A&A, 593, A114
Bell E. F., de Jong R. S., 2001, ApJ, 550, 212
Bershady M. A., Verheijen M. A. W., Swaters R. A., Andersen D. R., Westfall K. B., Martinsson T., 2010, ApJ, 716, 198
Bertola F., Bettoni D., Danziger J., Sadler E., Sparke L., de Zeeuw T., 1991, ApJ, 373, 369
Bosma A., 1978, PhD thesis, Groningen Univ.
Cappellari M., 2008, MNRAS, 390, 71
Cappellari M., Copin Y., 2003, MNRAS, 342, 345
Cappellari M., Emsellem E., 2004, PASP, 116, 138
Cappellari M. et al., 2006, MNRAS, 366, 1126
Cappellari M. et al., 2011, MNRAS, 416, 1680
Cappellari M. et al., 2013, MNRAS, 432, 1709
Catinella B., Haynes M. P., Giovanelli R., 2005, AJ, 130, 1037
Catinella B. et al., 2012, MNRAS, 420, 1959
Christensen L., Hjorth J., 2017, MNRAS, 470, 2599
Cid Fernandes R. et al., 2013, A&A, 557, A86
Cole S., Aragon-Salamanca A., Frenk C. S., Navarro J. F., Zepf S. E., 1994, MNRAS, 271, 781
Cortese L. et al., 2014, ApJ, 795, L37
Courteau S., Rix H.-W., 1999, ApJ, 513, 561
Courteau S. et al., 2014, Rev. Mod. Phys., 86, 47
Crain R. A. et al., 2015, MNRAS, 450, 1937
Cresci G. et al., 2009, ApJ, 697, 115
Croom S. M. et al., 2012, MNRAS, 421, 872
Desmond H., Wechsler R. H., 2017, MNRAS, 465, 820
Djorgovski S., Davis M., 1987, ApJ, 313, 59
Dressler A., Lynden-Bell D., Burstein D., Davies R. L., Faber S. M., Terlevich R., Wegner G., 1987, ApJ, 313, 42
Eisenstein D. J., Loeb A., 1996, ApJ, 459, 432
Emsellem E. et al., 2007, MNRAS, 379, 401
Emsellem E. et al., 2011, MNRAS, 414, 888
Faber S. M., Jackson R. E., 1976, ApJ, 204, 668
Falcón-Barroso J. et al., 2017, A&A, 597, A48
Firmani C., Avila-Reese V., 2000, MNRAS, 315, 457
Gallazzi A., Charlot S., Brinchmann J., White S. D. M., 2006, MNRAS, 370, 1106
García-Benito R. et al., 2015, A&A, 576, A135
Giovanelli R., Haynes M. P., Herter T., Vogt N. P., da Costa L. N., Freudling W., Salzer J. J., Wegner G., 1997, AJ, 113, 53
Gnerucci A. et al., 2011, A&A, 528, A88
Holmes L. et al., 2015, MNRAS, 451, 4397
Husemann B. et al., 2013, A&A, 549, A87
Kalinova V. et al., 2017, MNRAS, 469, 2539
Kassin S. A. et al., 2007, ApJ, 660, L35
Kelz A. et al., 2006, PASP, 118, 129
Leung G. Y. C. et al., 2018, MNRAS, 477, 254

Lorenzi . D., Debattista V. P., Gerhard O. E., 2006, in Stanghellini L., Walsh J. R., Douglas N. G., eds, Planetary Nebulae Beyond the Milky Way. p. 311

Lyubenova M. et al., 2016, MNRAS, 463, 3220

Mancillas B., Ávila-Reese V., Rodríguez-Puebla A., Valls-Gabaud D., 2017, in Galaxy Evolution Across Time, Proceedings of a conference held 12-16 June, 2017 in Paris. p. 92

Martinsson T. P. K., Verheijen M. A. W., Westfall K. B., Bershady M. A., Andersen D. R., Swaters R. A., 2013, A&A, 557, A131

Martín-Navarro I. et al., 2015, ApJ, 806, L31

Mathewson D. S., Ford V. L., Buchhorn M., 1992, ApJS, 81, 413

McGaugh S. S., Schombert J. M., Bothun G. D., de Blok W. J. G., 2000, ApJ, 533, L99

Mo H. J., Mao S., White S. D. M., 1998, MNRAS, 295, 319

Navarro J. F., Steinmetz M., 2000, ApJ, 538, 477

Oman K. A. et al., 2015, MNRAS, 452, 3650

Ouellette N. N.-Q. et al., 2017, ApJ, 843, 74

Persic M., Salucci P., 1988, MNRAS, 234, 131

Persic M., Salucci P., Stel F., 1996, MNRAS, 281, 27

Ponomareva A. A., Verheijen M. A. W., Peletier R. F., Bosma A., 2017, MNRAS, 469, 2387

Price S. H. et al., 2016, ApJ, 819, 80

Randriamampandry T. H., Combes F., Carignan C., Deg N., 2015, MNRAS, 454, 3743

Rodríguez-Puebla A., Avila-Reese V., Yang X., Foucaud S., Drory N., Jing Y. P., 2015, ApJ, 799, 130

Rogstad D. H., Lockhart I. A., Wright M. C. H., 1974, ApJ, 193, 309

Rong Yu, 2018, MNRAS, 477, 230

Roth M. M. et al., 2005, PASP, 117, 620

Salpeter E. E., 1955, ApJ, 121, 161

Schaye J. et al., 2015, MNRAS, 446, 521

Schoenmakers R. H. M., Franx M., de Zeeuw P. T., 1997, MNRAS, 292, 349

Schwarzschild M., 1979, ApJ, 232, 236

Sellwood J. A., Sánchez R. Z., 2010, MNRAS, 404, 1733

Spekkens K., Sellwood J. A., 2007, ApJ, 664, 204

Sánchez-Menguiano L. et al., 2017, A&A, 603, A113

Sánchez S. F. et al., 2012, A&A, 538, A8

Sánchez S. F. et al., 2016a, Rev. Mex. Astron. Astrofis., 52, 21

Sánchez S. F. et al., 2016b, Rev. Mex. Astron. Astrofis., 52, 171

Sánchez S. F. et al., 2016c, A&A, 594, A36

Sánchez S. F. et al., 2017, MNRAS, 469, 2121

Tully R. B., Fisher J. R., 1977, A&A, 54, 661

Valdes F., Gupta R., Rose J. A., Singh H. P., Bell D. J., 2004, ApJS, 152, 251

Valenzuela O., Rhee G., Klypin A., Governato F., Stinson G., Quinn T., Wadsley J., 2007, ApJ, 657, 773

Vergani D. et al., 2012, A&A, 546, A118

Verheijen M. A. W., 2001, ApJ, 563, 694

Vogt N. P., Haynes M. P., Herter T., Giovanelli R., 2004, AJ, 127, 3273

Walcher C. J. et al., 2014, A&A, 569, A1

Weiner B. J. et al., 2006, ApJ, 653, 1027

Wolf J., Martinez G. D., Bullock J. S., Kaplinghat M., Geha M., Muñoz R. R., Simon J. D., Avedo F. F., 2010, MNRAS, 406, 1220

Zaritsky D., Zabludoff A. I., Gonzalez A. H., 2008, ApJ, 682, 68

Zavala J., Avila-Reese V., Hernández-Toledo H., Firmani C., 2003, A&A, 412, 633

Zhu L. et al., 2018a, Nature Astron., 2, 233

Zhu L. et al., 2018b, MNRAS, 473, 3000

APPENDIX A: STELLAR AND DYNAMICAL MASSES

Dynamical masses were estimated within $1r_e$ using equation (5)

Table A1. Stellar masses and dynamical masses within the effective radius.

Name (1)	$M_\star$ [M$_\odot$] (2)	M_{dyn} [M$_\odot$] (3)	r_e [arcsec] (4)
IC5376	10.16 ± 0.10	10.53 ± 0.04	11.62
NGC 0036	10.76 ± 0.09	10.82 ± 0.02	19.34
UGC00148	9.71 ± 0.09	10.26 ± 0.06	13.54
MCG-02-02-030	10.00 ± 0.09	10.25 ± 0.03	13.86
UGC00005	10.62 ± 0.09	10.78 ± 0.01	14.45
NGC 7819	10.00 ± 0.08	10.14 ± 0.03	15.02
UGC00029	10.93 ± 0.10	11.19 ± 0.04	12.79
IC1528	10.04 ± 0.09	10.16 ± 0.03	16.95
NGC 7824	10.64 ± 0.09	10.75 ± 0.12	9.64
UGC00312	9.75 ± 0.09	10.57 ± 0.07	13.28
MCG-02-02-040	9.44 ± 0.09	10.11 ± 0.05	11.62
UGC00335NED02	10.43 ± 0.10	10.72 ± 0.04	16.64
NGC 0216	8.78 ± 0.09	9.38 ± 0.08	13.22
NGC 0214	10.66 ± 0.09	10.46 ± 0.04	14.88
NGC 0217	10.37 ± 0.09	10.83 ± 0.01	20.44
NGC 0237	10.11 ± 0.09	10.01 ± 0.05	11.05
NGC 0234	10.50 ± 0.08	10.00 ± 0.04	17.36
MCG-02-03-015	10.94 ± 0.10	10.62 ± 0.02	11.56
NGC 0257	10.61 ± 0.09	10.57 ± 0.02	15.10
NGC 0364	10.36 ± 0.09	10.66 ± 0.01	9.04
NGC 0429	10.09 ± 0.09	10.38 ± 0.04	7.14
IC1652	10.21 ± 0.09	10.27 ± 0.05	10.62
NGC 0447	10.55 ± 0.09	10.71 ± 0.05	18.56
NGC 0444	9.71 ± 0.10	10.22 ± 0.04	17.37
UGC00809	9.02 ± 0.08	10.21 ± 0.03	11.01
UGC00841	9.73 ± 0.11	10.28 ± 0.05	13.73
NGC 0477	10.39 ± 0.09	10.54 ± 0.03	18.58
IC1683	10.31 ± 0.09	10.18 ± 0.03	9.97
NGC 0499	10.64 ± 0.08	11.01 ± 0.03	13.16
NGC 0496	10.40 ± 0.11	10.30 ± 0.03	16.47
NGC 0504	9.72 ± 0.10	10.38 ± 0.03	8.53
NGC 0517	10.13 ± 0.10	10.40 ± 0.03	7.52
UGC00987	10.33 ± 0.09	10.40 ± 0.03	10.95
NGC 0528	10.46 ± 0.10	10.59 ± 0.02	9.01
NGC 0529	10.63 ± 0.09	10.84 ± 0.05	11.75
NGC 0551	10.33 ± 0.10	10.46 ± 0.04	14.37
UGC01057	10.11 ± 0.10	10.31 ± 0.03	11.00
UGC01271	10.28 ± 0.10	10.47 ± 0.04	8.17
NGC 0681	9.99 ± 0.08	10.28 ± 0.04	23.63
NGC 0741	11.17 ± 0.09	11.56 ± 0.02	25.68
NGC 0755	9.18 ± 0.08	9.91 ± 0.09	19.11
IC1755	10.43 ± 0.09	10.95 ± 0.01	13.50
NGC 0768	10.39 ± 0.08	10.67 ± 0.02	15.59
NGC 0774	10.50 ± 0.10	10.54 ± 0.03	13.31
NGC 0776	10.53 ± 0.08	10.07 ± 0.04	13.28
NGC 0781	11.18 ± 0.09	10.07 ± 0.04	8.99
NGC 0810	10.77 ± 0.10	11.39 ± 0.02	13.56
NGC 0825	8.95 ± 0.10	9.79 ± 0.03	2.02
NGC 0932	10.64 ± 0.09	10.47 ± 0.04	16.43
NGC 1056	9.87 ± 0.09	9.55 ± 0.07	7.90
NGC 1060	11.13 ± 0.09	11.40 ± 0.03	20.46
UGC02222	10.51 ± 0.10	10.47 ± 0.03	8.36
UGC02229	10.68 ± 0.09	10.96 ± 0.02	11.77
NGC 1093	10.23 ± 0.08	10.31 ± 0.02	8.50
UGC02403	10.21 ± 0.09	10.24 ± 0.02	11.71
NGC 1167	10.99 ± 0.09	11.04 ± 0.01	21.55
NGC 1349	10.87 ± 0.09	10.83 ± 0.02	14.13
NGC 1542	9.99 ± 0.10	10.24 ± 0.03	9.53
NGC 1645	10.43 ± 0.10	10.76 ± 0.01	14.09
UGC03151	10.41 ± 0.10	10.56 ± 0.03	15.50
NGC 1677	9.20 ± 0.08	9.68 ± 0.10	8.59
IC2101	9.82 ± 0.10	10.26 ± 0.05	14.10

Table A1 – *continued*

Name (1)	$M_\star$ [M$_\odot$] (2)	M_{dyn} [M$_\odot$] (3)	r_e [arcsec] (4)
UGC03253	10.07 ± 0.09	10.31 ± 0.02	12.67
NGC 2253	9.79 ± 0.10	9.59 ± 0.03	4.08
UGC03539	9.26 ± 0.08	10.02 ± 0.04	13.67
NGC 2347	10.50 ± 0.09	10.58 ± 0.03	13.78
UGC03899	8.95 ± 0.10	9.88 ± 0.08	9.55
UGC00036	10.45 ± 0.09	10.71 ± 0.01	10.05
NGC 0001	10.42 ± 0.09	10.19 ± 0.04	9.18
NGC 0023	10.83 ± 0.08	10.59 ± 0.06	10.78
NGC 2410	10.49 ± 0.09	10.76 ± 0.02	17.91
UGC03944	9.57 ± 0.12	10.00 ± 0.03	11.79
UGC03969	10.34 ± 0.11	10.70 ± 0.01	11.16
UGC03995	10.64 ± 0.09	10.74 ± 0.02	21.78
NGC 2449	10.30 ± 0.09	10.58 ± 0.01	12.86
UGC04029	10.09 ± 0.08	10.39 ± 0.01	14.97
IC0480	9.42 ± 0.10	10.19 ± 0.02	11.49
NGC 2476	10.36 ± 0.11	10.37 ± 0.05	7.99
NGC 2480	8.86 ± 0.10	9.69 ± 0.10	10.82
NGC 2481	9.68 ± 0.10	9.97 ± 0.03	7.54
NGC 2486	10.43 ± 0.09	10.51 ± 0.03	12.96
NGC 2487	10.51 ± 0.08	10.36 ± 0.04	18.81
UGC04132	10.40 ± 0.10	10.70 ± 0.02	13.18
UGC04145	10.01 ± 0.11	10.34 ± 0.03	7.93
NGC 2513	10.71 ± 0.08	11.21 ± 0.02	19.23
UGC04197	9.82 ± 0.10	10.57 ± 0.03	14.93
NGC 2540	10.31 ± 0.10	10.48 ± 0.02	15.42
UGC04280	9.76 ± 0.09	10.11 ± 0.05	11.18
IC2247	10.30 ± 0.09	10.53 ± 0.02	16.30
UGC04308	9.99 ± 0.08	10.15 ± 0.03	21.43
NGC 2553	10.21 ± 0.09	10.52 ± 0.03	8.52
NGC 2554	10.79 ± 0.09	10.87 ± 0.01	17.50
NGC 2592	9.83 ± 0.10	10.04 ± 0.01	7.62
NGC 2604	9.28 ± 0.10	9.77 ± 0.08	20.19
NGC 2639	10.41 ± 0.08	10.70 ± 0.01	13.36
UGC04722	8.07 ± 0.12	9.76 ± 0.05	17.59
NGC 2730	9.68 ± 0.08	9.96 ± 0.03	14.56
NGC 2880	9.90 ± 0.08	9.98 ± 0.01	13.71
IC2487	10.00 ± 0.10	10.45 ± 0.02	16.77
IC0540	9.35 ± 0.10	9.74 ± 0.03	14.88
NGC 2906	9.94 ± 0.08	10.10 ± 0.02	15.23
NGC 2916	10.40 ± 0.08	10.55 ± 0.02	20.60
UGC05108	10.48 ± 0.10	10.81 ± 0.03	9.58
NGC 2918	10.71 ± 0.10	10.93 ± 0.02	9.32
UGC05113	10.19 ± 0.10	10.71 ± 0.02	8.91
NGC 3106	10.83 ± 0.08	10.77 ± 0.03	17.30
NGC 3057	8.80 ± 0.09	9.26 ± 0.09	18.08
UGC05498NED01	9.71 ± 0.11	10.67 ± 0.02	10.52
NGC 3158	11.14 ± 0.10	11.64 ± 0.03	22.29
NGC 3160	10.28 ± 0.10	10.76 ± 0.01	12.77
UGC05598	9.84 ± 0.10	10.15 ± 0.04	11.40
NGC 3300	10.10 ± 0.10	10.30 ± 0.01	13.31
NGC 3303	10.63 ± 0.10	10.75 ± 0.03	9.24
UGC05771	10.54 ± 0.10	10.81 ± 0.03	8.01
NGC 3381	9.18 ± 0.07	9.18 ± 0.10	14.84
UGC05990	8.44 ± 0.12	9.24 ± 0.09	9.36
UGC06036	10.32 ± 0.10	10.94 ± 0.02	11.16
IC0674	10.53 ± 0.09	10.84 ± 0.02	11.48
UGC06312	10.55 ± 0.09	10.80 ± 0.02	12.77
NGC 3615	10.87 ± 0.09	11.10 ± 0.03	10.85
NGC 3687	9.99 ± 0.08	9.75 ± 0.04	15.42
NGC 3811	10.16 ± 0.09	10.08 ± 0.04	14.71
NGC 3815	9.90 ± 0.08	10.12 ± 0.03	8.81
NGC 3994	10.09 ± 0.10	10.27 ± 0.05	7.14

Table A1 – *continued*

Name (1)	$M_\star$ [M$_\odot$] (2)	M_{dyn} [M$_\odot$] (3)	r_e [arcsec] (4)
NGC 4003	10.48 ± 0.09	10.52 ± 0.05	9.41
UGC07012	9.39 ± 0.08	9.79 ± 0.10	11.88
NGC 4047	10.34 ± 0.09	10.41 ± 0.11	14.79
UGC07145	9.96 ± 0.10	10.38 ± 0.02	11.75
NGC 4149	9.70 ± 0.10	10.35 ± 0.04	11.48
NGC 4185	10.20 ± 0.08	10.51 ± 0.02	22.60
NGC 4210	9.85 ± 0.10	9.97 ± 0.02	16.92
NGC 4470	9.58 ± 0.09	9.33 ± 0.07	11.54
NGC 4644	10.11 ± 0.09	10.40 ± 0.02	14.27
NGC 4711	9.97 ± 0.08	10.18 ± 0.02	12.28
NGC 4816	10.75 ± 0.09	11.29 ± 0.03	20.36
NGC 4841A	10.82 ± 0.09	11.29 ± 0.05	13.68
NGC 4874	11.12 ± 0.09	11.68 ± 0.02	38.42
UGC08107	10.80 ± 0.09	11.29 ± 0.03	17.66
NGC 4956	10.53 ± 0.09	10.35 ± 0.03	8.68
NGC 4961	9.42 ± 0.09	9.68 ± 0.06	9.74
UGC08231	9.05 ± 0.11	10.28 ± 0.06	16.86
UGC08234	10.62 ± 0.10	10.51 ± 0.02	5.53
NGC 5000	10.22 ± 0.09	10.02 ± 0.04	10.18
NGC 5016	9.98 ± 0.10	10.00 ± 0.03	15.29
NGC 5029	10.86 ± 0.10	11.40 ± 0.03	15.45
NGC 5056	10.32 ± 0.08	10.30 ± 0.05	13.77
NGC 5205	9.43 ± 0.09	9.78 ± 0.04	16.41
NGC 5216	10.08 ± 0.08	10.33 ± 0.06	15.28
NGC 5218	10.15 ± 0.09	10.23 ± 0.01	12.30
UGC08733	8.96 ± 0.10	9.86 ± 0.04	19.90
IC0944	10.46 ± 0.11	10.84 ± 0.02	9.80
UGC08778	9.65 ± 0.10	10.08 ± 0.04	11.90
UGC08781	10.59 ± 0.08	10.70 ± 0.04	12.01
NGC 5378	10.04 ± 0.08	10.22 ± 0.03	19.29
NGC 5406	10.46 ± 0.08	10.70 ± 0.01	14.93
NGC 5480	9.56 ± 0.09	9.64 ± 0.06	17.41
NGC 5485	10.20 ± 0.08	10.48 ± 0.02	21.81
UGC09067	10.51 ± 0.09	10.69 ± 0.03	11.26
NGC 5520	9.63 ± 0.10	9.89 ± 0.03	11.87
NGC 5614	10.73 ± 0.08	10.67 ± 0.04	15.67
NGC 5631	10.20 ± 0.08	10.29 ± 0.03	17.44
NGC 5633	9.91 ± 0.09	9.93 ± 0.04	12.93
NGC 5630	9.37 ± 0.09	9.90 ± 0.05	13.78
NGC 5657	9.97 ± 0.10	10.13 ± 0.04	11.59
NGC 5682	8.87 ± 0.09	9.89 ± 0.10	19.63
NGC 5720	10.58 ± 0.10	10.66 ± 0.02	11.87
NGC 5732	9.77 ± 0.10	10.07 ± 0.06	12.28
UGC09476	9.78 ± 0.10	9.91 ± 0.03	15.46
UGC09537	10.57 ± 0.09	11.20 ± 0.05	15.76
UGC09542	9.98 ± 0.10	10.31 ± 0.03	12.89
NGC 5784	10.75 ± 0.08	10.88 ± 0.02	11.91
NGC 5797	10.47 ± 0.09	10.49 ± 0.02	13.71
IC1079	10.91 ± 0.10	11.23 ± 0.03	19.34
UGC09665	9.44 ± 0.10	9.88 ± 0.04	11.61
NGC 5876	10.19 ± 0.09	10.67 ± 0.01	15.05
NGC 5888	10.68 ± 0.10	10.99 ± 0.01	12.07
NGC 5908	10.28 ± 0.08	10.71 ± 0.01	14.60
NGC 5930	10.13 ± 0.08	10.18 ± 0.02	14.40
NGC 5934	10.20 ± 0.10	10.43 ± 0.06	6.75
UGC09873	9.85 ± 0.09	10.30 ± 0.03	14.82
UGC09892	9.96 ± 0.09	10.19 ± 0.02	13.68
NGC 5953	10.06 ± 0.09	9.63 ± 0.03	9.09
NGC 5971	9.96 ± 0.11	10.16 ± 0.04	10.18
NGC 5966	10.58 ± 0.09	10.88 ± 0.03	20.30
IC4566	10.49 ± 0.09	10.59 ± 0.01	13.16
NGC 5987	10.42 ± 0.09	10.71 ± 0.02	22.53

Table A1 – *continued*

Name (1)	$M_\star$ $[\mathrm{M}_\odot]$ (2)	M_{dyn} $[\mathrm{M}_\odot]$ (3)	r_e [arcsec] (4)
NGC 5980	10.39 ± 0.09	10.50 ± 0.03	12.64
NGC 6004	10.27 ± 0.07	10.21 ± 0.03	20.41
UGC10097	10.80 ± 0.10	10.96 ± 0.02	10.39
NGC 6020	10.38 ± 0.10	10.62 ± 0.04	11.59
NGC 6021	10.53 ± 0.09	10.51 ± 0.04	8.47
IC1151	9.49 ± 0.09	9.82 ± 0.05	19.34
UGC10123	9.88 ± 0.10	10.29 ± 0.02	11.01
NGC 6032	9.83 ± 0.10	10.16 ± 0.03	14.79
NGC 6060	10.49 ± 0.08	10.66 ± 0.01	20.20
UGC10205	10.69 ± 0.11	10.98 ± 0.02	13.95
NGC 6063	9.75 ± 0.10	10.05 ± 0.03	17.78
IC1199	10.33 ± 0.08	10.67 ± 0.01	18.76
UGC10257	9.86 ± 0.09	10.28 ± 0.04	15.25
NGC 6081	10.52 ± 0.10	10.75 ± 0.01	10.43
UGC10297	8.62 ± 0.09	9.53 ± 0.04	10.85
UGC10331	9.50 ± 0.10	10.14 ± 0.08	15.41
NGC 6125	10.66 ± 0.09	10.93 ± 0.01	15.38
UGC10337	10.61 ± 0.10	11.01 ± 0.01	14.85
NGC 6132	10.00 ± 0.09	10.36 ± 0.03	11.89
NGC 6146	11.06 ± 0.09	11.26 ± 0.02	11.00
UGC10380	10.52 ± 0.10	10.98 ± 0.03	12.83
NGC 6150	10.65 ± 0.10	11.11 ± 0.03	9.26
UGC10384	9.95 ± 0.11	10.35 ± 0.05	9.27
UGC10388	10.23 ± 0.09	10.44 ± 0.02	10.91
NGC 6173	11.18 ± 0.09	11.51 ± 0.02	18.52
NGC 6168	9.40 ± 0.10	9.85 ± 0.05	16.28
NGC 6186	9.96 ± 0.09	9.94 ± 0.04	12.67
UGC10650	8.80 ± 0.09	10.48 ± 0.10	15.29
NGC 6278	9.96 ± 0.10	10.38 ± 0.01	9.56
UGC10693	10.77 ± 0.09	11.28 ± 0.03	15.24
UGC10695	10.81 ± 0.09	11.12 ± 0.03	15.73
UGC10710	10.48 ± 0.09	10.88 ± 0.03	12.01
NGC 6310	10.02 ± 0.10	10.41 ± 0.02	15.84
NGC 6301	10.88 ± 0.08	10.94 ± 0.02	20.01
NGC 6314	10.57 ± 0.08	10.52 ± 0.03	8.72
NGC 6338	11.06 ± 0.10	11.50 ± 0.02	19.15
UGC10796	9.16 ± 0.12	9.78 ± 0.10	14.70
UGC10811	10.46 ± 0.09	10.90 ± 0.04	11.82
IC1256	10.19 ± 0.09	10.35 ± 0.02	14.60
NGC 6394	10.32 ± 0.09	10.68 ± 0.02	9.05
UGC10905	10.81 ± 0.09	11.04 ± 0.03	12.37
NGC 6411	10.54 ± 0.09	10.77 ± 0.03	17.82
NGC 6427	10.00 ± 0.10	10.30 ± 0.02	8.88
UGC10972	10.22 ± 0.10	10.51 ± 0.03	19.31
NGC 6478	10.83 ± 0.09	10.97 ± 0.02	17.36
NGC 6497	10.52 ± 0.08	10.74 ± 0.01	11.99
NGC 6515	10.79 ± 0.09	10.97 ± 0.04	13.07
UGC11228	10.55 ± 0.10	10.48 ± 0.03	7.23
NGC 6762	9.91 ± 0.09	10.03 ± 0.06	11.21
MCG-02-51-004	10.66 ± 0.09	10.75 ± 0.01	15.80
NGC 6941	10.64 ± 0.09	10.72 ± 0.01	15.04
NGC 6945	9.11 ± 0.08	10.41 ± 0.02	12.80
NGC 6978	10.49 ± 0.10	10.73 ± 0.01	12.15
UGC11649	10.14 ± 0.08	10.28 ± 0.02	14.54
UGC11680NED01	10.84 ± 0.09	10.94 ± 0.01	14.56
NGC 7025	10.82 ± 0.09	11.05 ± 0.02	18.20
NGC 7047	10.51 ± 0.10	10.70 ± 0.02	19.97
UGC11717	10.66 ± 0.09	10.44 ± 0.17	11.77
MCG-01-54-016	8.38 ± 0.11	9.82 ± 0.07	12.07
NGC 7194	10.75 ± 0.09	11.20 ± 0.05	11.96
UGC12054	8.58 ± 0.10	9.44 ± 0.07	10.41
NGC 7311	10.59 ± 0.09	10.59 ± 0.02	10.60

Table A1 – *continued*

Name (1)	$M_\star$ $[\mathrm{M}_\odot]$ (2)	M_{dyn} $[\mathrm{M}_\odot]$ (3)	r_e [arcsec] (4)
NGC 7321	10.65 ± 0.08	10.74 ± 0.03	12.04
UGC12127	11.01 ± 0.09	11.46 ± 0.04	18.86
NGC 7364	10.60 ± 0.10	10.57 ± 0.02	10.56
UGC12185	10.36 ± 0.08	10.57 ± 0.04	9.71
NGC 7436B	11.21 ± 0.10	11.52 ± 0.02	22.59
UGC12274	10.64 ± 0.09	10.85 ± 0.02	12.39
UGC12308	8.95 ± 0.10	10.03 ± 0.07	20.19
NGC 7466	10.55 ± 0.09	10.63 ± 0.02	12.64
NGC 7489	10.53 ± 0.08	10.42 ± 0.04	16.66
NGC 7550	10.87 ± 0.09	11.07 ± 0.03	16.66
NGC 7549	10.38 ± 0.09	10.60 ± 0.02	16.64
NGC 7563	10.28 ± 0.09	10.59 ± 0.01	8.88
NGC 7562	10.68 ± 0.09	10.85 ± 0.03	14.03
NGC 7591	10.62 ± 0.10	10.51 ± 0.03	13.08
UGC12494	9.33 ± 0.10	10.09 ± 0.17	14.49
IC5309	10.47 ± 0.11	10.05 ± 0.07	13.31
NGC 7608	9.13 ± 0.09	9.72 ± 0.03	7.61
NGC 7611	10.20 ± 0.11	10.71 ± 0.07	9.76
UGC12519	9.84 ± 0.09	10.12 ± 0.03	11.73
NGC 7619	10.80 ± 0.08	11.15 ± 0.02	21.44
NGC 7623	10.20 ± 0.09	10.14 ± 0.03	7.97
NGC 7625	9.64 ± 0.08	9.51 ± 0.03	9.80
NGC 7631	10.21 ± 0.09	10.28 ± 0.02	14.10
NGC 7653	10.46 ± 0.09	10.17 ± 0.04	12.28
NGC 7671	10.31 ± 0.10	10.60 ± 0.02	9.26
NGC 7683	10.46 ± 0.10	10.69 ± 0.03	12.80
NGC 7684	10.47 ± 0.10	10.48 ± 0.02	9.04
NGC 7691	10.25 ± 0.09	10.21 ± 0.03	22.82
NGC 7711	10.53 ± 0.09	10.69 ± 0.03	13.47
NGC 7716	10.17 ± 0.08	9.94 ± 0.04	14.16
NGC 7722	10.74 ± 0.09	10.91 ± 0.07	18.01
UGC12723	9.78 ± 0.13	10.27 ± 0.02	15.94
NGC 7738	10.67 ± 0.10	10.64 ± 0.01	11.51
UGC12810	10.43 ± 0.09	10.72 ± 0.02	13.56
UGC12816	9.74 ± 0.11	10.29 ± 0.05	12.85
NGC 7783NED01	10.64 ± 0.10	11.08 ± 0.03	9.98
NGC 7787	10.56 ± 0.10	10.59 ± 0.04	13.55
UGC12857	9.55 ± 0.10	9.83 ± 0.06	18.39
UGC12864	9.69 ± 0.10	9.95 ± 0.06	14.00
NGC 7800	8.93 ± 0.08	10.10 ± 0.07	16.30
NGC 5947	10.28 ± 0.10	10.26 ± 0.03	10.55
NGC 5947	10.28 ± 0.10	10.26 ± 0.03	10.55
NGC 5947	10.28 ± 0.10	10.26 ± 0.03	10.55
NGC 0180	10.72 ± 0.08	10.59 ± 0.04	20.19
NGC 0192	10.46 ± 0.09	10.49 ± 0.02	13.90
NGC 0155	10.72 ± 0.10	10.82 ± 0.02	13.55
NGC 0160	10.73 ± 0.09	10.87 ± 0.01	19.42
NGC 0169	10.88 ± 0.10	10.98 ± 0.06	19.42
NGC 0171	10.29 ± 0.08	9.89 ± 0.04	15.81
NGC 0177	10.35 ± 0.10	10.45 ± 0.04	17.53

Notes. Col. (1): Galaxy name. Col. (2): Stellar mass within r_e estimated from PIPE3D. Col. (3): Dynamical mass estimated from the kinematic parameter $S_{0.5}$. Col. (4): Effective radius r_e.

APPENDIX B: LINEAR FIT PARAMETERS AND SCATTERS FOR THE $M_\star$–$S_{0.5}$ CORRELATIONS

All scatters are estimated from the linear fit as the standard deviation of all residuals, we consider stellar mass, $M_\star$, as independent variable. $log(S_{0.5}) = a + blog(M_\star)$. $S_{0.5}$ is given in [km s^{-1}] and $M_\star$ in $\mathrm{M}_\odot$.

Fit	zero-point(a)	slope(b)	scatter
Integrated kinematics			
Gas			
Forward	− 0.95 ± 0.11	0.29 ± 0.01	0.087
Inverse	− 1.99 ± 0.18	0.38 ± 0.01	0.100
Bisector	− 1.46 ± 0.13	0.33 ± 0.01	0.090
Orthogonal	− 1.03 ± 0.12	0.29 ± 0.01	0.087
Stellar			
Forward	− 0.61 ± 0.10	0.25 ± 0.01	0.075
Inverse	− 1.52 ± 0.14	0.34 ± 0.01	0.086
Bisector	− 1.06 ± 0.11	0.29 ± 0.01	0.078
Orthogonal	− 0.67 ± 0.10	0.26 ± 0.01	0.075
Total (Gas+Stellar)			
Forward	− 0.72 ± 0.07	0.26 ± 0.01	0.082
Inverse	− 1.73 ± 0.11	0.36 ± 0.01	0.096
Bisector	− 1.22 ± 0.08	0.31 ± 0.01	0.086
Orthogonal	− 0.79 ± 0.07	0.27 ± 0.01	0.082
Resolved kinematics			
Gas			
Forward	− 0.89 ± 0.14	0.28 ± 0.01	0.053
Inverse	− 1.29 ± 0.18	0.32 ± 0.02	0.056
Bisector	− 1.09 ± 0.15	0.30 ± 0.01	0.054
Orthogonal	− 0.92 ± 0.13	0.29 ± 0.01	0.053
Stellar			
Forward	− 0.67 ± 0.12	0.26 ± 0.01	0.052
Inverse	− 1.40 ± 0.17	0.33 ± 0.01	0.056
Bisector	− 1.03 ± 0.14	0.29 ± 0.01	0.050
Orthogonal	− 0.72 ± 0.12	0.27 ± 0.01	0.052
Total (gas+stellar)			
Forward	− 0.66 ± 0.08	0.26 ± 0.01	0.054
Inverse	− 1.31 ± 0.13	0.32 ± 0.01	0.059
Bisector	− 0.98 ± 0.10	0.29 ± 0.01	0.055
Orthogonal	− 0.71 ± 0.11	0.27 ± 0.01	0.054
Only spiral galaxies			
Gas			
Forward	− 0.87 ± 0.15	0.28 ± 0.02	0.043
Inverse	− 0.98 ± 0.11	0.29 ± 0.01	0.044
Bisector	− 0.93 ± 0.14	0.29 ± 0.01	0.043
Orthogonal	− 0.88 ± 0.09	0.28 ± 0.01	0.043
Stellar			
Forward	− 0.88 ± 0.10	0.28 ± 0.01	0.051
Inverse	− 1.35 ± 0.12	0.32 ± 0.02	0.057
Bisector	− 1.12 ± 0.13	0.30 ± 0.01	0.054
Orthogonal	− 0.92 ± 0.12	0.28 ± 0.01	0.052
Total (gas+stellar)			
Forward	− 0.77 ± 0.12	0.27 ± 0.01	0.051
Inverse	− 1.16 ± 0.10	0.31 ± 0.01	0.056
Bisector	− 0.96 ± 0.16	0.29 ± 0.01	0.053
Orthogonal	− 0.80 ± 0.11	0.27 ± 0.01	0.051

This paper has been typeset from a TEX/LATEX file prepared by the author.

Chapter 3

Low surface brightness shells, streams and tidal tails: the merging history of red early-type galaxies

In the present Chapter I describe the analysis that I have performed on the identification and classification of faint substructures present in a early-type galaxy, simulated in a hydrodynamical cosmological simulation. The aim was to build a comprehensive interpretation of the properties of these structures by means of their census in mock images of surface brightness maps. This study is part of the deep imaging program MATLAS survey (Duc, 2017), which is based on the identification of several types of collisional debris, such as tidal tails, plumes, shells and stellar streams.

3.1 Overview

Deep imaging programs

Thanks to the facilities provided by the current developed and advanced observational techniques, it has been possible to carry out deep imaging programs of nearby galaxies, which has revealed prominent structures surrounding galaxies. These surveys include for example, the large field of view mosaic camera (CFHT/MegaCam, NGVS, Ferrarese et al., 2012), the particular LSB special telescope Dragonfly Telephoto Array (van Dokkum et al., 2014) or the advanced MATLAS deep imaging survey (see Figure 3.1)(Duc, 2017). All of them have taken advantage of the diffuse light detected on the external regions of galaxies. The importance of such detections, relies on the fact that collisional debris are tracers of merger events that record the mass assembly mainly in early-type galaxies. In particular, the MATLAS Survey has focused on the distinction between the morphologies of collisional debris in order to make inferences on the past merger events that a galaxy has undergone. Nonetheless, since collisional debris are intrinsically faint and also can be destroyed by subsequent accretion events, their detection is subjected to several factors, such as the surface brightness levels and the projection on the sky. Thus, simulations are of utmost importance to disentangle this problematic and estimate their survival time, allowing us to reconstruct their past merging history.

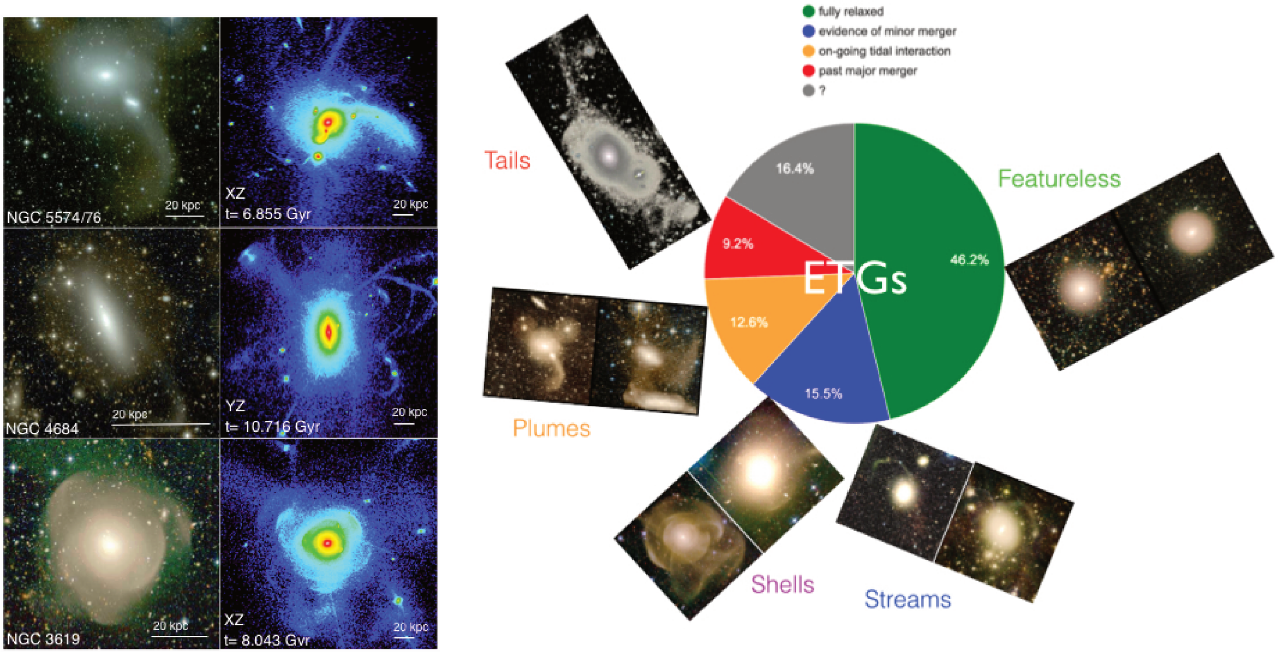

Figure 3.1: *Left side:* Comparison of LSB substructures around observed and simulated galaxies. Left panels: Examples of ETGs from MATLAS Survey. From top to bottom, the system NGC 5574/76 (tidal tails emanate from NGC 5576), stellar stream in NGC 4684 and interleaved shells in NGC 3619. Right panels: Examples of mock surface brightness images exhibiting prominent tidal tails, streams and shells at different times of the simulation in random projections. Note the white scale bar indicating 20 kpc: the scales are comparable in observations and simulations. *Right side:* The classification scheme used for the MATLAS deep imaging survey, which is based on the identification of various types of collisional debris. Examples of tails, plumes, shells and streams are illustrated in the insets. The pie chart summarizes the preliminary statistical results for the population of 240 massive Early Type Galaxies (Duc, 2017).

3.2 Conclusions and perspectives

The study performed inside of a cosmological context through the analysis of a particular numerical simulation complements the approach followed by observations on the exploration of the past mass assembly of galaxies, and provides a wider conception on the present topic which is currently being exploited. In the future, we expect to apply automatic techniques for the identification and classification of fine structures, since more and more are being detected. Several studies have applied automatic approaches (e.g. Pawlik et al., 2016; Hendel et al., 2019). However, it is still necessary to identify fine structures by eye in order to teach the machine how to make more precise image recognition, and to check the procedures. Additionally, different dark matter halo models should be explored, since the fine structures will strongly depend on the dark matter spatial distribution.

3.3 Paper: Probing the merger history of red early-type galaxies with their faint stellar substructures

A&A 632, A122 (2019)
https://doi.org/10.1051/0004-6361/201936320

A&A 632, A122 (2019)
https://doi.org/10.1051/0004-6361/201936320

Astronomy & Astrophysics

Probing the merger history of red early-type galaxies with their faint stellar substructures

Brisa Mancillas[1], Pierre-Alain Duc[2], Françoise Combes[1,3], Frédéric Bournaud[4], Eric Emsellem[5,6], Marie Martig[7], and Leo Michel-Dansac[6]

[1] Sorbonne Université, Observatoire de Paris, Université PSL Univ., CNRS, LERMA, 75014 Paris, France
e-mail: `brisa.mancillas@obspm.fr`
[2] Observatoire Astronomique de Strasbourg, Université de Strasbourg, CNRS, 11 Rue de l'Université, 67000 Strasbourg, France
[3] Collège de France, 11 Pl. Marcelin Berthelot, 75005 Paris, France
[4] Laboratoire AIM Paris-Saclay, CEA/IRFU/SAp, CNRS/INSU, Univ. Paris Diderot, 91191 Gif-sur-Yvette Cedex, France
[5] European Southern Observatory, Karl-Schwarzschild-Str. 2, 85748 Garching, Germany
[6] Univ. Lyon, Univ. Lyon1, ENS de Lyon, CNRS, Centre de Recherche Astrophysique de Lyon, UMR5574, 69230 Saint-Genis-Laval, France
[7] Astrophysics Research Institute, Liverpool John Moores University, 146 Brownlow Hill, Liverpool L3 5RF, UK

Received 15 July 2019 / Accepted 8 September 2019

ABSTRACT

Several detailed observations, such as those carried out at the Canada-France-Hawaii Telescope (CFHT), have revealed prominent Low Surface Brightness (LSB) fine structures that lead to a change in the apparent morphology of galaxies. Previous photometry surveys have developed observational techniques which make use of the diffuse light detected in the external regions of galaxies. In these studies, the outer perturbations have been identified and classified. These include tidal tails, stellar streams, and shells. These structures serve as tracers for interacting events and merging events and retain some memory of the mass assembly of galaxies. Cosmological numerical simulations are required to estimate their visibility timescale, among other properties, in order to reconstruct the merger history of galaxies. In the present work, we analyze a hydrodynamical cosmological simulation to build up a comprehensive interpretation of the properties of fine structures. We present a census of several types of LSB fine structures compiled using a visual inspection of individual snapshots at various points in time. We reconstruct the evolution of the number of fine structures detected around an early-type galaxy and we compare it with the merger history of the galaxy. We find that most fine structures are associated with major and intermediate mass merger events. Their survival timescale ranges between 0.7 and 4 Gyr. Shells and streams remain visible for a longer time, while tidal tails have a shorter lifetime. These estimates for the survival time of collisional debris provide clues for the interpretation of the shape and frequency of fine structures observed in deep images with regard to their mass assembly. We find that the detectability of stellar streams is most sensitive at the surface brightness limit, demonstrating greater visibility at the deepest surface brightness level used in our simulation. We see between two and three times more streams based on a surface brightness cut of 33 mag arcsec^{-2} than with 29 mag arcsec^{-2}. We find that the detection of shells is strongly dependent upon the projection angle.

Key words. galaxies: elliptical and lenticular, cD – galaxies: evolution – galaxies: interactions – galaxies: peculiar – galaxies: structure

1. Introduction

Within the frame of the Lambda cold dark matter (ΛCDM) cosmological model, galaxy interactions play a major role in hierarchical galaxy formation theory. The models suggest that galaxies are assembled through successive mergers and continuous processes of cold gas and dark matter accretion (White & Rees 1978; Bullock & Johnston 2005; Naab et al. 2007; Cooper et al. 2013, 2015; Rodriguez-Gomez et al. 2016). Early studies propose that massive early-type galaxies result from a violent relaxation following the merger of two equal mass disk galaxies (Toomre 1977). Numerical studies demonstrate that, at high redshifts, the so-called intermediate-mass mergers of stellar mass-ratio 4:1−10:1 could be progenitors of S0-like galaxies. In addition, multiple sequential mergers of mass ratios ranging from 4:1−50:1 or even 100:1 can lead to the build-up of elliptical galaxies (Bournaud et al. 2005, 2007; Stewart et al. 2008; Karademir et al. 2019). The main mode of mass growth for early-type galaxies is also dependent on redshift. It is expected that minor mergers, along with stellar accretion, dominate a galaxy's mass growth, rather than major mergers at $z < 1$, since they occur more frequently (Kaviraj et al. 2009; Peirani et al. 2010; Hilz et al. 2012). Nonetheless, gas-rich mergers dominate the galaxy mass assembly in the early formation phases ($2 < z < 8$) (e.g. Naab et al. 2007), although direct gas accretion from cold streams, as inferred from numerical simulations and, very likely, from observations (e.g. Argudo-Fernandez et al. 2016), may also play a key role in the building of galaxy disks.

Interactions have left vestiges of their existence in the outer regions of central galaxies from disrupted satellites and from equal-mass mergers (Helmi & White 1999; Ferguson et al. 2002; Majewski et al. 2003). This collisional debris is mainly made up of stellar streams, plumes, tidal tails and stellar shells (Mihos et al. 2005; McConnachie et al. 2009; Janowiecki et al. 2010; Martínez-Delgado et al. 2010; van Dokkum 2005; van Dokkum et al. 2014). The detection of each class of collisional debris is essential since they trace the last merger events and store information about the mass assembly of their progenitors. In addition, their identification may modify their apparent morphology and then their classification in optical imaging surveys, such as the Sloan Digital Sky Survey (SDSS York et al. 2000).

The present work emphasizes a qualitative analysis of low surface brightness (LSB) fine structures identified in a numerical simulation conducted in a cosmological context. The first imaging observations of collisional debris to exhibit the distinctive shapes of tidal tails and stellar streams, mainly in early-type galaxies, were published in the Atlas of Peculiar Galaxies catalog (Arp 1966). In the case of shell structures, Malin & Carter (1983) reported a catalog of 137 elliptical galaxies exhibiting shells or ripple-like structures. On the theoretical side, the first computational models of interacting galaxies revealed that the perturbations and debris are the outcome of gravity tides in disk galaxies (Toomre & Toomre 1972). Since that time, substantial efforts undertaken to develop observational techniques aimed at identifying these substructures. The techniques include, for example, the unsharp masking and amplification of photographic images (Malin 1977, 1978), sky subtraction of individual images (Mihos et al. 2005), and extraction of structural components with GALFIT (Peng et al. 2002). Additionally, the application of galactic archeology also allows us to establish a demography of LSB structures in nearby galaxies (McConnachie et al. 2009; Crnojević et al. 2013), although its application is restricted to galaxies at a very low redshift due to spatial resolution and sensitivity.

The search for diffuse light was also a task carried out by amateur astronomers using simple cameras (e.g. Martínez-Delgado et al. 2009). Their long-exposure observations revealed spectacular images that later inspired the implementation of new techniques in conventional telescopes (Martínez-Delgado et al. 2010). Nonetheless, in spite of these innovative techniques, the detection of merger remnants continues to be problematic. Low spatial resolution or a limited field of view make it more difficult to recognize tenuous morphologies in the outer regions of galaxies. Perhaps the main issue is related to low surface brightness, expected to be below the level of 28 mag arcsec^{-2} and, most frequently, below ~30 mag arcsec^{-2} (e.g. Johnston et al. 2008; Cooper et al. 2010). Thanks to the availability and advancement of deep imaging programs for nearby galaxies, it has been possible to detect the prominent structures that surround galaxies, with the large field of view provided by the mosaic camera (CFHT/MegaCam, NGVS, Ferrarese et al. 2012) or the specialized Dragonfly Telephoto Array, designed for LSB astronomy (van Dokkum et al. 2014).

In their pioneering work, Malin & Carter (1983) revealed that numerous shells could be observed as tracers of interactions and mergers in 137 early-type galaxies. In the survey of 36 field galaxies aimed at detecting fine structures, Schweizer & Ford (1985) identified 44% of weak shells and ~10% of plumes and tidal tails. In more recent studies, Tal et al. (2009) present an optical image sample of 55 luminous elliptical galaxies and, by using a tidal interaction parameter, they find that 73% of these displayed tidal features. Meanwhile, Atkinson et al. (2013) report ~26% of tidal features in their sample of 1781 galaxies from the CFHT Legacy Survey. On the other hand, Krajnović et al. (2011) identify 8% of tidal debris in a subsample of the ATLAS^{3D} sample of 260 early-type galaxies, whereas in the massive early-type galaxies of MATLAS deep imaging survey, it was found that ~16% displayed streams and shell-like features, and ~22% showed tails and plumes (Duc 2017). In the most recent studies, Hood et al. (2018) report an incidence of 17% of tidal features in the 1048 galaxies of the RESOLVE survey, as well as Kado-Fong et al. (2018), who identify 18% shell galaxies and 82% stellar stream systems from the subsample of 1201 galaxies of the SDSS spectroscopy images taken from the Hyper Suprime-Cam Subaru Strategic Program (HSC-SSP).

When it comes to numerical studies, only a few works have taken a census of tidal debris thus far. In the analysis of the hydrodynamical Illustris simulation, Pop et al. (2018) report that 18% of their massive galaxies display shell-like structures as a result of merger events with stellar mass ratios $\gtrsim$10:1. Karademir et al. (2019) explore a wide parameter space in mass ratios and relative orbits. They find that streams are formed by satellite infalling with a large angular momentum, while shells are the result of the radial infall of satellites with low angular momentum. More and more often, fine structures are being identified and classified through automatic techniques, such as those developed in Pawlik et al. (2016), Hendel et al. (2019), Walmsley et al. (2019). It is still necessary to identify fine structures visually in order to teach the machine how to improve the precision of image recognition and to verify procedures. In addition, different dark matter halo models should be explored since the fine structures will greatly depend on dark matter spatial distribution.

Several scenarios have been proposed to explain the morphology characteristics of tidal features. The disruption of merging galaxies may yield different features according to their relative orbits and the geometry of the encounter (Amorisco 2015; Hendel & Johnston 2015). Analytical and numerical studies show that stellar shell structures are the remnants of disrupted satellites on near-radial orbits, while stellar streams are generated by near-circular orbits (Quinn 1984; Dupraz & Combes 1986; Johnston et al. 2008; Karademir et al. 2019). Collisional debris is made up of transient structures that can last for short times or be disappear as a result of posterior interactions in a few Gyr (Stewart et al. 2008). Their recognition is primarily dependent on their surface brightness, in addition to several other factors, such as the type of substructure and orientation in the sky (Duc 2017). Thus, the determination of their survival timescale is crucial in reconstructing the merging history of galaxies, together with their numerical simulations. Until now, numerical works have been used to constrain these timescales. The earliest studies of semi-analytical models focus in the signatures of satellites orbiting the Milky Way. Johnston et al. (1999) reported a "preceding passage" of ~0.7 Gyr for tidal debris for the Sagittarius Dwarf Galaxy, demonstrating that the satellite is rapidly being disrupted and will only survive a few pericentric passages, that is, ~1.3 Gyr. Hybrid models composed of semi-analytical and N-body simulations of Milky Way-type stellar halos from Bullock & Johnston (2005) estimate a median accretion time of ~5 Gyr for their satellite systems.

Hydrodynamical simulations of equal-mass mergers performed in isolated environments have determined several timescales based on different methods. Lotz et al. (2008) report an average timescale of ~1.5 Gyr using the Gini coefficient. Meanwhile, Ji et al. (2014) use visual inspection to estimate a merger-feature time (the moment when faint features disappear) of ~1.38 Gyr (for $\mu = 25$ mag arcsec^{-2}), which is comparable to the timescale computed by Lotz et al. (2008). Current deep imaging surveys go much deeper and further studies are needed to estimate updated timescales.

The goal of the present work is to identify and classify the LSB features observed in a host halo based on the hydrodynamical simulation of Martig et al. (2009). These are zoom-in resimulations that reveal the fate of a typical massive galaxies in great detail after having undergone cold gas accretion and several mergers during a Hubble time. The cosmological context is taken from a previous large-scale simulation with reduced spatial resolution. The high resolution of the zoom-in simulation is capable of identifying most fine structures occurring at any epoch. In this analysis, five observers have visually classified a full mock catalog of stellar surface brightness maps (cf. the snapshots in the appendix). The aims of the classification are to: (i) characterize the shape of the faint stellar structures on the outskirts of the main central galaxy, (ii) take a census of the number of these structures and classify them into tidal tails, streams, and shells, (iii) to estimate the survival time of each substructure and study their dependence on the surface brightness limit and the projection on the sky plane.

In Sect. 2, we describe the numerical simulation carried out in a cosmological context (Sect. 2.1.1), the high-resolution resimulation (Sect. 2.1.2), and the phases of the galaxy evolution (Sect. 2.2). We describe the catalog of stellar surface brightness maps in Sect. 3. Results are reported in Sect. 4 and discussed in Sect. 5. Section 6 presents a summary of our conclusions.

2. Numerical simulations

2.1. Simulation technique

To analyze the galaxy evolution in the ΛCDM cosmological model, we use the numerical simulation of Martig et al. (2009). The approach demonstrates how the growth of a massive stellar spheroid through a series of mergers can be enough to stabilize a disk which is, by then, no longer self-gravitating, and therefore, quench star formation. Through this process, the galaxy becomes a red early-type object while continuing to accrete gas. The technique that was used consists of two steps: first a ΛCDM cosmological simulation is run, with only dark matter, while the merger and accretion history for a given halo is extracted. In the second step, the mass assembly history is re-simulated at a higher resolution, replacing each halo with a realistic galaxy, containing gas, stars, and dark matter.

2.1.1. Cosmological simulation

The cosmological simulation used to carry out this study was performed with the RAMSES code (Teyssier 2002), based on the Adaptive Mesh Refinement (AMR) technique. The box has a comoving length of $20\,h^{-1}$ Mpc, and contains 512^3 dark matter particles with a mass resolution of $6.9 \times 10^6\,M_\odot$. The dark matter halos are identified using the HOP algorithm of Eisenstein & Hut (1998), and the merger and accretion histories are extracted following the main halo from $z = 2$ to $z = 0$. All the halos (of the merger history) and diffuse particles (of the accretion history) that cross a fixed spherical boundary drawn around the target halo are recorded. The sphere is larger than the initial main halo at $z = 2$ and encompass satellites, as well as "diffuse" particles, that is, those that don't belong to any halo. The second step zoom-in resimulations were carried out for Milky Way-mass galaxies in low density environments (Martig et al. 2012). Within this sample, we selected a case where there is a major merger with a post-merger early-type phase galaxy. There is no particular selection bias, nor were the galaxies selected on the basis of an abundance of fine substructures.

2.1.2. High-resolution resimulation

The next step consisted of a high-resolution resimulation using a particle-mesh code described in Bournaud & Combes (2002, 2003), in which the gas dynamics is modeled using a sticky particle scheme. The maximal spatial resolution is 130 pc and the mass resolution is $1.4 \times 10^5\,M_\odot$ for stellar particles initially present in the galaxies, $2.1 \times 10^4\,M_\odot$ for gas and stellar particles formed during the simulation, and $4.4 \times 10^5\,M_\odot$ for dark matter particles. Star formation is computed following a Schmidt-Kennicutt Law (Kennicutt 1998), where the SFR is proportional to the gas density to the exponent of 1.5, setting a threshold for star formation at $0.003\,M_\odot\,\mathrm{pc}^{-3}$. The simulation does not include supernova explosions, nor AGN feedback.

The resimulation starts at redshift $z = 2$ and evolves down to $z = 0$, including all the halos and the "diffuse" particles embedded in the spherical boundary around the target halo, recording their mass, position, velocity and spin. Each halo is replaced by a realistic galaxy made of gas, stars and dark matter particles, and by replacing each diffuse particle with a blob of lower-mass, higher-resolution gas and dark matter particles (see Appendix A of Martig et al. 2009 for more details). Each small halo starts to interact with the main halo following the orbital and spin parameters given at the beginning of the cosmological simulation (e.g., Fig. 2 and subsequent figures).

2.2. Merger history and stellar mass growth of the studied galaxy

The central galaxy studied in this simulation has a mass similar to that of the Milky Way. Its corresponding host halo does not belong to a rich group or a galaxy cluster as most early-type galaxies (ETGs) in the MATLAS survey (see snapshots in the appendix for the galaxy environment). During the simulation, the host halo increases from a mass of $2 \times 10^{11}\,M_\odot$ at $z = 2$ to $1.4 \times 10^{12}\,M_\odot$ at $z = 0$. The galaxy evolution can be decomposed into 3 main phases (see the plot 3 of Martig et al. 2009). The simulation starts out with a gas-rich disk galaxy and an intense phase of minor mergers with a mass ratio between 1:4 and 1:10. This period lasts from $z = 2$ to $z \sim 1$. Afterwards, a quiet phase takes place between $z \simeq 1$ and $z \simeq 0.2$. This is a quiescent period studied by Martig et al. (2009) in which star formation is suppressed. Over this period, there is no major event occurring, however, diffuse gas is continuously being accreted. In the final phase, the galaxy undergoes a major merger event, along with an increase in the diffuse gas accretion rate, which lasts from $z = 0.2$ to $z = 0$. These three phases are representative of any merging history in the life of a galaxy and, thus, our estimations of life-time of fine structures will be statistically significant.

3. Surface brightness maps

3.1. Mock image generation

We use the models of Bruzual & Charlot (2003; BC03) to compute mock images of the stars in the simulation. We follow the technique developed in Michel-Dansac & Wozniak (2004). We briefly describe how the mock images are made. For all stellar particles in the simulation, we compute the stellar spectra with a linear interpolation of age in the BC03 tables. For this, we use tables based on a Salpeter IMF (Salpeter 1955). We assume a solar metallicity for the stellar particles. The simulation does not follow the chemical evolution. For one projection, particles are projected on a 2D grid using a Cloud in Cell (CIC) algorithm (Birdsall & Fuss 1969). Then, for each pixel we sum up the spectra of individual particles to get the composite spectrum. These spectra are finally integrated in the CFHT/MegaCam photometric filters in order to produce surface brightness maps.

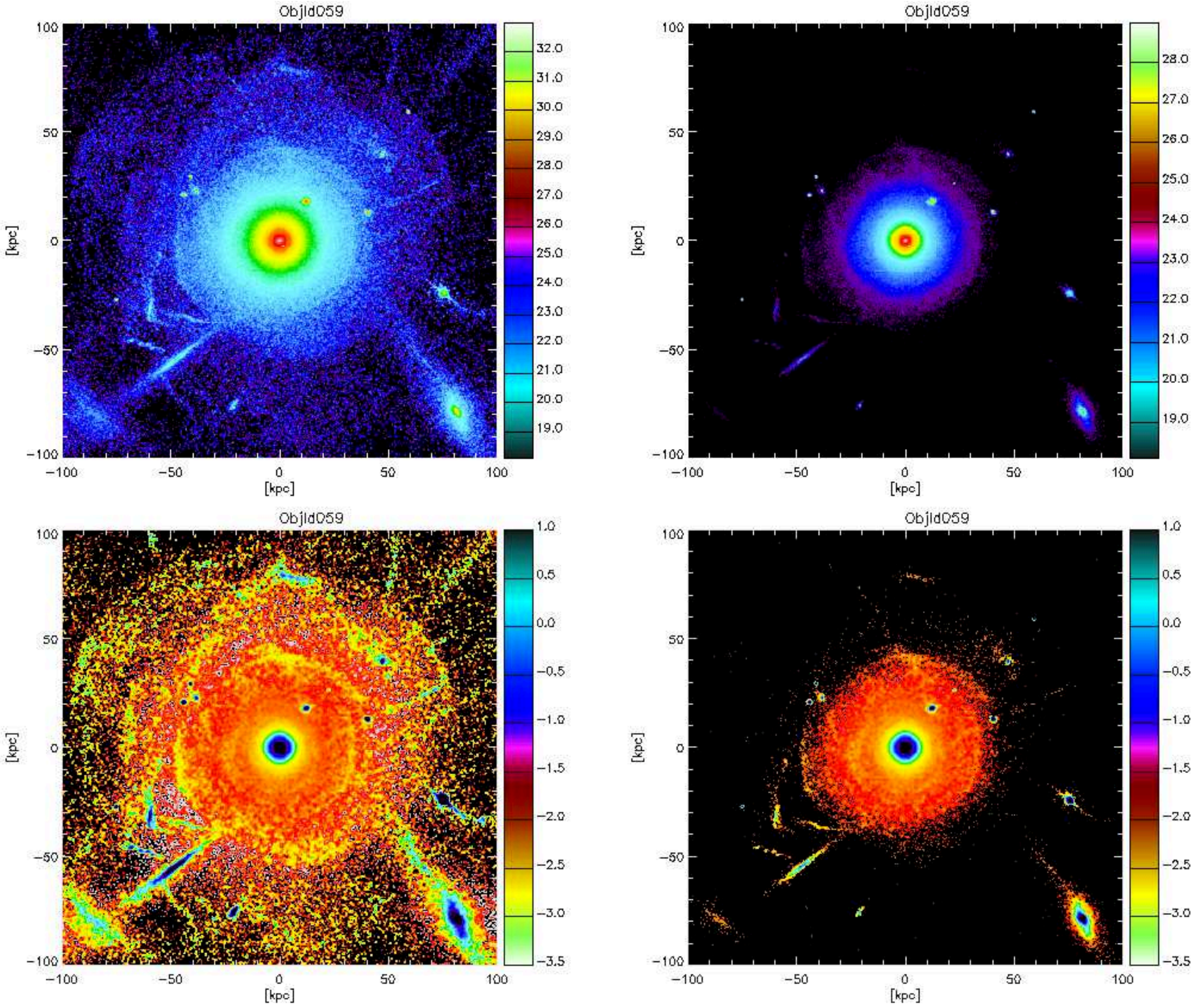

Fig. 1. Surface brightness map of central galaxy shown in *g*-band with two different color scales (resp., *upper and lower panels*) and with cut at 33 mag arcsec^{-2} (*left panels*) and 29 mag arcsec^{-2} (*right panels*).

We have compiled a catalog of images for the 35 snapshots of the simulation and the three projections, presenting a total of 105 images. For each image, we prepared two *g*-band maps: one with a cut at 33 mag arcsec^{-2} (Valls-Gabaud 2017) and the other at 29 mag arcsec^{-2}. The latter value corresponds to the surface brightness limit of the MATLAS survey. We also added unsharp masked maps, a technique that has proven very efficient in enhancing LSB substructures. The first snapshot starts at 3.5 Gyr and the last one ends at 13.7 Gyr (in addition to an extra simulation which evolved until 15.7 Gyr). The time interval is 0.3 Gyr. Below, we provide a phenomenological description of collisional debris, based on the observational work of Duc et al. (2015) (see e.g., Fig. 1). To visualize tidal streams, tails and shells, we believe that dust extinction is not significant because the fine-structure features are located in the outer parts of galaxies, where there is little gas or dust.

3.2. Visual classification

For the visual identification, we proceeded in a similar way to earlier observational surveys aimed at identifying substructures optically (e.g. Tal et al. 2009; Atkinson et al. 2013; Duc et al. 2015; Duc 2017). A team of five members carried out a visual inspection of each mock image. We identified and classified the fine structures that were observed and took a census of them for both surface brightness cuts. Note that all the images (various snapshots and projections) in the catalog have been randomly ordered for the classification in order to avoid two close snapshots in the same projection following the other in the catalog or two projections of the same snapshot. This ensures that our classification is not influenced by the stellar structures of recent history or another viewing angle. Indeed, in real observations, there is no equivalent of two consecutive snapshots of the same merger event. In our case, each image is initially considered entirely independently of any other. This also allows us to verify the consistency of the method once the merger history is reconstructed.

Figures 2–4 demonstrate three examples of tidal tails, stellar streams, and shells, respectively, each projected in two directions, and based on the case of the lowest surface brightness limit, that is, $\mu = 33$ mag arcsec^{-2}. Below, we define the substructures categorized within the three morphologies mentioned above.

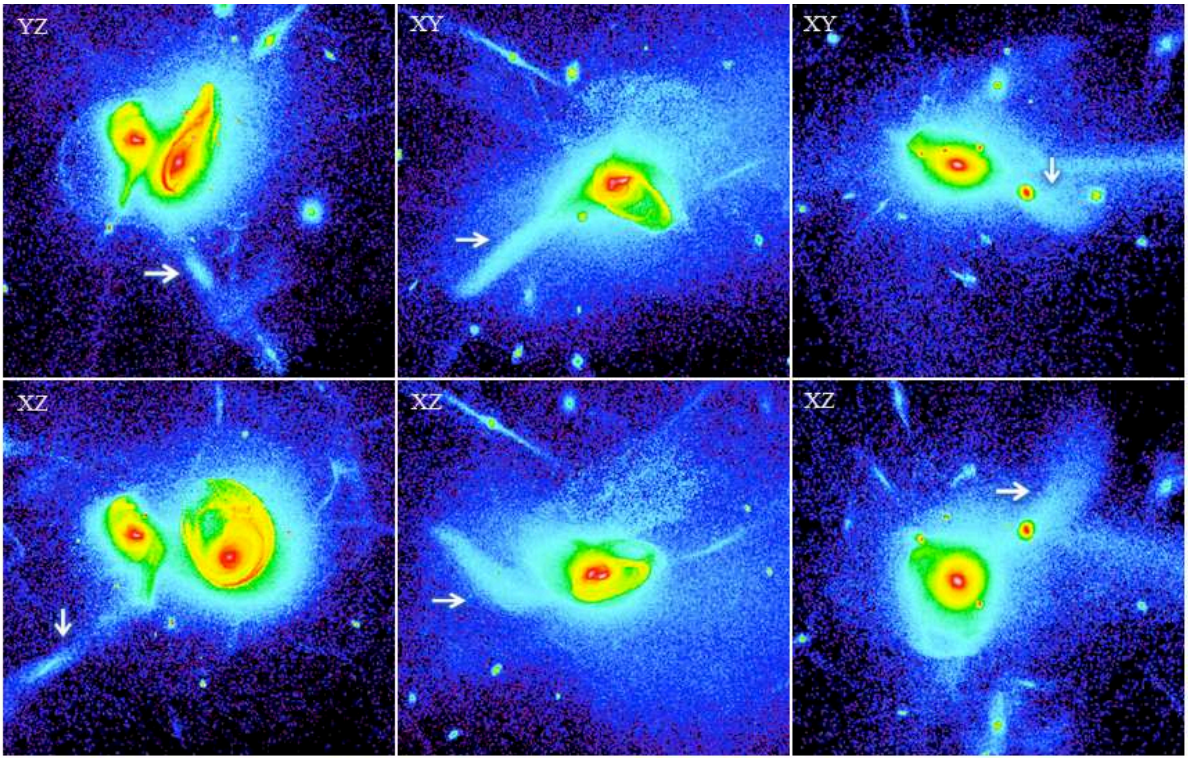

Fig. 2. Examples of interactions between central galaxy and its nearby companions, which demonstrate protuberant tidal tails (indicated with a white arrow) for three different objects (resp., *right, middle and left panels*) in two random projections: XY in the *upper panel* and XZ at the *bottom*.

Tidal tails are thick, radially elongated structures that are connected to the host galaxy. The visual impression is that the tidal tail appears to be emanating from the galaxy. In the case of any confusion between tail and stream, we relied on the aspect of thinness to distinguish between streams and tail; tails being thicker than streams. The thickness separation between the two is of the order of 300 pc. Over time, the dilution of tidal tails implies a widening, so there is no confusion.

Stellar streams are thin, elongated stellar structures which look like narrow, long filaments. They can be associated with galaxy satellites, exhibiting the known S-shaped structures that emanate from the main galaxy and characterize satellite disruption. But this is not a requisite, so they might also not be associated clearly with any galaxy, or physically associated with the central galaxy.

Shells have circular concentric shapes and are sharp-edge arc structures. Depending on their intrinsic nature and their projection, they appear to be aligned with a common axis or randomly spread around the central galaxy. When aligned to the major axis of the host, they are interleaved, meaning that they appear to accumulate alternatively on each side of the galaxy. This stellar accumulation can be associated with successive apocenters of an oscillating radial orbit following a satellite accretion event. When they extend to larger radii, they become more diffused.

To illustrate the three kinds of fine structures, we compare typical examples for each, in both observations and simulations, in Fig. 5.

4. Results

4.1. Evolution of stellar mass

The stellar mass of the central galaxy is plotted as a function of time in Fig. 6. We distinguish the provenance of the stellar mass into two categories. First, we show the contribution of the in situ mass, referring to the stars born inside of the main galaxy. Secondly, the ex situ mass, or accreted mass referring to the stars formed in the satellite galaxies and accreted afterwards into the main galaxy. We note that since the simulation starts at $z = 2$ with preprepared galaxy models, a third contribution to stellar mass is the initial mass of the galaxy. These three phases describe the evolution of the main galaxy. In addition, at larger scales, a number of satellites orbit the halo all over the simulation. In Table 1, we describe the properties of the most important satellites that interact with the main galaxy during the simulation. The merging satellites are identified using an arbitrary number. Their merging time, their stellar mass, and their mass ratio with respect to the main galaxy are all listed.

4.2. Identified substructures

Having defined the method and described the mock catalog of surface brightness images, we explore our findings and the substructure properties observed in this analysis.

In Figs. 7–9, we present the time evolution of the number of tidal tails, stellar streams and shells, respectively, for three different projections, $x - y$, $x - z$ and $y - z$ (as indicated in each panel). Time begins at the start of the resimulation ($z = 2$), and continues after the present time ($z = 0$), so that the future of fine structures can be estimated. The panels display the curves of the average value from the five team members who made the visual inspection for each time interval (snapshot) and their respective scatter. We present this census for both surface brightness limits $\mu = 29$ mag arcsec^{-2} ("detected") and $\mu = 33$ mag arcsec^{-2} ("total"), respectively.

In addition, in order to analyze the correlation between the generation of features and the presence of mergers, in Fig. 10 we

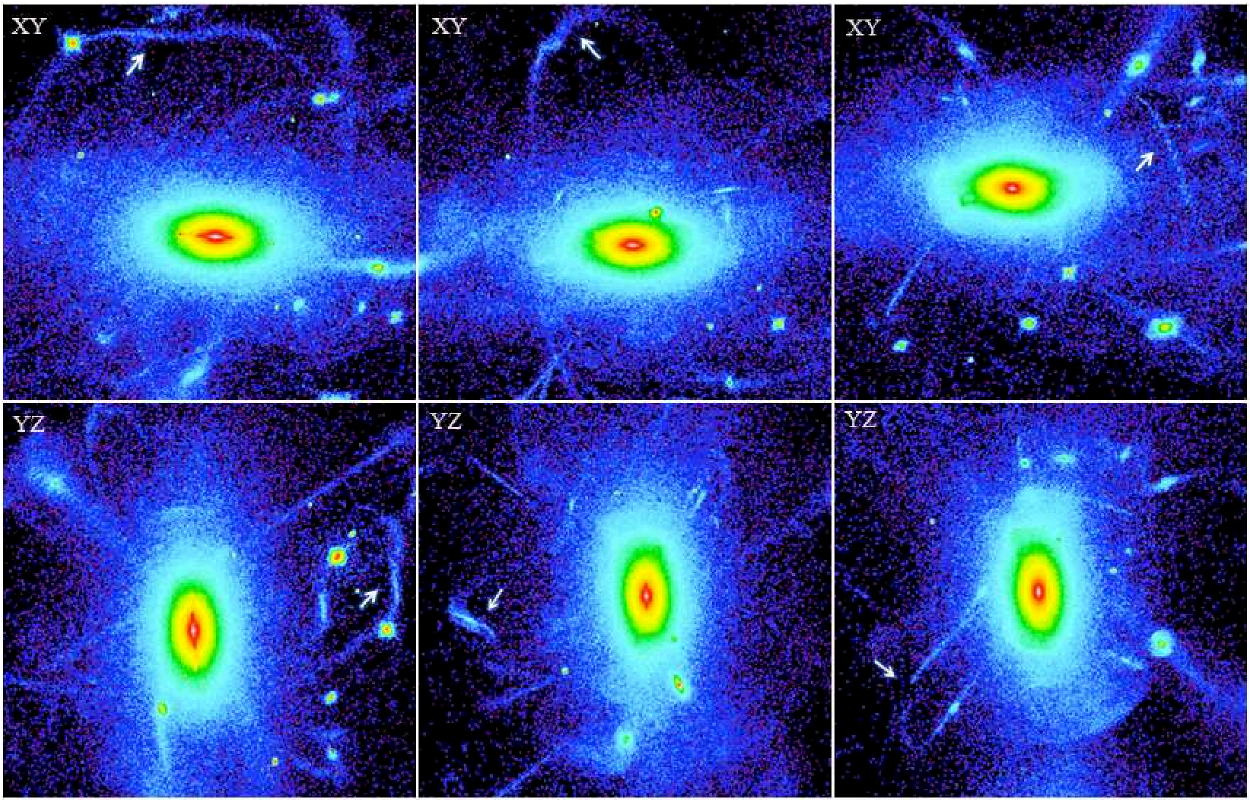

Fig. 3. Examples of central galaxy hosting disrupted satellites based on presence of prominent stellar streams (indicated with a white arrow) for three different objects (resp., *right, middle and left panels*) in two random projections: XY in the *upper panel*, and YZ at the *bottom*.

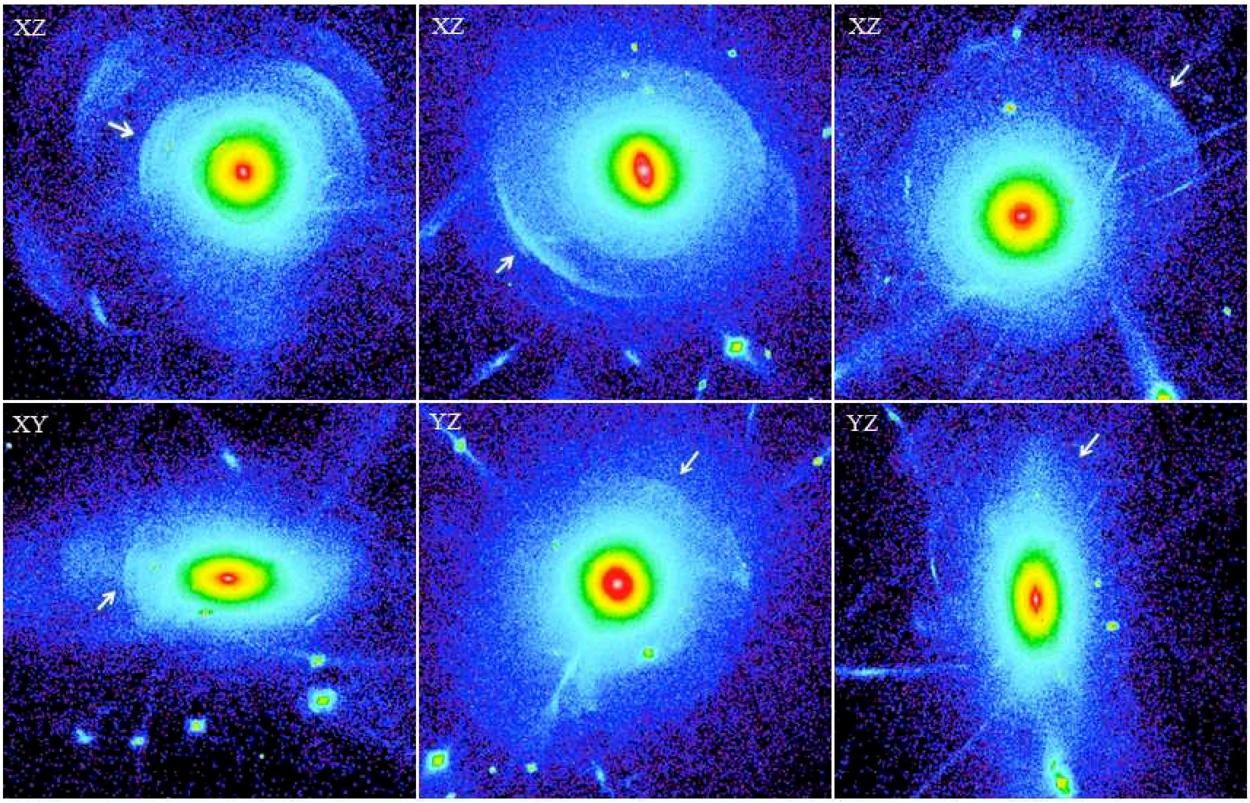

Fig. 4. Examples of central galaxy displaying several shells around it (indicated by white arrow) for three different objects (resp., *right, middle and left panels*) in three random projections: XZ in the *upper panel*, XY and YZ at the *bottom*.

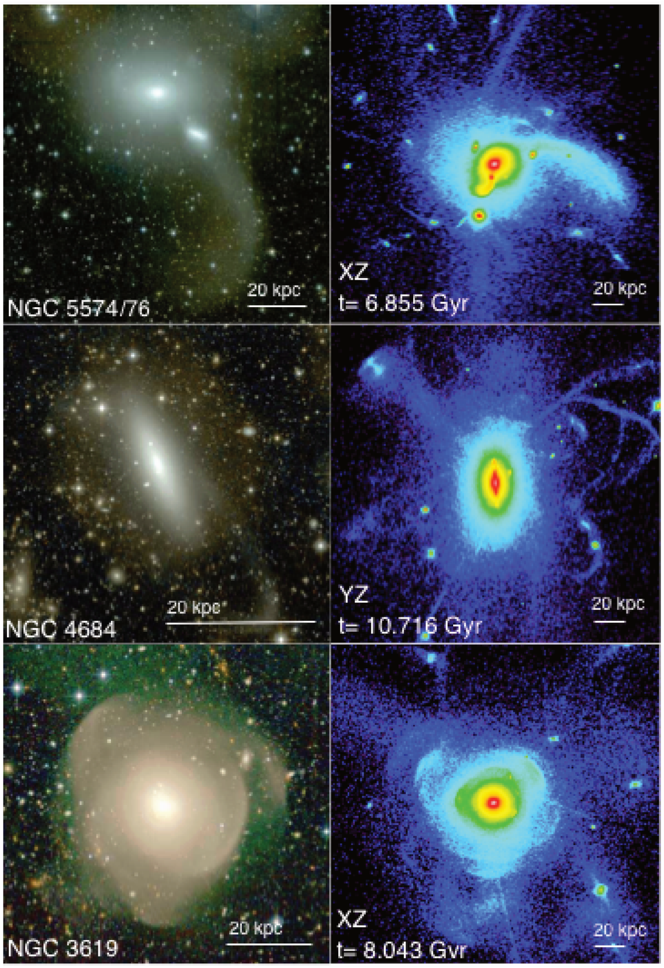

Fig. 5. Comparison of LSB substructures around observed and simulated galaxies. *Left panels*: examples of ETGs from MATLAS Survey. *From top to bottom*: system NGC 5574/76 (tidal tails emanating from NGC 5576), stellar stream in NGC 4684 and interleaved shells in NGC 3619. *Right panels*: examples of mock surface brightness images exhibiting prominent tidal tails, streams, and shells at different times of simulation in random projections. Note the white scale bar indicating 20 kpc: the scales are comparable across observations and simulations.

show the accreted stellar mass (red line in upper panel) and we use arrows to indicate where the mergers take place. We point out the most significant mergers and their mass ratios with red numbers. In the lower panel, we present the corresponding evolution of each fine structure. Here we plot the highest numbers of features over the three projections for tidal (blue dotted line), streams (green dotted and dashed line) and shells (black dashed line). The identification of each substructure detected during the formation of the galaxy corresponds to the time period of $t = 3.5$ Gyr ($z = 2$) to $t = 16$ Gyr ($z > 0$). The major merger at $T = 11.5$ Gyr is destroying most of the previous fine-structures; shells in particular. Some more shells and tails are rebuilt after that at the same rate as before. It will take some time to reach the same level of fine structures as was reached in the quiet phase.

We note that the curves indicating the number of fine structures as a function of time (Figs. 7–9) are reconstructed and reordered afterwards. It is remarkable that they make sense, that is, the correlations between individual consecutive snapshots as visible and as expected. Below, we describe the main characteristics of the census of tidal debris.

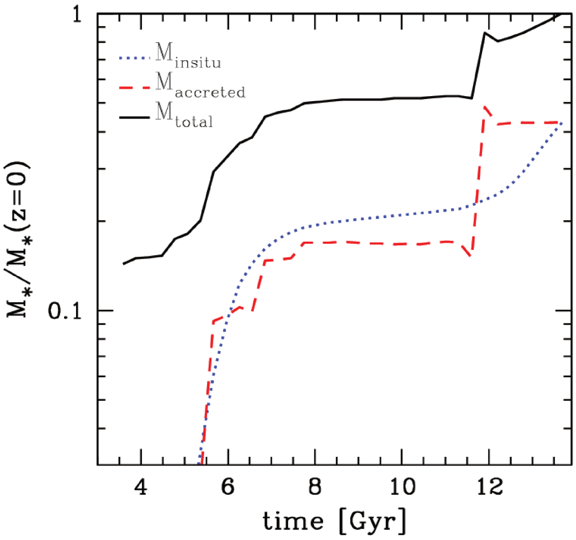

Fig. 6. Evolution of stellar mass for main galaxy as function of time. The total stellar mass (black solid line) has been decomposed into the in situ mass (blue dotted line), that is, stars formed in the main galaxy, and accreted mass (red dashed line), that is, stars formed in a companion galaxy and then accreted into the main galaxy.

Table 1. Stellar mass ratio of main mergers.

$t_{\rm merger}$ [Gyr]	$M_\star$ [$M_\odot$]	Stellar mass ratio
4.77	4.4×10^9	0.14 (7:1)
5.67	13.0×10^9	0.31 (3:1)
6.26	1.5×10^9	0.04 (25:1)
7.20	12.0×10^9	0.17 (6:1)
7.75	5.0×10^9	0.06 (16:1)
11.9	74.0×10^9	0.67 (1.5:1)

Notes. Stellar mass ratio has been measured just before galaxy merger.

4.3. Formation mechanism and survival time

The formation scenario for each substructure is the first bit of information we can infer from the evolution of the simulation. We know by construction all the merger events of the central galaxy in all its evolution phases. The counting of the substructures is, thus, a direct outcome and it allows us to draw correlations between individual substructures and the corresponding merger event. In Fig. 10, we represent the correlation between the generation of features and the occurrence of mergers.

4.3.1. Tidal tails

We find that tails are produced during the first and the third phase of galaxy evolution as a result of tidal forces acting within the host galaxy. In the first phase, we observe an average of two tails associated with the intermediate-mass merger and major merger events (mass ratios between 7:1 and 3:1). In the second phase, their detection drastically decreases due to the lack of any kind of mergers. In the last phase, a peak of incidence appears when the major merger (mass ratio of 1.5:1) takes place. Prominent tidal tails can be evaluated through visual inspection at 6.8 Gyr and 11.9 Gyr in the snapshot evolution (see Figs. A.1–A.3). We estimate a survival time of ~2 Gyr.

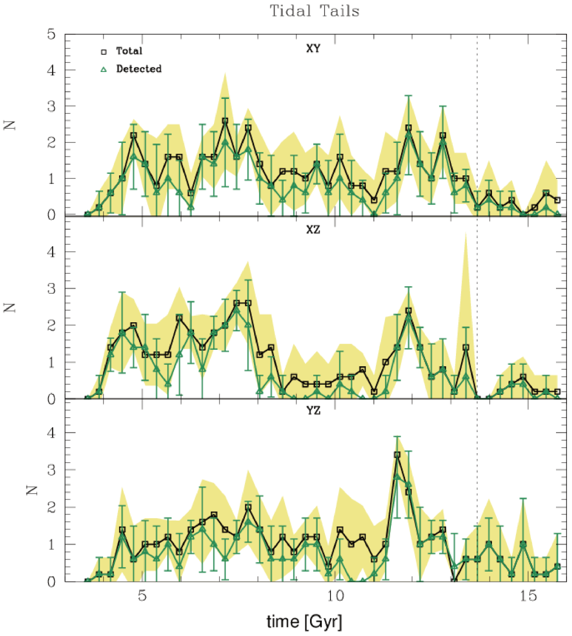

Fig. 7. Evolution of tidal tail numbers. The three panels show the results for the three projections (XY, XZ, and YZ). In each panel, the black lines and the yellow shaded area represent the total number of tidal tails and their respective scatter, whereas the green ones are the number of tidal tails that are detectable on images with a cut in surface brightness at 29 mag arcsec^{-2}. The time ($t = 0$) corresponds to the Big-Bang, and the re-simulation is longer than a Hubble time, beyond $z = 0$, to estimate the future of fine structures.

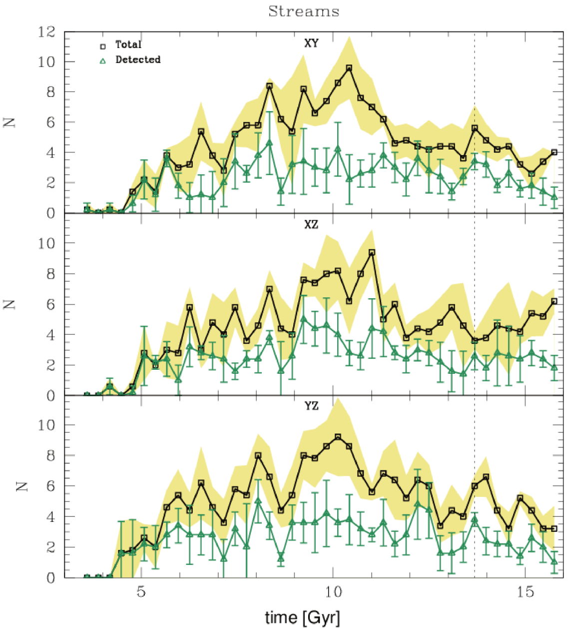

Fig. 8. Evolution of stellar stream numbers. Three panels show results for three projections. In each panel, the black lines and the yellow shaded area are the total number of stellar streams and their respective scatter, whereas the green ones represent the number of stellar streams that are detectable on images with a cut in surface brightness at 29 mag arcsec^{-2}. The time ($t = 0$) corresponds to the Big-Bang.

4.3.2. Stellar streams

Streams are the most frequent fine structure features in our simulation (an average of ~8 streams detected through visual inspection, see Fig. 8). They appear in the first series of consecutive minor mergers, increasing in number over time, although some of them are destroyed when the following merger events occur. The highest peak of incidence is reached during the quiescent phase (second phase). The absence of important mergers during this phase allows for the increase in the production of streams and their survival time by the lack of processes to that would eliminate them. They trace the initial orbit of the satellites which are disrupted during this quiet phase, producing long, extended narrow streams. We observe a decrease in the detection number when the major merger appears and eliminates many of them in the last phase of the simulation. Under all the physical conditions explained above, we derive a life time of ~3 Gyr.

The stellar streams are present during the quiescent phase of the galaxy, and even demonstrate their peak in this period, while there is no minor merger (nor major one) in all this phase. This may look paradoxical. Either the stellar streams develop from the minor mergers coalesced in the previous phase, or there is another mechanism to form these streams. The latter could be due to the accretion of cold gas (e.g. Bournaud et al. 2005).

4.3.3. Shells

In our simulation, shell formation is associated with both intermediate-mass mergers and major mergers. Previous works have shown they are commonly related with intermediate-mass mergers (e.g. Pop et al. 2018; Karademir et al. 2019). The largest generation of shells is visible during the quiet phase, just after the first phase of mergers has occurred, whereas a second peak of shells is produced just after the major merger takes place. We attribute this high incidence of shells to the same phenomenon as in the case of streams, that is: when there are no violent processes to eliminate them, they remain numerous in the quiet phase. Following the snapshot evolution (see Fig. A.1), we note that once the corresponding satellite falls into the central potential, shells appear and acquire their known arc-like shape. Initially, they are spread around the galaxy at small distances from the center and are distributed in an interleaved way. They accumulate near the apocenters of their orbits, and develop progressively to the outskirts of the central galaxy. Consequently, due to their density wave nature, they propagate towards larger and larger distances, and their numbers increase. According to the duration of their incidence peak, that is, from the width of the curves in Fig. 9, and assuming that no shell is produced during the quiet phase, we estimate a lifetime of ~4 Gyr.

4.4. *Sensitivity on the surface brightness cut*

The surface brightness limit is one of the main issues relevant to the identification of fine features, according to observational studies. Traditional images from the SDSS survey (York et al. 2000) reach a value of 26.4 mag arcsec^{-2} in the g-band. In the sample from CFHT Legacy Survey (Atkinson et al. 2013) and the observations with the MegaCam of Tal et al. (2009), also in the g-band, they barely detect substructures at ~28 mag arcsec^{-2}. Deeper observations like the LSB-optimized NGVS Survey (Ferrarese et al. 2012), the ETG from ATLAS^{3D} (Duc et al. 2015), and the Large Program MATLAS Survey (Duc 2017) achieve a value of 29 mag arcsec^{-2}. These values relate to the local surface brightness. However, it is possible to define integrated-light surface brightness, and a very low level of scattered light (one order of magnitude below the best-performing

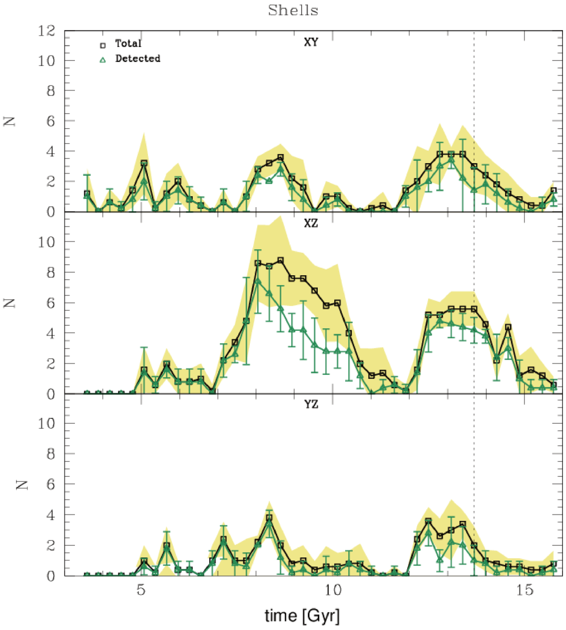

Fig. 9. Evolution of shell numbers. Three panels show results for three projections. In each panel, the black lines and the yellow shaded area are the total number of shells and their respective scatter, whereas the green ones represent the number of shells that are detectable on images with a cut in surface brightness at 29 mag arcsec^{-2}.

telescopes), with the lowest limit achieved with the Dragonfly Telephoto Array (van Dokkum et al. 2014), having a value of 32 mag arcsec^{-2}. The latter reveals spectacular hidden substructures in the external regions of galaxies. These surface brightness limits could be reached locally by dedicated space-based missions, such as the Messier project (Valls-Gabaud 2017).

On the simulation side, there is the freedom to reproduce deep images with low surface brightness. The values range from 28 mag arcsec^{-2} (Ji et al. 2014) to even 38 mag arcsec^{-2} (Bullock & Johnston 2005; Johnston et al. 2008). Motivated by all these previous studies on the detectability of faint features in merger remnants, the present study selects two values of the surface brightness limits, $\mu = 29$ mag arcsec^{-2} and $\mu = 33$ mag arcsec^{-2}, respectively, to take a census of LSB substructures.

4.4.1. Tidal tails

We do not find any substantial dependency on the surface brightness for this type of substructure. We detect a comparable number of tidal tails for both surface brightness cuts per time step (snapshot). The curves in the three panels of Fig. 7 follow the same trend over the course of the evolution. We attribute this result to their prominent nature, which is a result of major interactions and, therefore, fall above the detection threshold.

4.4.2. Stellar streams

We find a high dependence on the surface brightness limit for this type of substructure. As seen in the three panels of Fig. 8, the incidence of streams is considerably higher for $\mu = 33$ mag arcsec^{-2} than for $\mu = 29$ mag arcsec^{-2}. The peak of incidence reaches an average number of 9 streams for the first cut, while for the second cut, the peak only reaches 4 streams. Streams are tracers of minor mergers and, hence, they have a narrow morphology, making their detection difficult. They are faint, but as they are more narrow, they may be identifiable for longer than the more diffuse tails. Figure 11 presents the surface brightness map of a particular stream, under the two cuts, to illustrate a clear example of this difference. With the low level of surface brightness (left panel), a wide variety of extended streams surround the central galaxy, along with the tail of a prominent satellite, in the higher surface brightness cut (right panel), and only the central regions of the whole system are seen. Stellar streams are the type of substructure which present the strongest dependency on surface brightness in comparison with tails and shells.

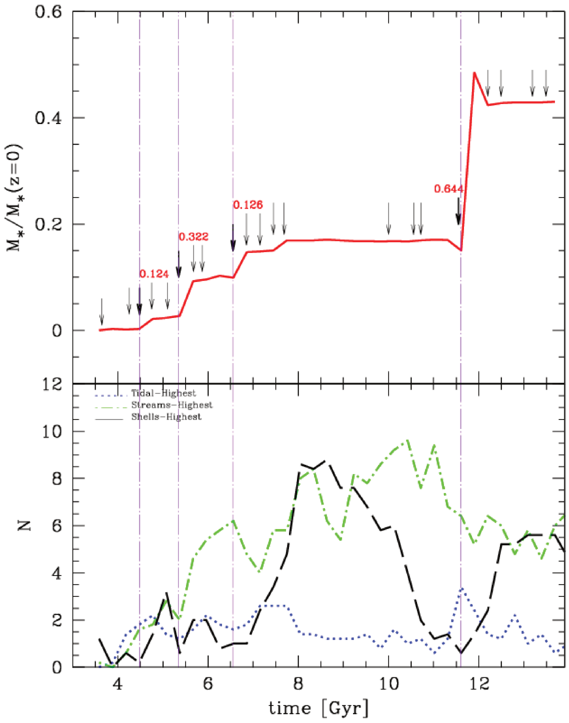

Fig. 10. Comparison between accreted stellar mass and all types of fine structures. *Upper panel*: red line represents evolution of accreted mass. Arrows indicate when mergers occur. Red numbers over bold arrows correspond to intermediate mass and major mergers. *Lower panel*: evolution of highest value of three projections in each fine structure. Blue dotted line is for tidal tails, green dotted and dashed line is for streams and black dashed line is for shells. Purple dotted and dashed lines in both panels indicate the correlation between main mergers and substructures.

4.4.3. Shells

Shells are slightly sensitive to surface brightness. A significant difference is observable between the maximal peaks of the two curves in the middle panel of Fig. 9 (projection $y - z$). For this peak, we detect, on average, two shells more for the case of $\mu = 33$ mag arcsec^{-2} than for $\mu = 29$ mag arcsec^{-2}.

4.5. *Dependence on the projection*

Another important issue relevant to the identification of substructures using visual inspection is the effect of the projection. Fortunately, our approach reproduces three projections for each snapshot in order to consider the effects of the sky orientation on each class of substructures.

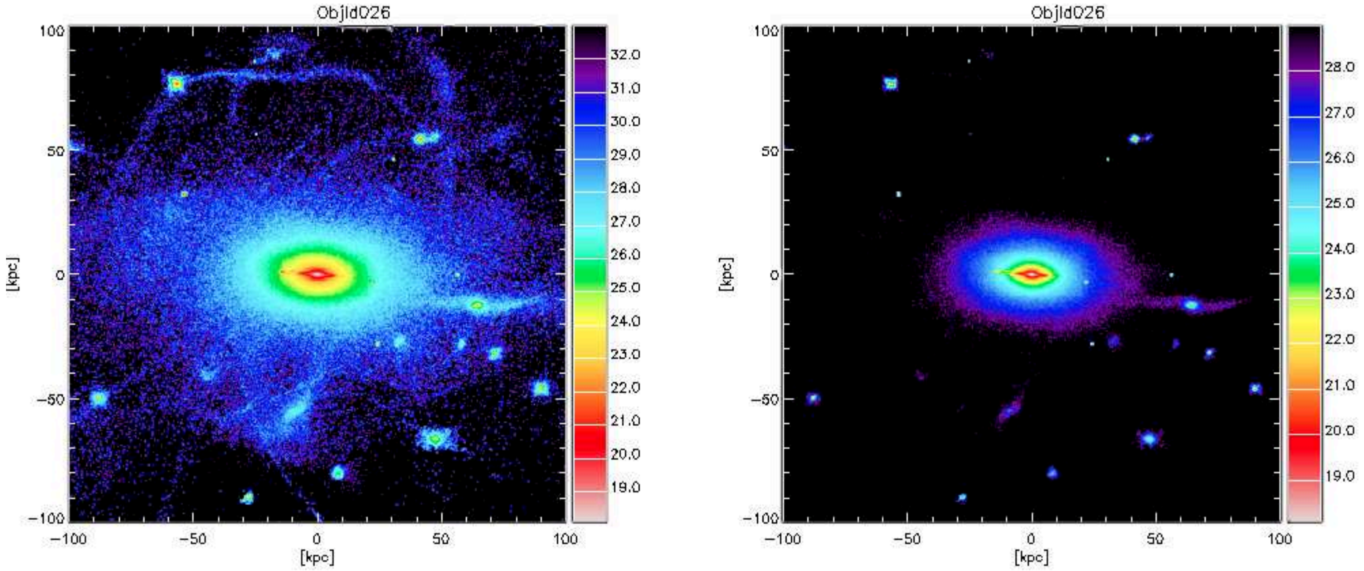

Fig. 11. Example of stellar stream appearance with a cut at 33 mag arcsec^{-2} (*left panel*) and 29 mag arcsec^{-2} (*right panel*).

4.5.1. Tidal tails

with the phrase in bold as this format amounts to the equivalent of bullet points. We do not find any dependence on the projection. We compare the three projections in the corresponding panels of Fig. 7 and we find a similar tendency for the curves across all periods of time. The same number of tidal tails can be detected in any projection of the simulation. We attribute this behavior to the 3D nature of tails when encounters are not coplanar.

4.5.2. Stellar streams

Streams do not exhibit dependence on the orientation. They are visible in all directions. The same number of streams can be detected in any projection. Curves in the three panels of Fig. 8 follow the same trend.

4.5.3. Shells

This class of substructures is highly dependent on the projection effects. The middle panel of Fig. 9 (XZ-projection) demonstrates this result in particular. The incidence of shells is much higher in this projection than in the other two orientations. In Fig. 4 can be appreciated shells in only one orientation. The explanation is that shells are aligned with each other, either along one axis (prolate case) or a common equatorial plane (oblate case) of the central galaxy (Dupraz & Combes 1986).

Table 2. Summary of results: properties of fine structures.

Property	Tidal tails	Shells	Streams
Formation mechanism	−1st and 3rd peak: mass ratio (1:8) −2nd and 4th peak: (1:3, 1:1.55)	−1st peak: ratio (1:8) −2nd peak: ratio (1:1.55)	−1st peak: ratio (1:3) −2nd peak: ratio (1:8)
Visibility	0.7–1 Gyr	3–4 Gyr	1.5–3 Gyr
Surface brightness sensitivity	No	Mild	High
Orientation dependency	No	High	No
Color ($B-V$)	Blue: −2.5 to −1.5	Red: −1.5 to 0	Blue: −3 to −1

5. Discussion

Table 2 summarizes some of our findings and the characteristics of the three classes of fine structures. Colors are not considered in this paper given the difficulty to derive them in real observations, although they are provided in the simulations. With the deeper surface brightness limit, it is possible to detect shells in the most favorable orientation up until 4 Gyr, stellar streams when they are not destroyed by further minor mergers and until 3 Gyr; and tidal tails up until 2 Gyr. Tidal tails are considered the main tracer of major merger but they vanish more quickly. Streams are thinner and more frequent since they are produced in minor mergers, which have a much greater occurrence. Shells are highly dependent on sky orientation and they are the oldest vestiges of intermediate-mass mergers. In addition, their number increases over time, although their surface brightness decreases simultaneously.

It is interesting to compare these results with previous studies. Lotz et al. (2008) and Ji et al. (2014) identify different timescales for different merger stages of their simulated pair encounters. From their series of hydrodynamical simulations of equal-mass gas-rich disc galaxy mergers, Lotz et al. (2008) find characteristic perturbed and asymmetric morphologies during the merging time, but quite relaxed ones afterwards. Their observability timescales for the resulting fine structures are dependent on numerous parameters (viewing angle, orbit geometry, gas fraction, etc.) but are typically found in the same order as the coalescence timescale. The remains of the intense starburst triggered by the major merger is more easy to see than morphological perturbations. Their merger remnants appear disk-like and dusty, while exhibiting a massive bulge. Our simulation is of a different character as it follows a series of minor mergers and gas accretion in a cosmological context that is undergone by a central galaxy which is become an early-type quenched object. The observability timescales are therefore more realistic, taking into account successive mergers which are capable of destroying the vestiges of previous ones.

Ji et al. (2014) also follow a series of mergers, but their study is based on different mass ratios and use hydrodynamical simulations. They consider the survival timescales of the fine structures according to the surface brightness limit and galaxy environment. When isolated, the survival time is, on average, twice the coalescence time for a surface brightness limit of 25 mag arcsec^{-2}, i.e. ~2.5 Gyr. This timescale can be twice as long (~5 Gyr) for a deeper surface brightness limit of 28 mag arcsec^{-2}. Again, our simulation is more realistic since the central galaxy is the result of several satellite mergers during its formation and evolution, with different mass ratios ranging from 25:1 to 1.5:1, making the system more chaotic. For a minor merger of a small mass ratio, the final fine structure timescale can be quite long since the coalescence timescale itself is longer than for a major merger. The occurrence of minor mergers is traced more frequently by stellar streams than by tidal tails (which tend to characterize major mergers).

The advantages of our method, relative to the systematic study of individual mergers, is that we can study the survival time of fine structures based on a complex merging history. The results are then directly comparable to observations because, in addition, we use the same classification method sensitive to LSB features. To counterbalance these advantages, there are obvious limits to our method: we focus on only one merger history, and more computational efforts will be required to obtain a wider set of statistics. Also, it is difficult to follow individual substructures from one snapshot to the other: we only count the total number of features, and there is some degeneracy when one feature is destroyed and another one created, resulting in the same number. To reduce the degeneracy, more frequent snapshots should be documented, which would prove more demanding for the process of visual classification.

We demonstrate how fine structures in the outer parts and stellar halos of galaxies can help to trace back the merger history and the mass assembly of present day galaxies. A study of stellar halos of Milky Way-like galaxies in the nearby universe, compared with Illustris simulations, have shown that the morphology of galaxies are, indeed, closely linked to the significance of their halos (Elias et al. 2018). Galaxies which demonstrate a small stellar halo mass relative to their total mass are disk galaxies which are still forming stars, whereas those with a large fraction of their mass in their halos are quenched. Simulations by Karademir et al. (2019) show that minor mergers enrich the stellar halos of galaxies much more than their centers and that they are able to increase the size of galaxy disks, as has been observed (e.g., Newman et al. 2012).

In recent years, machine learning algorithms have been developed to identify fine structures in galaxy halos, both in observations and simulations (e.g. Walmsley et al. 2019; Hendel et al. 2019). Comparisons to visual classifications provide promising results and these methods will be inevitable for large surveys in the future.

Mantha et al. (2019) propose a tool for identifying tidal debris in CANDELS deep fields and in the VELA simulations as well, which helps to disentangle viewing effects and the subjectivity of visual inspections. Automatic tools like this will help to improve the characterization of the merger rate as a function of redshift.

6. Conclusions

We used a hydrodynamical simulation that has been resimulated within a cosmological context in order to analyze and interpret the morphologies and survival timescales of fine structures, as well as tracers of mergers and of the mass assembly of present day early-type galaxies. We took a census of three types of fine structures based on visual inspection: tidal tails, stellar streams, and shells. The observation of the number of fine structures detected around the central galaxy versus time allows us to reconstruct its merger history. We find three phases in the central galaxy evolution, the second one characterized as a very quiet phase. The census of fine structures are taken in correspondence with the merger events that have been identified. This allows us to establish that:

- Tidal tails result from major mergers events (1.5:1), stellar streams from minor mergers (10:1) and shells from major and intermediate-mass mergers (4:1).
- Tidal tails and shells have long survival times, ~2 Gyr and ~3 Gyr, respectively, but streams remains visible across all phases of galaxy evolution.
- The detection of stellar streams are highly dependent on the surface brightness limit. We see between two and three times more streams with a surface brightness cut of 33 mag arcsec^{-2} than with 29 mag arcsec^{-2}.
- The detection of shells depends considerably on the projection angle and orientation on the sky plane.

Our results are compatible with previous simulations of comparable scope, however, conducting the zoom-in resimulation in a cosmological context introduces more realistic conditions to estimate the survival timescales of fine structures around today's early-type galaxies.

As for the observer's point of view, the reconstruction of the merger history is obtained more optimally with shells, which have longer timescales. The number of shells can also indicate the time that has passed since the last merger. Streams have shorter timescales, so when no fine structure is observed, this means either no event has occurred since 2 Gyr, or it has been limited to a very minor merger with a large angular momentum, which produces more streams than shells.

Acknowledgements. We thank the anonymous referee for their constructive comments, and David Valls-Gabaud for the helpful discussion. B. Mancillas was supported in part by the CONACYT grant, CVU 420397.

References

Adams, S. M., Zaritsky, D., Sand, D. J., et al. 2012, AJ, 144, 128
Amorisco, N. C. 2015, MNRAS, 450, 575
Argudo-Fernandez, M., Shen, S., & Sabater, J. 2016, A&A, 592, A30
Arp, H. 1966, ApJS, 14, 1
Atkinson, A. M., Abraham, R. G., & Ferguson, A. M. N. 2013, ApJ, 765, 28
Bell, E. F., Wolf, C., Meisenheimer, K., et al. 2004, ApJ, 608, 752
Bender, R., Burstein, D., & Faber, S. M. 1992, ApJ, 399, 462
Birdsall, C. K., & Fuss, D. 1969, J. Comput. Phys., 3, 494
Bruzual, G., & Charlot, S. 2003, MNRAS, 344, 1000
Bournaud, F., & Combes, F. 2002, A&A, 392, 83
Bournaud, F., & Combes, F. 2003, A&A, 401, 817
Bournaud, F., Jog, C. J., & Combes, F. 2005, A&A, 437, 69
Bournaud, F., Jog, C. J., & Combes, F. 2007, A&A, 476, 1179
Bullock, J. S., & Johnston, K. V. 2005, ApJ, 635, 931
Cappellari, M., Emsellem, E., Krajnović, D., et al. 2011, MNRAS, 413, 813
Conselice, C. J. 2003, ApJS, 147, 1
Conselice, C. J., Bershady, M. A., & Jangren, A. 2000, ApJ, 529, 886
Cooper, A. P., Cole, S., Frenk, C. S., et al. 2010, MNRAS, 406, 744
Cooper, A. P., D'Souza, R., Kauffmann, G., et al. 2013, MNRAS, 434, 3348
Cooper, A. P., Gao, L., Guo, Q., et al. 2015, MNRAS, 451, 2703

Cox, T. J., Jonsson, P., Primack, J. R., & Somerville, R. S. 2006, MNRAS, 373, 1013
Crnojević, D., Ferguson, A. M. N., Irwin, M. J., et al. 2013, MNRAS, 432, 832
Di Matteo, P., Combes, F., Melchior, A.-L., & Semelin, B. 2007, A&A, 468, 61
Duc, P.-A. 2017, Form. Evol. Galaxy Outskirts, 321, 180
Duc, P.-A., Cuillandre, J.-C., Karabal, E., et al. 2015, MNRAS, 446, 120
Dupraz, C., & Combes, F. 1986, A&A, 166, 53
Eisenstein, D. J., & Hut, P. 1998, ApJ, 498, 137
Elias, L. M., Sales, L. V., Creasey, P., et al. 2018, MNRAS, 479, 4004
Feldmann, R., Mayer, L., & Carollo, C. M. 2008, ApJ, 684, 1062
Ferguson, A. M. N., Irwin, M. J., Ibata, R. A., Lewis, G. F., & Tanvir, N. R. 2002, AJ, 124, 1452
Ferrarese, L., Côté, P., Cuillandre, J.-C., et al. 2012, ApJS, 200, 4
Fioc, M., & Rocca-Volmerange, B. 1999, ArXiv e-prints [arXiv:`astro-ph/9912179`]
Guo, Q., White, S., Boylan-Kolchin, M., et al. 2011, MNRAS, 413, 101
Helmi, A., & White, S. D. M. 1999, MNRAS, 307, 495
Hendel, D., & Johnston, K. V. 2015, MNRAS, 454, 2472
Hendel, D., Johnston, K. V., Patra, R. K., & Sen, B. 2019, MNRAS, 486, 3604
Hilz, M., Naab, T., Ostriker, J. P., et al. 2012, MNRAS, 425, 3119
Hood, C. E., Kannappan, S. J., Stark, D. V., et al. 2018, ApJ, 857, 144
Janowiecki, S., Mihos, J. C., Harding, P., et al. 2010, ApJ, 715, 972
Ji, I., Peirani, S., & Yi, S. K. 2014, A&A, 566, A97
Jedrzejewski, R. I. 1987, MNRAS, 226, 747
Johnston, K. V., Majewski, S. R., Siegel, M. H., Reid, I. N., & Kunkel, W. E. 1999, AJ, 118, 1719
Johnston, K. V., Bullock, J. S., Sharma, S., et al. 2008, ApJ, 689, 936
Kado-Fong, E., Greene, J. E., Hendel, D., et al. 2018, ApJ, 866, 103
Karademir, G. S., Remus, R.-S., Burkert, A., et al. 2019, MNRAS, 487, 318
Kaviraj, S., Peirani, S., Khochfar, S., Silk, J., & Kay, S. 2009, MNRAS, 394, 1713
Kennicutt, Jr., R. C. 1998, ApJ, 498, 541
Krajnović, D., Emsellem, E., Cappellari, M., et al. 2011, MNRAS, 414, 2923
Levinson, F. H., & Roberts, Jr., W. W. 1981, ApJ, 245, 465
Lotz, J. M., Jonsson, P., Cox, T. J., & Primack, J. R. 2008, MNRAS, 391, 1137
Majewski, S. R., Skrutskie, M. F., Weinberg, M. D., & Ostheimer, J. C. 2003, ApJ, 599, 1082
Malin, D. F. 1977, AAS Photo Bull., 16, 10
Malin, D. F. 1978, Nature, 276, 591
Malin, D. F., & Carter, D. 1983, ApJ, 274, 534
Mantha, K. B., McIntosh, D. H., Ciaschi, C. P., et al. 2019, MNRAS, 486, 2643
Martig, M., Bournaud, F., Teyssier, R., & Dekel, A. 2009, ApJ, 707, 250
Martig, M., Bournaud, F., Croton, D. J., Dekel, A., & Teyssier, R. 2012, ApJ, 756, 26
Martínez-Delgado, D., Pohlen, M., Gabany, R. J., et al. 2009, ApJ, 692, 955
Martínez-Delgado, D., Gabany, R. J., Crawford, K., et al. 2010, AJ, 140, 962
McConnachie, A. W., Irwin, M. J., Ibata, R. A., et al. 2009, Nature, 461, 66
Michel-Dansac, L., & Wozniak, H. 2004, A&A, 421, 863
Mihos, J. C., Harding, P., Feldmeier, J., & Morrison, H. 2005, ApJ, 631, L41
Miskolczi, A., Bomans, D. J., & Dettmar, R.-J. 2011, A&A, 536, A66
Naab, T., Johansson, P. H., Ostriker, J. P., & Efstathiou, G. 2007, ApJ, 658, 710
Newman, A. B., Ellis, R. S., Bundy, K., & Treu, T. 2012, ApJ, 746, 162
Pawlik, M. M., Wild, V., & Walcher, C. J. 2016, MNRAS, 456, 3032
Peirani, S., Crockett, R. M., Geen, S., et al. 2010, MNRAS, 405, 2327
Peng, C. Y., Ho, L. C., Impey, C. D., & Rix, H.-W. 2002, AJ, 124, 266
Pop, A.-R., Pillepich, A., Amorisco, N. C., & Hernquist, L. 2018, MNRAS, 480, 1715
Quinn, P. J. 1984, ApJ, 279, 596
Rodriguez-Gomez, V., Pillepich, A., Sales, L. V., et al. 2016, MNRAS, 458, 2371
Salpeter, E. E. 1955, ApJ, 121, 161
Schweizer, F. 1983, Int. Kinematics Dyn. Galaxies, 100, 319
Schweizer, F., & Ford, Jr., W. K. 1985, New Aspects of Galaxy Photometry, 232, 145
Stewart, K. R., Bullock, J. S., Wechsler, R. H., Maller, A. H., & Zentner, A. R. 2008, ApJ, 683, 597
Tal, T., & van Dokkum, P. G. 2011, ApJ, 731, 89
Tal, T., van Dokkum, P. G., Nelan, J., & Bezanson, R. 2009, AJ, 138, 1417
Teyssier, R. 2002, A&A, 385, 337
Toomre, A. 1977, Evolution of Galaxies and Stellar Populations (New Haven: Yale University Observatory), 401
Toomre, A., & Toomre, J. 1972, ApJ, 178, 623
Valls-Gabaud, D., & MESSIER Collaboration 2017, Form. Evol. Galaxy Outskirts, 321, 199
van Dokkum, P. G. 2005, AJ, 130, 2647
van Dokkum, P. G., Abraham, R., & Merritt, A. 2014, ApJ, 782, L24
Walmsley, M., Ferguson, A. M. N., Mann, R. G., et al. 2019, MNRAS, 483, 2968
Wen, Z. Z., & Zheng, X. Z. 2016, ApJ, 832, 90
White, S. D. M., & Rees, M. J. 1978, MNRAS, 183, 341
York, D. G., Adelman, J., Anderson, Jr., J. E., et al. 2000, AJ, 120, 1579

Appendix A: Snapshot evolution

In the following three figures (Figs. A.1–A.3), we present the whole ensemble of snapshots of the zoom-in simulation of the three projections.

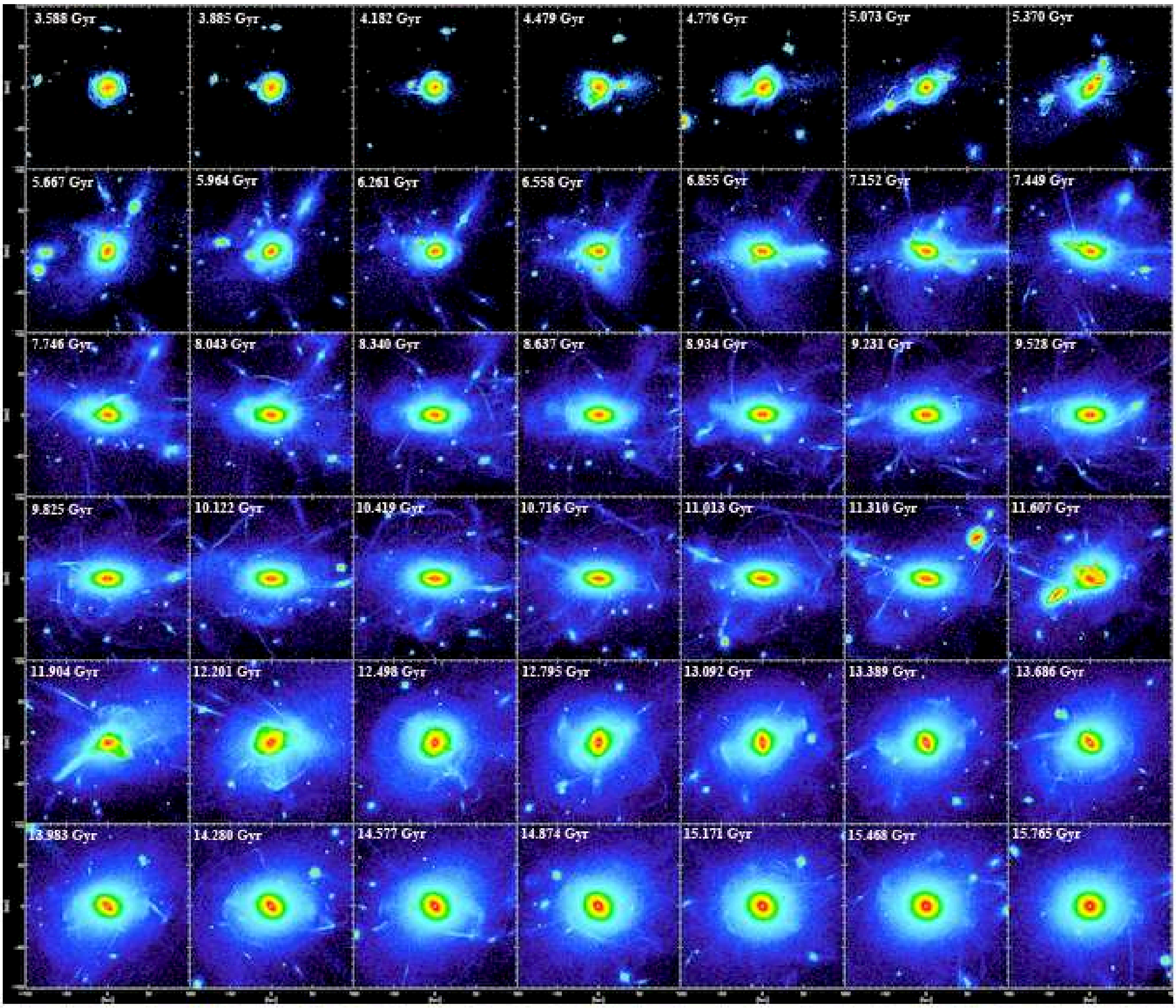

Fig. A.1. Snapshot evolution in XY-projection.

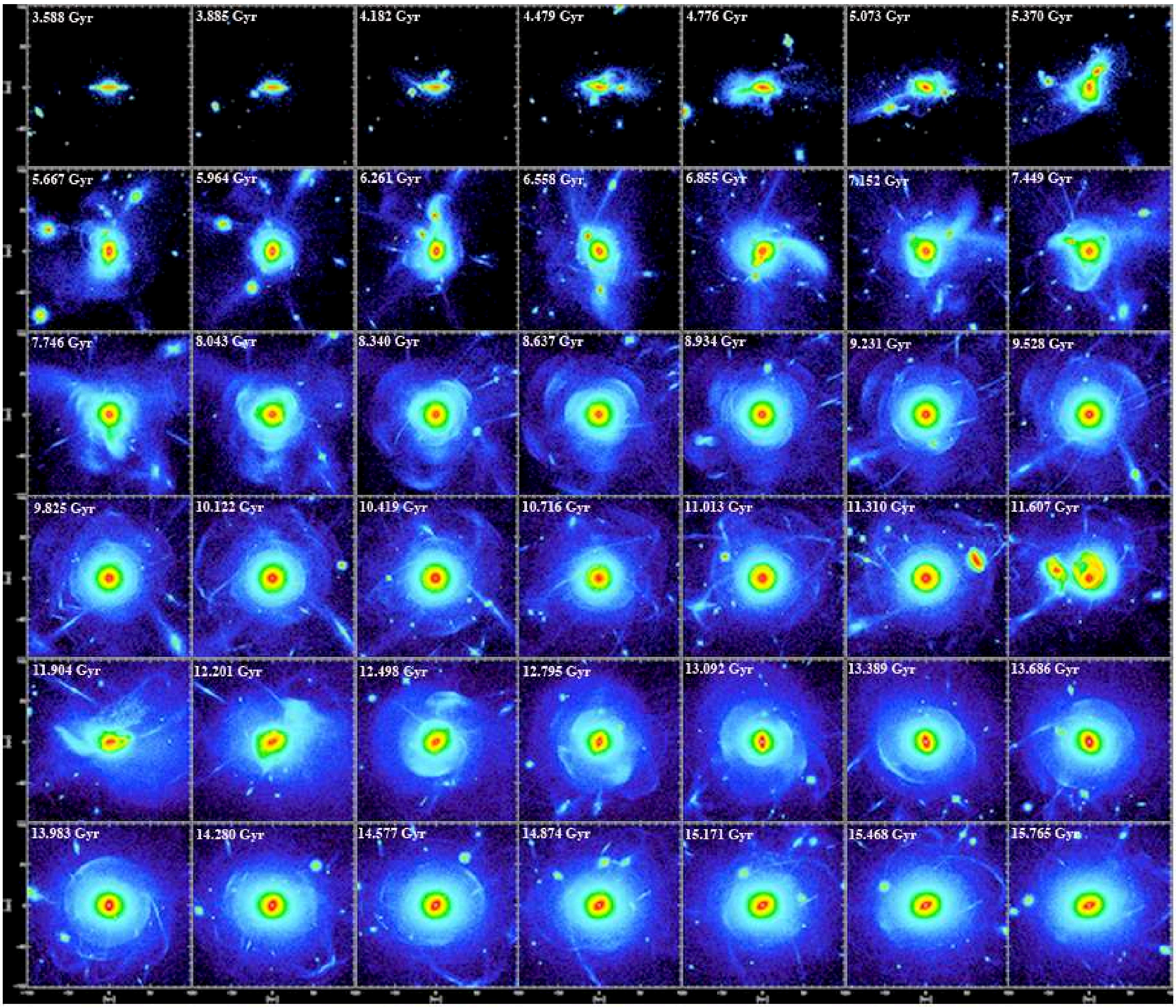

Fig. A.2. Snapshot evolution in YZ-projection.

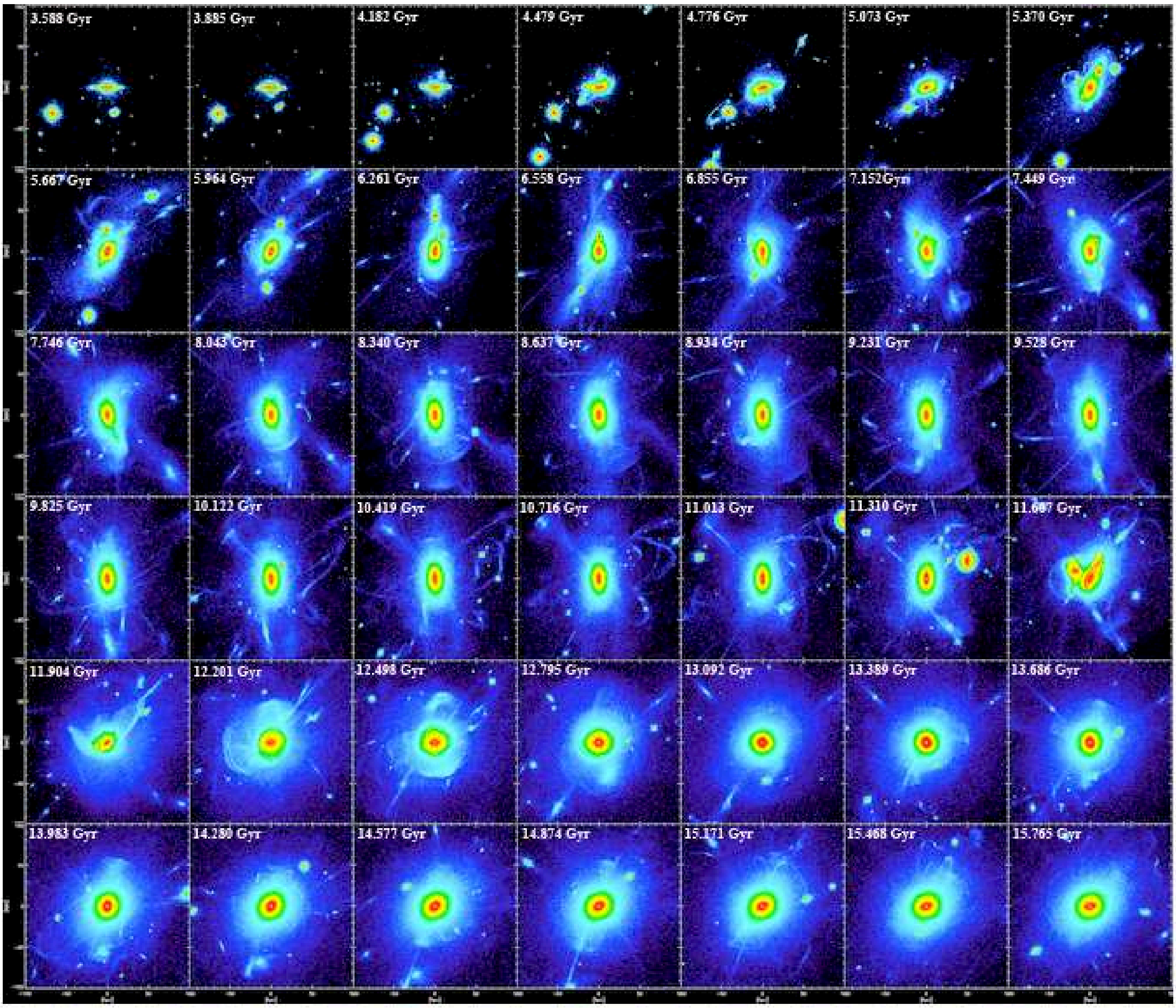

Fig. A.3. Snapshot evolution in the XZ-projection.

Chapter 4

The molecular gas content of shell galaxies

This Chapter is dedicated to the study on the detection and distribution of gas content in shell galaxies. I describe each selected target, the details of CO observations, the specific regions in each galaxy where we searched for the ^{12}CO molecule and the implications of the results found. Some of the specific objectives are, for example: to test the shell formation mechanism through phase wrapping during a radial minor mergers previously proposed in the numerical simulation models, as well as to examine the expected association between the stellar and gaseous (HI or CO) shells, and thus discuss possible scenarios also taking into account the predictions from N-body numerical simulations.

4.1 Overview

4.1.1 First shell galaxy detection: Examples

Shell galaxies are elliptical or S0 galaxies which exhibit low surface brightness circular shapes and shape-edged inner structures in their external regions. The discovery of these concentric arc-like shape structures, also known as ripples, was done in the 1960's. First images of shells galaxies were reported by Halton Arp in 1966 in the *"Atlas of peculiar galaxies (Arp)"* composed by 338 objects (Arp, 1966). One of the particular examples displaying inner and outer shell structures distributed in only one direction is Arp 230 (see Figure 4.1.1). Currently, the main shell galaxy catalog is *"A catalog of elliptical galaxies with shells"* by (Malin and Carter, 1983) which contains 137 galaxies from the southern hemisphere (declination south -17°) displaying shell structures at large distances from the central galaxy. With a naked eye, they identified faint structures of $\mu \sim 26.5$ mag arcsec^{-2}. A prominent and famous example is NGC 3923. This is a normal elliptical galaxy which exhibit $\sim$ 25 remarkable shell-like structures aligned perpendicular to the major axis of the galaxy and extended up to 200 kpc from the center.

4.1.2 Incidence of shell galaxies

The abundance of shell galaxies represent the 10 % of E and E/S0, 6 % of S0 and only $\sim$ 1 % of spiral galaxies (Schweizer and Seitzer, 1988). In the pioneering work of (Malin and Carter, 1983), who present a catalog of shell galaxies, it was found that 47.5 % are isolated galaxies, 30.9 % belongs to a group, 3.6 % are in a cluster or rich groups and 18 % are shell galaxies from groups of two or five galaxies. These percentages indicate that shell galaxies do not form in high galaxy density regions. This result can be attributed to the low velocity of tidal effects of neighboring galaxies which disrupt the shell structures or the collision between two encounters

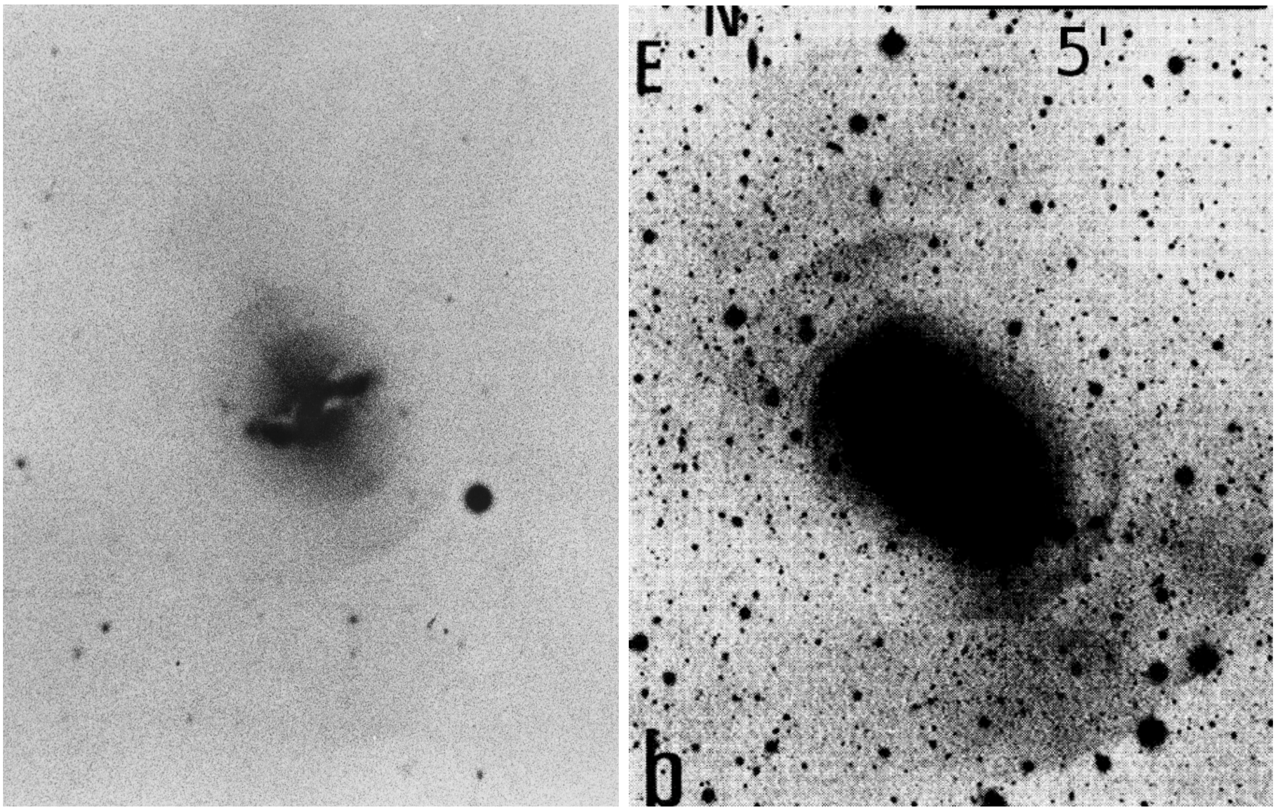

Figure 4.1: *Left*: The overprocessed negative detail image of Arp 230 Arp (1966) *Right*: NGC 3923 from Malin and Carter (1983).

that produce the shell formation. Besides, in the clusters, where the environment has a high galaxy density, there are regions with high relative velocity.

On the other hand, in the survey of 36 southern field giant ellipticals of Schweizer and Ford (1985), it was reported that 44 % were galaxies which exhibit shells (e.g. NGC 1316, NGC 5128, NGC 5018). Afterwards, Schweizer and Seitzer (1988) presented a study of a larger sample composed of 145 galaxies (110 galaxies outside of Virgo Cluster and 35 Virgo galaxy cluster members). In this work, they showed that shells are also present in northern spiral galaxies with Hubble types S0, S0/Sa and Sa (e.g., NGC 3032, NGC 4382, NGC 5739, NGC 7600).

More than 20 years later, Tal et al. (2009) estimated that 22 % of their sample of 55 nearby luminous elliptical galaxies were shell galaxies, which made them the most common collisional debris present in their whole sample. In the work from Krajnović et al. (2011) aimed to study several properties, among them to characterize quantitatively the morphological and kinematic features and determine their frequency, it was reported that 3.5 % of their ATLAS^{3D} sample of 260 early-type galaxies were shell galaxies. In the same year Ramos Almeida et al. (2011) presented a study based in a sample of 46 southern 2 Jy radio galaxies in order to investigate the role of galaxy interactions in the triggering of powerful radio galaxies (PRGs). In that study, they found that the most common signature of morphological disruption in the PRGs was shell features with a percentage of 35 % of the total sample.

In another work based in a sample of 65 early-type galaxies from *Spitzer* Survey of Stellar Structure in Galaxies (S^{4}G), Kim et al. (2012) identified vestiges of tidal interactions in the GALFIT residual images of 11 galaxies, such as shells and tidal tails. From these galaxies, 4 exhibit shell features (NGC 474, NGC 2634, NGC 3032, NGC 5018). In addition, Atkinson et al. (2013), examined a large sample of 1781 luminous galaxies from the wide-field component of the Canada-France-Hawaii Telescope Legacy Survey, aimed to identify faint tidal features. In their study, they found that the occurrence of shells are larger in red early-type galaxies (14 %) than in blue late-type galaxies (6 %). In the pilot survey of eight isolated spiral galaxies of Martínez-Delgado et al. (2010) addressed to study interaction signatures, was identified shell-like structures or *umbrella-shaped tidal debris structure* in three of their galaxies, i.e., NGC 4652, NGC 7531 and NGC 3521. Similarly, de Blok et al. (2014) observed a shell-like structure in the galaxy NGC 4414, indicating that the galaxy was undergoing a minor interaction. According to the asymmetry between the sharp edge of the shell towards the west and the much more diffuse distribution in the other directions suggest that this galaxy suffered an interaction that was not entirely radial.

In the most recent studies, Duc (2017) presented a sample of massive early-type galaxies from MATLAS deep imaging survey taken with CFHT/MegaCam, finding that ∼ 16 % of its galaxies displayed streams and shell-like features. Similarly, Hood et al. (2018) reported ∼ 26 % “broad” shell-like features in the gas-poor tidal features of their sample of 1048 galaxies from the REsolved Spectroscopy Of a Local VolumE (RESOLVE) survey. Finally, Kado-Fong et al. (2018), identified 18 % shell galaxies from the subsample of 1201 galaxies of the SDSS spectroscopy images, taken from the Hyper Suprime-Cam Sabaru Strategic Program (HSC-SSP).

4.1.3 Shell galaxy properties

Different properties of shell structures detected around galaxies, such as geometrical and environmental, provide clues to constrain the models of shell formation. Several works have been focus to study these galaxy properties (Quinn, 1984; Dupraz and Combes, 1986). In their studies, they have analyzed several shell galaxies observed with high-contrast prints and unsharp masked photographs. The following summary of shell galaxy properties was presented in their analysis:

- Shell structures were detected in both normal ellipticals (e.g., NGC 3923, left panel of Figure 4.1.1) and special ellipticals (e.g., Centaurus A (NGC 5128)). In the sample of Schweizer and Ford (1985) half dozen lenticular galaxies display shells. Shells are also detected in S0 galaxies and they seem to be present in field galaxies, i.e., in environments of low galaxy density.

- The angular distribution of shells is highly related to the eccentricity of the host galaxy. Shell structures are randomly spread around the galactic center when the elliptical is nearly E0 (NGC 474, NGC and UKS 0422-476). On the opposite side, shells tend to be aligned to its major axis and distributed in an interleaved way in radius of both sides of the center when the elliptical is a more flattened system (>E6) (Arp 230, NGC 3923, NGC 1344 and NGC 5018).

- Shells present a three-dimensional structure. They do not complete an entire circle, instead they appear as concentric semi-circles around galaxies with higher ellipticity and they tend to be aligned with their major axis of the host galaxy. Usually their ellipticity is low, but it is directly correlated with the eccentricity of the elliptical galaxy.

- Shells are numerous and appear over a large range of radius. The distance between two successive shells increases with their distance to the center of the galaxy. In general, they are accommodated in an interleaved way with the radius, i.e., the next outermost shell is on the opposite side of the nucleus.

A recent work in (Bílek et al., 2016) have obtained the deepest image so far of NGC 3923 with the Mega Cam Camera at the Canada-France-Hawaii Telescope in the g'-band and reanalyzed an archival HST image of the galaxy. The image reached a surface brightness limit of 29 mag arcsec^{-2}. For this galaxy, they detected up to 42 shells! The highest number of shells detected in a galaxy so far (see Figure 4.2). They discovered a probable progenitor and concluded that the shell system was likely originated from two or more progenitors.

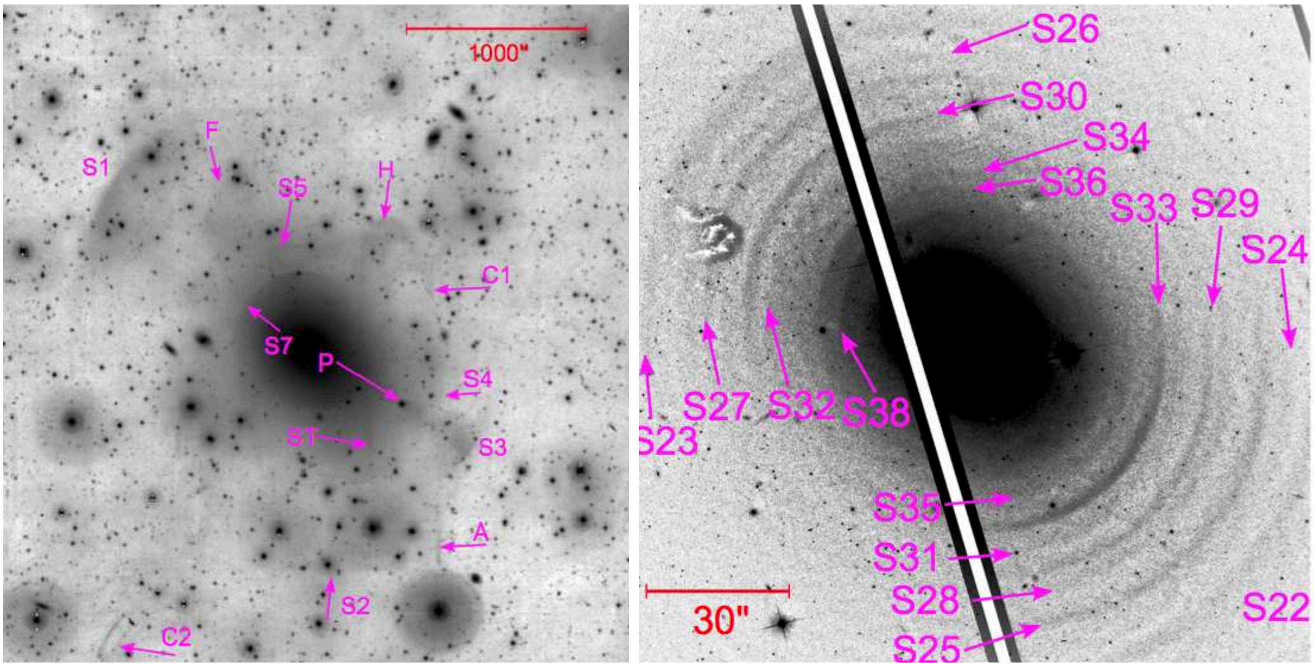

Figure 4.2: Images of the individual features found in MegaCam image (Bílek et al., 2016) and in the archival HST image (Sikkema et al., 2006), showing filamentary structure. North is to the top and east is to the left. The abbreviations indicate the following: S_n - shells, F - other tidal features, C_n - probable galactic cirri, H - a hook-like structure.

4.2 History of the theories of shell galaxy formation

After the publication of the largest catalog of shell galaxies by Malin and Carter (1983), a huge interest to obtain deep images to disentangle the physical process behind these new types of galaxies arose from the scientific community. Several works were focused also into proposing and describing different scenarios for the mechanism of shell formation. By that time, it was thought that shells detection around galaxies was the outcome of internal mechanisms such as ejection, explosions, or magnetic forces (see e.g. Athanassoula and Bosma, 1985). Nonetheless, the tests with dynamical and numerical models of galaxy interactions favored the merging processes itself as the most acceptable explanation to describe collisional debris (Toomre and Toomre, 1972).

One of the first models to explain the phenomenon of shell formation, was presented by Fabian et al. (1980). In this theory, it was suggested that the shells are regions of star formation in a shocked galactic wind in elliptical galaxies, which are preceded by a subsequent star formation under a specific conditions. However, observations did not support this hypothesis (Carter et al., 1982).

Williams and Christiansen (1985) proposed that visible stellar shells at larger distances from the center of isolated elliptical galaxies were generated for a blast wave expelled during an active nucleus phase in the early stages of the galaxy, sweeping the interstellar medium out of the galaxy into an expanding gaseous shell which radiatively cools behind its leading shock front. If the nuclear activity stops, then a shell can cool enough to allow a brief episode of star formation that ends when the shell is heated by a supernova. Thus, this model were based on the fact that these stars would spend most of their time near to the apogalacticum of their radial bound orbits, producing the appearance of shells. Nonetheless, since shells are remarkable sharp features, such scenario would imply that stars could continue moving in phase after 20 or more crossing times, which is a very large amount!.

On the other hand, in the simulations of Quinn (1984) it was shown that shell formation in normal ellipticals were produced by a disruption of a small companion (disk) induced by a big elliptical galaxy of 10 to 100 times more massive than the companion. In (Quinn, 1984) and (Dupraz and Combes, 1986) was supported the merging model to describe the phenomenon of shell formation. In their N-body simulations small disks are modeled as a self-consistently system, where shells are considered as a test particle phenomenon.

Quinn (1984) and Dupraz and Combes (1986) tested the Schweizer's model (Schweizer, 1980), where is assumed that shells are the result of mergers or accretions involving disk systems. The simple N-body models developed by Quinn (1984) turned out to be consistent with structures formed as a result of collision between a elliptical and a disk galaxy. Concretely, it was shown that shells arise from a phase wrapping of the dynamical cold disk in the fixed potential well of the elliptical galaxy. The test particle dynamics of the shells, as well as the large range in radius that they cover, allowed them to develop an impression of the detailed shape of potential wells in elliptical galaxies. In addition, since shells display a lower surface brightness in comparison with the central elliptical galaxy, this would imply that the total mass of shells is small compared to the elliptical mass. Therefore, Quinn (1984) assumed that self-gravity was not important for the generation of shells and thus the elliptical galaxy can be modeled as a rigid potential well. In their study, limited to a reduced number of particles and the variation of the merger mass ratio, they found that the occurrence of shells was related to the coldness or the lack of random motions in the ripped system and the rigidity and smoothness of the potential field in the target galaxy.

4.3 Current mechanisms of shell formation

A convincing theory has been developed to account for the formation of shells around early-type galaxies (Quinn, 1984; Dupraz and Combes, 1986, 1987; Hernquist and Quinn, 1989). According to the N-body simulations, the mechanism of shell formation depends on whether the *angular momentum of the encounters is high or low.* This physical condition gives place to a phase-wrapping or a space-wrapping phenomena.

4.3.1 Phase-wrapping scenario

Low-angular momentum encounters result in a phase wrapping of a companion falling on a radial or nearly radial orbit into the fixed potential well of an elliptical galaxy. Stars are modeled as collisionless particles, which were originally bound to the merging galaxies. The stars of the companion are liberated by tidal forces and start to oscillate in the potential of the primary galaxy. In each turning point, the stars have the minimum velocity and are accumulated.

These periodic oscillations of stars behave like an outward-propagating wave forming arc-like structures in their apocenters.

Quinn (1984) described the shell formation on a one-dimensional example by using test particles and a rigid potential well. Figure 4.3, describes the phase evolution of the system. The maximum spatial trajectory of each space wrap corresponds to a sharply defined density maxima. The density maxima occurs near the apocenters of the particle orbits. Initially, the maximal radial position of the orbit is reached by the most tightly bound particles. But as the velocity of the most distant particles becomes zero in each turning point, the particles return back and the density wave propagates slowly in radius to the outermost turning point established by the least bound particles. These particles in phase space form the shell-like structures.

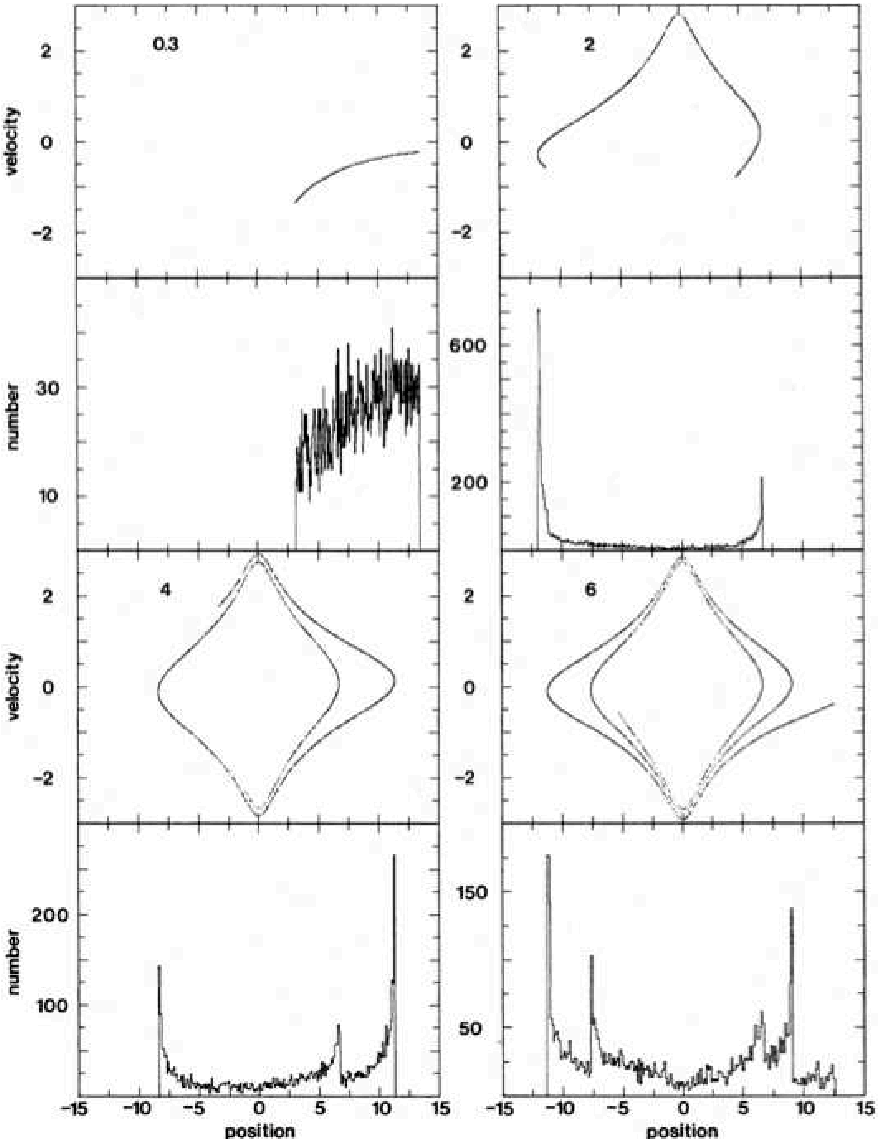

Figure 4.3: The phase space and configuration space, time evolution of 5000 test particles falling from rest into an isochrone potential. The number in the top left of each phase plane plot are the time passed in units of the radial period of the most tightly bound particle. The configuration space distribution of the particles at each time is shown directly below the corresponding phase plot. Positions are in units of the isochrone scale length, and velocities are in units of $(GM/10a)^{1/2}$, where M is de total mass and a the scale length. By Quinn (1984).

The shell spacings should decrease with decreasing radius, as confirmed by observations, and their number should increase with time. This phenomenon is also predicted to occur in the last phase of any merging between two *spiral* galaxies. The end-product appears to be an elliptical with a de Vaucouleurs law as light profile (e.g., Schweizer, 1990). The late infall of tidal tails and debris, predominantly consisting of stars, initiates the phase-wrapping and subsequent shell formation. Most spiral merger remnants, such as the prototypical NGC 7252, indeed appear to possess shells (Schweizer, 1990).

The morphology of shells may help to reveal the 3D-structure of the galaxy potential. Numerical simulations in (Dupraz and Combes, 1986) make predictions on the geometry of shell systems. Radial oscillations in a prolate potential, result in an alternate arrangement of shells, i.e., shells align along the major axis and are interleaved in radius. In the case of less radial oscillations with angular momentum, shells form randomly around the equatorial plane of an oblate potential and keep some rotational velocity in the edges (see Figure 4.4).

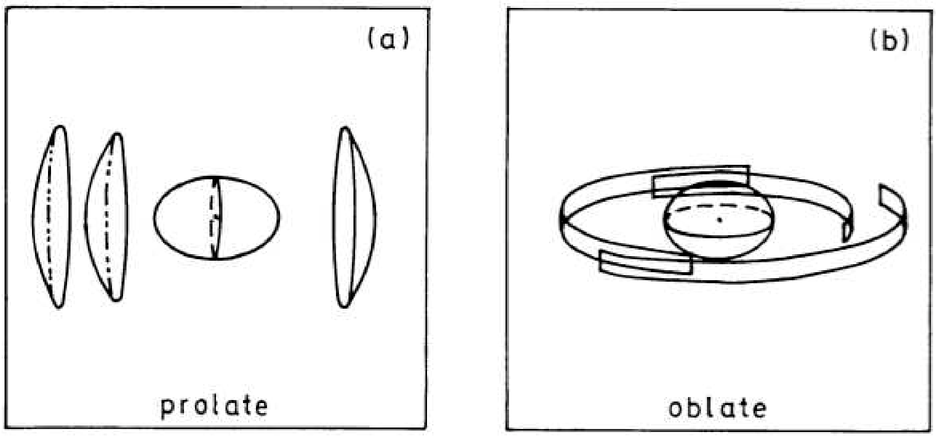

Figure 4.4: The sketches of the geometry in space of the shell system surrounding: (a) a prolate elliptical galaxy, and (b) an oblate elliptical galaxy. By Dupraz and Combes (1986).

4.3.2 Space-wrapping scenario

High orbital momentum encounters where the center of mass motion of an infalling companion is non-radial, results in a spatial wrapping of this companion which produces encircling crossing structures different to the shells observed. The fact that we do not observe them is due to the low frequency of these encounters.

4.4 Atomic and molecular gas in shell galaxies

This space-wrapping scenario was invoked when neutral hydrogen was observed in systems containing shells. Schiminovich et al. (1994) and Schiminovich et al. (1995) have detected diffuse HI gas associated with the stellar shells (Centaurus A and NGC 2865). These observations were a priori surprising in the phase-wrapped scenario, since we believe that the diffuse gaseous and stellar components do not have the same behavior when approaching to the center of the potential well in quasi-radial orbits (Weil and Hernquist, 1993). The gas was expected to infall into the center without being able to oscillate back. However, part of the gas could be structured in clouds and less dissipative, and also the orbits might be less radial. Simulating a minor merger with clumpy gas, Combes et al. (2000) have shown that indeed, a large fraction of the gas may have followed the stars in phase-wrapped shells. Since the gas in the outer parts of the merging companion is less bound than the stars, it is liberated first and less slowed down by dynamical friction: gaseous shells have a slightly larger radius than the stellar ones. In Centaurus A, the HI is associated with the outermost faint stellar shells (see Figure 4.5). It is displaced to the outside of the optical shells and has a high rotation velocity, suggesting that only a companion with a more circular orbit is able to produce this HI ring (Schiminovich et al., 1994). Other cases of HI shells displaced with respect to the stellar shells have been reported (Schiminovich et al., 1997; van Gorkom, 2000).

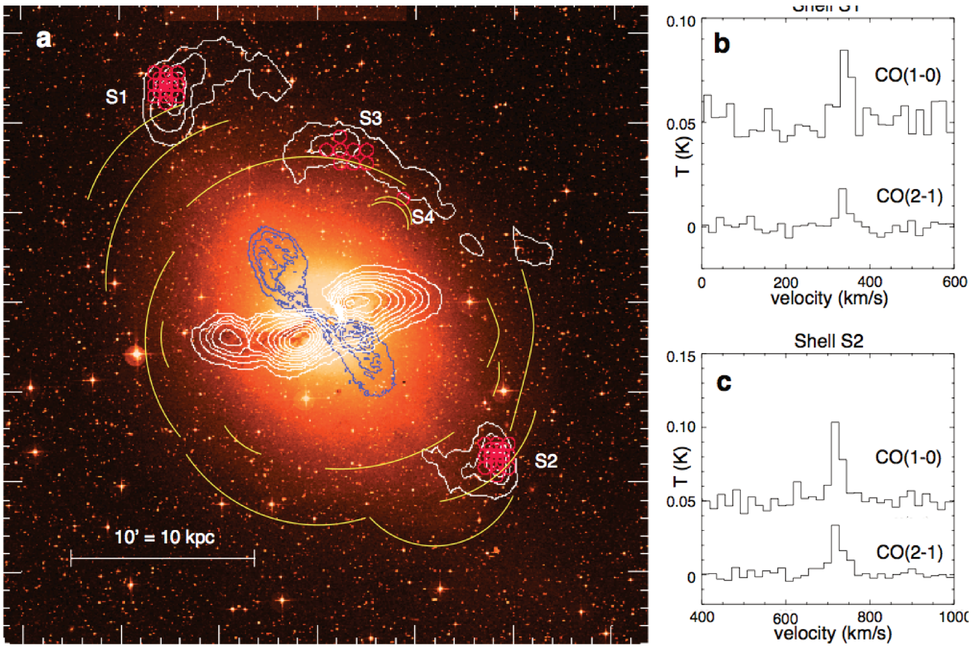

Figure 4.5: **a**) A Digitized Sky Survey optical image of CenA with the contours of HI gas (from (Schiminovich et al., 1994)) superimposed in white. The HI contour levels are 1, 4, 7, 10, 15, 30, 35, 40 × 10^{20} cm^{-2}. North is up and east is to the left, while the image scale is shown by the horizontal bar. The positions observed in CO are marked with the red circles whose size corresponds to the SEST 44 beam of CO(1-0). The type of each map (half-beam spacing or simple pointing) is evident by the placement of the circles. The locations of the outer stellar shells are underlined by the yellow solid lines (see also Fig. 1a of (Schiminovich et al., 1994)). The inner 6cm radio continuum lobes (from Clarke et al., 1992) are depicted by the blue contours (contour levels 0.01, 0.05, 0.1 Jy/beam). Note the jet alignment with the location of the CO detections. The outer radio lobes are far more extended. **b**) CO(1-0) and CO(2-1) spectra towards the northern shell S1 with the temperature scale in main beam T_{mb} , smoothed to 18 km s^{-1}. **c**) Same as in b) but for the southern shell S2.

4.5 Conclusions and perspectives

In this study, it was obtained several results. In first instance, molecular gas was detected in six of the nine observed shell galaxies, together with two of the companions. In Arp 10, NGC 3656 and NGC 3934 molecular gas was detected in their shells with a molecular masses estimated between 10^8 and 10^9 $M_\odot$. Secondly, for the cases of Arp 10 and NGC 3656 the formation mechanism for their shells was through a phase-wrapping in a nearly radial orbit.

The spectra detected in these galaxies displayed a double-horn shape, indicating two different angular momenta, and some rotation added to the radial motions of the gas in shells. As a future work, we will perform observations in NOEMA telescope to map CO emission in the shells of Arp 10, NGC 3656 and NGC 3934. The aim is (1) *to determine a possible radial shift between the gas and stellar shell*, if made through phase-wrap, as predicted by the theory (Combes and Charmandaris, 2000); (2) *to determine exactly the kinematics of the shell*, since the spatial resolution will split the emission according to the velocity gradient expected (while we only see the integrated spectrum with the single dish).

4.6 Paper: The molecular gas content of shell galaxies

A&A 630, A112 (2019)
https://doi.org/10.1051/0004-6361/201935968

A&A 630, A112 (2019)
https://doi.org/10.1051/0004-6361/201935968

Astronomy & Astrophysics

Molecular gas content of shell galaxies★

B. Mancillas[1], F. Combes[1,2], and P.-A. Duc[3]

[1] Observatoire de Paris, LERMA, PSL University, CNRS, Sorbonne University, UPMC, Paris, France
e-mail: `brisa.mancillas@obspm.fr`
[2] Collège de France, 11 place Marcelin Berthelot, 75005 Paris, France
[3] Université de Strasbourg, CNRS, Observatoire de Strasbourg, 67000 Strasbourg, France

Received 27 May 2019 / Accepted 22 August 2019

ABSTRACT

Shells are fine stellar structures that are identified by their arc-like shapes around a galaxy. They are currently thought to be vestiges of galaxy interactions and/or mergers. The study of their number, geometry, stellar populations, and gas content can help us to derive the interaction or merger history of a galaxy. Numerical simulations have proposed a mechanism of shell formation through phase wrapping during a radial minor merger. Alternatively, there could be merely a space wrapping, when particles have not yet radially oscillated, but are bound by their radial expansion, or produce an edge-brightened feature. These can be distinguished because they are expected to keep a high radial velocity. While shells are first a stellar phenomenon, HI and CO observations have revealed neutral gas associated with shells. Some of the gas, the most diffuse and dissipative, is expected to be quickly driven to the center if it is traveling on nearly radial orbits. Molecular gas, which is distributed in dense clumps, is less dissipative, and may be associated with shells. It can then determine the shell velocity, which is too difficult to obtain from stars. We present here a search for molecular gas in nine shell galaxies with the IRAM-30 m telescope. Six of them are detected in their galaxy center, and in three galaxies, we clearly detect molecular gas in shells. The derived amount of molecular gas varies from 1.5×10^8 to 3.4×10^9 $M_\odot$ in the shells. For two of them (Arp 10 and NGC 3656), the shells are characteristic of an oblate system. Their velocity is nearly systemic, and we conclude that these shells are phase wrapped. In the third galaxy (NGC 3934), the shells appear to participate in the rotation. Follow-up with higher spatial resolution is required to conclude.

Key words. galaxies: interactions – galaxies: ISM – galaxies: kinematics and dynamics – galaxies: peculiar – galaxies: structure

1. Introduction

It is well accepted that galaxy interactions frequently lead to merging, and that it must have played a fundamental role in the formation and evolution of galaxies (Toomre & Toomre 1972). Most of our understanding of galaxy interactions has been obtained through numerical simulations (see for a review Barnes & Hernquist 1992). Among the best vestiges of galaxy interactions are shells and ripples (Schweizer & Seitzer 1992), which are often present around merger remnants. Shells, which are composed of stars, were originally observed around elliptical and S0 galaxies, which are poor-gas systems (Carter et al. 1982). A convincing theory has been developed to account for the formation of shells around early-type galaxies as a phase-wrapping phenomenon (Quinn 1984; Dupraz & Combes 1986, 1987; Hernquist & Quinn 1989). According to the theory, the stars modeled as collisionless particles, which were originally bound to the merging companions, are liberated and oscillate with different periods of oscillation around the primary galaxy. They accumulate near the apocenters of their orbits to form shell-like features. This phenomenon is also predicted to occur in the last phase of any merging between two spiral galaxies. The end-product appears to be an elliptical, with a de Vaucouleurs law as light profile (e.g., Schweizer 1990). The late infall of tidal tails and debris, predominantly consisting of stars, initiates the phase wrapping and subsequent shell formation. Most spiral merger remnants, such as the prototypical NGC 7252, appear indeed to possess shells (Schweizer 1990).

The morphology of shells may help to reveal the 3D structure of the galaxy potential: if the galaxy is prolate, shells align along the major axis and are interleaved in radius, while the shells are found randomly in azimuth near the equatorial plane of an oblate galaxy (Dupraz & Combes 1986). All these are phase-wrapped shells, where stars are accumulating at the apocenter of their oscillations. However, as Hernquist & Quinn (1988) have pointed out, there could also be some features such as tails or streams, edge-brightened or only space-bounded, that do not fall under phase wrapping, but only under space wrapping.

This space-wrapping scenario was invoked when neutral hydrogen was observed in systems containing shells. Schiminovich et al. (1994, 1995) have detected diffuse HI gas associated with the stellar shells (Centaurus A and NGC 2865). These observations were a priori surprising in the phase-wrapped scenario because we believe that the diffuse gaseous and stellar components do not have the same behavior when they approach the center of the potential well in quasi-radial orbits (Weil & Hernquist 1993). The gas was expected to infall to the center, without being able to oscillate back. However, part of the gas could be structured in clouds and be less dissipative, and the orbits might also be less radial. Simulating a minor merger with clumpy gas, Combes & Charmandaris (2000) have shown that indeed, a large fraction of the gas could follow the stars in phase-wrapped shells. Because the gas in the outer parts of the merging companion is less strongly bound than the stars, it is liberated first and is less slowed down by dynamical friction: gaseous

---

★ Based on observations carried out with the 30 m telescope of Institute of RAdioastronomy in Millimeter (IRAM).

shells have a slightly larger radius than stellar shells. In Centaurus A, the HI is associated with the outermost faint stellar shells. It is displaced to the outside of the optical shells, and has a high rotation velocity, suggesting that only a companion with a more circular orbit is able to produce this HI ring (Schiminovich et al. 1994). Other cases of HI shells displaced with respect to the stellar shells have been reported (Schiminovich et al. 1997; van Gorkom 2000).

Detecting gas in shells is useful to be able to determine their velocity. Obtaining a stellar velocity is costly and requires the use of spectrographs with IFU capabilities on large telescopes. The HI maps suffer from low spatial resolution, therefore molecular gas might be one of the best ways to determine shell kinematics. The latter is important to try distinguishing between the different scenarios: in the phase-wrapping model, stars have zero radial velocity in the shells, which correspond to their apocenter. Velocities might be much higher in the space-wrapping model. In order to obtain more insight into the process of gaseous shell formation and into the behavior of gas in shell galaxies in general, we performed observations of CO(1–0) and CO(2–1) emission lines in the shell regions of eight early-type galaxies, two of them taken from the CO survey of ATLAS^{3D} sample (Young et al. 2011), and in five of them,H_2 gas is detected in their center. In all cases, we re-observed the center positions to obtain a better signal-to-noise ratio (S/N). We detected CO emission associated with shells in three galaxies and detected molecular gas in six galaxies, where we made small maps. Out of the nine systems we observed, only two were not detected at all (NGC 5018 and NGC 7600). NGC 474 is not detected in its center, but CO is present in its companion. We then examine the expected association between the stellar and gaseous (HI or CO) shells, and discuss the various scenarios, taking the predictions from N-body numerical simulations into account.

The observations are described in Sect. 2, the sample of shell galaxies in Sect. 3, and the results are presented in Sect. 4. Finally, the interpretation and discussion are gathered in Sect. 5, and the conclusions in Sect. 6.

2. Observations and data reduction

Observations of the ^{12}CO(1–0) and ^{12}CO(2–1) emission have been carried out at the IRAM 30-m telescope at Pico Veleta, Granada, Spain, during 2017 July (for Arp 230, NGC 474, and NGC 3934), then September, October, and 2000 November (for the remaining sources). The beam full width at half-maximum (FWHM) was 23″ and 11″ at the frequencies of 115 GHz and 230 GHz, respectively. The SIS receivers (EMIR) were used for observations in the wobbler-switching mode, with reference positions offset by ±120 arcsec in azimuth. The main-beam efficiency of IRAM is $\eta_{\rm mb} = T_A^*/T_{\rm mb} = 0.82$ and 0.64 at 115 GHz and 230 GHz, respectively. The system temperatures ranged between 190 K and 420 K at 2.6 mm and between 240 K and 600 K at 1.3 mm. The pointing was regularly checked every 2 h on a nearby planet or a bright continuum source, and the focus was reviewed after each sunrise or if a suitable planet was available, as well as at the beginning of each night. The time on source typically ranged from 30 min to 1 h; this depended on the weather. Two backends were used simultaneously, the autocorrelator WILMA, and the Fourier transform spectrometer FTS. The rms noise level was $\sigma_{\rm mb} \sim 1.5$ mK $[T_A^*]$ with a spectrometer resolution of 40 km s^{-1} for 114 GHz and $\sigma_{\rm mb} \sim 3.0$ mK $[T_A^*]$ with a spectrometer resolution of 20 km s^{-1} for 230 GHz. The various pointings observed on the shell galaxies are indicated in Figs. 1–8.

3. Sample

We have selected shell galaxies that can be observed from the northern hemisphere, which were previously observed in HI-21 cm and in CO in the millimeter domain (see Table 1). In general, they are quite rich in neutral gas, except for NGC 7600. The properties of the nine shell galaxies selected in our sample are gathered in Table 1. The H_2 masses in this table are those that were known before our study, and all luminosities and masses were scaled to the adopted distances. References in this table are for HI and H_2. We list the detailed properties of each system below.

3.1. Arp 230

Arp (1966) was the first to classify the galaxy as peculiar because of its faint stellar arcs, which were not yet called shells. Arp 230 (IC51) is now considered to be one of the prototypes for shell galaxies that have formed around a prolate object, with shells phase wrapped from the radial infall of a small satellite (Quinn 1984). The geometry of the shells is characteristic (see Fig. 1), they are aligned with the major axis, and interleaved in their distance to the center (Dupraz & Combes 1986). At least eight shells can be counted, the most distant lies at 11 kpc, which is rather rare, although not as complex as the situation in NGC 3923 (Prieur 1988). As is frequently the case in shell systems, the first shell of Arp 230 (i.e., the most distant) is connected to the primary galaxy by a faint distorted tail or plume.

An HI mass of $1.59\times10^9\ M_\odot$ has been detected in this merged system with the Green Bank 140foot telescope (Richter et al. 1994). Schiminovich et al. (2013) mapped the HI in Arp 230 with the Very Large Array (VLA) and a resolution of ~0.8 kpc. The HI is not aligned with the stellar shells, but perpendicular to the major axis, like a polar ring, aligned with the dust lane. The total HI mass detected with the VLA is $1.1\times10^9\ M_\odot$. McGaugh & Bothun (1990) together with Prieur (1988) found that the color of the shells is bluer than the main body of the Arp 230 galaxy, suggesting that the merger provided gas and star formation to the shells.

Galletta et al. (1997) have detected CO(1–0) in the center with the Kitt Peak 12 m telescope (beam of 1 arcmin), and derived $M(H_2) = 8.9\times10^8\ M_\odot$. The central dust lane corresponds to a molecular disk in rotation in the center, mapped in CO(1–0) with ALMA at ~0.5 kpc resolution (Ueda et al. 2014). The corresponding H_2 mass is $1.7\times10^8\ M_\odot$.

3.2. NGC 474/470 (Arp 227)

The group has been observed in the optical by Rampazzo et al. (2006, 2007), and with high sensitivity by Duc et al. (2015). In the latter CFH-Megacam image, NGC 474 appears as a spectacular shell system, where shells are distributed randomly at all azimuth (see Fig. 2). This geometry corresponds to stellar shells that are aligned in the equatorial band of an oblate galaxy (Dupraz & Combes 1986). Superposed on the shell systems is a radial tail or plume that stems from the past merger.

The first HI observations did not separate the two galaxies of the pair (Huchtmeier 1982). Interferometric observations with the VLA have shown that most of the HI reservoir belongs to the spiral NGC 470, but a long tail and bridge cover NGC 474, and therefore the early-type shell galaxy may possess some interstellar gas (Rampazzo et al. 2006), see also Fig. 3.

As early as 1993, Sofue et al. (1993) detected CO(1–0) emission toward Arp 227A (NGC 470), the late-type galaxy of the

Table 1. Properties of the nine shell galaxies.

Name	RA J2000	Dec J2000	cz km s^{-1}	D Mpc	M(HI) log $M_\odot$	L(IR) log $L_\odot$	M(H$_2$) log $M_\odot$	Ref.	Type NED
Arp 230	00:46:24.2	−13:26:32	1720	24.2	9.20	9.49	8.95	(1)	S0pec
NGC 474	01:20:06.7	+03:24:55	2315	32.2	9.63	8.03	<7.7	(2)	SA0
Arp 10	02:18:26.3	+05:39:14	9108	120.0	10.2	10.5	–	(3)	S?
NGC 3032	09:52:08.1	+29:14:10	1562	21.2	8.15	9.34	8.42	(4)	SAB0
NGC 3656	11:23:38.6	+53:50:32	2870	42.6	9.27	9.99	9.67	(5)	I0pec
NGC 3934	11:52:12.5	+16:51:05	3779	49.2	9.51	9.98	9.32	(6)	S?
NGC 5018	13:13:01.0	−19:31:05	2816	37.5	8.81	9.54	<7.4	(7)	E3
NGC 7600	23:18:53.8	−07:34:50	3483	39.0	<7.5	–	–	(8)	S0
Arp 295N	23:42:00.8	−03:36:55	6966	93.0	10.2	10.9	10.2	(9)	Sbpec

Notes. All H$_2$ data are centered and are representative of the total molecular content. L(IR) data are from the NED.
References. (1) Schiminovich et al. (2013) for HI, Ueda et al. (2014) for CO – (2) Rampazzo et al. (2006) for HI, Combes et al. (2007) for CO – (3) Charmandaris & Appleton (1996) for HI – (4) Lucero & Young (2013) for HI, Combes et al. (2007) for CO – (5) Balcells et al. (2001) for HI, Young (2002) for CO – (6) Galletta et al. (1997) for HI and CO – (7) Kim et al. (1988) for HI, Ueda et al. (2014) for CO – (8) Serra et al. (2008) for HI – (9) Hibbard & van Gorkom (1996) for HI and CO.

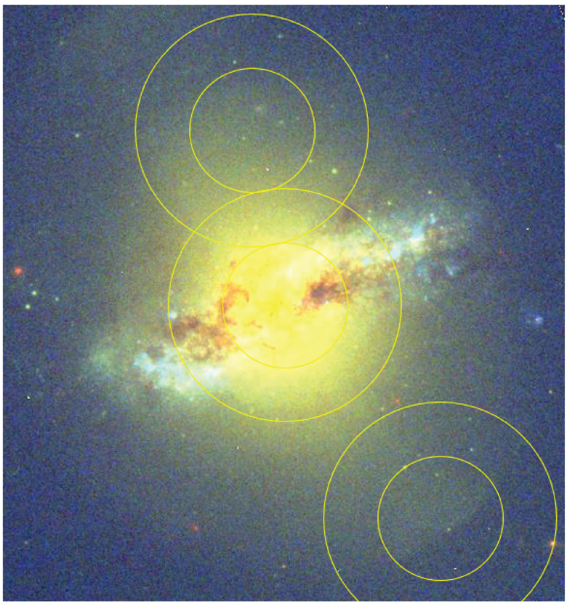

Fig. 1. CO(1–0) 23″ and CO(2–1) 11″ beams observed toward Arp 230 are overlaid on an HST composite image (F336W, F555W, and F814W). The two offset positions (NE and SW) are centered on shells.

pair, and derived an H$_2$ mass of $2.3 \times 10^8\ M_\odot$. However, toward the shell early-type galaxy NGC 474, Combes et al. (2007) found an upper limit of $M(\mathrm{H_2}) < 3.8 \times 10^7\ M_\odot$, with the IRAM-30 m telescope. We here obtain a lower upper limit for the CO emission toward the center, and then did not point toward the shells because the emission there is expected to be even lower. We observed the companion NGC 470 to determine how much available gas mass existed there that could have fallen towards NGC 474.

Lim et al. (2017) studied the globular cluster (GC) population in the NGC 474 galaxy. GCs and their color and age are good tracers of the merging history of a system. The violent starbursts triggered by the major mergers of gas-rich spirals favor the formation of metal-rich and red GC (Whitmore et al. 1993; Chien et al. 2007; Renaud et al. 2015), while the dry minor merger of small-mass satellites brings relatively blue GCs into the halo of a massive primary. In the outer parts of NGC 474, the spatial correlation between GCs and stellar fine-structure (shells, tails, radial streams) is remarkable, while GCs are blue, likely to have formed in low-metallicity satellites, and accreted later. In the center of the galaxy, GCs have an intermediate color that is compatible with their formation in situ, when star formation occurred 7–8 Gyr ago. With passive evolution until 13 Gyr, they will become red, as expected in a massive elliptical today (Lim et al. 2017).

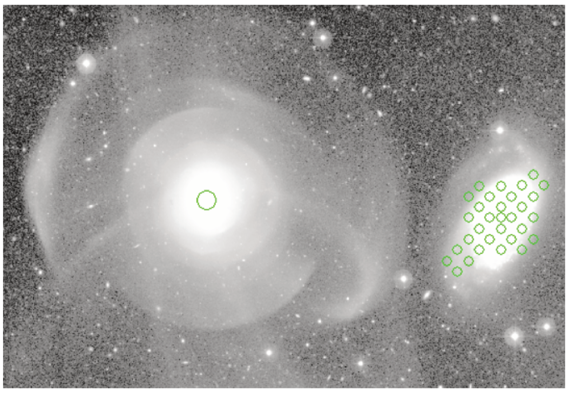

Fig. 2. Image in the g band from the CFHT Megacam of NGC 474 and companion NGC 470, enhancing the low surface brightness features, such as the shells (Duc et al. 2015). The CO(1–0) 23″ beam is indicated at the center of NGC 474, and the maps of the CO(2–1) 11″ beams cover its companion (see the appendix).

3.3. Arp 10

This peculiar galaxy reveals loops, ripples, and shells in its outer parts (Charmandaris & Appleton 1996). The HI VLA map from the latter work shows a neutral gas extension beyond the deepest optical shells. The HI appears in two components: one more relaxed in a rotating disk in the inner parts, although with non-circular motions, and the other component quite similar to a shell system, with no one-to-one correspondence with the optical shells. Bizyaev et al. (2007) showed that the inner parts of the optical disk are dominated by a collisional ring, and the intruder that is responsible for the expanding wave is found 5″ to the southwest from the nucleus of Arp10 (see Fig. 4). Its mass could

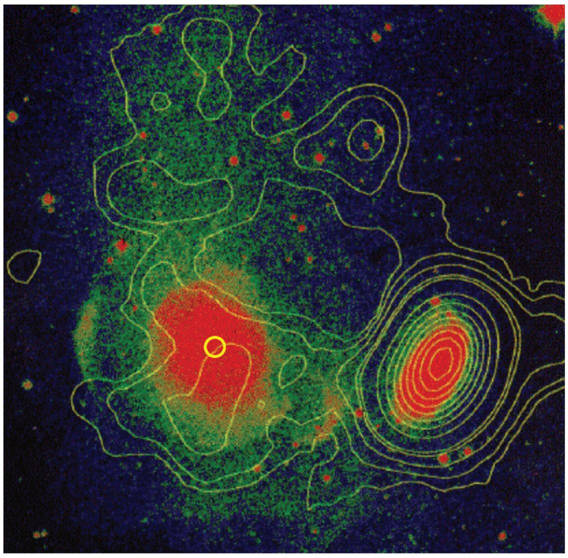

Fig. 3. VLA HI map over Arp 227 (NGC 470 at the right and NGC 474 at the left), from Schiminovich et al. (1997) and van der Hulst (priv. comm.). The CO(1–0) 23″ beam is indicated with a yellow circle.

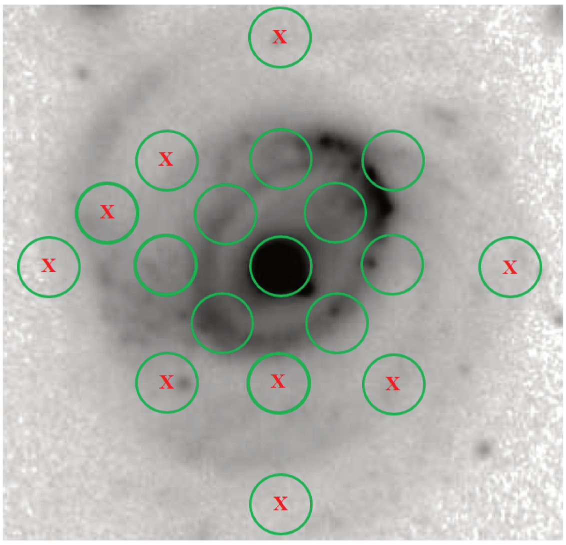

Fig. 4. CO(2–1)-11″ observed beams in Arp 10, overlaid on the blue optical image, from Bizyaev et al. (2007). The nine pointings selected to be outside the ring are indicated as red crosses (see Fig. 12). They can all be considered to cover part of a shell.

be one-fourth of the mass of Arp10. Star formation has been triggered in the ring by the collision.

3.4. NGC 3032

This early-type galaxy is classified as a weakly barred lenticular. Its optical image is very smooth, with some dusty inner disk, however, and a large-scale shell system in which the galaxy is embedded (see Fig. 5 and Duc et al. 2015). This galaxy has certainly acquired its gas recently because the HI map shows counter-rotation with respect to the stars (Oosterloo et al. 2010). While all gas components (ionized, atomic, and molecular) corotate, the main stellar body counter-rotates, but some young stars that have probably formed since the gas accretion event corotate with the gas in the very center (McDermid et al. 2006).

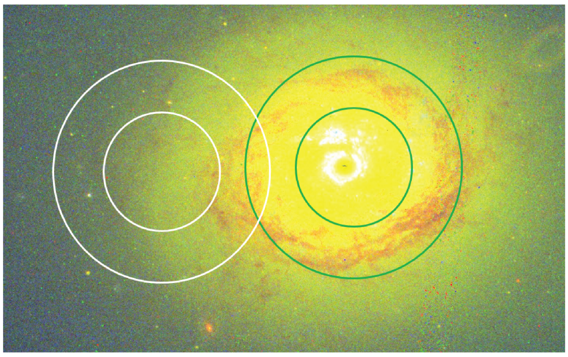

Fig. 5. CO(1–0) and CO(2–1) observed beams on NGC 3032, overlaid on an HST composite image. The eastern offset is centered on a shell.

Sage & Wrobel (1989) detected CO(1–0) emission toward the peculiar lenticular NGC 3032 with the Kitt Peak 12 m telescope (60″ beam), and derived an H_2 mass of $3.6\times10^8\ M_\odot$, computed with the same distance and CO-to-H_2 conversion factor as here. The latter is somewhat higher than that found by Combes et al. (2007), of $2.5\times10^8\ M_\odot$, but this could be explained because the IRAM-30 m beam is 23″ (2.4 kpc) in CO(1–0) and may miss some outer emission. The Combined Array for Research in Millimeter-Wave Astronomy (CARMA) interferometer mapped the inner disk, but did not cover more than the IRAM-30 m beam (Alatalo et al. 2013).

3.5. NGC 3656

This peculiar galaxy (Arp 55) has been classified as a shell elliptical galaxy, with several shells, and one particularly strong shell 9 kpc south of the center (Balcells et al. 2001), as is shown in Fig. 6. Two kinematical components have been identified, with perpendicular axes (Balcells & Stanford 1990). The inner (1 kpc) stellar core rotates with a major axis E-W, and the larger stellar and gaseous disk (radius 7 kpc) rotates with a major axis N-S. The VLA HI map from Balcells et al. (2001) shows two gas components: an edge-on and warped inner disk that extends up to 7 kpc ($M(\mathrm{HI}) = 2\times10^9\ M_\odot$), aligned north-south along an inner dust lane; and a more extended outer structure, distributed in shells or rings, that is roughly correlated to the optical shells but is more extended. The HI southern shell at 9 kpc coincides with the stellar shell, and has the systemic velocity.

Wiklind et al. (1995) detected CO emission toward the merger system NGC 3656 and derived an H_2 mass of $2.2\times10^9\ M_\odot$. A CO map was made with the Berkeley-Illinois-Maryland Association millimeter wave interferometer (BIMA) by Young (2002) and revealed the same N-S alignment as the HI disk. The map was not sensitive enough to detect CO in the southern shell.

3.6. NGC 3934

This peculiar disk galaxy is a candidate polar ring (Whitmore et al. 1990), belonging to a compact group, similar to a Hickson group (Bettoni et al. 2011). It has a strong linear dust lane in the center that irregularly obscures the inner and brighter regions of the galaxy (see Fig. 7). Spurs and shells are visible in the inner parts, but especially in the outskirts of the galaxy. The latter have an average $B-R\sim1.2$, which is not as blue as typical spiral arms, although they are bluer than the central parts that are reddened by the dust lane. The galaxy has then a rich shell

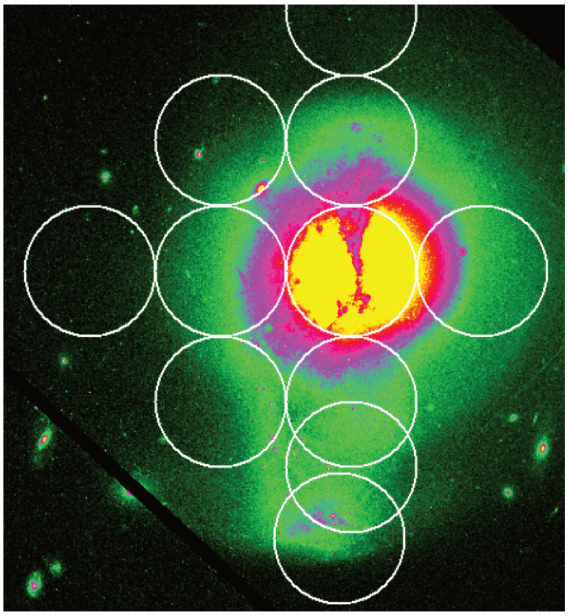

Fig. 6. CO(1–0) 23″ beams observed toward NGC 3656, superposed on an F606W HST image. The N-S dust lane is prominent, and the southern shell lies the bottom of the image. All CO beams partially cover some shell, except for the central beam, which includes the dust lane.

system, dispatched all around the center, in apparent random order. This shell morphology can be reproduced in models with oblate galaxies, with shells near the equatorial plane (Dupraz & Combes 1986). NGC 3934 is rich in gas, it was detected in HI, with a mass of $5 \times 10^9\,M_\odot$ (van Driel et al. 2000) and in CO (Galletta et al. 1997) with $M(H_2) = 2.1 \times 10^9\,M_\odot$. It has a star formation rate of SFR = $1.6\,M_\odot\,\mathrm{yr}^{-1}$, derived from its far-infrared IRAS flux. Bettoni et al. (2011) proposed a formation in a dissipative merger through hydrodynamical SPH simulations. From this formation mechanism, molecular gas might be expected in the shells.

3.7. NGC 5018

Like NGC 7252, NGC 5018 is one of the prototypes of a recent merger, 3 Gyr ago, which is becoming a giant elliptical (gE) (Buson et al. 2004). It is the dominant gE of a small group. It has been detected by IRAS, with an SFR = $0.7\,M_\odot\,\mathrm{yr}^{-1}$. The galaxy reveals sharp outer shells (Rampazzo et al. 2007) and a central linear dust lane. Kim et al. (1988) mapped the HI, and found $M(\mathrm{HI}) = 6.1 \times 10^8\,M_\odot$. Conversely, the galaxy is not detected in CO(1–0) with the Atacama Large Millimeter/submillimeter Array (ALMA) (Ueda et al. 2014), with $M(H_2) < 2.3 \times 10^7\,M_\odot$, but is detected in the 3 mm continuum.

3.8. NGC 7600

This is a typical shell galaxy with many shells that are aligned and interleaved along the major axis. The main body is a flattened early-type galaxy that is classified as a lenticular. Turnbull et al. (1999) counted 16 shells; the first lies at 40 kpc from the center. Cooper et al. (2011) revealed some even deeper external features, and easily reproduced the system of shells from a simulation of phase wrapping during the radial merger of a small companion. There is only an upper limit for HI in this galaxy (Sansom et al. 2000; Serra et al. 2008). It was selected in our sample, however, because of its high degree of fine stellar structures.

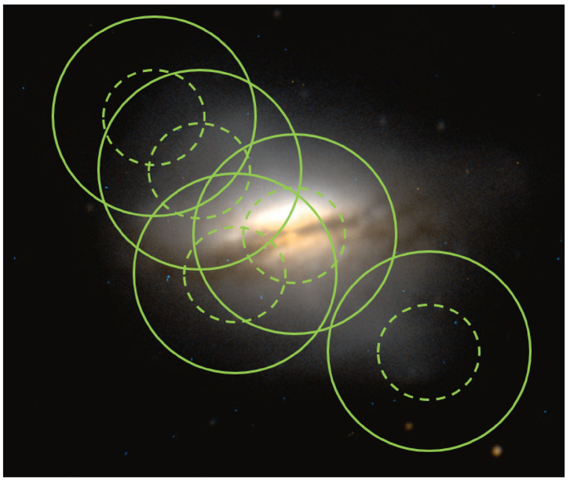

Fig. 7. CO(1–0) 23″ and CO(2–1) 11″ beams observed toward NGC 3934, overlaid on a composite optical image from the SDSS. All offset beams cover some shells, which are expected to show plateau emission before a sharp edge.

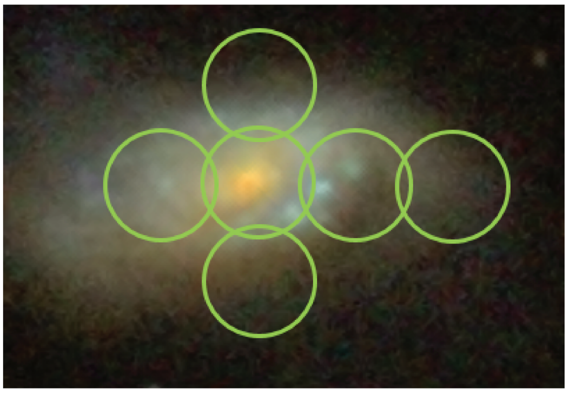

Fig. 8. CO(2–1) 11″ beams observed toward Arp 295N, overlaid on a composite SDSS image. The western offsets cover shells.

3.9. Arp 295N

The system Arp 295 is a pair of galaxies in an early merger stage. The northern member reveals large plumes, shells, and loops of Hα emission up to 9 kpc north and south of the minor axis (see Fig. 8). The northern galaxy is undergoing a retrograde encounter with its southern companion. The HI was mapped with the VLA by Hibbard & van Gorkom (1996), who found an HI mass of $1.7 \times 10^{10}\,M_\odot$ and an SFR = $17\,M_\odot\,\mathrm{yr}^{-1}$. They also reported our IRAM-30 m observations of CO emission, which were not published, with a molecular mass of $M(H_2) = 8.5 \times 10^9\,M_\odot$. The SFR of the ensemble has been estimated to be $21.9\,M_\odot\,\mathrm{yr}^{-1}$ from Paα by Tateuchi et al. (2015).

4. Results

In each shell galaxy, the center was observed first to determine whether it contained molecular gas, and if present, the shell regions were also observed. Gas in shells is expected to come from the infall of a gas-rich satellite (Charmandaris et al. 2000; Combes & Charmandaris 2000). The gas in the satellite is first liberated and may oscillate in the potential of the primary galaxy, just before the satellite stars form the shells. Some gas is expected to fall in the center through dissipation. Gas in the

Table 2. CO results.

Galaxy	Offsets	CO(1–0) Int-flux			CO(2–1) Int-flux			$M(H_2)$	$\Sigma(H_2)$
	(″,″)	Int-flux Jy km s^{-1}	V km s^{-1}	ΔV km s^{-1}	Int-flux Jy km s^{-1}	V km s^{-1}	ΔV km s^{-1}	10^8 $M_\odot$	$M_\odot$ pc^{-2}
ARP 230	(0,0)	9.2 ± 0.9	−54 ± 6	125 ± 15	14.7 ± 1	−42 ± 5	111 ± 11	0.57 ± 0.06	11
	(4.4,17)	3.7 ± 0.7	5 ± 17	190 ± 40	<3	–	–	0.23 ± 0.04	4
	(−14,−21)	<1.6	–	–	<1.7	–	–	<0.1	<2
NGC 474	(0,0)	<1.4	–	–	<3.1	–	–	<0.15	<1.6
ARP 10	(0,0)	29.7 ± 1	10 ± 4	208 ± 7	38.8 ± 2.7	25 ± 8	224 ± 16	44.6 ± 1.5	35
	See	18 pt	Map						
NGC 3032	(0,0)	71 ± 1.3	57 ± 1	129 ± 2	86.5 ± 2	47 ± 1	108 ± 3	3.6 ± 0.06	90
	(20,0)	8 ± 0.8	80 ± 3	53 ± 6	<5	–	–	0.4 ± 0.04	10
NGC 3656	(0,0)	119.6 ± 2.2	−34 ± 4	433 ± 8	200 ± 4.5	−31 ± 7	407 ± 23	22.9 ± 0.41	142
	(22,22)	9.2 ± 1.3	−192 ± 8	112 ± 17	29.8 ± 4.0	6 ± 10	322 ± 45	1.7 ± 0.25	11
	(0,22)	9.4 ± 1.6	−184 ± 12	153 ± 33	<8	–	–	1.8 ± 0.3	11
	(22,0)	47.6 ± 2.0	−20 ± 9	433 ± 18	2.7 ± 0.8	−78 ± 8	51 ± 19	9.1 ± 0.4	57
	(22,−22)	8.6 ± 1.7	107 ± 14	143 ± 32	5.7 ± 1.0	106 ± 6	73 ± 14	1.64 ± 0.3	10
	(0,−22)	18.6 ± 1.5	130 ± 9	232 ± 23	<7	–	–	3.55 ± 0.3	22
	(0,−33)	3.6 ± 1.0	126 ± 18	135 ± 46	4.8 ± 1.0	91 ± 16	149 ± 30	0.69 ± 0.2	4.3
	(2,−45)	1.5 ± 0.3	179 ± 15	139 ± 29	2.5 ± 0.8	105 ± 34	187 ± 67	0.29 ± 0.06	1.8
	See	11 pt	Map						
NGC 3934	(0,0)	42.8 ± 0.8	22 ± 4	384 ± 7	78.9 ± 1.7	30 ± 4	396 ± 9	11 ± 0.2	51
	(7,−5)	21.4 ± 0.8	−17 ± 7	350 ± 13	18.7 ± 3	−78 ± 19	210 ± 67	5.5 ± 0.2	25
	(16,14)	3.7 ± 0.4	−128 ± 7	115 ± 17	1.2 ± 0.4	−119 ± 17	86 ± 27	0.9 ± 0.1	4
	(−16,−14)	6.6 ± 1	134 ± 18	255 ± 77	3 ± 0.5	184 ± 7	90 ± 19	1.7 ± 0.2	8
	(11,12)	<10	–	–	<90	–	–	<2.5	<11
NGC 5018	(0,0)	<1.8	–	–	<4	–	–	<0.27	<2
	(44,−22)	<3	–	–	<4	–	–	<0.45	<3.6
	(−22,22)	<3	–	–	<3	–	–	<0.45	<3.6
NGC 7600	(0,0)	<3	–	–	<4.8	–	–	<0.5	<3.6
	(143,32)	<2	–	–	<5	–	–	<0.3	<2
ARP 295N	(0,0)	58 ± 4	−54 ± 11	333 ± 24	38 ± 5	−42 ± 20	268 ± 40	53 ± 4	69
	(−10,0)	45 ± 3.8	16 ± 14	340 ± 33	25.8 ± 5.6	85 ± 14	136 ± 35	41 ± 3.4	53
	(−20,0)	7.6 ± 2.2	110 ± 13	93 ± 35	<2	–	–	6.9 ± 2	9
	See	6 pt	Map						

Notes. Integrated flux, velocity, and FWHM obtained through Gaussian fits. Velocities are counted from the central redshifts indicated in Table 1. The H_2 masses are estimated within the CO(1–0) beam of 23″, with the standard conversion factor of the Milky Way $\alpha = 4.36\,M_\odot\,(\mathrm{K\,km\,s^{-1}\,pc^2})^{-1}$. Upper limits are given at 3σ, assuming an FWHM of 300 km s^{-1}.

center is therefore a necessary condition for finding gas in shells, but is not sufficient because the primary galaxy could also have had some gas before the collision. Out of the nine shell galaxies of our sample, three were not detected in their center (NGC 474, NGC 5018, and NGC 7600) and we did not search for gas in their shells. The upper limits are displayed in Table 2. Three of the six remaining shell galaxies were mapped extensively, and we show spectra maps in CO(1–0) and CO(2–1) for Arp 10 (Figs. 10 and 11), NGC 3656 (Fig. 17), and Arp 295N in Figs. 19 and 20. In Table 2 we characterize only the central beam and the offset beams that cover a shell and are detected in CO(1–0). For the three other galaxies (Arp 230, NGC 3032, and NGC 3934), only a few spectra are shown in Figs. 9, 14, and 18. All these points are detailed in Table 2.

4.1. Molecular gas content

To quantify the amount of molecular gas found in each pointing, we relied on the empirically established proportionality between the CO(1–0) luminosity and H_2 mass for a large number of Milky Way-like galaxies (e.g., Bolatto et al. 2013). We converted the integrated intensities in each beam (in $T_{\rm mb}$) into integrated fluxes $S(\mathrm{CO})\mathrm{d}V$, with the conversion of 5 Jy per Kelvin, as appropriate for the IRAM-30 m telescope. From the integrated flux $S(\mathrm{CO})\mathrm{d}V$ (Jy km s^{-1}) found within each region, the derived molecular mass was obtained through the formula

$$L'_{\rm CO}(\mathrm{K\,km\,s^{-1}\,pc^{-2}}) = 3.25\times10^{7}\,\frac{S(\mathrm{CO})\mathrm{d}V}{(1+z)}\left(\frac{D_{\rm L}}{\nu_{\rm rest}}\right)^{2},$$

where $\nu_{\rm rest} = 115.271$ GHz, and $D_{\rm L}$ is the luminosity distance in megaparsec (e.g., Solomon & Vanden Bout 2005). The molecular mass, including helium, was then derived from

$$M(H_2) = 4.36 L'_{\rm CO}$$

assuming the standard CO-to-H_2 conversion factor of $X_{\rm CO} = 2\times10^{20}\,\mathrm{cm^{-2}\,(K\,km\,s^{-1})^{-1}}$, as applicable to Milky Way-like galaxies. Although shell galaxies are interacting, they are mildly perturbed and are certainly not starbursts, or ultra-luminous infrared galaxies (ULIRG), where a lower conversion factor might apply.

Molecular masses, corresponding to each CO(1–0) pointing are displayed in Table 2. In most cases, we did not observe the whole galaxy disks, and an estimation of the total molecular masses would need some extrapolation.

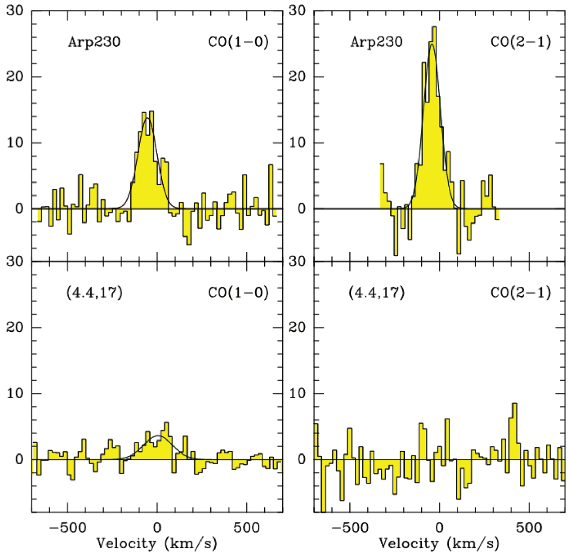

Fig. 9. CO spectra in Arp 230, central position and offset (in arcsec). The vertical axis is the main-beam temperature in mK.

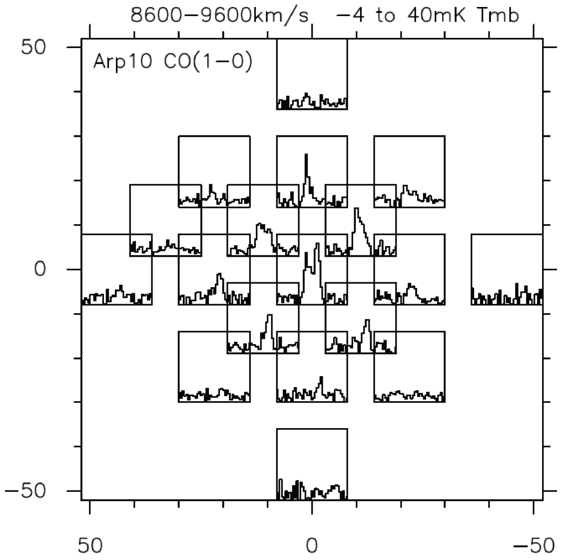

Fig. 10. CO(1–0) map of spectra in Arp 10. The RA and Dec offsets are in arcsec. The scales of all spectral boxes in velocity and main-beam temperature are indicated at the top.

The last column of Table 2 reports the average molecular surface density within the CO(1–0) beam of 23″ for each galaxy. This shows that galaxies of later type (e.g., NGC 3656 or NGC 3934) tend to have a richer content in molecular gas, which might be due to their own gas before the accretion event. We verified that the total molecular content is correlated to the far-infrared (FIR) luminosity (see Table 1), and that galaxies of our sample are compatible with the global Kennicutt-Schmidt (KS) diagram, as shown for local early-type galaxies by Combes et al. (2007). However, we have not enough sensitivity in Hα or far-ultraviolet (FUV) or near-ultraviolet (NUV) (GALEX) images to be able to determine the star formation surface density on shells, and compare this to the molecular surface densities to study the KS diagram of shells.

4.2. CO spectra

For most of the shell galaxies with detected in CO emission at least in their center, we tried to cover the outer stellar shells through simultaneous pointing in the CO(1–0) and CO(2–1) lines. Shells are not only reduced to their sharp edges, but also extend inside these arcs in a nearly flat plateau emission, as we show in Fig. 2 for example. With the large CO beams, we can thus hope to collect emission from these regions as well. The best resolution we have, 11 arcsec, typically corresponds to 1–5 kpc in the galaxies, and is just sufficient to separate the shell regions from the center, while the 23″ beam is not. Frequently, the CO(1–0) emission is detected in the shell offset position, but the CO(2–1) is not, which can be interpreted as the absence of detection in the shell itself. The CO(1–0) emission is then only due to some central emission seen at the border of the beam.

This is clearly the case for Arp 230, as is shown in Fig. 9. CO emission towards the center is highly concentrated, which results in the peak main-beam temperature being nearly twice in CO(2–1) with respect to CO(1–0). The offset beam, at 17.5″ = 2 kpc from the center, is detected in CO(1–0) but is consistent with emission from the central disk. The offset is not detected in CO(2–1), whose beams does not overlap with the disk. Ueda et al. (2014) have mapped the CO(1–0) emission with ALMA with 4 arcsec resolution and showed that it is confined in a thin rotating edge-on disk, 5 kpc in diameter, corresponding to the dust lane that is prominent in Fig. 1. Because no emission at all is detected in the farthest shell, at 3kpc from the center, we conclude that there no gas can be detected in the shells.

The case of Arp 10 is different because the collision at the origin of the shells also produced a collisional ring in the center, that is, a wave propagating radially outward from the center as a result of the excitation of a head-on collision with a small impact parameter (e.g., Appleton & Struck-Marcell 1996). In the CO(2–1) map of spectra of Fig. 11, the emission is clearly extended, not only in the ring, but also in the shells. The comparison between the two lines (Figs. 10 and 11) suggests that the gas has indeed been detected as far as ~26 kpc from the center in ripples and shells caused by the interaction. To better quantify the amount of gas involved, we have stacked all the spectra that lie clearly outside the ring: the nine offsets considered are indicated by red crosses in Fig. 4. These nine offsets correspond to the shells. The resulting stacked spectra of the CO(1–0) and CO(2–1) lines are plotted in Fig. 12. All these positions outside the ring were stacked, and their velocity was recentered around the systemic velocity of 9100 km s^{-1}. The resulting CO(2–1) spectrum is the most significant because of the smaller beam, which excludes overlap with the center. The strength of the CO(2–1) is similar to and even stronger than that of CO(1–0), which signifies molecular gas outside the ring in the shells. From this stacked spectrum, we derived a molecular content of $M(H_2) = 3.4 \times 10^9\ M_\odot$ in the shells, assuming the conversion factor adopted in Sect. 4.1. An overview of the CO(1–0) and CO(2–1) surface densities and velocity fields is displayed in Fig. 13. The velocity gradient is comparable to that of the ionized gas, and is limited because the inclination is almost face-on ($i = 22°$) (Bizyaev et al. 2007).

The case of NGC 3032 is quite similar to the map shown in Arp 230. Figure 14 is typical of a quite concentrated CO emission, with the main-beam temperature of the CO(2–1) line peaking higher than that of the CO(1–0). The offset shell region does not overlap the center with the 11 arcsec beam, and no CO(2–1) is detected there, while the CO(1–0) line shows the redshifted part of the emission, compatible with the inner rotating disk, which is expected to coincide with the dust lanes (see Fig. 5). We conclude that the shell region is not detected in the molecular gas.

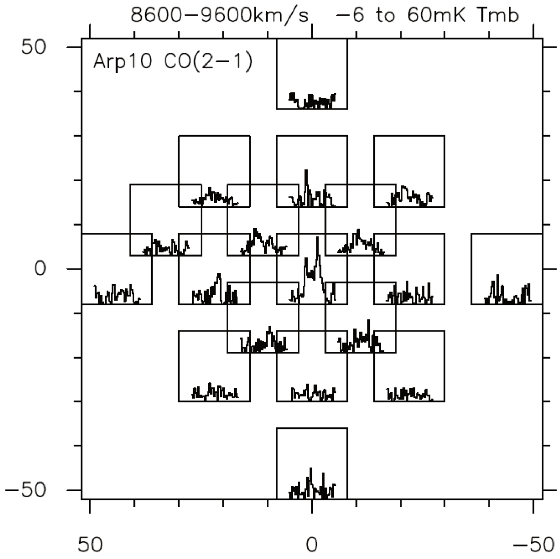

Fig. 11. CO(2–1) map of spectra in Arp 10.

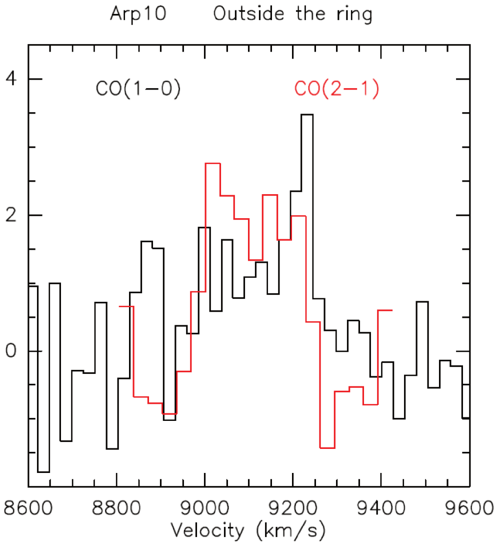

Fig. 12. Stacked CO spectra in Arp 10, considering only the positions outside the ring that cover the shells (see Fig. 4). The vertical axis is the main-beam temperature in mK.

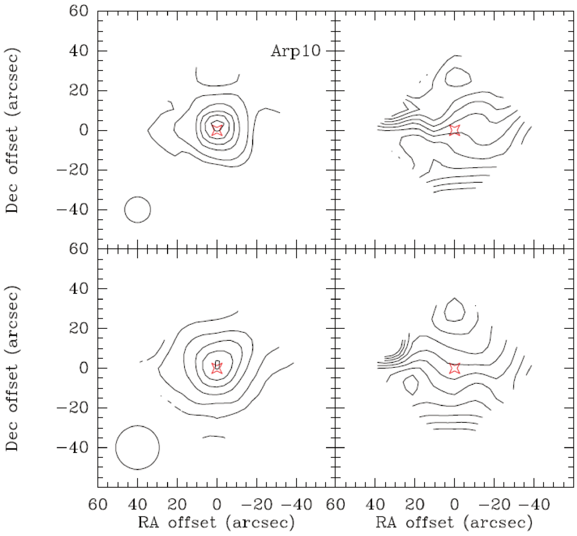

Fig. 13. Isocontours of the integrated intensities in Arp 10 for CO(2–1) (*upper panels*) and CO(1–0) (*lower panels*), with linear contours spaced by 1.52 and 1.15 K km s^{-1}, respectively, and maximum contours at 7.6 and 5.7 K km s^{-1}, respectively. The right panels display the corresponding velocity fields. The isovels are spaced by 30 km s^{-1}, they start at 8990 km s^{-1} in the north and extend to 9290 km s^{-1} in the south. The beam sizes are indicated in the bottom left corner.

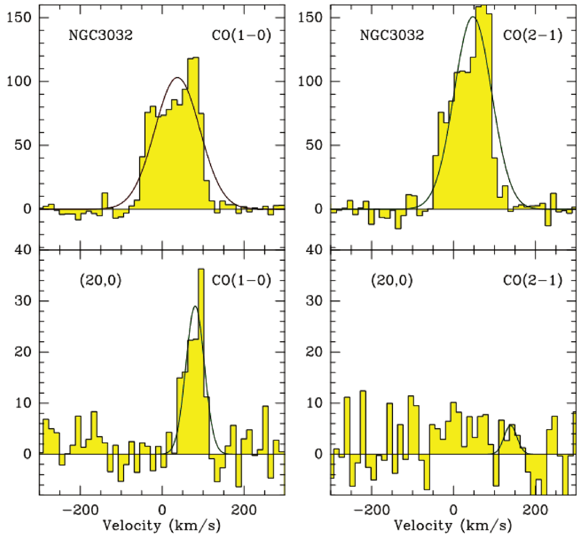

Fig. 14. CO spectra in NGC 3032, central position and offset (in arcsec). The vertical axis is the main-beam temperature in mK.

The shell galaxy NGC 3656 appears to be one of the best cases of an elliptical galaxy that has accreted a companion and has formed shells through phase wrapping (Balcells et al. 2001). The accreted companion must have been rich in gas because it left a N-S dust lane that is terminated by the southern shell at 9 kpc. This southern shell is clearly detected in molecular gas, as seen through the comparison of the CO(2–1) and CO(1–0) spectra in Fig. 15 and the corresponding map (Fig. 17). There are also shells in the outer north, east, and west observed beams, which show CO(1–0) emission, but no clear CO(2–1) (Fig. 16 and Table 2). CO(1–0) and CO(2–1) are simultaneously clearly detected only in the (22,22), (22,−22), and (0,−33) positions. The velocity of the CO gas in the shells spans a range around the systemic velocity, as does the velocity of stars in the southern shell (Balcells et al. 2001). In the extremity of the southern shell, the velocity profile is broad: it shows a double-horn shape from 2700 to 3100 km s^{-1} at (0,−33) and a single component from 2900 to 3100 km s^{-1} at (2,−45) in CO(1–0). In other places, it also shows a two-horn shape, which is usually only seen in the central beam for rotating disks, but is not compatible with a rotating disk in the outer parts. This means that two components with different angular momentum exist. The HI component also shows a trend of counter-rotation, as claimed by Balcells et al. (2001). The inner disk does rotate, however: it is redshifted in the south and blueshifted in the north, as is the HI disk observed by Balcells et al. (2001). The fact that the CO emission observed toward the southern shell has a velocity different from what is expected from the disk rotation confirms its origin in a phase-wrapped shell.

Averaging over the three observed beams that cover the southern shell, we obtain a surface density of $\Sigma = 9\,M_\odot\,\mathrm{pc}^{-2}$ and we derive a molecular content of $M(\mathrm{H_2}) = 3.8 \times 10^8\,M_\odot$ in the 9 kpc-shell assuming the conversion factor adopted in Sect. 4.1.

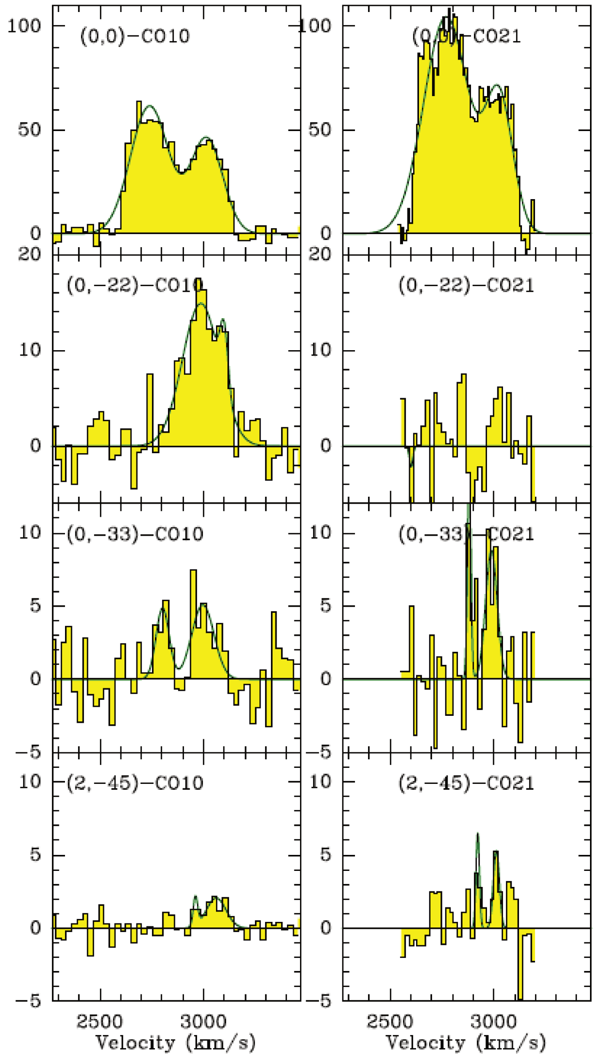

Fig. 15. CO spectra in NGC 3656 for the center and the offsets (in arcsec), covering the southern shell. The vertical axis is the main-beam temperature in mK.

NGC 3934 is a late-type galaxy with randomly oriented shells around a nearly edge-on disk that is traced by a linear dust lane. It has been confused with a polar ring galaxy, but this is not the correct classification (Bettoni et al. 2011). The beams clearly point to the shells, and do not overlap with the disk (see Fig. 7). With symmetrical offsets of 21″ = 5 kpc from the center, they are clearly detected in both CO(1–0) and CO(2–1), as shown in Fig. 18. Therefore molecular gas is detected in the shells. There is no shift in average velocity for the gas in the shells with respect to the disk. However, the line profiles in the shells show a two-horn shape, indicating two opposite signs of the relative angular momentum of the shell material relative to the primary galaxy. This two-horn shape is frequently observed toward the center of galaxies and is characteristic of a disk in rotation. The reason is that the observing beam covers both the receding (red) and approaching (blue) sides. In the outer parts, only one velocity component is expected for a rotating disk. A two-horn shape in the outer profiles supports the gas-shell scenario. That the ratios of CO(2–1) to CO(1–0) vary from one position to the other is due to the different beams and helps to distinguish the possible contamination in the larger CO(1–0) beam.

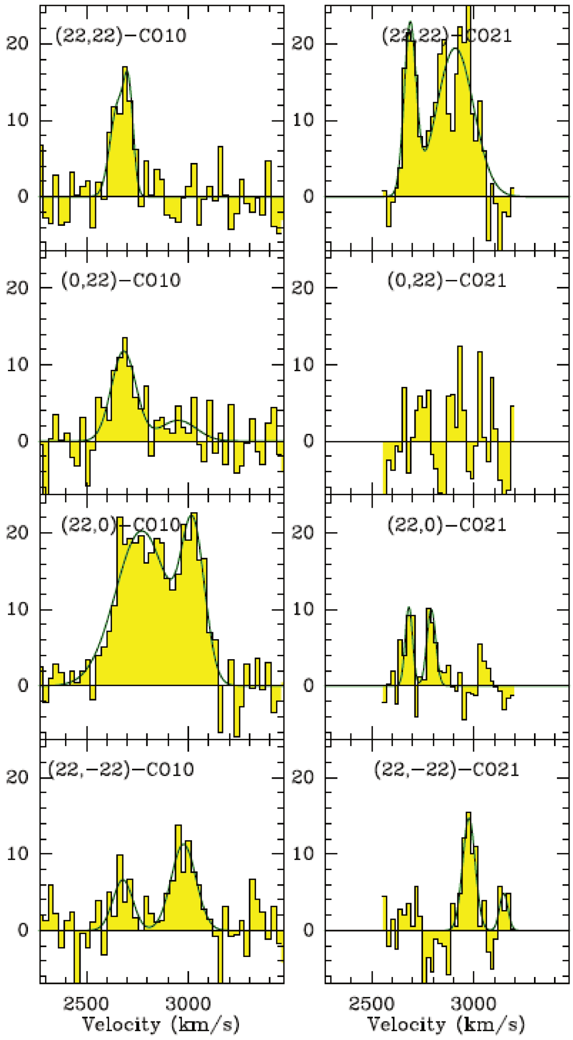

Fig. 16. Same as Fig. 15 for the offsets of NGC 3656 that cover a shell (other than the southern one), and detected in CO(1–0).

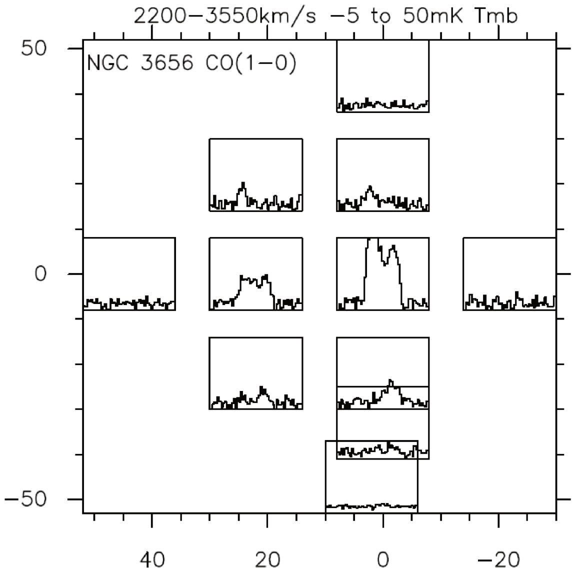

Fig. 17. CO(1–0) map of spectra in NGC 3656. The CO emission is most visible in the southern shell, but is visible in the other three directions.

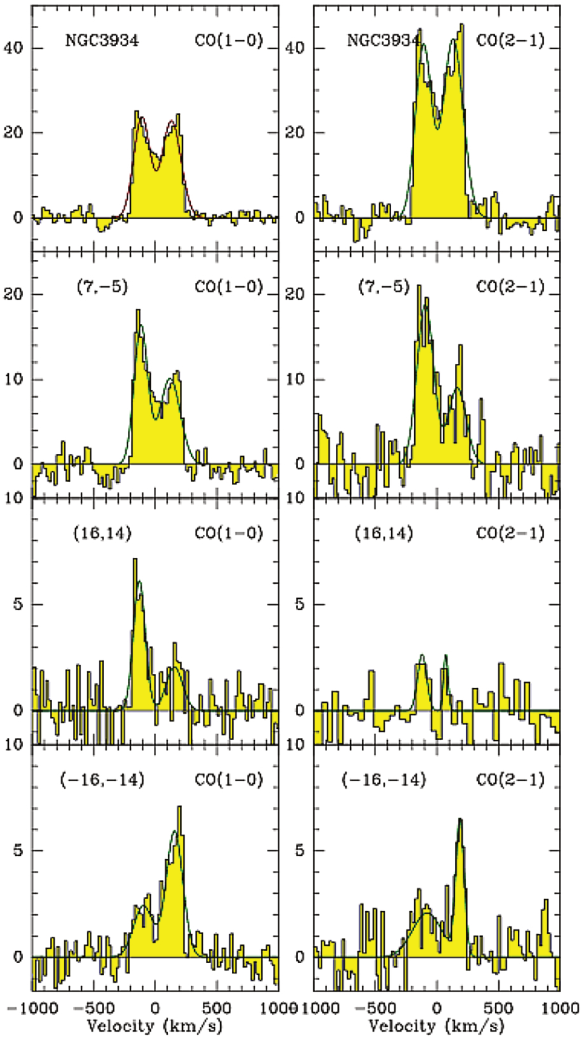

Fig. 18. CO(1–0) (*left*) and CO(2–1) (*right*) spectra in NGC 3934, central position and offsets (in arcsec). The vertical axis is the main-beam temperature in mK. The two last offsets cover the outer shells without contamination from the center.

Summing the molecular content of the two detected shells, we find $M(H_2) = 2.6 \times 10^8\ M_\odot$, see Table 2.

The northern galaxy of the Arp 295 pair is a nearly edge-on spiral, which is strongly perturbed by the interaction and shows disordered shells and ripples. The observed spectra in Figs. 19 and 20 are essentially compatible with molecular gas in the disk, with some extension in the western shell (see Table 2). However, the emission does not extend far in the most western offset, so it is still marginal.

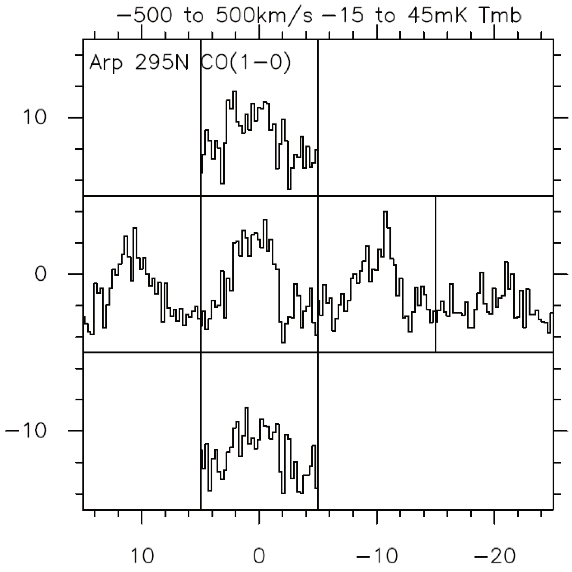

Fig. 19. CO(1–0) map of spectra in Arp 295N.

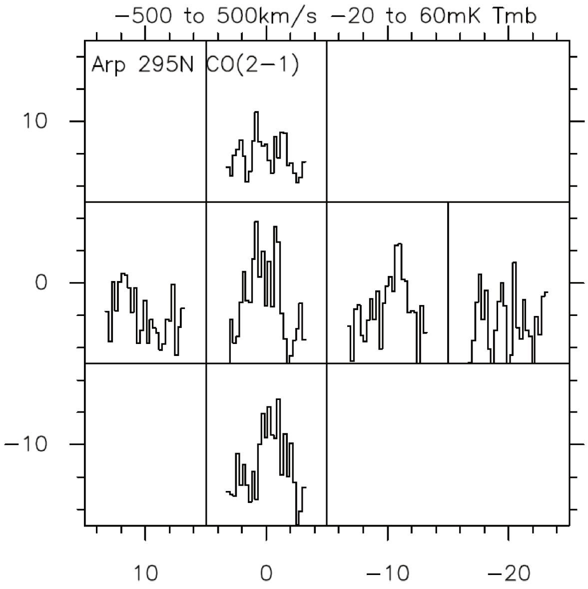

Fig. 20. CO(2–1) map of spectra in Arp 295N.

5. Discussion

The dynamical mechanism that forms shells through phase wrapping has been described in detail (Quinn 1984; Dupraz & Combes 1986, 1987). Stars from a companion, liberated by tidal forces, oscillate in the potential of the primary galaxy, and a sharp edge forms as an outward-propagating wave at their apocenters. There could be radial oscillation in a prolate potential, forming alternate shells with zero velocity at their edge, or less radial ones with angular momentum, forming shells around the equatorial plane of an oblate potential, keeping some rotational velocity at their edge. Another mechanism is space wrapping, where shells occur as ordinary loops in interactions and mergers, with higher velocities.

5.1. Molecular clouds in shells

Because gas is dissipative, it may appear surprising to find gas in shells. During radial oscillations, the diffuse gas is expected to fall into the center. Dense gas clouds do experience much less dissipation than diffuse HI gas. Moreover, numerical modeling of the shell formation (Combes & Charmandaris 2000) using a realistic distribution of its stellar and gaseous component showed that the observed spatial distribution of gaseous and stellar shells can be easily reproduced within the standard models of the theory of shell formation. The detection of molecular gas associated with the shells in Centaurus A confirmed this model (Charmandaris et al. 2000). Using the Swedish-ESO Submillimetre Telescope (SEST), Charmandaris and collaborators detected a molecular gas of 4.3×10^7 $M_\odot$ with the same kinematical characteristics as the HI shells.

The model predicts that a significant fraction of the merger-remnant dense molecular clouds has a dynamical behavior similar to that of the stellar component. Our detection of molecular clouds in shells through CO emission supports the model. With higher spatial resolution, it will be possible to determine the difference in position between the gas and stars in shells, and infer the loss of angular momentum during the encounter.

5.2. CO velocity in shells

CO emission in shells was clearly detected for three galaxies: Arp 10, NGC 3656, and NGC 3934. In the case of Arp 10, the inclination on the plane of the sky is small (i = 14° from Hyperleda), and the small velocity difference with respect to the systemic recession velocity for the gas in the shells is compatible with both phase and space wrapping. For the two other galaxies, the inclination is relatively large (i = 51° and i = 46° for NGC 3656 and 3934, respectively), and the average velocity with respect to the systemic velocity of the shells is relatively low. However, the CO profiles in the shells are broad and show a two-horn shape even in both NGC 3656 and NGC 3934. This means that the CO beam that covers a large shell region, where the material is not only in radial orbits, but keeps a tangential velocity at the apocenter. In the line of sight toward the observer some material with positive and negative angular momentum with respect to the galaxy is projected.

This configuration is impossible to encounter with a disk in rotation. Two-horn profiles are only seen when the observation beam covers a wide region near the center, including both the approaching and receding sides. For an observation far from the center of the rotating disk, only one velocity peak (either blue or red) is expected. For shells, in contrast, the material from the companion is infalling on a nearly radial orbit, and part of the matter may arrive with a positive and part with a negative angular momentum with respect to the primary galaxy. In the shell region far from the center, it is possible to have the two velocity signs toward the same line of sight. The two-horn profile shape therefore supports the CO detection in shells. Confirmation of this scenario is required through observations with higher spatial resolution.

5.3. Comparison with HI in shells

HI has been mapped in Arp 230 (Schiminovich et al. 2013), NGC 474 (Rampazzo et al. 2006), Arp 10 (Charmandaris & Appleton 1996), NGC 3032 (Oosterloo et al. 2010), NGC 3656 (Balcells et al. 2001), and Arp 295 (Hibbard & van Gorkom 1996). In all these six galaxies, the HI is extended enough to cover the shells, and in NGC 3656, the HI is clearly seen associated with the southern stellar shell, with compatible kinematics. In most cases, however, the spatial resolution is not sufficient to clearly conclude that the gas provided by a small merging companion has crossed the system and oscillates in the shells. The only system with a clear presence of HI gas in shells is NGC 3656, which Balcells et al. (2001) compared to NGC 5128 (Centaurus A), where the first HI shells were discovered (Schiminovich et al. 1994). Given the orientation of the gas and dusty disk, which is perpendicular to the main stellar body, this shell system must have been formed through phase wrapping of material in radial orbits. HI and CO emission in the shells can only be explained by clumpy gas with a low-filling factor and with low dissipation (Combes & Charmandaris 2000).

6. Summary

We have carried out CO(1–0) and CO(2–1) line observations of nine shell galaxies with the IRAM-30 m telescope. Molecular gas was detected in six of them, together with two of the companions. In three of the detected galaxies (Arp 230, NGC 3032, and Arp 205N), we cannot conclude that gas is detected in the shells; the detection is compatible with gas in the inner rotating disk. In the three remaining galaxies (Arp 10, NGC 3656, and NGC 3934), molecular gas is clearly detected in the shells, with a velocity close to systemic, and not in continuity with the inner rotating disk. The amount of molecular gas is estimated as $M(\mathrm{H_2}) = 3.4 \times 10^9$ $M_\odot$ in the shells outside the ring in Arp 10, 3.8×10^8 $M_\odot$ in the southern shell of NGC 3656, and 2.6×10^8 $M_\odot$ in the two detected shells of NGC 3934.

The mechanism that formed these gaseous shells might be different. For two cases at least (Arp 10 and NGC 3656), the encounter with the small companion had a very small impact parameter, and the phase wrapping in a nearly radial orbit must have played the main role. The morphology of Arp 10 corresponds to an oblate system; this also holds for most shells in NGC 3656. However, the main shell might be only the end of the tidal tail. The gas of the companion of NGC 3656 has left a radial trace that is visible as a contrasted dust lane, and the main shell is found in continuity, indicating the companion orbit and that of the tidal debris. The main body of NGC 3934 is seen nearly edge-on in the sky, and the situation is less clear. Shells that are distributed symmetrically at about 40° of the minor axis are clearly detected in molecular gas. The fact that gas can be detected in shells tends to support the clumpiness and low dissipative character of a large part of the interstellar medium. The line profiles in the shells reveal a two-horn shape, indicating both positive and negative angular momentum relative to the primary galaxy. This supports the CO detection in shells because it is impossible to explain a two-horn profile in the outer parts of the disk of a rotating galaxy. Material from the companion must have infallen in a nearly radial orbit, part of it with a positive and the other part a negative impact parameter. The material acquired a tangential velocity at the apocenter. The shells are then also phase wrapped. Follow-up with higher spatial resolution is required to test the relative position of gas and stellar shells to confirm the dynamical mechanism.

Acknowledgements. We warmly thank the referee for constructive comments and suggestions. This work is based on observations carried out with the IRAM 30m telescope. IRAM is supported by INSU/CNRS (France), MPG (Germany) and IGN (Spain). This publication has made use of data products from the NASA/IPAC Extragalactic Database (NED). We acknowledge the usage of the HyperLeda database (`http://leda.univ-lyon1.fr`).

References

Alatalo, K., Davis, T. A., Bureau, M., et al. 2013, MNRAS, 432, 1796
Appleton, P. N., & Struck-Marcell, C. 1996, Fund. Cosmic Phys., 16, 111
Arp, H. 1966, ApJS, 14, 1
Balcells, M., & Stanford, S. A. 1990, ApJ, 362, 443
Balcells, M., van Gorkom, J. H., Sancisi, R., & del Burgo, C. 2001, AJ, 122, 1758
Barnes, J. E., & Hernquist, L. 1992, ARA&A, 30, 705
Bettoni, D., Galletta, G., Rampazzo, R., et al. 2011, A&A, 534, A24
Bizyaev, D. V., Moiseev, A. V., & Vorobyov, E. I. 2007, ApJ, 662, 304
Bolatto, A. D., Wolfire, M., & Leroy, A. K. 2013, ARA&A, 51, 207
Buson, L. M., Bertola, F., Bressan, A., Burstein, D., & Cappellari, M. 2004, A&A, 423, 965
Carter, D., Allen, D. A., & Malin, D. F. 1982, Nature, 295, 126
Charmandaris, V., & Appleton, P. N. 1996, ApJ, 460, 686
Charmandaris, V., Combes, F., & van der Hulst, J. M. 2000, A&A, 356, L1

Chien, L.-H., Barnes, J. E., Kewley, L. J., & Chambers, K. C. 2007, ApJ, 660, L105

Combes, F., & Charmandaris, V. 2000, in Dynamics of Galaxies: from the Early Universe to the Present, eds. F. Combes, G. A. Mamon, & V. Charmandaris, ASP Conf. Ser., 197, 339

Combes, F., Young, L. M., & Bureau, M. 2007, MNRAS, 377, 1795

Cooper, A. P., Martínez-Delgado, D., Helly, J., et al. 2011, ApJ, 743, L21

Duc, P.-A., Cuillandre, J.-C., Karabal, E., et al. 2015, MNRAS, 446, 120

Dupraz, C., & Combes, F. 1986, A&A, 166, 53

Dupraz, C., & Combes, F. 1987, A&A, 185, L1

Galletta, G., Sage, L. J., & Sparke, L. S. 1997, MNRAS, 284, 773

Hernquist, L., & Quinn, P. J. 1988, ApJ, 331, 682

Hernquist, L., & Quinn, P. J. 1989, ApJ, 342, 1

Hibbard, J. E., & van Gorkom, J. H. 1996, AJ, 111, 655

Huchtmeier, W. K. 1982, A&A, 110, 121

Kim, D.-W., Guhathakurta, P., van Gorkom, J. H., Jura, M., & Knapp, G. R. 1988, ApJ, 330, 684

Lim, S., Peng, E. W., Duc, P.-A., et al. 2017, ApJ, 835, 123

Lucero, D. M., & Young, L. M. 2013, AJ, 145, 56

McDermid, R. M., Emsellem, E., Shapiro, K. L., et al. 2006, MNRAS, 373, 906

McGaugh, S. S., & Bothun, G. D. 1990, AJ, 100, 1073

Oosterloo, T., Morganti, R., Crocker, A., et al. 2010, MNRAS, 409, 500

Prieur, J.-L. 1988, ApJ, 326, 596

Quinn, P. J. 1984, ApJ, 279, 596

Rampazzo, R., Alexander, P., Carignan, C., et al. 2006, MNRAS, 368, 851

Rampazzo, R., Marino, A., Tantalo, R., et al. 2007, MNRAS, 381, 245

Renaud, F., Bournaud, F., & Duc, P.-A. 2015, MNRAS, 446, 2038

Richter, O.-G., Sackett, P. D., & Sparke, L. S. 1994, AJ, 107, 99

Sage, L. J., & Wrobel, J. M. 1989, ApJ, 344, 204

Sansom, A. E., Hibbard, J. E., & Schweizer, F. 2000, AJ, 120, 1946

Schiminovich, D., van Gorkom, J. H., van der Hulst, J. M., & Kasow, S. 1994, ApJ, 423, L101

Schiminovich, D., van Gorkom, J. H., van der Hulst, J. M., & Malin, D. F. 1995, ApJ, 444, L77

Schiminovich, D., van Gorkom, J., van der Hulst, T., Oosterloo, T., & Wilkinson, A. 1997, in The Nature of Elliptical Galaxies; 2nd Stromlo Symposium, eds. M. Arnaboldi, G. S. Da Costa, & P. Saha, ASP Conf. Ser., 116, 362

Schiminovich, D., van Gorkom, J. H., & van der Hulst, J. M. 2013, AJ, 145, 34

Schweizer, F. 1990, Interactions in Our Time, ed. R. Wielen (Berlin, Heidelberg: Springer), 60

Schweizer, F., & Seitzer, P. 1992, AJ, 104, 1039

Serra, P., Trager, S. C., Oosterloo, T. A., & Morganti, R. 2008, A&A, 483, 57

Sofue, Y., Wakamatsu, K.-I., Taniguchi, Y., & Nakai, N. 1993, PASJ, 45, 43

Solomon, P. M., & Vanden Bout, P. A. 2005, ARA&A, 43, 677

Tateuchi, K., Konishi, M., Motohara, K., et al. 2015, ApJS, 217, 1

Toomre, A., & Toomre, J. 1972, ApJ, 178, 623

Turnbull, A. J., Bridges, T. J., & Carter, D. 1999, MNRAS, 307, 967

Ueda, J., Iono, D., Yun, M. S., et al. 2014, ApJS, 214, 1

van Driel, W., Arnaboldi, M., Combes, F., & Sparke, L. S. 2000, A&AS, 141, 385

van Gorkom, J. 2000, in Radio interferometry: The Saga and the Science, eds. D. G. Finley, & W. M. Goss, 137

Weil, M. L., & Hernquist, L. 1993, ApJ, 405, 142

Whitmore, B. C., Lucas, R. A., McElroy, D. B., et al. 1990, AJ, 100, 1489

Whitmore, B. C., Schweizer, F., Leitherer, C., Borne, K., & Robert, C. 1993, AJ, 106, 1354

Wiklind, T., Combes, F., & Henkel, C. 1995, A&A, 297, 643

Young, L. M. 2002, AJ, 124, 788

Young, L. M., Bureau, M., Davis, T. A., et al. 2011, MNRAS, 414, 940

Appendix A: Molecular content of the companions

The companion of the shell galaxy NGC 474 (Arp 227) is a late-type spiral galaxy, NGC 470, which is rich in HI and CO emission. It is likely that the HI extension that covers NGC 474 (see Fig. 3) has been accreted from this companion. The beams observed in NGC 470 are displayed in Fig. 2. The spectra maps in CO(1–0) and CO(2–1) are displayed in Figs. A.1 and A.2, respectively. Isocontours of the surface density and the velocity fields are plotted in Fig. A.3.

The other member of the pair in Arp 295 is an edge-on spiral galaxy that is rich in molecular gas. The pointings are displayed in an *Hubble* Space Telescope (HST) F814W image in Fig. A.4. CO spectra in Arp 295S are plotted in Figs. A.5 and A.6. The molecular content in each beam is detailed in Table A.1.

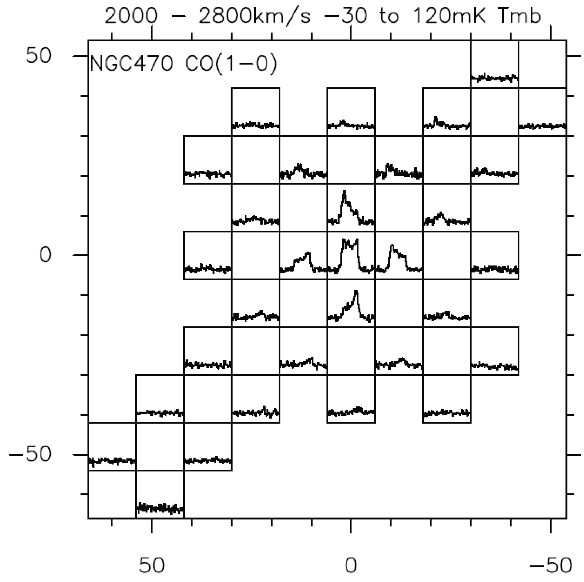

Fig. A.1. CO(1–0) map of spectra in NGC 470.

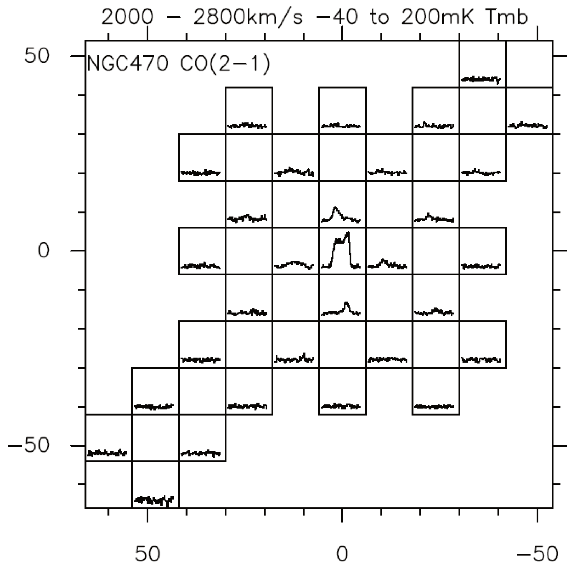

Fig. A.2. CO(2–1) map of spectra in NGC 470.

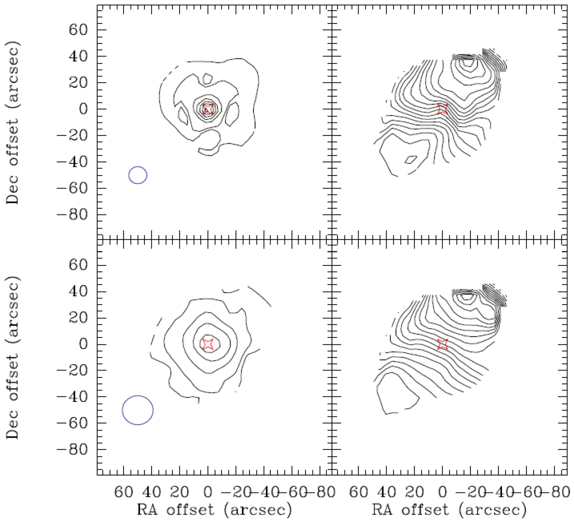

Fig. A.3. Isocontours of NGC 470 for CO(2–1) (*upper panels*) and CO(1–0) (*lower panels*), the *right panels* display the corresponding velocity fields. The isovels are spaced by 20 km s^{-1}; they range from 2200 km s^{-1} (NW) to 2560 km s^{-1} (SE).

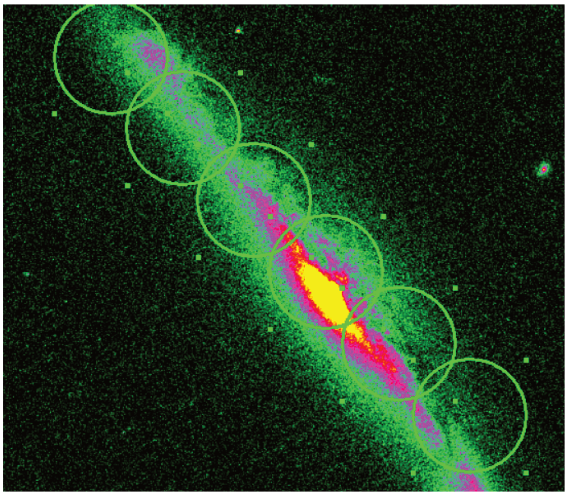

Fig. A.4. CO(2–1) 11″ beams observed toward Arp 295S, overlaid on an HST F814W image.

Table A.1. CO results for the companions.

Galaxy	Offsets	CO(1–0)			CO(2–1)				
	($''$,$''$)	Int-flux Jy km s^{-1}	V km s^{-1}	ΔV km s^{-1}	Int-flux Jy km s^{-1}	V km s^{-1}	ΔV km s^{-1}	M(H$_2$) 10^8 $M_\odot$	Σ(H$_2$) $M_\odot$ pc^{-2}
NGC 470	(0,0) see	126 ± 2 31 pt	66 ± 2 map	252 ± 4	216 ± 2	88 ± 1	246 ± 2	14 ± 0.2	151
ARP 295S	(0,0)	35.3 ± 3	82 ± 22	512 ± 48	<4	–	–	32.5 ± 3	42
	(−7,−7)	39 ± 3.5	−82 ± 16	355 ± 40	27.1 ± 2.5	−74 ± 11	256 ± 24	36 ± 3	47
	(−14,−14)	19 ± 1.6	−173 ± 10	248 ± 25	6.4 ± 1.3	−150 ± 7	80 ± 23	17 ± 1.5	22
	(7,7)	22 ± 2	−192 ± 12	238 ± 27	6.5 ± 3	239 ± 38	176 ± 96	20.3 ± 2	26
	(14,14)	9.2 ± 1.1	256 ± 11	169 ± 25	<2.5	–	–	8.5 ± 1	11
	(21,21)	3.6 ± 0.7	272 ± 7	71 ± 17	<2.5	–	–	3.3 ± 0.6	4

Notes. Integrated flux, velocity, and FWHM obtained through Gaussian fits. Velocities are counted from the central redshifts indicated in Table 1 for the companion galaxy. The H_2 masses are estimated within the CO(1–0) beam of 23$''$, with the standard conversion factor of the Milky Way $\alpha = 4.36\,M_\odot\,(\mathrm{K\,km\,s^{-1}\,pc^2})^{-1}$. Upper limits are given at 3σ, assuming an FWHM of 300 km s^{-1}.

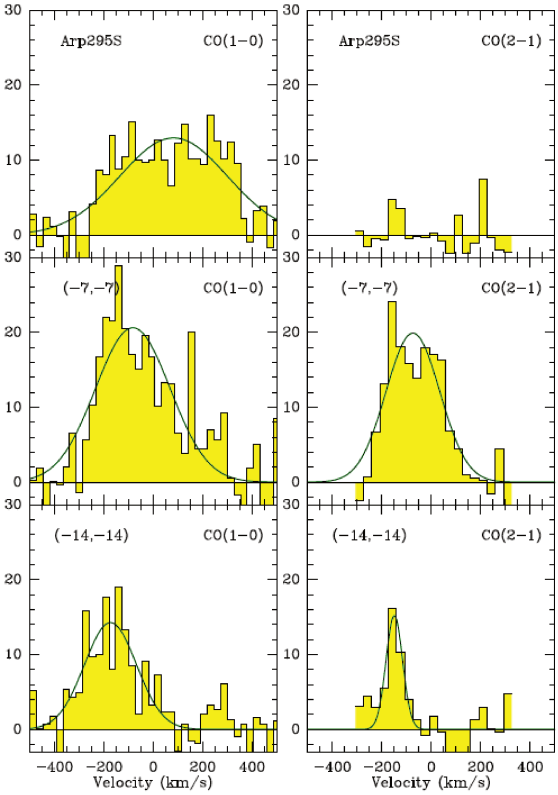

Fig. A.5. CO spectra in Arp 295S, central position and offsets (in arcsec). The vertical axis is the main-beam temperature in mK.

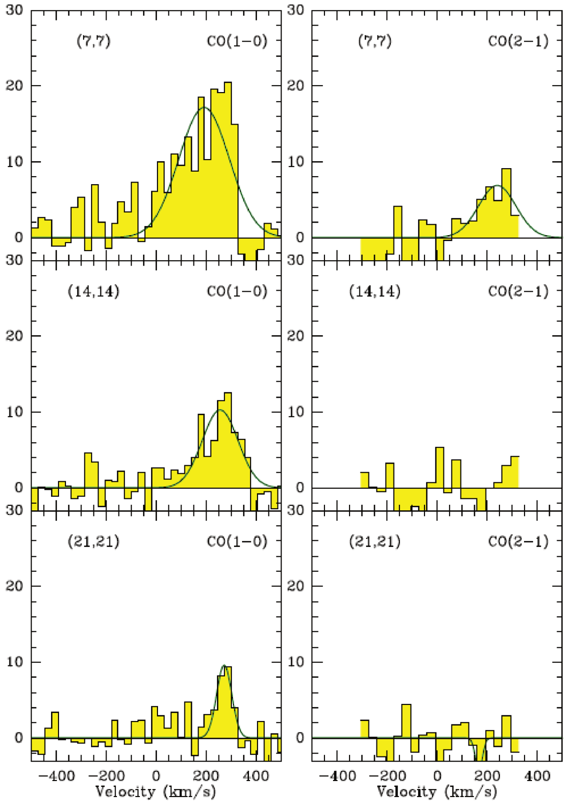

Fig. A.6. CO spectra in Arp 295S (following), northern offsets (in arcsec). The vertical axis is the main-beam temperature in mK.

Chapter 5

The molecular gas content of ultra-diffuse galaxies

5.1 Overview

One of the most lively debates over the past four years in extragalactic astronomy has been the detection of a large number of galaxies dubbed as Ultra-Diffuse Galaxies (UDG). They are known as UDG since they are mainly characterized by very faint central surface brightness (μ(g,0)) = 24 − 28 mag arcsec^{-2}) and large effective radii ($R_{\mathrm{eff}} \sim$ 800 pc − 1.5 kpc), even as large as our own galaxy, the Milky Way. Therefore, they are considered as dwarfs in terms of luminosity yet giants in terms of size. UDGs appear to be more numerous than the galaxy population of higher surface brightness, span a wide range of environments (from clusters to filaments), and are extremely dark matter dominated (stellar masses of $\sim 10^7 \cdots 5\times 10^8$ M$_\odot$, while dynamical masses are $\sim 10^{10}$ M$_\odot$, Beasley et al., 2016).

5.1.1 Incidence of UDGs

UDGs have been detected mainly in high density environments. The first UDGs were identified in the Coma cluster by van Dokkum et al. (2015a,b), where it was reported a sample of 47 UDGs observed thanks to the facilities of the Dragonfly Array Telescope (Abraham and van Dokkum, 2014). Most UDGs reported in this study appear to be close to the red sequence, although there are sometimes trails of blue populations, similar to those observed in LSB galaxies, which are, however, bluer and brighter (see e.g., McGaugh et al., 1995; Impey et al., 1988; Schombert et al., 2011).

After these detections, more UDGs were identified in galaxy clusters by means of state-of-the-art data reduction pipelines applied to existing archives (see e.g., MegaCam Camera, CFHT, Duc et al., 2015). For example, Koda et al. (2015) discovered 854 UDGs in the Coma cluster using deep R band images (with partial B, i, and H$_\alpha$ band coverage), observed with the Subaru telescope, of which 332 UDGs were Milky Way-sized with very large effective radii of R$_e$ > 1.5 kpc. Muñoz et al. (2015) reported the first detection of 158 undetected dwarf galaxies, including UDGs, in the Fornax cluster for the u, g, and i band image obtained with the wide field Dark Energy camera installed on the 4-m Blanco telescope at the Cerro Tololo Interamerican Observatory as part of the Next Generation Fornax Survey (NGFS). Mihos et al. (2015), identified three UDGs in Virgo Cluster using deep, wide-field imaging with the Burrell Schmidt telescope, exhibiting a very low surface brightness limit of $\mu_{V,0}$ = 27 mag arcsec^{-2} and effective radius between 3 and 10 kpc. Yagi et al. (2016) presented a catalog of 854 deep Suprime-Cam/Subaru R-band images of UDGs, with data covering the 1°.7 × 2.°7 region of the Coma cluster. Román and Trujillo (2017) studied the spatial distribution of Ultra-Diffuse galaxies within an area of 8×8 Mpc^2 centered around the galaxy cluster Abell 168 (z = 0.045). They found 80 UDGs in the cluster and for the first time in the large-scale structure that surrounds it. Around 50 % of their UDGs analyzed in the selected area inhabit the cluster region, whereas the remaining UDGs were found outside the main cluster structure (∼50 %). van der Burg et al. (2017) measured the abundance of UDGs in 325 spectroscopically selected groups from the Galaxy And Mass Assembly (GAMA) survey, finding ∼2500 UDGs. They concluded that in comparison to bright galaxies, UDGs are relatively more abundant in massive clusters than in groups. Venhola et al. (2017) identified 9 UDGs from deep g', r' and i'-band images of the Fornax Deep Survey, in an area of 4 deg^2 in the center of the Fornax cluster. In the most recent study so far, He et al. (2019) discovered 11 edge-on HI-bearing Ultra-Diffuse Sources (HUDS) after correcting the observed central surface brightness to a face-on perspective, from the 40% ALFALFA catalog, which is based on SDSS g- and r-band images.

Many UDGs also have been detected in low density environments and in few group samples (Merritt et al., 2016; Martínez-Delgado et al., 2016; Trujillo et al., 2017; Román and Trujillo, 2017; Shi et al., 2017; Spekkens and Karunakaran, 2018; Bennet et al., 2018), as well as isolated sources, such as HI-bearing Ultra-Diffuse Sources (HUDS) from ALFALFA survey by Leisman et al. (2017), and two extended dwarf irregular galaxies similar to UDGs found in Bellazzini et al. (2017).

5.1.2 Origin and formation mechanisms of UDGs

It is unclear whether UDGs have low metallicity populations of young stars, and hence a signature of recent star formation, or evolved populations consistent with the red integrated colors. Morphologically they seem to fit well with a Sérsic profile with $n \sim 1$, similar to exponential discs (see e.g. Koda et al., 2015; van Dokkum et al., 2015a), n<1 (Yagi et al., 2016; Merritt et al., 2016; Venhola et al., 2017), and only a few with n >1 (or even n∼4) (Yagi et al., 2016; Lee et al., 2017; Müller et al., 2018). Some of them show signs of tidal disruption, like those in the Virgo cluster (Mihos et al., 2015). Their stellar mass densities are very low (a few $\mathrm{M}_\odot\ \mathrm{pc}^{-2}$, some two orders of magnitude smaller than Milky Way-type galaxies) and constitute a challenge for galaxy formation models.

There is a very active discussion in the scientific community on UDGs, since their origin is still unclear and speculative. Initially, van Dokkum et al. (2015a) proposed that UDGs were "failed" L_* galaxies, i.e., giant Milky Way galaxies that stopped forming stars, whilst some authors suggested that they were dwarf galaxies with an unusually extending size (Di Cintio et al., 2019; Amorisco and Loeb, 2016; Lim et al., 2018). Nonetheless, new studies pointed out that UDGs may have diverse origins (see e.g., van Dokkum et al., 2015b; Muñoz et al., 2015; Zaritsky, 2017).

UDGs formation mechanism is still a mystery. They may have several formation scenarios, such as head-on collisions of galaxies or through tidal stripping of dwarf galaxies within clusters (Baushev, 2018; Carleton et al., 2019). Specifically, a possibility is that they are formed in processes into the cluster environment, and either started out as small, low mass galaxies or as very extended, low surface brightness disks (see e.g., Gnedin, 2003; Collins et al., 2013; Yozin and Bekki, 2015). Another suggestion is that tides have been responsible for the generation of some of the largest and faintest galaxies in the Local Group (Collins et al., 2013), and such processes are expected to be very effective in clusters (Yozin and Bekki, 2015). One more

Table 5.1: Summary of the properties of the sources.

Source	RA J2000	DEC J2000	Distance [Mpc]	cz [km s^{-1}]	R_{eff} ["]	M_* log$L_\odot$
DGSAT I	01:17:36	+33:31:42	78	5450±40	12.0	$\sim 4\ 10^8$
Dragonfly 44	13:00:58	+26:58:35	100	6340±60	8.7	$\sim 3\ 10^8$

hypothesis is that UDGs may represent the most rapidly rotating tail of the distribution of dwarf galaxies, since the size and surface brightness of a galaxy are related to its spin (Amorisco and Loeb, 2016).

5.1.3 The gas mass content

The role that gas plays in the UDGs formation may be paramount, although its participation is also unclear. One hypothesis is that as gas infalls into dark haloes it settles into a rotationally-supported disc at the lowest energy state given its specific angular momentum. Amorisco and Loeb (2016) argued that perhaps the large sizes of UDGs arise from very high angular momentum gas and the stars formed follow this distribution. Yet, their surface density appears to be smaller than the critical one to form stars (McKee and Krumholz, 2010), implying that some high-density gas had to be present to form the current stellar populations.

The gas may have left through ram pressure stripping (but there are UDGs in the field) or through feedback-driven galactic winds (but the efficiency of star formation appears to be very low), while quenching by the cluster (Yozin and Bekki, 2015) cannot be generic, just like a possible formation through outflows (Di Cintio et al., 2017). Perhaps the large dark matter content prevents the escape of stars and gas. Clearly, these galaxies are perhaps the best laboratories to understand star formation in the low density regime. The detection of cold atomic or molecular gas is hence crucial for the understanding of this new population of galaxies, with far-reaching implications for galaxy evolution.

5.2 Target Selection: DGSAT I and Dragonfly 44

Up to now there are over 1500 UDGs detected thus far, however at the time of the observations only two have measured redshifts at high precision: DGSAT I (see Figure 5.1) (Martínez-Delgado et al., 2016) and Dragonfly 44 (see Figure 5.2) (van Dokkum et al., 2016). Table 5.1 summarizes the main properties of these two galaxies, which are located in different environments (Dragonfly 44 in the Coma cluster, DGSAT I in the filament of Perseus-Pisces supercluster).

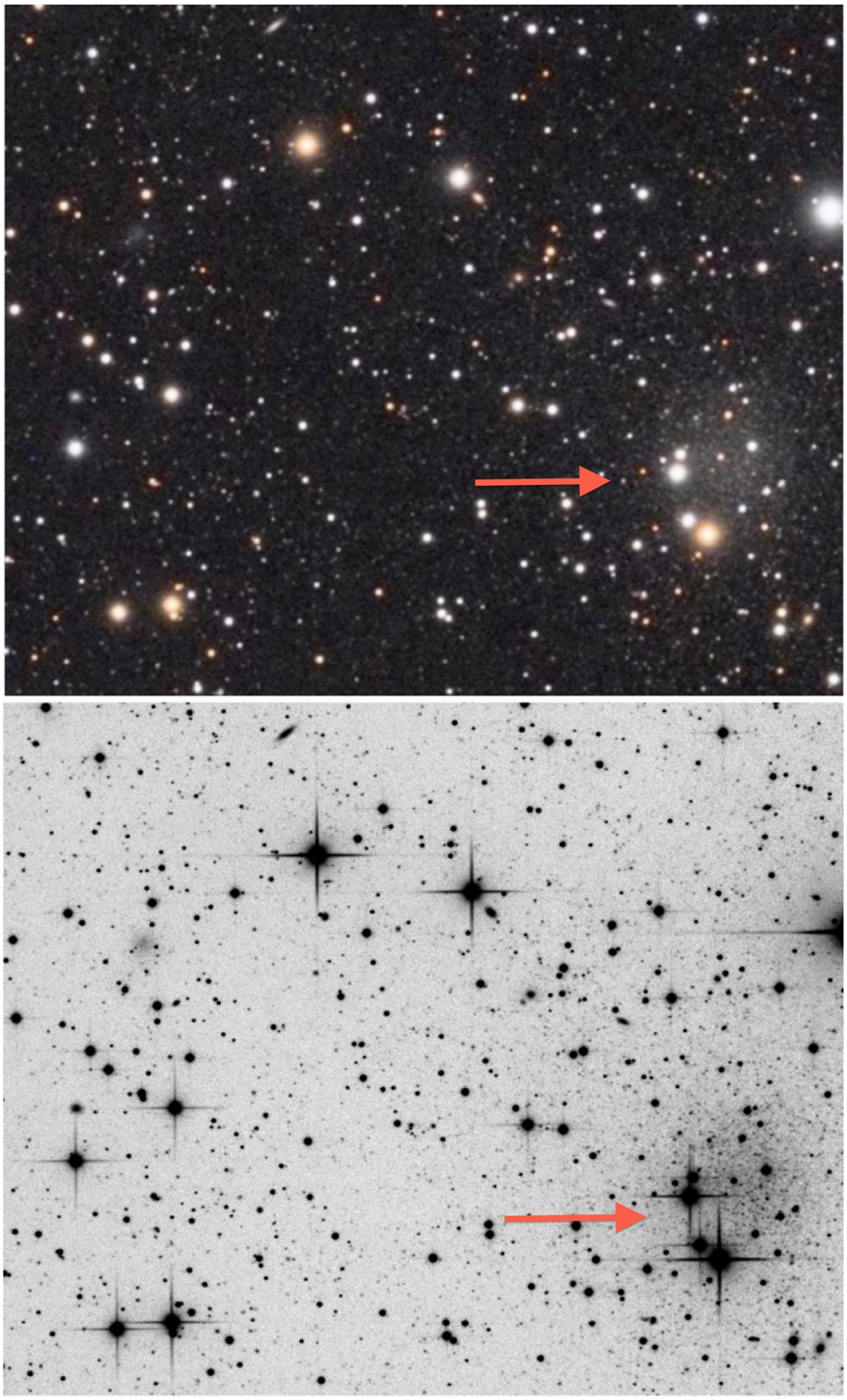

Figure 5.1: Follow-up small telescope images of DGSAT I (indicated with a red arrow): (top) color image obtained with the FNO TOA-150 refractor; (bottom) luminance filter image obtained with the ROSA 0.4 m telescope. The new dwarf is detected as a small cloud (top left) close to the And II dSph (bottom right), visible only ∼15' to the west. North is top, east is left. The field of view of these cropped images is ∼19' × 11' (Martínez-Delgado et al., 2016).

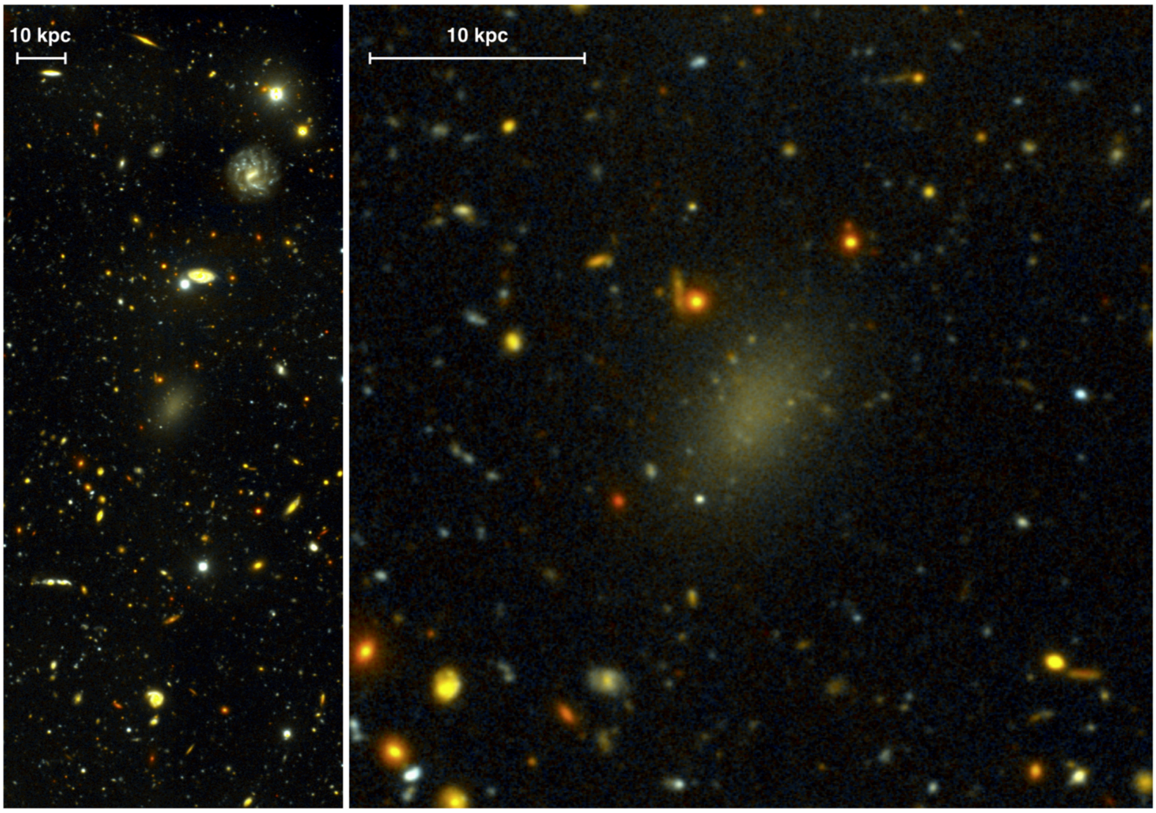

Figure 5.2: Deep Gemini g and i images were combined to create a color image of Dragonfly 44 and its immediate surroundings. The galaxy has a remarkable appearance: it is a low surface brightness, spheroidal object that is peppered with faint, compact sources. (van Dokkum et al., 2016).

5.3 Observations and data reduction

5.3.1 IRAM 30-m observations

Observations of the ^{12}CO(1-0) and ^{12}CO(2-1) line emission towards DGSAT I and Dragonfly 44 have been carried out at IRAM-30m telescope at Pico Veleta, Granada, Spain, during two sessions (December 2016 and March 2017). We used the E090 and the E230 EMIR bands simultaneously. The E090 band was tuned at the redshifted frequencies of the CO(1-0) line for DGSAT I and Dragonfly 44 (i.e., 113.2 GHz and 112.9 GHz, respectively) and the E230 band was tuned at the redshifted frequencies of the CO(2-1) line (i.e., 226.4 GHz and 225.8 GHz). The angular resolution was $\sim$ 22" and $\sim$11"at 3mm and at 1mm respectively. We use the WILMA autocorrelator (16 GHz of bandwidth) and the FTS200 autocorrelator (32 GHz of bandwidth), we observe both polarizations (H and V) to optimize the integration time. The observations were performed in beam switching mode, with a throw of 120", in oder to ensure flat baselines. The temperature scale used is in main beam temperature, T_{mb} . The main-beam efficiency is $\eta_{mb} = T^*_A / T_{mb} = 0.83$ and $S/T^*_A = 6.0$ Jy/K at 3mm, while at 1mm $\eta_{mb} = 0.64$ and $S/T^*_A = 7.5$ Jy/K. The pointing model was checked against bright, nearby calibrators for every source and every $\sim$1.6 hrs for long integrations, it was found to be accurate within $\sim$2 - 5". Calibration scans on the standard two load system were taken every 12 minutes. The line calibration was checked by observations toward the source calibrator DR21.

The data reduction was done with the CLASS program of the GILDAS software package (`http://www.iram.fr/IRAMFR/GILDAS`), and involved only the subtraction of (flat) baselines from individual integrations and the averaging of the total spectra. The spectra are given at a velocity resolution of 2 MHz = ~5.3 km s^{-1} at 3mm and at 1mm 2 MHz = ~ 2.6 km $^{-1}$. The total integration time was about 14.0 hrs and 18.7 hrs for DGSAT I and Dragonfly 44, respectively. Yielding a noise level of ~0.96 mK (T$_{mb}$) and ~0.82 mK (T$_{mb}$) at 3mm for DGSAT I and Dragonfly 44, respectively, and a noise level of ~2.14 mK (T$_{mb}$) and ~ 1.86 mK (T$_{mb}$) at 1mm for DGSAT I and Dragonfly 44 (see Table 5.3 for a summary).

5.3.2 Nançay observations

We use the Nançay Radio Telescope (NRT, France) in order to observe the HI line at 1420.40 MHz. The NRT is a transit instrument of the unusual Kraus-type design, with two mirrors. The flat, tilting primary mirror consists of ten panels, each 20 m long and 40 m high; it reflects radio waves towards the fixed secondary mirror 460 m to the south. The secondary mirror is shaped as a section of a sphere with a radius of 560 m. Its collecting area is about 8000 m^2, equivalent to that of a 94-m-diameter parabolic dish. The half-power beam width at 21 cm is 3'.06 (E-W) × 22'(N-S) at zero declination. The NRT is a high sensitivity (1.4 K/Jy at 21cm) telescope, for which the maximum integration time per day for a source at δ = 0 deg is typically about one hour (ON +OFF), this time increases as 1/cos (DEC), whereas the efficiency decreases at the same factor. The HI observations were carried out during January 2017. We use the Low Frequency Receiver (1.1-1.8 GHz). The digital auto-correlator was set to have a total bandwidth 50 MHz. The 8192 frequency channels were split into four banks. The system temperatures are about 35 K at 21cm.

The Nançay data reduction was done with the CLASS program of the GILDAS software package. The spectra are given at a (Hanning-smoothed) velocity resolution of 25.1 kHz = ~5.3 km s^{-1}. The total integration time was about 2.55 hrs and 1.2 hrs for DGSAT I and Dragonfly 44, respectively, yielding a noise level of ~2.19 mK (T$_A^*$) and ~ 2.78 mK (T$_A^*$). We considered an efficiency of 1.18 K/Jy for DGSAT I and of 1.25 K/Jy for Dragonfly 44.

5.4 Preliminary results

5.4.1 Upper limits on the content of atomic and molecular gas

To compute the **upper limit of the atomic gas** we used the following relation,

$$M_{HI} = 2.36 \times 10^5 D_L^2 S_{HI} \Delta v \tag{5.1}$$

where $S_{HI}\Delta v$ is the integrated line flux density in Jy km/s, D$_L$ is the luminosity distance to the source in Mpc (Roberts, 1962). We assume a v=50 kms^1. For a 3-sigma upper limit and using equation 5.1, we obtained the upper limit estimation of the atomic gas M$_{HI}$ = 5.57×10^8 M$_\odot$ for DGSAT I and M$_{HI}$ = 1.23×10^9 M$_\odot$ for Dragonfly 44 (see Table 5.2 and Figure 5.3).

Table 5.2: Summary of the HI line observations using the Nançay telescope. We have calculated the M_{HI} assuming a 3σ upper limit.

Source	rms [mK]	Δv [km s^{-1}]	M_{HI} [M$_\odot$]
DGSAT I	2.19	5.3	5.57×10^8
Dragonfly 44	2.78	5.4	1.23×10^9
Stack	1.80	6.0	-

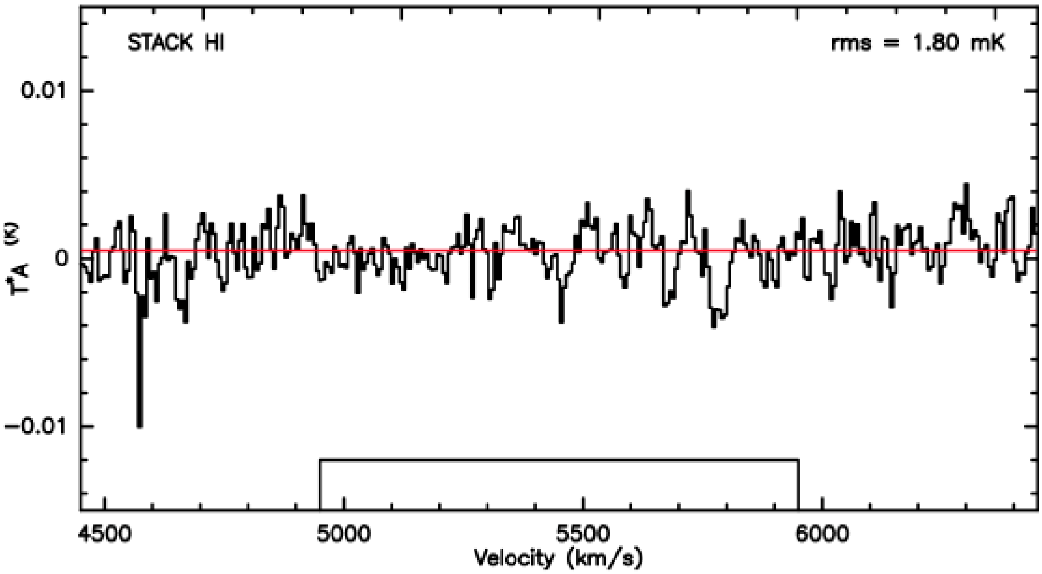

Figure 5.3: Stacking of the data for the HI line.

To compute the **upper limit of the molecular gas** we used the following relation in which we take into the account the factor correction for helium,

$$\frac{M_{mol}}{M_\odot} = 1.35\alpha_{CO}\frac{L_{CO}}{Kkms^{-1}pc^2} \tag{5.2}$$

We assume a α_{CO}=4.3 M$_\odot$(Kkms^{-1})$^{-1}$. The L_{CO} relate to the observed integrated flux density in galaxies via:

$$L_{CO} = 2.453 S_{CO}\Delta v\frac{D_L^2}{1+z} \tag{5.3}$$

where $S_{CO}\Delta v$ is the integrated line flux density in Jy km/s, D$_L$ is the luminosity distance to the source in Mpc, and z is the redshift (Solomon and Vanden Bout, 2005). We assume Δv=50 km s^{-1}. For a 3 sigma upper limit, we obtained a L_{CO}=1.27×10^7 K km s^{-1} pc^2 for DGSAT I and L_{CO}=1.77×10^8 K km s^{-1} pc^2 for Dragonfly 44. Using equation 5.2, we deduce an upper gas limit of M_{mol}= 7.37×10^7 M$_\odot$ for DGSAT I and M_{mol}= 1.03×10^8 M$_\odot$ for Dragonfly 44 (see Table 5.3, the spectra in Figures 5.4, 5.5 and the stacking in Figures 5.6, 5.7).

Table 5.3: Summary of the CO line observations using the IRAM 30-m telescope. We have calculated the M_{H2} assuming a 3σ upper limit.

Source	rms (CO(1-0)) [mK]	$\Delta v(CO(1-0))$ [km s^{-1}]	rms (CO(2-1)) [mK]	$\Delta v(CO(2-1))$ [km s^{-1}]	M_{H2} [$M_\odot$]
DGSAT I	0.96	5.3	2.14	2.6	7.37×10^{7}
Dragonfly 44	0.82	5.3	1.86	2.7	1.03×10^{8}
Stack	0.56	6.0	1.10	6.0	-

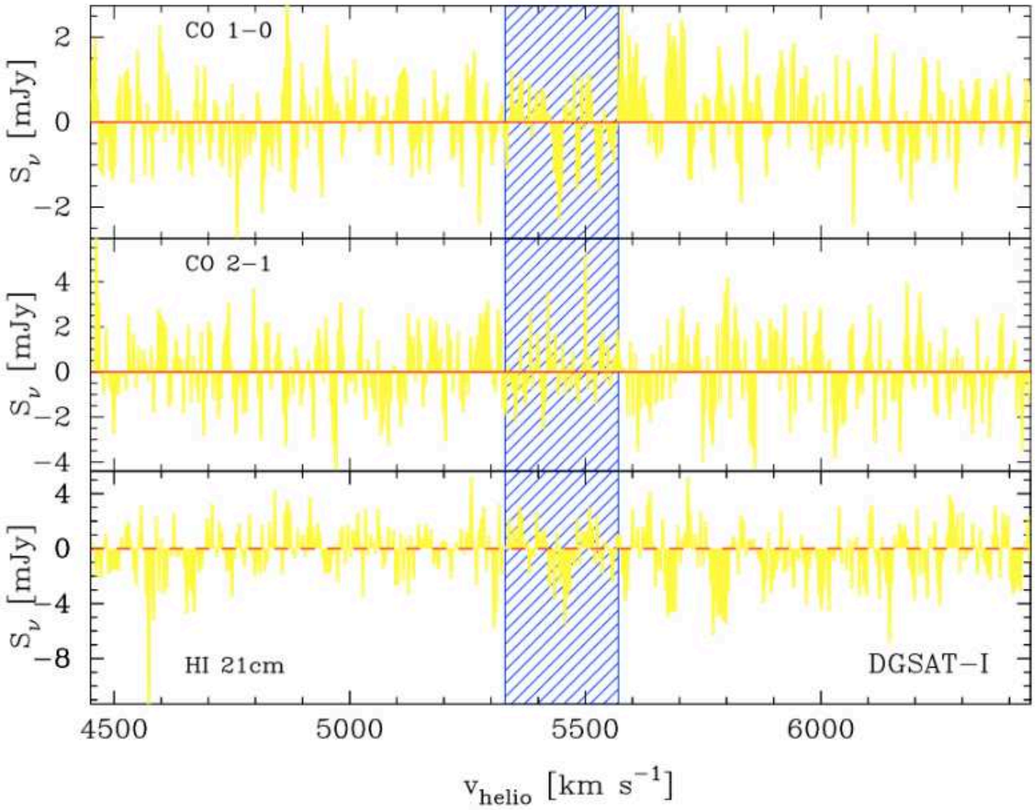

Figure 5.4: Upper limits for CO(1-0), CO(2-1) and HI-21 cm emission lines for DGSAT-I.

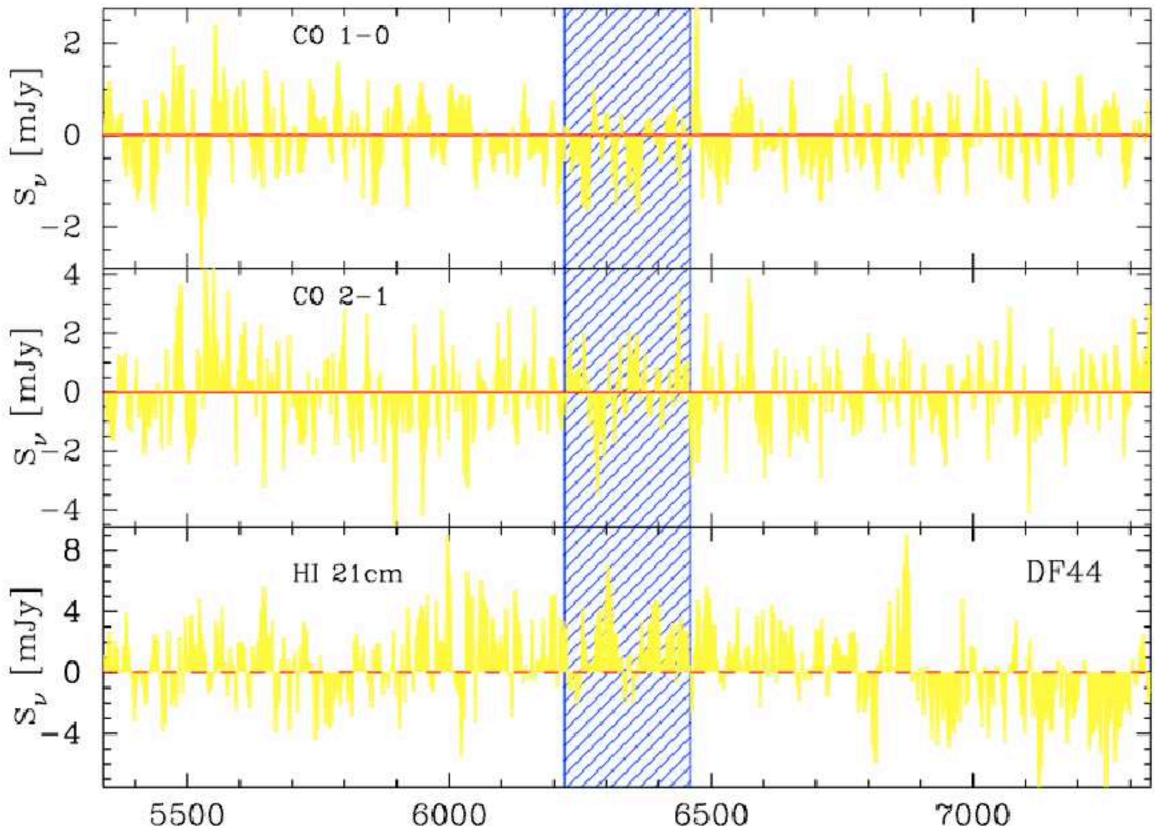

Figure 5.5: Upper limits for CO(1-0), CO(2-1) and HI-21 cm emission lines for Dragonfly 44.

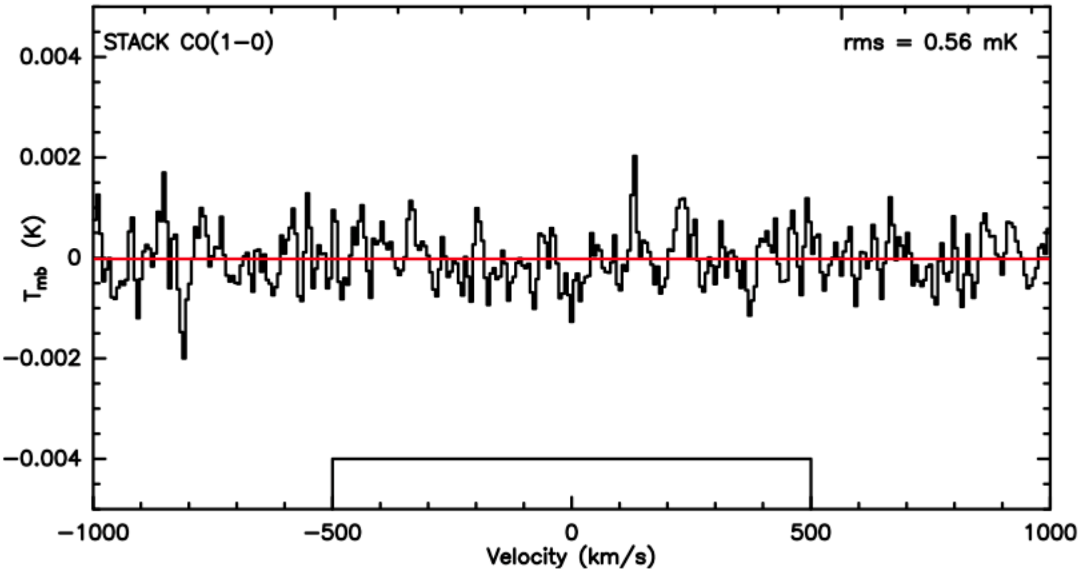

Figure 5.6: Stacking of the data for the CO (1-0) line.

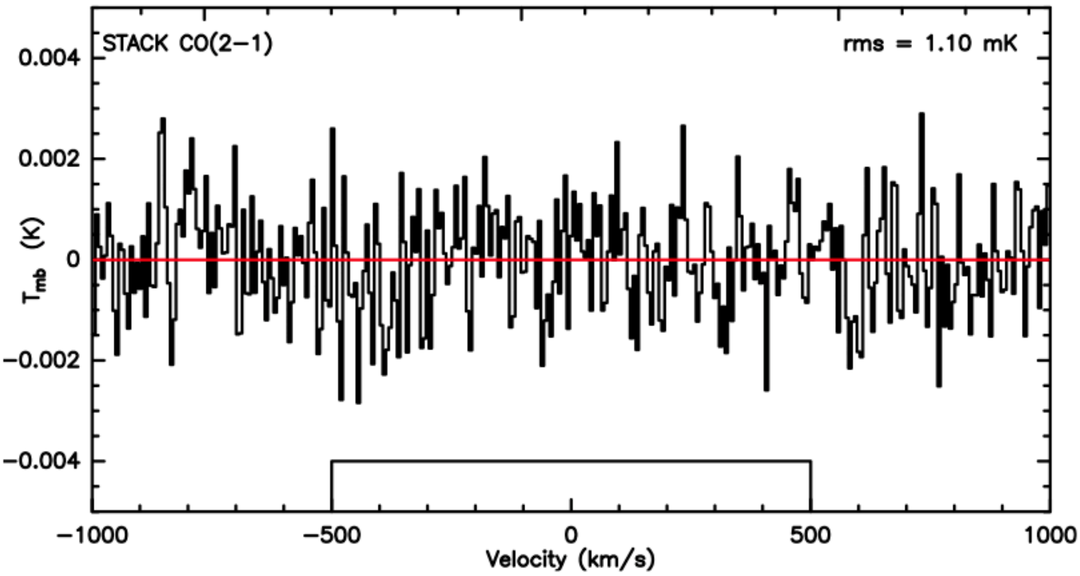

Figure 5.7: Stacking of the data for the CO (2-1) line .

5.5 Conclusions and perspectives

The lack of cold gas, both in the atomic and molecular phases, sets stringent constraints on the current star formation efficiency in ultra–diffuse galaxies. Should this efficiency be the same at earlier times, it would imply a major revision of their star formation histories, and indeed on the way star formation proceeds in environments where the stellar and gas mass surface densities are very low.

Chapter 6

Conclusions

This PhD project has been dedicated to the study of galaxies under the regime of the low surface brightness Universe, from both observational and theoretical perspectives. Specifically, I have used semi-empirical models, hydro-dynamical numerical simulations and observations on molecular gas content in LSB galaxies, in order to have a comprehensive analysis and make inferences on the origin and mechanism formation for this type of galaxies. Below I summarize the results obtained in this thesis.

Chapter 1 describes a powerful statistical method that links the properties of the baryonic galaxy and dark matter halo by inspecting the galaxy scaling relations and their internal mass distributions. Our results constrain the models and N-body simulations of galaxy evolution and allow us to constrain the key astrophysical processes as a function of the mass. By using these restrictions for both early- and late-type galaxies, we have mapped different correlations for galactic disk-bulge-halo systems, as well as for the luminous-to-dynamical mass ratios (including dark matter) evaluated at different effective radius. We have made comparisons between predictions of the semi-empirical approach with the structural-dynamic correlations of observed galaxies and the internal dynamic as well. We have generated a mock catalog of a volume-complete local galaxy population into boxes of the Bolshoi-Planck, Small MultiDark-Planck and MultiDark-Planck ΛCDM numerical simulations and we have used HI and H_2 mass fractions. For each mock galaxy seeded in its respective halo, we applied a static model, where a disk-bulge is loaded inside the halo (taking into account the adiabatic contraction) in order to generate a disk-bulge-halo in centrifugal equilibrium, computing its stellar and gas radial distributions. After to applying an heuristic approach and including a merger fraction in order to tune the underlying parameters, we have reproduced the observational correlations of radius-M_*, B/T–M_* at high masses, making our method a sophisticated tool to estimate the *initial spin parameter of the baryons from which disc galaxies form*, $\lambda_{\rm bar}$. Up to $\log(M_h/{\rm M}_\odot)\sim 11.5$, $\lambda_{\rm bar}$ and its dispersion are the same than those of dark matter halos, but at larger masses $\lambda_{\rm bar}$ decreases with M_h (and hence M_*). The predicted stellar and baryonic TF relations agree with observations. There is no problem with the zero point, since by construction our models are in agreement with the observed baryonic (and stellar) mass function. After having explored the effects of the global $M_{\rm bar}$–M_h relation and its dispersion on the internal mass distributions of our mock galaxies, we found that those disk galaxies with a disk-to-total velocity ratio at 2.2 scale radius are always of sub-maximal type. The "luminous" mass fraction evaluated at one effective radius (1 R_e) has its maximum (about 0.5 on average) for galaxies with $V_{\rm max} \approx 200$ km/s, ≈ 500 ${\rm M}_\odot/{\rm pc}^2$ and $M_* \approx 5 \times 10^{10}$ ${\rm M}_\odot$. For lower values than B/T≤ 0.5, disk galaxies are more dominated by dark matter at 1 R_e, but for larger values, a clear print of the $M_{\rm bar}$–M_h relation shape is shown.

In Chapter 2 we have exploited a hydrodynamical simulation, re-simulated from a cosmological context, in order to analyze and interpret the morphologies and survival time-scales of fine structures, which are tracers of mergers and of the mass assembly history of present day early-type galaxies. We made a census of three types of fine structures by visual inspection: tidal tails, stellar streams and shells. The number of fine structures detected around the central galaxy versus time allows us to reconstruct its merger history. We find three phases in the central galaxy evolution, the second one being a very quiet phase. The census of fine structures are made in correspondence with the identified merger events. This allowed us to establish several specific points. Tidal tails results from major mergers events (1.5:1), stellar streams from minor mergers (10:1) and shells from major and intermediate-mass mergers (4:1). Tidal tails and shells have long survival times, ∼2 Gyr and ∼3Gyr, respectively, but streams remains visible in all phases of galaxy evolution. The detection of stellar streams are strongly dependent on the surface brightness limit. We see between two and three times more streams based on a surface brightness cut of 33 mag arcsec^{-2} than with 29 mag arcsec^{-2}. The detection of shells depends strongly dependent upon the projection angle. Our results are compatible with previous comparable simulations; however, our zoom-in re-simulation from a cosmological context brings more realistic conditions to estimate the survival time-scales of fine structures around today early-type galaxies. As for an observer point of view, the reconstruction of the merger history is better obtained with shells, which have the longer time-scales. The number of shells can also indicate the time since the last merger. Streams have shorter time-scales, so when no fine structure is observed, this means either no event since 2 Gyr, or very minor merger with a large angular momentum, which produces more streams than shells.

Chapter 3 describes the results from observations of molecular gas detections on several regions in some shell galaxies. We have carried out CO(1-0) and CO(2-1) line observations of nine shell galaxies with the IRAM-30m telescope. Molecular gas was detected in six of them, together with two of the companions. In three of the detected galaxies (Arp 230, NGC 3032 and Arp 205N), we cannot conclude that gas is detected in the shells, the detection is compatible with gas in the inner rotating disk. In the three remaining galaxies (Arp 10, NGC 3656 and NGC 3934), molecular gas is clearly detected in the shells, with a velocity close to systemic and not in continuity with the inner rotating disk. The amount of molecular gas is estimated at $M(H_2) = 3.4\ 10^9\ M_\odot$ in the shells outside the ring in Arp 10, $3.8\ 10^8\ M_\odot$ in the southern shell of NGC 3656, and $2.6\ 10^8\ M_\odot$ in the two detected shells of NGC 3934. The mechanism to form those gaseous shells might be different. For two cases at least (Arp 10, NGC 3656), the encounter with the small companion had a very small impact parameter, and the phase-wrapping in a nearly radial orbit must be playing the major role. The morphology of Arp 10 corresponds to an oblate system, as well as most shells in NGC 3656. However, the major shell might be only the end of the tidal tail. The gas of the companion of NGC 3656 has left a radial trace, visible as a contrasted dust lane, and the major shell is found in continuity, indicating the companion orbit and that of the tidal debris. NGC 3934 main body is seen nearly edge-on on the sky, and the situation is less clear. Shells distributed symmetrically at about 40° of the minor axis are clearly detected in molecular gas. The fact that gas can be detected in shells tend to support the clumpiness and low dissipative character of a large part of the interstellar medium. The line profiles in the shells reveal a two-horn shape, indicating the presence of both positive and negative angular momentum relative to the primary galaxy. This supports the CO detection in shells, since it is impossible to explain a two-horn profile in the outer parts of a rotating galaxy disk. Material from the companion must have infallen in a nearly radial orbit, part of it with a positive and the other part a negative impact parameter. The material acquired a tangential velocity at apocenter. The shells are then also phase-wrapped. Follow-up with higher spatial resolution is required to test the relative position of gas and stellar shells, to confirm the dynamical mechanism.

In Chapter 4 we report the upper mass limits for two ultra-diffuse galaxies, which have been highly discussed in the literature due to their particular properties. We have performed observations of the ^{12}CO(1-0) and ^{12}CO(2-1) line emission towards DGSAT I and Dragonfly 44 Ultra-Diffuse Galaxies, carried out at IRAM-30m telescope at Pico Veleta, Granada, Spain and at Nançay Radio-Telescope in France. The target galaxies have a measured redshift. We have obtained the upper limit estimation of the atomic gas M_{HI} = 5.57×10^8 $M_\odot$ for DGSAT I and M_{HI} =1.23×10^9 $M_\odot$ for Dragonfly 44. For a 3 sigma upper limit, we have deduced an upper gas limit of M_{mol}= 7.37×10^7 $M_\odot$ for DGSAT I and M_{mol}= 1.03×10^8 $M_\odot$ for Dragonfly 44. We conclude that the lack of cold gas, both in the atomic and molecular phases, sets stringent constraints on the current star formation efficiency in Ultra–Diffuse Galaxies. Should this efficiency be the same at earlier times, it would imply a major revision of their star formation histories, and indeed on the way star formation proceeds in environments where the stellar and gas mass surface densities are very low.

Bibliography

Abraham, R. G. and van Dokkum, P. G. (2014). Ultra-Low Surface Brightness Imaging with the Dragonfly Telephoto Array. *PASP*, 126:55.

Akritas, M. G. and Bershady, M. A. (1996). Linear Regression for Astronomical Data with Measurement Errors and Intrinsic Scatter. *ApJ*, 470:706.

Alatalo, K., Davis, T. A., Bureau, M., Young, L. M., Blitz, L., Crocker, A. F., Bayet, E., Bois, M., Bournaud, F., Cappellari, M., Davies, R. L., de Zeeuw, P. T., Duc, P.-A., Emsellem, E., Khochfar, S., Krajnović, D., Kuntschner, H., Lablanche, P.-Y., Morganti, R., McDermid, R. M., Naab, T., Oosterloo, T., Sarzi, M., Scott, N., Serra, P., and Weijmans, A.-M. (2013). The ATLAS^{3D} project - XVIII. CARMA CO imaging survey of early-type galaxies. *MNRAS*, 432:1796–1844.

Allen, J. T., Croom, S. M., Konstantopoulos, I. S., Bryant, J. J., Sharp, R., Cecil, G. N., Fogarty, L. M. R., Foster, C., Green, A. W., Ho, I.-T., Owers, M. S., Schaefer, A. L., Scott, N., Bauer, A. E., Baldry, I., Barnes, L. A., Bland-Hawthorn, J., Bloom, J. V., Brough, S., Colless, M., Cortese, L., Couch, W. J., Drinkwater, M. J., Driver, S. P., Goodwin, M., Gunawardhana, M. L. P., Hampton, E. J., Hopkins, A. M., Kewley, L. J., Lawrence, J. S., Leon-Saval, S. G., Liske, J., López-Sánchez, Á. R., Lorente, N. P. F., McElroy, R., Medling, A. M., Mould, J., Norberg, P., Parker, Q. A., Power, C., Pracy, M. B., Richards, S. N., Robotham, A. S. G., Sweet, S. M., Taylor, E. N., Thomas, A. D., Tonini, C., and Walcher, C. J. (2015). The SAMI Galaxy Survey: Early Data Release. *MNRAS*, 446:1567–1583.

Amorisco, N. C. (2015). On feathers, bifurcations and shells: the dynamics of tidal streams across the mass scale. *MNRAS*, 450:575–591.

Amorisco, N. C. and Loeb, A. (2016). Ultradiffuse galaxies: the high-spin tail of the abundant dwarf galaxy population. *MNRAS*, 459:L51–L55.

Appleton, P. N. and Struck-Marcell, C. (1996). Collisional Ring Galaxies. *Fund. Cosmic Phys.*, 16:111–220.

Aquino-Ortíz, E., Valenzuela, O., Sánchez, S. F., Hernández-Toledo, H., Ávila-Reese, V., van de Ven, G., Rodríguez-Puebla, A., Zhu, L., Mancillas, B., Cano-Díaz, M., and García-Benito, R. (2018). Kinematic scaling relations of CALIFA galaxies: A dynamical mass proxy for galaxies across the Hubble sequence. *MNRAS*, 479:2133–2146.

Argudo-Fernández, M., Shen, S., Sabater, J., Duarte Puertas, S., Verley, S., and Yang, X. (2016). The effect of local and large-scale environments on nuclear activity and star formation. *A&A*, 592:A30.

Arp, H. (1966). Atlas of Peculiar Galaxies. *ApJS*, 14:1.

Athanassoula, E. and Bosma, A. (1985). Shells and rings around galaxies. *ARA&A*, 23:147–168.

Atkinson, A. M., Abraham, R. G., and Ferguson, A. M. N. (2013). Faint Tidal Features in Galaxies within the Canada-France-Hawaii Telescope Legacy Survey Wide Fields. *ApJ*, 765:28.

Avila-Reese, V. (2007). Understanding Galaxy Formation and Evolution. *Astrophysics and Space Science Proceedings*, 2:115.

Avila-Reese, V., Carrillo, A., Valenzuela, O., and Klypin, A. (2005). Secular evolution of galactic discs: constraints on phase-space density. *MNRAS*, 361(3):997–1004.

Avila-Reese, V. and Firmani, C. (2000). Properties of Disk Galaxies in a Hierarchical Formation Scenario. *RevMexAA*, 36:23.

Avila-Reese, V., Firmani, C., and Hernández, X. (1998). On the Formation and Evolution of Disk Galaxies: Cosmological Initial Conditions and the Gravitational Collapse. *ApJ*, 505(1):37–49.

Avila-Reese, V., Zavala, J., Firmani, C., and Hernández-Toledo, H. M. (2008). On the Baryonic, Stellar, and Luminous Scaling Relations of Disk Galaxies. *AJ*, 136:1340–1360.

Avila-Reese, V., Zavala, J., and Lacerna, I. (2014). The growth of galactic bulges through mergers in Λ cold dark matter haloes revisited - II. Morphological mix evolution. *MNRAS*, 441:417–430.

Bacon, R., Copin, Y., Monnet, G., Miller, B. W., Allington-Smith, J. R., Bureau, M., Carollo, C. M., Davies, R. L., Emsellem, E., Kuntschner, H., Peletier, R. F., Verolme, E. K., and de Zeeuw, P. T. (2001). The SAURON project - I. The panoramic integral-field spectrograph. *MNRAS*, 326(1):23–35.

Balcells, M. and Stanford, S. A. (1990). A counterrotating core in the merger remnant candidate NGC 3656 (ARP 155). *ApJ*, 362:443–448.

Balcells, M., van Gorkom, J. H., Sancisi, R., and del Burgo, C. (2001). H I in the Shell Elliptical Galaxy NGC 3656. *AJ*, 122:1758–1769.

Baldry, I. K., Glazebrook, K., and Driver, S. P. (2008). On the galaxy stellar mass function, the mass-metallicity relation and the implied baryonic mass function. *MNRAS*, 388:945–959.

Barnes, J. E. and Hernquist, L. (1992). Dynamics of interacting galaxies. *ARA&A*, 30:705–742.

Baushev, A. N. (2018). Galaxy collisions as a mechanism of ultra diffuse galaxy (UDG) formation. , 60:69–73.

Beasley, M. A., Romanowsky, A. J., Pota, V., Navarro, I. M., Martinez Delgado, D., Neyer, F., and Deich, A. L. (2016). An Overmassive Dark Halo around an Ultra-diffuse Galaxy in the Virgo Cluster. *ApJ*, 819:L20.

Begeman, K. G. (1989). HI rotation curves of spiral galaxies. I. NGC 3198. *A&A*, 223:47–60.

Behroozi, P. S., Conroy, C., and Wechsler, R. H. (2010). A Comprehensive Analysis of Uncertainties Affecting the Stellar Mass-Halo Mass Relation for 0 < z < 4. *ApJ*, 717:379–403.

Behroozi, P. S., Wechsler, R. H., and Conroy, C. (2013). The Average Star Formation Histories of Galaxies in Dark Matter Halos from z = 0-8. *ApJ*, 770:57.

Bekeraité, S., Walcher, C. J., Falcón-Barroso, J., Garcia Lorenzo, B., Lyubenova, M., Sánchez, S. F., Spekkens, K., van de Ven, G., Wisotzki, L., Ziegler, B., Aguerri, J. A. L., Barrera-Ballesteros, J., Bland-Hawthorn, J., Catalán-Torrecilla, C., and García-Benito, R. (2016). Space density distribution of galaxies in the absolute magnitude - rotation velocity plane: a volume-complete Tully-Fisher relation from CALIFA stellar kinematics. *A&A*, 593:A114.

Bell, E. F. and de Jong, R. S. (2001). Stellar Mass-to-Light Ratios and the Tully-Fisher Relation. *ApJ*, 550(1):212–229.

Bellazzini, M., Belokurov, V., Magrini, L., Fraternali, F., Testa, V., Beccari, G., Marchetti, A., and Carini, R. (2017). Redshift, metallicity and size of two extended dwarf Irregular galaxies: a link between dwarf Irregulars and ultra diffuse galaxies? *MNRAS*, 467:3751–3758.

Bennet, P., Sand, D. J., Zaritsky, D., Crnojević, D., Spekkens, K., and Karunakaran, A. (2018). Evidence for Ultra-diffuse Galaxy Formation through Galaxy Interactions. *ApJ*, 866:L11.

Berlind, A. A. and Weinberg, D. H. (2002). The Halo Occupation Distribution: Toward an Empirical Determination of the Relation between Galaxies and Mass. *ApJ*, 575:587–616.

Bernardi, M., Meert, A., Vikram, V., Huertas-Company, M., Mei, S., Shankar, F., and Sheth, R. K. (2012). Systematic effects on the size-luminosity relation: dependence on model fitting and morphology. *arXiv e-prints*.

Bershady, M. A., Martinsson, T. P. K., Verheijen, M. A. W., Westfall, K. B., Andersen, D. R., and Swaters, R. A. (2011). Galaxy Disks are Submaximal. *ApJ*, 739:L47.

Bershady, M. A., Verheijen, M. A. W., Swaters, R. A., Andersen, D. R., Westfall, K. B., and Martinsson, T. (2010). The DiskMass Survey. I. Overview. *ApJ*, 716(1):198–233.

Berta, Z. K., Jimenez, R., Heavens, A. F., and Panter, B. (2008). The role of spin in the formation and evolution of galaxies. *MNRAS*, 391:197–204.

Bertola, F., Bettoni, D., Danziger, J., Sadler, E., Sparke, L., and de Zeeuw, T. (1991). Testing the Gravitational Field in Elliptical Galaxies: NGC 5077. *ApJ*, 373:369.

Bettoni, D., Galletta, G., Rampazzo, R., Marino, A., Mazzei, P., and Buson, L. M. (2011). NGC 3934: a shell galaxy in a compact galaxy environment. *A&A*, 534:A24.

Bílek, M., Cuillandre, J.-C., Gwyn, S., Ebrová, I., Bartošková, K., Jungwiert, B., and Jílková, L. (2016). Deep imaging of the shell elliptical galaxy NGC 3923 with MegaCam. *A&A*, 588:A77.

Birdsall, C. K. and Fuss, D. (1969). Clouds-in-clouds, clouds-in-cells physics for many-body plasma simulation. *Journal of Computational Physics*, 3:494–511.

Bizyaev, D. V., Moiseev, A. V., and Vorobyov, E. I. (2007). Propagating Star Formation in the Collisional Ring Galaxy Arp 10. *ApJ*, 662:304–321.

Blumenthal, G. R., Faber, S. M., Flores, R., and Primack, J. R. (1986). Contraction of Dark Matter Galactic Halos Due to Baryonic Infall. *ApJ*, 301:27.

Bolatto, A. D., Wolfire, M., and Leroy, A. K. (2013). The CO-to-H_2 Conversion Factor. *ARA&A*, 51:207–268.

Bosma, A. (1978). *The distribution and kinematics of neutral hydrogen in spiral galaxies of various morphological types.* PhD thesis, -.

Bottema, R. (1993). The Stellar Kinematics of Galactic Disks. *A&A*, 275:16.

Bournaud, F. and Combes, F. (2002). Gas accretion on spiral galaxies: Bar formation and renewal. *A&A*, 392:83–102.

Bournaud, F. and Combes, F. (2003). Formation of polar ring galaxies. *A&A*, 401:817–833.

Bournaud, F., Jog, C. J., and Combes, F. (2005). Galaxy mergers with various mass ratios: Properties of remnants. *A&A*, 437:69–85.

Bournaud, F., Jog, C. J., and Combes, F. (2007). Multiple minor mergers: formation of elliptical galaxies and constraints for the growth of spiral disks. *A&A*, 476:1179–1190.

Boylan-Kolchin, M., Ma, C.-P., and Quataert, E. (2005). Dissipationless mergers of elliptical galaxies and the evolution of the fundamental plane. *MNRAS*, 362:184–196.

Bruce, V. A., Dunlop, J. S., Cirasuolo, M., McLure, R. J., Targett, T. A., Bell, E. F., Croton, D. J., Dekel, A., Faber, S. M., Ferguson, H. C., Grogin, N. A., Kocevski, D. D., Koekemoer, A. M., Koo, D. C., Lai, K., Lotz, J. M., McGrath, E. J., Newman, J. A., and van der Wel, A. (2012). The morphologies of massive galaxies at $1 < z < 3$ in the CANDELS-UDS field: compact bulges, and the rise and fall of massive discs. *MNRAS*, 427:1666–1701.

Bruzual, G. and Charlot, S. (2003). Stellar population synthesis at the resolution of 2003. *MNRAS*, 344:1000–1028.

Buitrago, F., Trujillo, I., Conselice, C. J., and Häußler, B. (2013). Early-type galaxies have been the predominant morphological class for massive galaxies since only z
1. *MNRAS*, 428:1460–1478.

Bullock, J. S. and Johnston, K. V. (2005). Tracing Galaxy Formation with Stellar Halos. I. Methods. *ApJ*, 635:931–949.

Bundy, K., Bershady, M. A., Law, D. R., Yan, R., Drory, N., MacDonald, N., Wake, D. A., Cherinka, B., Sánchez-Gallego, J. R., Weijmans, A.-M., Thomas, D., Tremonti, C., Masters, K., Coccato, L., Diamond-Stanic, A. M., Aragón-Salamanca, A., Avila-Reese, V., Badenes, C., Falcón-Barroso, J., Belfiore, F., Bizyaev, D., Blanc, G. A., Bland-Hawthorn, J., Blanton, M. R., Brownstein, J. R., Byler, N., Cappellari, M., Conroy, C., Dutton, A. A., Emsellem, E., Etherington, J., Frinchaboy, P. M., Fu, H., Gunn, J. E., Harding, P., Johnston, E. J., Kauffmann, G., Kinemuchi, K., Klaene, M. A., Knapen, J. H., Leauthaud, A., Li, C., Lin, L., Maiolino, R., Malanushenko, V., Malanushenko, E., Mao, S., Maraston, C., McDermid, R. M., Merrifield, M. R., Nichol, R. C., Oravetz, D., Pan, K., Parejko, J. K., Sanchez, S. F., Schlegel, D., Simmons, A., Steele, O., Steinmetz, M., Thanjavur, K., Thompson, B. A., Tinker, J. L., van den Bosch, R. C. E., Westfall, K. B., Wilkinson, D., Wright, S., Xiao, T., and Zhang, K. (2015). Overview of the SDSS-IV MaNGA Survey: Mapping nearby Galaxies at Apache Point Observatory. *ApJ*, 798:7.

Buson, L. M., Bertola, F., Bressan, A., Burstein, D., and Cappellari, M. (2004). Is the giant elliptical galaxy NGC 5018 a post-merger remnant? *A&A*, 423:965–968.

Calette, A. R., Avila-Reese, V., Rodríguez-Puebla, A., Hernández-Toledo, H., and Papastergis, E. (2018). The HI- and H_2-to-Stellar Mass Correlations of Late- and Early-Type Galaxies and their Consistency with the Observational Mass Functions. *RevMexAA*, 54:443–483.

Cappellari, M. (2008). Measuring the inclination and mass-to-light ratio of axisymmetric galaxies via anisotropic Jeans models of stellar kinematics. *MNRAS*, 390(1):71–86.

Cappellari, M., Bacon, R., Bureau, M., Damen, M. C., Davies, R. L., de Zeeuw, P. T., Emsellem, E., Falcón-Barroso, J., Krajnović, D., Kuntschner, H., McDermid, R. M., Peletier, R. F., Sarzi, M., van den Bosch, R. C. E., and van de Ven, G. (2006). The SAURON project - IV. The mass-to-light ratio, the virial mass estimator and the Fundamental Plane of elliptical and lenticular galaxies. *MNRAS*, 366(4):1126–1150.

Cappellari, M. and Copin, Y. (2003). Adaptive spatial binning of integral-field spectroscopic data using Voronoi tessellations. *MNRAS*, 342(2):345–354.

Cappellari, M. and Emsellem, E. (2004). Parametric Recovery of Line-of-Sight Velocity Distributions from Absorption-Line Spectra of Galaxies via Penalized Likelihood. *PASP*, 116(816):138–147.

Cappellari, M., Emsellem, E., Krajnović, D., McDermid, R. M., Scott, N., Verdoes Kleijn, G. A., Young, L. M., Alatalo, K., Bacon, R., Blitz, L., Bois, M., Bournaud, F., Bureau, M., Davies, R. L., Davis, T. A., de Zeeuw, P. T., Duc, P.-A., Khochfar, S., Kuntschner, H., Lablanche, P.-Y., Morganti, R., Naab, T., Oosterloo, T., Sarzi, M., Serra, P., and Weijmans, A.-M. (2011a). The ATLAS^{3D} project - I. A volume-limited sample of 260 nearby early-type galaxies: science goals and selection criteria. *MNRAS*, 413:813–836.

Cappellari, M., Emsellem, E., Krajnović, D., McDermid, R. M., Serra, P., Alatalo, K., Blitz, L., Bois, M., Bournaud, F., Bureau, M., Davies, R. L., Davis, T. A., de Zeeuw, P. T., Khochfar, S., Kuntschner, H., Lablanche, P.-Y., Morganti, R., Naab, T., Oosterloo, T., Sarzi, M., Scott, N., Weijmans, A.-M., and Young, L. M. (2011b). The ATLAS^{3D} project - VII. A new look at the morphology of nearby galaxies: the kinematic morphology-density relation. *MNRAS*, 416(3):1680–1696.

Cappellari, M., Scott, N., Alatalo, K., Blitz, L., Bois, M., Bournaud, F., Bureau, M., Crocker, A. F., Davies, R. L., Davis, T. A., de Zeeuw, P. T., Duc, P.-A., Emsellem, E., Khochfar, S., Krajnović, D., Kuntschner, H., McDermid, R. M., Morganti, R., Naab, T., Oosterloo, T., Sarzi, M., Serra, P., Weijmans, A.-M., and Young, L. M. (2013). The ATLAS^{3D} project - XV. Benchmark for early-type galaxies scaling relations from 260 dynamical models: mass-to-light ratio, dark matter, Fundamental Plane and Mass Plane. *MNRAS*, 432(3):1709–1741.

Carleton, T., Errani, R., Cooper, M., Kaplinghat, M., Peñarrubia, J., and Guo, Y. (2019). The formation of ultra-diffuse galaxies in cored dark matter haloes through tidal stripping and heating. *MNRAS*, 485:382–395.

Carter, D., Allen, D. A., and Malin, D. F. (1982). Nature of the shells of NGC1344. *Nature*, 295:126–128.

Catinella, B., Giovanelli, R., and Haynes, M. P. (2006). Template Rotation Curves for Disk Galaxies. *ApJ*, 640:751–761.

Catinella, B., Haynes, M. P., and Giovanelli, R. (2005). Rotational Widths for Use in the Tully-Fisher Relation. I. Long-Slit Spectroscopic Data. *AJ*, 130(3):1037–1048.

Catinella, B., Kauffmann, G., Schiminovich, D., Lemonias, J., Scannapieco, C., Wang, J., Fabello, S., Hummels, C., Moran, S. M., Wu, R., Cooper, A. P., Giovanelli, R., Haynes, M. P., Heckman, T. M., and Saintonge, A. (2012). The GALEX Arecibo SDSS Survey - IV. Baryonic mass-velocity-size relations of massive galaxies. *MNRAS*, 420(3):1959–1976.

Cervantes-Sodi, B., Hernandez, X., Park, C., and Kim, J. (2008). Environment and mass dependencies of galactic λ spin parameter: cosmological simulations and observed galaxies compared. *MNRAS*, 388:863–872.

Charmandaris, V. and Appleton, P. N. (1996). The Neutral Hydrogen Disk of ARP 10 (=VV 362): A Nonequilibrium Disk Associated with a Galaxy with Rings and Ripples. *ApJ*, 460:686.

Charmandaris, V., Combes, F., and van der Hulst, J. M. (2000). First detection of molecular gas in the shells of CenA. *A&A*, 356:L1–L4.

Chien, L.-H., Barnes, J. E., Kewley, L. J., and Chambers, K. C. (2007). Multiobject Spectroscopy of Young Star Clusters in NGC 4676. *ApJ*, 660:L105–L108.

Christensen, L. and Hjorth, J. (2017). A break in the high-redshift stellar mass Tully-Fisher relation. *MNRAS*, 470(3):2599–2610.

Christodoulou, D. M., Shlosman, I., and Tohline, J. E. (1995). A new criterion for bar-forming instability in rapidly rotating gaseous and stellar systems. 1: Axisymmetric form. *ApJ*, 443:551–562.

Cibinel, A., Carollo, C. M., Lilly, S. J., Bonoli, S., Miniati, F., Pipino, A., Silverman, J. D., van Gorkom, J. H., Cameron, E., Finoguenov, A., Norberg, P., Peng, Y., and Rudick, C. S. (2013). The Zurich Environmental Study of Galaxies in Groups along the Cosmic Web. III. Galaxy Photometric Measurements and the Spatially Resolved Color Properties of Early- and Late-type Satellites in Diverse Environments. *ApJ*, 777:116.

Cid Fernandes, R., Pérez, E., García Benito, R., González Delgado, R. M., de Amorim, A. L., Sánchez, S. F., Husemann, B., Falcón Barroso, J., Sánchez-Blázquez, P., Walcher, C. J., and Mast, D. (2013). Resolving galaxies in time and space. I. Applying STARLIGHT to CALIFA datacubes. *A&A*, 557:A86.

Ciotti, L. (1991). Stellar systems following the R1/m luminosity law. *A&A*, 249:99–106.

Clarke, D. A., Burns, J. O., and Norman, M. L. (1992). VLA observations of the inner lobes of Centaurus A. *ApJ*, 395:444–452.

Cole, S., Aragon-Salamanca, A., Frenk, C. S., Navarro, J. F., and Zepf, S. E. (1994). A recipe for galaxy formation. *MNRAS*, 271:781–806.

Collins, M. L. M., Chapman, S. C., Rich, R. M., Ibata, R. A., Martin, N. F., Irwin, M. J., Bate, N. F., Lewis, G. F., Peñarrubia, J., Arimoto, N., Casey, C. M., Ferguson, A. M. N., Koch, A., McConnachie, A. W., and Tanvir, N. (2013). A Kinematic Study of the Andromeda Dwarf Spheroidal System. *ApJ*, 768:172.

Combes, F. and Charmandaris, V. (2000). *Formation of Gaseous Shells*, volume 197 of *Astronomical Society of the Pacific Conference Series*, page 339.

Combes, F., Mamon, G. A., and Charmandaris, V., editors (2000). *Dynamics of Galaxies: from the Early Universe to the Present*, volume 197 of *Astronomical Society of the Pacific Conference Series*.

Combes, F., Young, L. M., and Bureau, M. (2007). Molecular gas and star formation in the SAURON early-type galaxies. *MNRAS*, 377:1795–1807.

Conselice, C. J., Wilkinson, A., Duncan, K., and Mortlock, A. (2016). The Evolution of Galaxy Number Density at z < 8 and Its Implications. *ApJ*, 830:83.

Cooper, A. P., Cole, S., Frenk, C. S., White, S. D. M., Helly, J., Benson, A. J., De Lucia, G., Helmi, A., Jenkins, A., Navarro, J. F., Springel, V., and Wang, J. (2010). Galactic stellar haloes in the CDM model. *MNRAS*, 406:744–766.

Cooper, A. P., D'Souza, R., Kauffmann, G., Wang, J., Boylan-Kolchin, M., Guo, Q., Frenk, C. S., and White, S. D. M. (2013). Galactic accretion and the outer structure of galaxies in the CDM model. *MNRAS*, 434:3348–3367.

Cooper, A. P., Gao, L., Guo, Q., Frenk, C. S., Jenkins, A., Springel, V., and White, S. D. M. (2015). Surface photometry of brightest cluster galaxies and intracluster stars in ΛCDM. *MNRAS*, 451:2703–2722.

Cortese, L., Fogarty, L. M. R., Bekki, K., van de Sande, J., Couch, W., Catinella, B., Colless, M., Obreschkow, D., Taranu, D., Tescari, E., Barat, D., Bland-Hawthorn, J., Bloom, J., Bryant, J. J., Cluver, M., Croom, S. M., Drinkwater, M. J., d'Eugenio, F., Konstantopoulos, I. S., Lopez-Sanchez, A., Mahajan, S., Scott, N., Tonini, C., Wong, O. I., Allen, J. T., Brough, S., Goodwin, M., Green, A. W., Ho, I.-T., Kelvin, L. S., Lawrence, J. S., Lorente, N. P. F., Medling, A. M., Owers, M. S., Richards, S., Sharp, R., and Sweet, S. M. (2016). The SAMI Galaxy Survey: the link between angular momentum and optical morphology. *MNRAS*, 463:170–184.

Cortese, L., Fogarty, L. M. R., Ho, I. T., Bekki, K., Bland-Hawthorn, J., Colless, M., Couch, W., Croom, S. M., Glazebrook, K., Mould, J., Scott, N., Sharp, R., Tonini, C., Allen, J. T., Bloom, J., Bryant, J. J., Cluver, M., Davies, R. L., Drinkwater, M. J., Goodwin, M., Green, A., Kewley, L. J., Kostantopoulos, I. S., Lawrence, J. S., Mahajan, S., Medling, A. M., Owers, M., Richards, S. N., Sweet, S. M., and Wong, O. I. (2014). The SAMI Galaxy Survey: Toward a Unified Dynamical Scaling Relation for Galaxies of All Types. *ApJ*, 795(2):L37.

Courteau, S., Cappellari, M., de Jong, R. S., Dutton, A. A., Emsellem, E., Hoekstra, H., Koopmans, L. V. E., Mamon, G. A., Maraston, C., Treu, T., and Widrow, L. M. (2014). Galaxy masses. *Reviews of Modern Physics*, 86(1):47–119.

Courteau, S., Dutton, A. A., van den Bosch, F. C., MacArthur, L. A., Dekel, A., McIntosh, D. H., and Dale, D. A. (2007). Scaling Relations of Spiral Galaxies. *ApJ*, 671:203–225.

Courteau, S. and Rix, H.-W. (1999). Maximal Disks and the Tully-Fisher Relation. *ApJ*, 513(2):561–571.

Cox, T. J., Jonsson, P., Primack, J. R., and Somerville, R. S. (2006). Feedback in simulations of disc-galaxy major mergers. *MNRAS*, 373:1013–1038.

Crain, R. A., Schaye, J., Bower, R. G., Furlong, M., Schaller, M., Theuns, T., Dalla Vecchia, C., Frenk, C. S., McCarthy, I. G., Helly, J. C., Jenkins, A., Rosas-Guevara, Y. M., White, S. D. M., and Trayford, J. W. (2015). The EAGLE simulations of galaxy formation: calibration of subgrid physics and model variations. *MNRAS*, 450(2):1937–1961.

Cresci, G., Hicks, E. K. S., Genzel, R., Schreiber, N. M. F., Davies, R., Bouché, N., Buschkamp, P., Genel, S., Shapiro, K., Tacconi, L., Sommer-Larsen, J., Burkert, A., Eisenhauer, F., Gerhard, O., Lutz, D., Naab, T., Sternberg, A., Cimatti, A., Daddi, E., Erb, D. K., Kurk, J., Lilly, S. L., Renzini, A., Shapley, A., Steidel, C. C., and Caputi, K. (2009). The SINS Survey: Modeling the Dynamics of z ~2 Galaxies and the High-z Tully-Fisher Relation. *ApJ*, 697(1):115–132.

Crnojević, D., Ferguson, A. M. N., Irwin, M. J., Bernard, E. J., Arimoto, N., Jablonka, P., and Kobayashi, C. (2013). The outer halo of the nearest giant elliptical: a VLT/VIMOS survey of the resolved stellar populations in Centaurus A to 85 kpc. *MNRAS*, 432:832–847.

Croom, S. M., Lawrence, J. S., Bland-Hawthorn, J., Bryant, J. J., Fogarty, L., Richards, S., Goodwin, M., Farrell, T., Miziarski, S., Heald, R., Jones, D. H., Lee, S., Colless, M., Brough, S., Hopkins, A. M., Bauer, A. E., Birchall, M. N., Ellis, S., Horton, A., Leon-Saval, S., Lewis, G., López-Sánchez, Á. R., Min, S.-S., Trinh, C., and Trowland, H. (2012). The Sydney-AAO Multi-object Integral field spectrograph. *MNRAS*, 421(1):872–893.

de Blok, W. J. G., Józsa, G. I. G., Patterson, M., Gentile, G., Heald, G. H., Jütte, E., Kamphuis, P., Rand, R. J., Serra, P., and Walterbos, R. A. M. (2014). HALOGAS observations of NGC 4414: fountains, interaction, and ram pressure. *A&A*, 566:A80.

Dekel, A. and Birnboim, Y. (2008). Gravitational quenching in massive galaxies and clusters by clumpy accretion. *MNRAS*, 383(1):119–138.

Dekel, A., Birnboim, Y., Engel, G., Freundlich, J., Goerdt, T., Mumcuoglu, M., Neistein, E., Pichon, C., Teyssier, R., and Zinger, E. (2009). Cold streams in early massive hot haloes as the main mode of galaxy formation. *Nature*, 457:451–454.

Desmond, H. and Wechsler, R. H. (2017). The Faber-Jackson relation and Fundamental Plane from halo abundance matching. *MNRAS*, 465(1):820–833.

Di Cintio, A., Brook, C. B., Dutton, A. A., Macciò, A. V., Obreja, A., and Dekel, A. (2017). NIHAO - XI. Formation of ultra-diffuse galaxies by outflows. *MNRAS*, 466:L1–L6.

Di Cintio, A., Brook, C. B. A., Dutton, A. A., Macciò, A. V., Obreja, A., and Dekel, A. (2019). Ultra-Diffuse Galaxies: a formation scenario. In Montesinos, B., Asensio Ramos, A., Buitrago, F., Schödel, R., Villaver, E., Pérez-Hoyos, S., and Ordóñez-Etxeberria, I., editors, *Highlights on Spanish Astrophysics X*, pages 116–121.

Disney, M. J. (1976). Visibility of galaxies. *Nature*, 263:573–575.

Djorgovski, S. and Davis, M. (1987). Fundamental Properties of Elliptical Galaxies. *ApJ*, 313:59.

Dressler, A., Lynden-Bell, D., Burstein, D., Davies, R. L., Faber, S. M., Terlevich, R., and Wegner, G. (1987). Spectroscopy and Photometry of Elliptical Galaxies. I. New Distance Estimator. *ApJ*, 313:42.

Duc, P.-A. (2017). Using deep images and simulations to trace collisional debris around massive galaxies. In Gil de Paz, A., Knapen, J. H., and Lee, J. C., editors, *Formation and Evolution of Galaxy Outskirts*, volume 321 of *IAU Symposium*, pages 180–182.

Duc, P.-A., Cuillandre, J.-C., Karabal, E., Cappellari, M., Alatalo, K., Blitz, L., Bournaud, F., Bureau, M., Crocker, A. F., Davies, R. L., Davis, T. A., de Zeeuw, P. T., Emsellem, E., Khochfar, S., Krajnović, D., Kuntschner, H., McDermid, R. M., Michel-Dansac, L., Morganti, R., Naab, T., Oosterloo, T., Paudel, S., Sarzi, M., Scott, N., Serra, P., Weijmans, A.-M., and Young, L. M. (2015). The ATLAS^{3D} project - XXIX. The new look of early-type galaxies and surrounding fields disclosed by extremely deep optical images. *MNRAS*, 446:120–143.

Dupraz, C. and Combes, F. (1986). Shells around galaxies - Testing the mass distribution and the 3-D shape of ellipticals. *A&A*, 166:53–74.

Dupraz, C. and Combes, F. (1987). Dynamical friction and shells around elliptical galaxies. *A&A*, 185:L1–L4.

Dutton, A. A. (2009). On the origin of exponential galaxy discs. *MNRAS*, 396:121–140.

Dutton, A. A. (2012). The baryonic Tully-Fisher relation and galactic outflows. *MNRAS*, 424:3123–3128.

Dutton, A. A., van den Bosch, F. C., Dekel, A., and Courteau, S. (2007). A Revised Model for the Formation of Disk Galaxies: Low Spin and Dark Halo Expansion. *ApJ*, 654:27–52.

Dutton, A. A., van den Bosch, F. C., Faber, S. M., Simard, L., Kassin, S. A., Koo, D. C., Bundy, K., Huang, J., Weiner, B. J., Cooper, M. C., Newman, J. A., Mozena, M., and Koekemoer, A. M. (2011). On the evolution of the velocity-mass-size relations of disc-dominated galaxies over the past 10 billion years. *MNRAS*, 410:1660–1676.

Eisenstein, D. J. and Hut, P. (1998). HOP: A New Group-Finding Algorithm for N-Body Simulations. *ApJ*, 498:137–142.

Eisenstein, D. J. and Loeb, A. (1996). Can the Tully-Fisher Relation Be the Result of Initial Conditions? *ApJ*, 459:432.

Elias, L. M., Sales, L. V., Creasey, P., Cooper, M. C., Bullock, J. S., Rich, R. M., and Hernquist, L. (2018). Stellar halos in Illustris: probing the histories of Milky Way-mass galaxies. *MNRAS*, 479:4004–4016.

Elmegreen, B. G. (2011). Gravitational Instabilities in Two-component Galaxy Disks with Gas Dissipation. *ApJ*, 737(1):10.

Emsellem, E., Cappellari, M., Krajnović, D., Alatalo, K., Blitz, L., Bois, M., Bournaud, F., Bureau, M., Davies, R. L., Davis, T. A., de Zeeuw, P. T., Khochfar, S., Kuntschner, H., Lablanche, P.-Y., McDermid, R. M., Morganti, R., Naab, T., Oosterloo, T., Sarzi, M., Scott, N., Serra, P., van de Ven, G., Weijmans, A.-M., and Young, L. M. (2011). The ATLAS^{3D} project - III. A census of the stellar angular momentum within the effective radius of early-type galaxies: unveiling the distribution of fast and slow rotators. *MNRAS*, 414(2):888–912.

Emsellem, E., Cappellari, M., Krajnović, D., van de Ven, G., Bacon, R., Bureau, M., Davies, R. L., de Zeeuw, P. T., Falcón-Barroso, J., Kuntschner, H., McDermid, R., Peletier, R. F., and Sarzi, M. (2007). The SAURON project - IX. A kinematic classification for early-type galaxies. *MNRAS*, 379(2):401–417.

Faber, S. M. and Jackson, R. E. (1976). Velocity dispersions and mass-to-light ratios for elliptical galaxies. *ApJ*, 204:668–683.

Fabian, A. C., Nulsen, P. E. J., and Stewart, G. C. (1980). Star formation in a galactic wind. *Nature*, 287:613.

Falcón-Barroso, J., Lyubenova, M., van de Ven, G., Mendez-Abreu, J., Aguerri, J. A. L., García-Lorenzo, B., Bekeraité, S., Sánchez, S. F., Husemann, B., García-Benito, R., Mast, D., Walcher, C. J., Zibetti, S., Barrera-Ballesteros, J. K., Galbany, L., Sánchez-Blázquez, P., Singh, R., van den Bosch, R. C. E., Wild, V., Zhu, L., Bland -Hawthorn, J., Cid Fernandes, R., de Lorenzo-Cáceres, A., Gallazzi, A., González Delgado, R. M., Marino, R. A., Márquez, I., Pérez, E., Pérez, I., Roth, M. M., Rosales-Ortega, F. F., Ruiz-Lara, T., Wisotzki, L., Ziegler, B., and Califa Collaboration (2017). Stellar kinematics across the Hubble sequence in the CALIFA survey: general properties and aperture corrections. *A&A*, 597:A48.

Ferguson, A. M. N., Irwin, M. J., Ibata, R. A., Lewis, G. F., and Tanvir, N. R. (2002). Evidence for Stellar Substructure in the Halo and Outer Disk of M31. *AJ*, 124:1452–1463.

Ferrarese, L., Côté, P., Cuillandre, J.-C., Gwyn, S. D. J., Peng, E. W., MacArthur, L. A., Duc, P.-A., Boselli, A., Mei, S., Erben, T., McConnachie, A. W., Durrell, P. R., Mihos, J. C., Jordán, A., Lançon, A., Puzia, T. H., Emsellem, E., Balogh, M. L., Blakeslee, J. P., van Waerbeke, L., Gavazzi, R., Vollmer, B., Kavelaars, J. J., Woods, D., Ball, N. M., Boissier, S., Courteau, S., Ferriere, E., Gavazzi, G., Hildebrandt, H., Hudelot, P., Huertas-Company, M., Liu, C., McLaughlin, D., Mellier, Y., Milkeraitis, M., Schade, D., Balkowski, C., Bournaud, F., Carlberg, R. G., Chapman, S. C., Hoekstra, H., Peng, C., Sawicki, M., Simard, L., Taylor, J. E., Tully, R. B., van Driel, W., Wilson, C. D., Burdullis, T., Mahoney, B., and Manset, N. (2012). The Next Generation Virgo Cluster Survey (NGVS). I. Introduction to the Survey. *ApJS*, 200:4.

Firmani, C. and Avila-Reese, V. (2000). Disc galaxy evolution models in a hierarchical formation scenario: structure and dynamics. *MNRAS*, 315:457–472.

Gadotti, D. A. (2009). Structural properties of pseudo-bulges, classical bulges and elliptical galaxies: a Sloan Digital Sky Survey perspective. *MNRAS*, 393(4):1531–1552.

Gallazzi, A., Charlot, S., Brinchmann, J., and White, S. D. M. (2006). Ages and metallicities of early-type galaxies in the Sloan Digital Sky Survey: new insight into the physical origin of the colour-magnitude and the Mg_2-σ_V relations. *MNRAS*, 370(3):1106–1124.

Galletta, G., Sage, L. J., and Sparke, L. S. (1997). Molecular gas in polar-ring galaxies. *MNRAS*, 284:773–784.

García-Benito, R., Zibetti, S., Sánchez, S. F., Husemann, B., de Amorim, A. L., Castillo-Morales, A., Cid Fernandes, R., Ellis, S. C., Falcón-Barroso, J., Galbany, L., Gil de Paz, A., González Delgado, R. M., Lacerda, E. A. D., López-Fernandez, R., de Lorenzo-Cáceres, A., Lyubenova, M., Marino, R. A., Mast, D., Mendoza, M. A., Pérez, E., Vale Asari, N., Aguerri, J. A. L., Ascasibar, Y., Bekeraitė, S., Bland-Hawthorn, J., Barrera-Ballesteros, J. K., Bomans, D. J., Cano-Díaz, M., Catalán-Torrecilla, C., Cortijo, C., Delgado-Inglada, G., Demleitner, M., Dettmar, R. J., Díaz, A. I., Florido, E., Gallazzi, A., García-Lorenzo, B., Gomes, J. M., Holmes, L., Iglesias-Páramo, J., Jahnke, K., Kalinova, V., Kehrig, C., Kennicutt, R. C., López-Sánchez, Á. R., Márquez, I., Masegosa, J., Meidt, S. E., Mendez-Abreu, J., Mollá, M., Monreal-Ibero, A., Morisset, C., del Olmo, A., Papaderos, P., Pérez, I., Quirrenbach, A., Rosales-Ortega, F. F., Roth, M. M., Ruiz-Lara, T., Sánchez-Blázquez, P., Sánchez-Menguiano, L., Singh, R., Spekkens, K., Stanishev, V., Torres-Papaqui, J. P., van de Ven, G., Vilchez, J. M., Walcher, C. J., Wild, V., Wisotzki, L., Ziegler, B., Alves, J., Barrado, D., Quintana, J. M., and Aceituno, J. (2015). CALIFA, the Calar Alto Legacy Integral Field Area survey. III. Second public data release. *A&A*, 576:A135.

Giovanelli, R., Haynes, M. P., Herter, T., Vogt, N. P., da Costa, L. N., Freudling, W., Salzer, J. J., and Wegner, G. (1997). The I Band Tully-Fisher Relation for Cluster Galaxies: a Template Relation, its Scatter and Bias Corrections. *AJ*, 113:53–79.

Gnedin, O. Y. (2003). Dynamical Evolution of Galaxies in Clusters. *ApJ*, 589:752–769.

Gnedin, O. Y., Weinberg, D. H., Pizagno, J., Prada, F., and Rix, H.-W. (2007). Dark Matter Halos of Disk Galaxies: Constraints from the Tully-Fisher Relation. *ApJ*, 671:1115–1134.

Gnerucci, A., Marconi, A., Cresci, G., Maiolino, R., Mannucci, F., Calura, F., Cimatti, A., Cocchia, F., Grazian, A., Matteucci, F., Nagao, T., Pozzetti, L., and Troncoso, P. (2011). Dynamical properties of AMAZE and LSD galaxies from gas kinematics and the Tully-Fisher relation at z ~3. *A&A*, 528:A88.

Gottlöber, S., Klypin, A., and Kravtsov, A. V. (2001). Merging History as a Function of Halo Environment. *ApJ*, 546(1):223–233.

Graham, A. W. and Driver, S. P. (2005). A Concise Reference to (Projected) Sérsic $R^{1/n}$ Quantities, Including Concentration, Profile Slopes, Petrosian Indices, and Kron Magnitudes. , 22(2):118–127.

Guth, A. H. (1981). Inflationary universe: A possible solution to the horizon and flatness problems. *Phys. Rev. D*, 23:347–356.

He, M., Wu, H., Du, W., Wicker, J., Zhao, P., Lei, F., and Liu, J. (2019). Edge-on H I-bearing Ultra-diffuse Galaxy Candidates in the 40% ALFALFA Catalog. *ApJ*, 880(1):30.

Helmi, A. and White, S. D. M. (1999). Building up the stellar halo of the Galaxy. *MNRAS*, 307:495–517.

Hendel, D. and Johnston, K. V. (2015). Tidal debris morphology and the orbits of satellite galaxies. *MNRAS*, 454:2472–2485.

Hendel, D., Johnston, K. V., Patra, R. K., and Sen, B. (2019). A machine-vision method for automatic classification of stellar halo substructure. *MNRAS*, 486:3604–3616.

Hernquist, L. (1990). An Analytical Model for Spherical Galaxies and Bulges. *ApJ*, 356:359.

Hernquist, L. and Quinn, P. J. (1988). Formation of shell galaxies. I - Spherical potentials. *ApJ*, 331:682–698.

Hernquist, L. and Quinn, P. J. (1989). Formation of shell galaxies. II - Nonspherical potentials. *ApJ*, 342:1–16.

Hibbard, J. E. and van Gorkom, J. H. (1996). HI, HII, and R-Band Observations of a Galactic Merger Sequence. *AJ*, 111:655.

Hilz, M., Naab, T., Ostriker, J. P., Thomas, J., Burkert, A., and Jesseit, R. (2012). Relaxation and stripping - The evolution of sizes, dispersions and dark matter fractions in major and minor mergers of elliptical galaxies. *MNRAS*, 425:3119–3136.

Hoffmann, V. and Romeo, A. B. (2012). The effect of ISM turbulence on the gravitational instability of galactic discs. *MNRAS*, 425(2):1511–1520.

Holmes, L., Spekkens, K., Sánchez, S. F., Walcher, C. J., García-Benito, R., Mast, D., Cortijo-Ferrero, C., Kalinova, V., Marino, R. A., Mendez-Abreu, J., and Barrera-Ballesteros, J. K. (2015). The incidence of bar-like kinematic flows in CALIFA galaxies. *MNRAS*, 451(4):4397–4411.

Hood, C. E., Kannappan, S. J., Stark, D. V., Dell'Antonio, I. P., Moffett, A. J., Eckert, K. D., Norris, M. A., and Hendel, D. (2018). The Origin of Faint Tidal Features around Galaxies in the RESOLVE Survey. *ApJ*, 857:144.

Hopkins, P. F., Bundy, K., Croton, D., Hernquist, L., Keres, D., Khochfar, S., Stewart, K., Wetzel, A., and Younger, J. D. (2010). Mergers and Bulge Formation in ΛCDM: Which Mergers Matter? *ApJ*, 715(1):202–229.

Huchtmeier, W. K. (1982). Global properties of Sa-galaxies from H I-observations. *A&A*, 110:121–137.

Husemann, B., Jahnke, K., Sánchez, S. F., Barrado, D., Bekeraitė, S., Bomans, D. J., Castillo-Morales, A., Catalán-Torrecilla, C., Cid Fernand es, R., Falcón-Barroso, J., García-Benito, R., González Delgado, R. M., Iglesias-Páramo, J., Johnson, B. D., Kupko, D., López-Fernandez, R., Lyubenova, M., Marino, R. A., Mast, D., Miskolczi, A., Monreal-Ibero, A., Gil de Paz, A., Pérez, E., Pérez, I., Rosales-Ortega, F. F., Ruiz-Lara, T., Schilling, U., van de Ven, G., Walcher, J., Alves, J., de Amorim, A. L., Backsmann, N., Barrera-Ballesteros, J. K., Bland-Hawthorn, J., Cortijo, C., Dettmar, R. J., Demleitner, M., Díaz, A. I., Enke, H., Florido, E., Flores, H., Galbany, L., Gallazzi, A., García-Lorenzo, B., Gomes, J. M., Gruel, N., Haines, T., Holmes, L., Jungwiert, B., Kalinova, V., Kehrig, C., Kennicutt, R. C., Klar, J., Lehnert, M. D., López-Sánchez, Á. R., de Lorenzo-Cáceres, A., Mármol-Queraltó, E., Márquez, I., Mendez-Abreu, J., Mollá, M., del Olmo, A., Meidt, S. E., Papaderos, P., Puschnig, J., Quirrenbach, A., Roth, M. M., Sánchez-Blázquez, P., Spekkens, K., Singh, R., Stanishev, V., Trager, S. C., Vilchez, J. M., Wild, V., Wisotzki, L., Zibetti, S., and Ziegler, B. (2013). CALIFA, the Calar Alto Legacy Integral Field Area survey. II. First public data release. *A&A*, 549:A87.

Impey, C., Bothun, G., and Malin, D. (1988). Virgo dwarfs - New light on faint galaxies. *ApJ*, 330:634–660.

Janowiecki, S., Mihos, J. C., Harding, P., Feldmeier, J. J., Rudick, C., and Morrison, H. (2010). Diffuse Tidal Structures in the Halos of Virgo Ellipticals. *ApJ*, 715:972–985.

Ji, I., Peirani, S., and Yi, S. K. (2014). Lifetime of merger features of equal-mass disk mergers. *A&A*, 566:A97.

Johnston, K. V., Bullock, J. S., Sharma, S., Font, A., Robertson, B. E., and Leitner, S. N. (2008). Tracing Galaxy Formation with Stellar Halos. II. Relating Substructure in Phase and Abundance Space to Accretion Histories. *ApJ*, 689:936–957.

Johnston, K. V., Majewski, S. R., Siegel, M. H., Reid, I. N., and Kunkel, W. E. (1999). Constraining the History of the Sagittarius Dwarf Galaxy Using Observations of Its Tidal Debris. *AJ*, 118:1719–1726.

Kado-Fong, E., Greene, J. E., Hendel, D., Price-Whelan, A. M., Greco, J. P., Goulding, A. D., Huang, S., Johnston, K. V., Komiyama, Y., Lee, C.-H., Lust, N. B., Strauss, M. A., and Tanaka, M. (2018). Tidal Features at $0.05 < z < 0.45$ in the Hyper Suprime-Cam Subaru Strategic Program: Properties and Formation Channels. *ApJ*, 866:103.

Kalinova, V., Colombo, D., Rosolowsky, E., Kannan, R., Galbany, L., García-Benito, R., González Delgado, R., Sánchez, S. F., Ruiz-Lara, T., Méndez-Abreu, J., Catalán-Torrecilla, C., Sánchez-Menguiano, L., de Lorenzo-Cáceres, A., Costantin, L., Florido, E., Kodaira, K., Marino, R. A., Läsker, R., and Bland -Hawthorn, J. (2017). Towards a new classification of galaxies: principal component analysis of CALIFA circular velocity curves. *MNRAS*, 469(3):2539–2594.

Karademir, G. S., Remus, R.-S., Burkert, A., Dolag, K., Hoffmann, T. L., Moster, B. P., Steinwandel, U. P., and Zhang, J. (2019). The outer stellar halos of galaxies: how radial merger mass deposition, shells, and streams depend on infall-orbit configurations. *MNRAS*, 487:318–332.

Kassin, S. A., Weiner, B. J., Faber, S. M., Koo, D. C., Lotz, J. M., Diemand, J., Harker, J. J., Bundy, K., Metevier, A. J., Phillips, A. C., Cooper, M. C., Croton, D. J., Konidaris, N., Noeske, K. G., and Willmer, C. N. A. (2007). The Stellar Mass Tully-Fisher Relation to z = 1.2 from AEGIS. *ApJ*, 660(1):L35–L38.

Kaviraj, S., Peirani, S., Khochfar, S., Silk, J., and Kay, S. (2009). The role of minor mergers in the recent star formation history of early-type galaxies. *MNRAS*, 394:1713–1720.

Kelz, A., Verheijen, M. A. W., Roth, M. M., Bauer, S. M., Becker, T., Paschke, J., Popow, E., Sánchez, S. F., and Laux, U. (2006). PMAS: The Potsdam Multi-Aperture Spectrophotometer. II. The Wide Integral Field Unit PPak. *PASP*, 118(839):129–145.

Kennicutt, Jr., R. C. (1998). The Global Schmidt Law in Star-forming Galaxies. *ApJ*, 498:541–552.

Kereš, D., Katz, N., Weinberg, D. H., and Davé, R. (2005). How do galaxies get their gas? *MNRAS*, 363:2–28.

Kim, D.-W., Guhathakurta, P., van Gorkom, J. H., Jura, M., and Knapp, G. R. (1988). H I observations of the elliptical galaxies NGC 2974 and NGC 5018. *ApJ*, 330:684–694.

Kim, T., Sheth, K., Hinz, J. L., Lee, M. G., Zaritsky, D., Gadotti, D. A., Knapen, J. H., Schinnerer, E., Ho, L. C., Laurikainen, E., Salo, H., Athanassoula, E., Bosma, A., de Swardt, B., Muñoz-Mateos, J.-C., Madore, B. F., Comerón, S., Regan, M. W., Menéndez-Delmestre, K., Gil de Paz, A., Seibert, M., Laine, J., Erroz-Ferrer, S., and Mizusawa, T. (2012). Early-type Galaxies with Tidal Debris and Their Scaling Relations in the Spitzer Survey of Stellar Structure in Galaxies (S^4G). *ApJ*, 753:43.

Klypin, A., Yepes, G., Gottlöber, S., Prada, F., and Heß, S. (2016). MultiDark simulations: the story of dark matter halo concentrations and density profiles. *MNRAS*, 457:4340–4359.

Knebe, A., Pearce, F. R., Lux, H., Ascasibar, Y., Behroozi, P., Casado, J., Moran, C. C., Diemand, J., Dolag, K., Dominguez-Tenreiro, R., Elahi, P., Falck, B., Gottlöber, S., Han, J., Klypin, A., Lukić, Z., Maciejewski, M., McBride, C. K., Merchán, M. E., Muldrew, S. I., Neyrinck, M., Onions, J., Planelles, S., Potter, D., Quilis, V., Rasera, Y., Ricker, P. M., Roy, F., Ruiz, A. N., Sgró, M. A., Springel, V., Stadel, J., Sutter, P. M., Tweed, D., and Zemp, M. (2013). Structure finding in cosmological simulations: the state of affairs. *MNRAS*, 435:1618–1658.

Koda, J., Yagi, M., Yamanoi, H., and Komiyama, Y. (2015). Approximately a Thousand Ultra-diffuse Galaxies in the Coma Cluster. *ApJ*, 807:L2.

Kormendy, J. (2013). *Secular Evolution in Disk Galaxies*, page 1.

Kormendy, J. and Kennicutt, Robert C., J. (2004). Secular Evolution and the Formation of Pseudobulges in Disk Galaxies. *ARA&A*, 42(1):603–683.

Krajnović, D., Emsellem, E., Cappellari, M., Alatalo, K., Blitz, L., Bois, M., Bournaud, F., Bureau, M., Davies, R. L., Davis, T. A., de Zeeuw, P. T., Khochfar, S., Kuntschner, H., Lablanche, P.-Y., McDermid, R. M., Morganti, R., Naab, T., Oosterloo, T., Sarzi, M., Scott, N., Serra, P., Weijmans, A.-M., and Young, L. M. (2011). The ATLAS^{3D} project - II. Morphologies, kinemetric features and alignment between photometric and kinematic axes of early-type galaxies. *MNRAS*, 414:2923–2949.

Lee, M. G., Kang, J., Lee, J. H., and Jang, I. S. (2017). Detection of a Large Population of Ultradiffuse Galaxies in Massive Galaxy Clusters: Abell S1063 and Abell 2744. *ApJ*, 844:157.

Leisman, L., Haynes, M. P., Janowiecki, S., Hallenbeck, G., Józsa, G., Giovanelli, R., Adams, E. A. K., Bernal Neira, D., Cannon, J. M., Janesh, W. F., Rhode, K. L., and Salzer, J. J. (2017). (Almost) Dark Galaxies in the ALFALFA Survey: Isolated H I-bearing Ultra-diffuse Galaxies. *ApJ*, 842:133.

Leung, G. Y. C., Leaman, R., van de Ven, G., Lyubenova, M., Zhu, L., Bolatto, A. D., Falcón-Barroso, J., Blitz, L., Dannerbauer, H., Fisher, D. B., Levy, R. C., Sanchez, S. F., Utomo, D., Vogel, S., Wong, T., and Ziegler, B. (2018). The EDGE-CALIFA survey: validating stellar dynamical mass models with CO kinematics. *MNRAS*, 477(1):254–292.

Lim, S., Peng, E. W., Côté, P., Sales, L. V., den Brok, M., Blakeslee, J. P., and Guhathakurta, P. (2018). The Globular Cluster Systems of Ultra-diffuse Galaxies in the Coma Cluster. *ApJ*, 862:82.

Lim, S., Peng, E. W., Duc, P.-A., Fensch, J., Durrell, P. R., Harris, W. E., Cuillandre, J.-C., Gwyn, S., Lançon, A., and Sánchez-Janssen, R. (2017). Globular Clusters as Tracers of Fine Structure in the Dramatic Shell Galaxy NGC 474. *ApJ*, 835:123.

Lin, L., Patton, D. R., Koo, D. C., Casteels, K., Conselice, C. J., Faber, S. M., Lotz, J., Willmer, C. N., Hsieh, B. C., Chiueh, T., Newman, J. A., Novak, G. S., Weiner, B. J., and Cooper, M. C. (2008). The Redshift Evolution of Wet, Dry, and Mixed Galaxy Mergers from Close Galaxy Pairs in the DEEP2 Galaxy Redshift Survey. *The Astrophysical Journal*, 681:232–243.

Linde, A. D. (1982). A new inflationary universe scenario: A possible solution of the horizon, flatness, homogeneity, isotropy and primordial monopole problems. *Physics Letters B*, 108:389–393.

Lotz, J. M., Jonsson, P., Cox, T. J., and Primack, J. R. (2008). Galaxy merger morphologies and time-scales from simulations of equal-mass gas-rich disc mergers. *MNRAS*, 391:1137–1162.

Lucero, D. M. and Young, L. M. (2013). A High-resolution Study of the Atomic Hydrogen in CO-rich Early-type Galaxies. *AJ*, 145:56.

Lyubenova, M., Martín-Navarro, I., van de Ven, G., Falcón-Barroso, J., Galbany, L., Gallazzi, A., García-Benito, R., González Delgado, R., Husemann, B., La Barbera, F., Marino, R. A., Mast, D., Mendez-Abreu, J., Peletier, R. F. P., Sánchez-Blázquez, P., Sánchez, S. F., Trager, S. C., van den Bosch, R. C. E., Vazdekis, A., Walcher, C. J., Zhu, L., Zibetti, S., Ziegler, B., Bland-Hawthorn, J., and CALIFA Collaboration (2016). IMF shape constraints from stellar populations and dynamics from CALIFA. *MNRAS*, 463(3):3220–3225.

Majewski, S. R., Skrutskie, M. F., Weinberg, M. D., and Ostheimer, J. C. (2003). A Two Micron All Sky Survey View of the Sagittarius Dwarf Galaxy. I. Morphology of the Sagittarius Core and Tidal Arms. *ApJ*, 599:1082–1115.

Malin, D. F. (1977). Unsharp masking. *AAS Photo Bulletin*, 16:10–13.

Malin, D. F. (1978). Photographic amplification of faint astronomical images. *Nature*, 276:591–593.

Malin, D. F. and Carter, D. (1983). A catalog of elliptical galaxies with shells. *ApJ*, 274:534–540.

Mancillas, B., Ávila-Reese, V., Rodríguez-Puebla, A., and Valls-Gabaud, D. (2017). Projection Of The Stellar To Halo Mass Relation Into The Scaling Relations Of A Disc Galaxy Population. In *Galaxy Evolution Across Time, Proceedings of a conference held 12-16 June, 2017 in Paris. Online at ¡A href="https://galaxiesinparis.sciencesconf.org/"¿ https://galaxiesinparis.sciencesconf.org/¡/A¿, id. 92*, page 92.

Mandelbaum, R., Wang, W., Zu, Y., White, S., Henriques, B., and More, S. (2016). Strong bimodality in the host halo mass of central galaxies from galaxy-galaxy lensing. *MNRAS*, 457:3200–3218.

Mantha, K. B., McIntosh, D. H., Ciaschi, C. P., Evan, R., Ferguson, H. C., Fries, L. B., Guo, Y., Koekemoer, A. M., Landry, L. D., McGrath, E. J., Simons, R. C., Snyder, G. F., Thompson, S. E., Bell, E. F., Ceverino, D., Hathi, N. P., Pacifici, C., Primack, J. R., Rafelski, M., and Rodriguez-Gomez, V. (2019). Studying the physical properties of tidal features - I. Extracting morphological substructure in CANDELS observations and VELA simulations. *MNRAS*, 486:2643–2659.

Martig, M., Bournaud, F., Croton, D. J., Dekel, A., and Teyssier, R. (2012). A Diversity of Progenitors and Histories for Isolated Spiral Galaxies. *ApJ*, 756:26.

Martig, M., Bournaud, F., Teyssier, R., and Dekel, A. (2009). Morphological Quenching of Star Formation: Making Early-Type Galaxies Red. *ApJ*, 707:250–267.

Martín-Navarro, I., Vazdekis, A., La Barbera, F., Falcón-Barroso, J., Lyubenova, M., van de Ven, G., Ferreras, I., Sánchez, S. F., Trager, S. C., García-Benito, R., Mast, D., Mendoza, M. A., Sánchez-Blázquez, P., González Delgado, R., Walcher, C. J., and CALIFA Team (2015). IMF&ndashMetallicity: A Tight Local Relation Revealed by the CALIFA Survey. *ApJ*, 806(2):L31.

Martínez-Delgado, D., Gabany, R. J., Crawford, K., Zibetti, S., Majewski, S. R., Rix, H.-W., Fliri, J., Carballo-Bello, J. A., Bardalez-Gagliuffi, D. C., Peñarrubia, J., Chonis, T. S., Madore, B., Trujillo, I., Schirmer, M., and McDavid, D. A. (2010). Stellar Tidal Streams in Spiral Galaxies of the Local Volume: A Pilot Survey with Modest Aperture Telescopes. *AJ*, 140:962–967.

Martínez-Delgado, D., Läsker, R., Sharina, M., Toloba, E., Fliri, J., Beaton, R., Valls-Gabaud, D., Karachentsev, I. D., Chonis, T. S., Grebel, E. K., Forbes, D. A., Romanowsky, A. J., Gallego-Laborda, J., Teuwen, K., Gómez-Flechoso, M. A., Wang, J., Guhathakurta, P., Kaisin, S., and Ho, N. (2016). Discovery of an Ultra-diffuse Galaxy in the Pisces–Perseus Supercluster. *AJ*, 151:96.

Martínez-Delgado, D., Pohlen, M., Gabany, R. J., Majewski, S. R., Peñarrubia, J., and Palma, C. (2009). Discovery of a Giant Stellar Tidal Stream Around The Disk Galaxy NGC 4013. *ApJ*, 692:955–963.

Martinsson, T. P. K., Verheijen, M. A. W., Westfall, K. B., Bershady, M. A., Andersen, D. R., and Swaters, R. A. (2013). The DiskMass Survey. VII. The distribution of luminous and dark matter in spiral galaxies. *A&A*, 557:A131.

Mathewson, D. S., Ford, V. L., and Buchhorn, M. (1992). A Southern Sky Survey of the Peculiar Velocities of 1355 Spiral Galaxies. *ApJS*, 81:413.

McConnachie, A. W., Irwin, M. J., Ibata, R. A., Dubinski, J., Widrow, L. M., Martin, N. F., Côté, P., Dotter, A. L., Navarro, J. F., Ferguson, A. M. N., Puzia, T. H., Lewis, G. F., Babul, A., Barmby, P., Bienaymé, O., Chapman, S. C., Cockcroft, R., Collins, M. L. M., Fardal, M. A., Harris, W. E., Huxor, A., Mackey, A. D., Peñarrubia, J., Rich, R. M., Richer, H. B., Siebert, A., Tanvir, N., Valls-Gabaud, D., and Venn, K. A. (2009). The remnants of galaxy formation from a panoramic survey of the region around M31. *Nature*, 461:66–69.

McDermid, R. M., Emsellem, E., Shapiro, K. L., Bacon, R., Bureau, M., Cappellari, M., Davies, R. L., de Zeeuw, T., Falcón-Barroso, J., Krajnović, D., Kuntschner, H., Peletier, R. F., and Sarzi, M. (2006). The SAURON project - VIII. OASIS/CFHT integral-field spectroscopy of elliptical and lenticular galaxy centres. *MNRAS*, 373:906–958.

McGaugh, S. S. and Bothun, G. D. (1990). Stellar populations in shell galaxies. *AJ*, 100:1073–1085.

McGaugh, S. S., Schombert, J. M., and Bothun, G. D. (1995). The Morphology of Low Surface Brightness Disk Galaxies. *AJ*, 109:2019.

McGaugh, S. S., Schombert, J. M., Bothun, G. D., and de Blok, W. J. G. (2000). The Baryonic Tully-Fisher Relation. *ApJ*, 533(2):L99–L102.

McKee, C. F. and Krumholz, M. R. (2010). The Atomic-to-Molecular Transition in Galaxies. III. A New Method for Determining the Molecular Content of Primordial and Dusty Clouds. *ApJ*, 709:308–320.

Merritt, A., van Dokkum, P., Danieli, S., Abraham, R., Zhang, J., Karachentsev, I. D., and Makarova, L. N. (2016). The Dragonfly Nearby Galaxies Survey. II. Ultra-Diffuse Galaxies near the Elliptical Galaxy NGC 5485. *ApJ*, 833:168.

Michel-Dansac, L. and Wozniak, H. (2004). Photometric and dynamic evolution of an isolated disc galaxy simulation. *A&A*, 421:863–876.

Mihos, J. C., Durrell, P. R., Ferrarese, L., Feldmeier, J. J., Côté, P., Peng, E. W., Harding, P., Liu, C., Gwyn, S., and Cuillandre, J.-C. (2015). Galaxies at the Extremes: Ultra-diffuse Galaxies in the Virgo Cluster. *ApJ*, 809:L21.

Mihos, J. C., Harding, P., Feldmeier, J., and Morrison, H. (2005). Diffuse Light in the Virgo Cluster. *ApJ*, 631:L41–L44.

Mo, H., van den Bosch, F. C., and White, S. (2010). *Galaxy Formation and Evolution.*

Mo, H. J., Mao, S., and White, S. D. M. (1998). The formation of galactic discs. *MNRAS*, 295:319–336.

More, S., van den Bosch, F. C., Cacciato, M., Skibba, R., Mo, H. J., and Yang, X. (2011). Satellite kinematics - III. Halo masses of central galaxies in SDSS. *MNRAS*, 410:210–226.

Mortlock, A., Conselice, C. J., Hartley, W. G., Ownsworth, J. R., Lani, C., Bluck, A. F. L., Almaini, O., Duncan, K., van der Wel, A., Koekemoer, A. M., Dekel, A., Davé, R., Ferguson, H. C., de Mello, D. F., Newman, J. A., Faber, S. M., Grogin, N. A., Kocevski, D. D., and Lai, K. (2013). The redshift and mass dependence on the formation of the Hubble sequence at $z > 1$ from CANDELS/UDS. *MNRAS*, 433:1185–1201.

Mosleh, M., Williams, R. J., and Franx, M. (2013). On the Robustness of z = 0-1 Galaxy Size Measurements through Model and Non-parametric Fits. *ApJ*, 777:117.

Moster, B. P., Naab, T., and White, S. D. M. (2013). Galactic star formation and accretion histories from matching galaxies to dark matter haloes. *MNRAS*, 428:3121–3138.

Moster, B. P., Somerville, R. S., Maulbetsch, C., van den Bosch, F. C., Macciò, A. V., Naab, T., and Oser, L. (2010). Constraints on the Relationship between Stellar Mass and Halo Mass at Low and High Redshift. *ApJ*, 710:903–923.

Muñoz, R. P., Eigenthaler, P., Puzia, T. H., Taylor, M. A., Ordenes-Briceño, Y., Alamo-Martínez, K., Ribbeck, K. X., Ángel, S., Capaccioli, M., Côté, P., Ferrarese, L., Galaz, G., Hempel, M., Hilker, M., Jordán, A., Lançon, A., Mieske, S., Paolillo, M., Richtler, T., Sánchez-Janssen, R., and Zhang, H. (2015). Unveiling a Rich System of Faint Dwarf Galaxies in the Next Generation Fornax Survey. *ApJ*, 813:L15.

Mukhanov, V. F. and Chibisov, G. V. (1981). Quantum fluctuations and a nonsingular universe. *Soviet Journal of Experimental and Theoretical Physics Letters*, 33:532.

Müller, O., Jerjen, H., and Binggeli, B. (2018). The Leo-I group: new dwarf galaxy and ultra diffuse galaxy candidates. *A&A*, 615:A105.

Naab, T., Johansson, P. H., Ostriker, J. P., and Efstathiou, G. (2007). Formation of Early-Type Galaxies from Cosmological Initial Conditions. *ApJ*, 658:710–720.

Naab, T., Oser, L., Emsellem, E., Cappellari, M., Krajnović, D., McDermid, R. M., Alatalo, K., Bayet, E., Blitz, L., Bois, M., Bournaud, F., Bureau, M., Crocker, A., Davies, R. L., Davis, T. A., de Zeeuw, P. T., Duc, P.-A., Hirschmann, M., Johansson, P. H., Khochfar, S., Kuntschner, H., Morganti, R., Oosterloo, T., Sarzi, M., Scott, N., Serra, P., van de Ven, G., Weijmans, A., and Young, L. M. (2014). The ATLAS^{3D} project - XXV. Two-dimensional kinematic analysis of simulated galaxies and the cosmological origin of fast and slow rotators. *MNRAS*, 444:3357–3387.

Naab, T. and Ostriker, J. P. (2017). Theoretical Challenges in Galaxy Formation. *ARA&A*, 55:59–109.

Navarro, J. F., Frenk, C. S., and White, S. D. M. (1997). A Universal Density Profile from Hierarchical Clustering. *ApJ*, 490(2):493–508.

Navarro, J. F. and Steinmetz, M. (2000). Dark Halo and Disk Galaxy Scaling Laws in Hierarchical Universes. *ApJ*, 538(2):477–488.

Nelson, D., Vogelsberger, M., Genel, S., Sijacki, D., Kereš, D., Springel, V., and Hernquist, L. (2013). Moving mesh cosmology: tracing cosmological gas accretion. *MNRAS*, 429:3353–3370.

Newman, A. B., Ellis, R. S., Bundy, K., and Treu, T. (2012). Can Minor Merging Account for the Size Growth of Quiescent Galaxies? New Results from the CANDELS Survey. *ApJ*, 746:162.

Oman, K. A., Navarro, J. F., Fattahi, A., Frenk, C. S., Sawala, T., White, S. D. M., Bower, R., Crain, R. A., Furlong, M., Schaller, M., Schaye, J., and Theuns, T. (2015). The unexpected diversity of dwarf galaxy rotation curves. *MNRAS*, 452(4):3650–3665.

Oosterloo, T., Morganti, R., Crocker, A., Jütte, E., Cappellari, M., de Zeeuw, T., Krajnović, D., McDermid, R., Kuntschner, H., Sarzi, M., and Weijmans, A.-M. (2010). Early-type galaxies in different environments: an HI view. *MNRAS*, 409:500–514.

Ouellette, N. N.-Q., Courteau, S., Holtzman, J. A., Dutton, A. A., Cappellari, M., Dalcanton, J. J., McDonald, M., Roediger, J. C., Taylor, J. E., Tully, R. B., Côté, P., Ferrarese, L., and Peng, E. W. (2017). The Spectroscopy and H-band Imaging of Virgo Cluster Galaxies (SHIVir) Survey: Scaling Relations and the Stellar-to-total Mass Relation. *ApJ*, 843:74.

Pawlik, M. M., Wild, V., Walcher, C. J., Johansson, P. H., Villforth, C., Rowlands, K., Mendez-Abreu, J., and Hewlett, T. (2016). Shape asymmetry: a morphological indicator for automatic detection of galaxies in the post-coalescence merger stages. *MNRAS*, 456:3032–3052.

Peirani, S., Crockett, R. M., Geen, S., Khochfar, S., Kaviraj, S., and Silk, J. (2010). Composite star formation histories of early-type galaxies from minor mergers: prospects for WFC3. *MNRAS*, 405:2327–2338.

Peng, C. Y., Ho, L. C., Impey, C. D., and Rix, H.-W. (2002). Detailed Structural Decomposition of Galaxy Images. *AJ*, 124:266–293.

Perez, J., Valenzuela, O., Tissera, P. B., and Michel-Dansac, L. (2013). Clumpy disc and bulge formation. *MNRAS*, 436(1):259–265.

Persic, M. and Salucci, P. (1988). Dark and visible matter in spiral galaxies. *MNRAS*, 234:131–154.

Persic, M., Salucci, P., Bertola, F., and Pizzella, A. (1997). Trends of Central Dark Matter Density in Galaxies. In Arnaboldi, M., Da Costa, G. S., and Saha, P., editors, *The Nature of Elliptical Galaxies; 2nd Stromlo Symposium*, volume 116 of *Astronomical Society of the Pacific Conference Series*, page 151.

Persic, M., Salucci, P., and Stel, F. (1996). The universal rotation curve of spiral galaxies — I. The dark matter connection. *MNRAS*, 281(1):27–47.

Petric, A. O. and Rupen, M. P. (2007). H I Velocity Dispersion in NGC 1058. *AJ*, 134(5):1952–1962.

Planck Collaboration, Aghanim, N., Akrami, Y., Ashdown, M., Aumont, J., Baccigalupi, C., Ballardini, M., Banday, A. J., Barreiro, R. B., Bartolo, N., Basak, S., Battye, R., Benabed, K., Bernard, J.-P., Bersanelli, M., Bielewicz, P., Bock, J. J., Bond, J. R., Borrill, J., Bouchet, F. R., Boulanger, F., Bucher, M., Burigana, C., Butler, R. C., Calabrese, E., Cardoso, J.-F., Carron, J., Challinor, A., Chiang, H. C., Chluba, J., Colombo, L. P. L., Combet, C., Contreras, D., Crill, B. P., Cuttaia, F., de Bernardis, P., de Zotti, G., Delabrouille, J., Delouis, J.-M., Di Valentino, E., Diego, J. M., Doré, O., Douspis, M., Ducout, A., Dupac, X., Dusini, S., Efstathiou, G., Elsner, F., Enßlin, T. A., Eriksen, H. K., Fantaye, Y., Farhang, M., Fergusson, J., Fernandez-Cobos, R., Finelli, F., Forastieri, F., Frailis, M., Franceschi, E., Frolov, A., Galeotta, S., Galli, S., Ganga, K., Génova-Santos, R. T., Gerbino, M., Ghosh, T., González-Nuevo, J., Górski, K. M., Gratton, S., Gruppuso, A., Gudmundsson, J. E., Hamann, J., Handley, W., Herranz, D., Hivon, E., Huang, Z., Jaffe, A. H., Jones, W. C., Karakci, A., Keihänen, E., Keskitalo, R., Kiiveri, K., Kim, J., Kisner, T. S., Knox, L., Krachmalnicoff, N., Kunz, M., Kurki-Suonio, H., Lagache, G., Lamarre, J.-M., Lasenby, A., Lattanzi, M., Lawrence, C. R., Le Jeune, M., Lemos, P., Lesgourgues, J., Levrier, F., Lewis, A., Liguori, M., Lilje, P. B., Lilley, M., Lindholm, V., López-Caniego, M., Lubin, P. M., Ma, Y.-Z., Macías-Pérez, J. F., Maggio, G., Maino, D., Mandolesi, N., Mangilli, A., Marcos-Caballero, A., Maris, M., Martin, P. G., Martinelli, M., Martínez-González, E., Matarrese, S., Mauri, N., McEwen, J. D., Meinhold, P. R., Melchiorri, A., Mennella, A., Migliaccio, M., Millea, M., Mitra, S., Miville-Deschênes, M.-A., Molinari, D., Montier, L., Morgante, G., Moss, A., Natoli, P., Nørgaard-Nielsen, H. U., Pagano, L., Paoletti, D., Partridge, B., Patanchon, G., Peiris, H. V., Perrotta, F., Pettorino, V., Piacentini, F., Polastri, L., Polenta, G., Puget, J.-L., Rachen, J. P., Reinecke, M., Remazeilles, M., Renzi, A., Rocha, G., Rosset, C., Roudier, G., Rubiño-Martín, J. A., Ruiz-Granados, B., Salvati, L., Sandri, M., Savelainen, M., Scott, D., Shellard, E. P. S., Sirignano, C., Sirri, G., Spencer, L. D., Sunyaev, R., Suur-Uski, A.-S., Tauber, J. A., Tavagnacco, D., Tenti, M., Toffolatti, L., Tomasi, M., Trombetti, T., Valenziano, L., Valiviita, J., Van Tent, B., Vibert, L., Vielva, P., Villa, F., Vittorio, N., Wandelt, B. D., Wehus, I. K., White, M., White, S. D. M., Zacchei, A., and Zonca, A. (2018). Planck 2018 results. VI. Cosmological parameters. *arXiv e-prints*.

Ponomareva, A. A., Verheijen, M. A. W., Peletier, R. F., and Bosma, A. (2017). The multiwavelength Tully-Fisher relation with spatially resolved H I kinematics. *MNRAS*, 469(2):2387–2400.

Pop, A.-R., Pillepich, A., Amorisco, N. C., and Hernquist, L. (2018). Formation and incidence of shell galaxies in the Illustris simulation. *MNRAS*, 480:1715–1739.

Price, S. H., Kriek, M., Shapley, A. E., Reddy, N. A., Freeman, W. R., Coil, A. L., de Groot, L., Shivaei, I., Siana, B., Azadi, M., Barro, G., Mobasher, B., Sand ers, R. L., and Zick, T. (2016). The MOSDEF Survey: Dynamical and Baryonic Masses and Kinematic Structures of Star-forming Galaxies at 1.4 $\leq$ z $\leq$ 2.6. *ApJ*, 819(1):80.

Prieur, J.-L. (1988). The shell system around NGC 3923 and its implications for the potential of the galaxy. *ApJ*, 326:596–615.

Quinn, P. J. (1984). On the formation and dynamics of shells around elliptical galaxies. *ApJ*, 279:596–609.

Ramos Almeida, C., Tadhunter, C. N., Inskip, K. J., Morganti, R., Holt, J., and Dicken, D. (2011). The optical morphologies of the 2 Jy sample of radio galaxies: evidence for galaxy interactions. *MNRAS*, 410:1550–1576.

Rampazzo, R., Alexander, P., Carignan, C., Clemens, M. S., Cullen, H., Garrido, O., Marcelin, M., Sheth, K., and Trinchieri, G. (2006). The hot, warm and cold gas in Arp 227 - an evolving poor group. *MNRAS*, 368:851–863.

Rampazzo, R., Marino, A., Tantalo, R., Bettoni, D., Buson, L. M., Chiosi, C., Galletta, G., Grützbauch, R., and Rich, R. M. (2007). The Galaxy Evolution Explorer UV emission in shell galaxies: tracing galaxy ‘rejuvenation’ episodes. *MNRAS*, 381:245–262.

Randriamampandry, T. H., Combes, F., Carignan, C., and Deg, N. (2015). Estimating non-circular motions in barred galaxies using numerical N-body simulations. *MNRAS*, 454(4):3743–3759.

Renaud, F., Bournaud, F., and Duc, P.-A. (2015). A parsec-resolution simulation of the Antennae galaxies: formation of star clusters during the merger. *MNRAS*, 446:2038–2054.

Richter, O.-G., Sackett, P. D., and Sparke, L. S. (1994). A neutral hydrogen survey of polar-ring galaxies, 1: Green Bank observations of the northern sample. *AJ*, 107:99–117.

Roberts, M. S. (1962). A study of neutral hydrogen in IC 10. *AJ*, 67:431–436.

Rodriguez-Gomez, V., Pillepich, A., Sales, L. V., Genel, S., Vogelsberger, M., Zhu, Q., Wellons, S., Nelson, D., Torrey, P., Springel, V., Ma, C.-P., and Hernquist, L. (2016). The stellar mass assembly of galaxies in the Illustris simulation: growth by mergers and the spatial distribution of accreted stars. *MNRAS*, 458:2371–2390.

Rodríguez-Puebla, A., Avila-Reese, V., and Drory, N. (2013). The Galaxy-Halo/Subhalo Connection: Mass Relations and Implications for Some Satellite Occupational Distributions. *ApJ*, 767:92.

Rodríguez-Puebla, A., Avila-Reese, V., Yang, X., Foucaud, S., Drory, N., and Jing, Y. P. (2015). The Stellar-to-Halo Mass Relation of Local Galaxies Segregates by Color. *ApJ*, 799:130.

Rodríguez-Puebla, A., Behroozi, P., Primack, J., Klypin, A., Lee, C., and Hellinger, D. (2016). Halo and subhalo demographics with Planck cosmological parameters: Bolshoi-Planck and MultiDark-Planck simulations. *MNRAS*, 462:893–916.

Rodríguez-Puebla, A., Primack, J. R., Avila-Reese, V., and Faber, S. M. (2017). Constraining the galaxy-halo connection over the last 13.3 Gyr: star formation histories, galaxy mergers and structural properties. *MNRAS*, 470:651–687.

Roediger, J. C. and Courteau, S. (2015). On the uncertainties of stellar mass estimates via colour measurements. *MNRAS*, 452(3):3209–3225.

Rogstad, D. H., Lockhart, I. A., and Wright, M. C. H. (1974). Aperture-synthesis observations of H I in the galaxy M83. *ApJ*, 193:309–319.

Román, J. and Trujillo, I. (2017). Spatial distribution of ultra-diffuse galaxies within large-scale structures. *MNRAS*, 468:703–716.

Romeo, A. B. and Wiegert, J. (2011). The effective stability parameter for two-component galactic discs: is $\mathrm{Q}^{-1} \approx \mathrm{Q}^{-1}{}_{stars} + \mathrm{Q}^{-1}{}_{gas}$? *MNRAS*, 416(2):1191–1196.

Rong, Y., Li, H., Wang, J., Gao, L., Li, R., Ge, J., Jing, Y., Pan, J., Fernández-Trincado, J. G., Valenzuela, O., and Ortíz, E. A. (2018). SDSS-IV MaNGA: a distinct mass distribution explored in slow-rotating early-type galaxies. *MNRAS*, 477(1):230–235.

Roth, M. M., Kelz, A., Fechner, T., Hahn, T., Bauer, S.-M., Becker, T., Böhm, P., Christensen, L., Dionies, F., Paschke, J., Popow, E., Wolter, D., Schmoll, J., Laux, U., and Altmann, W. (2005). PMAS: The Potsdam Multi-Aperture Spectrophotometer. I. Design, Manufacture, and Performance. *PASP*, 117(832):620–642.

Sage, L. J. and Wrobel, J. M. (1989). Detection of CO emission from S0 galaxies. *ApJ*, 344:204–209.

Salim, S., Rich, R. M., Charlot, S., Brinchmann, J., Johnson, B. D., Schiminovich, D., Seibert, M., Mallery, R., Heckman, T. M., Forster, K., Friedman, P. G., Martin, D. C., Morrissey, P., Neff, S. G., Small, T., Wyder, T. K., Bianchi, L., Donas, J., Lee, Y.-W., Madore, B. F., Milliard, B., Szalay, A. S., Welsh, B. Y., and Yi, S. K. (2007). UV Star Formation Rates in the Local Universe. *ApJS*, 173(2):267–292.

Salpeter, E. E. (1955). The Luminosity Function and Stellar Evolution. *ApJ*, 121:161.

Sánchez, S. F., Kennicutt, R. C., Gil de Paz, A., van de Ven, G., Vílchez, J. M., Wisotzki, L., Walcher, C. J., Mast, D., Aguerri, J. A. L., Albiol-Pérez, S., Alonso-Herrero, A., Alves, J., Bakos, J., Bartáková, T., Bland-Hawthorn, J., Boselli, A., Bomans, D. J., Castillo-Morales, A., Cortijo-Ferrero, C., de Lorenzo-Cáceres, A., Del Olmo, A., Dettmar, R.-J., Díaz, A., Ellis, S., Falcón-Barroso, J., Flores, H., Gallazzi, A., García-Lorenzo, B., González Delgado, R., Gruel, N., Haines, T., Hao, C., Husemann, B., Iglésias-Páramo, J., Jahnke, K., Johnson, B., Jungwiert, B., Kalinova, V., Kehrig, C., Kupko, D., López-Sánchez, Á. R., Lyubenova, M., Marino, R. A., Mármol-Queraltó, E., Márquez, I., Masegosa, J., Meidt, S., Mendez-Abreu, J., Monreal-Ibero, A., Montijo, C., Mourão, A. M., Palacios-Navarro, G., Papaderos, P., Pasquali, A., Peletier, R., Pérez, E., Pérez, I., Quirrenbach, A., Relaño, M., Rosales-Ortega, F. F., Roth, M. M., Ruiz-Lara, T., Sánchez-Blázquez, P., Sengupta, C., Singh, R., Stanishev, V., Trager, S. C., Vazdekis, A., Viironen, K., Wild, V., Zibetti, S., and Ziegler, B. (2012). CALIFA, the Calar Alto Legacy Integral Field Area survey. I. Survey presentation. *A&A*, 538:A8.

Sandage, A. (1976). High-latitude reflection nebulosities illuminated by the galactic plane. *AJ*, 81:954.

Sansom, A. E., Hibbard, J. E., and Schweizer, F. (2000). The Cold and Hot Gas Content of Fine-Structure E and S0 Galaxies. *AJ*, 120:1946–1953.

Schaye, J., Crain, R. A., Bower, R. G., Furlong, M., Schaller, M., Theuns, T., Dalla Vecchia, C., Frenk, C. S., McCarthy, I. G., Helly, J. C., Jenkins, A., Rosas-Guevara, Y. M., White, S. D. M., Baes, M., Booth, C. M., Camps, P., Navarro, J. F., Qu, Y., Rahmati, A., Sawala, T., Thomas, P. A., and Trayford, J. (2015). The EAGLE project: simulating the evolution and assembly of galaxies and their environments. *MNRAS*, 446(1):521–554.

Schiminovich, D., van Gorkom, J., van der Hulst, T., Oosterloo, T., and Wilkinson, A. (1997). Imaging and Kinematics of Neutral Hydrogen in and around "Shell Galaxies". In Arnaboldi, M., Da Costa, G. S., and Saha, P., editors, *The Nature of Elliptical Galaxies; 2nd Stromlo Symposium*, volume 116 of *Astronomical Society of the Pacific Conference Series*, page 362.

Schiminovich, D., van Gorkom, J. H., and van der Hulst, J. M. (2013). Extended Neutral Hydrogen in the Aligned Shell Galaxies Arp 230 and MCG -5-7-1: Formation of Disks in Merging Galaxies? *AJ*, 145:34.

Schiminovich, D., van Gorkom, J. H., van der Hulst, J. M., and Kasow, S. (1994). Discovery of Neutral Hydrogen Associated with the Diffuse Shells of NGC 5128 (Centaurus A). *ApJ*, 423:L101.

Schiminovich, D., van Gorkom, J. H., van der Hulst, J. M., and Malin, D. F. (1995). Neutral hydrogen associated with shells and other fine structure in NGC 2865: A dynamically young elliptical? *ApJ*, 444:L77–L80.

Schoenmakers, R. H. M., Franx, M., and de Zeeuw, P. T. (1997). Measuring non-axisymmetry in spiral galaxies. *MNRAS*, 292(2):349–364.

Schombert, J., Maciel, T., and McGaugh, S. (2011). Stellar Populations and the Star Formation Histories of LSB GalaxiesPart I: Optical and Hα Imaging. *Advances in Astronomy*, 2011:143698.

Schwarzschild, M. (1979). A numerical model for a triaxial stellar system in dynamical equilibrium. *ApJ*, 232:236–247.

Schweizer, F. (1980). An optical study of the giant radio galaxy NGC 1316 /Fornax A/. *ApJ*, 237:303–318.

Schweizer, F. (1990). *Interactions in our time.*, pages 60–71.

Schweizer, F. and Ford, Jr., W. K. (1985). Fine Structure in Elliptical Galaxies. In Nieto, J.-L., editor, *New Aspects of Galaxy Photometry*, volume 232 of *Lecture Notes in Physics, Berlin Springer Verlag*, page 145.

Schweizer, F. and Seitzer, P. (1988). Ripples in disk galaxies. *ApJ*, 328:88–92.

Schweizer, F. and Seitzer, P. (1992). Correlations between UBV colors and fine structure in E and S0 galaxies - A first attempt at dating ancient merger events. *AJ*, 104:1039–1067.

Sellwood, J. A. and Sánchez, R. Z. (2010). Quantifying non-circular streaming motions in disc galaxies. *MNRAS*, 404(4):1733–1744.

Serra, P., Trager, S. C., Oosterloo, T. A., and Morganti, R. (2008). Stellar populations, neutral hydrogen, and ionised gas in field early-type galaxies. *A&A*, 483:57–69.

Sérsic, J. L. (1963). Influence of the atmospheric and instrumental dispersion on the brightness distribution in a galaxy. *Boletin de la Asociacion Argentina de Astronomia La Plata Argentina*, 6:41.

Sersic, J. L. (1968). Proceedings of the Conference on Seyfert Galaxies and Related Objects: 32. Statistics of Galaxies with Peculiar Nuclei. *AJ*, 73:892.

Shadmehri, M. and Khajenabi, F. (2012). On the gravitational stability of a galactic disc as a two-fluid system. *MNRAS*, 421(1):841–846.

Shen, S., Mo, H. J., White, S. D. M., Blanton, M. R., Kauffmann, G., Voges, W., Brinkmann, J., and Csabai, I. (2003). The size distribution of galaxies in the Sloan Digital Sky Survey. *MNRAS*, 343:978–994.

Shi, D. D., Zheng, X. Z., Zhao, H. B., Pan, Z. Z., Li, B., Zou, H., Zhou, X., Guo, K., An, F. X., and Li, Y. B. (2017). Deep Imaging of the HCG 95 Field. I. Ultra-diffuse Galaxies. *ApJ*, 846:26.

Sikkema, G., Peletier, R. F., Carter, D., Valentijn, E. A., and Balcells, M. (2006). Globular cluster systems of six shell galaxies. *A&A*, 458:53–67.

Sofue, Y., Wakamatsu, K.-I., Taniguchi, Y., and Nakai, N. (1993). CO observations of Arp's interacting galaxies. *PASJ*, 45:43–55.

Solomon, P. M. and Vanden Bout, P. A. (2005). Molecular Gas at High Redshift. *ARA&A*, 43:677–725.

Somerville, R. S. and Davé, R. (2015). Physical Models of Galaxy Formation in a Cosmological Framework. *ARA&A*, 53:51–113.

Spekkens, K. and Karunakaran, A. (2018). Atomic Gas in Blue Ultra Diffuse Galaxies around Hickson Compact Groups. *ApJ*, 855:28.

Stewart, K. R., Bullock, J. S., Wechsler, R. H., Maller, A. H., and Zentner, A. R. (2008). Merger Histories of Galaxy Halos and Implications for Disk Survival. *ApJ*, 683:597–610.

Tal, T., van Dokkum, P. G., Nelan, J., and Bezanson, R. (2009). The Frequency of Tidal Features Associated with Nearby Luminous Elliptical Galaxies From a Statistically Complete Sample. *AJ*, 138:1417–1427.

Tamburro, D., Rix, H. W., Leroy, A. K., Mac Low, M. M., Walter, F., Kennicutt, R. C., Brinks, E., and de Blok, W. J. G. (2009). What is Driving the H I Velocity Dispersion? *AJ*, 137(5):4424–4435.

Tateuchi, K., Konishi, M., Motohara, K., Takahashi, H., Mitani Kato, N., Kitagawa, Y., Todo, S., Toshikawa, K., Sako, S., Uchimoto, Y. K., Ohsawa, R., Asano, K., Ita, Y., Kamizuka, T., Komugi, S., Koshida, S., Manabe, S., Nakamura, T., Nakashima, A., Okada, K., Takagi, T., Tanabé, T., Uchiyama, M., Aoki, T., Doi, M., Handa, T., Kawara, K., Kohno, K., Minezaki, T., Miyata, T., Morokuma, T., Soyano, T., Tamura, Y., Tanaka, M., Tarusawa, K., and Yoshii, Y. (2015). Ground-based Paα Narrow-band Imaging of Local Luminous Infrared Galaxies. I. Star Formation Rates and Surface Densities. *ApJS*, 217:1.

Teyssier, R. (2002). Cosmological hydrodynamics with adaptive mesh refinement. A new high resolution code called RAMSES. *A&A*, 385:337–364.

Toomre, A. (1964). On the gravitational stability of a disk of stars. *ApJ*, 139:1217–1238.

Toomre, A. (1977). Mergers and Some Consequences. In Tinsley, B. M. and Larson, D. Campbell, R. B. G., editors, *Evolution of Galaxies and Stellar Populations*, page 401.

Toomre, A. and Toomre, J. (1972). Galactic Bridges and Tails. *ApJ*, 178:623–666.

Trujillo, I., Roman, J., Filho, M., and Sánchez Almeida, J. (2017). The Nearest Ultra Diffuse Galaxy: UGC 2162. *ApJ*, 836:191.

Tully, R. B. and Fisher, J. R. (1977). Reprint of 1977A&A....54..661T. A new method of determining distance to galaxies. *A&A*, 500:105–117.

Tumlinson, J., Peeples, M. S., and Werk, J. K. (2017). The Circumgalactic Medium. *ARA&A*, 55:389–432.

Turnbull, A. J., Bridges, T. J., and Carter, D. (1999). Imaging of the shell galaxies NGC 474 and 7600, and implications for their formation. *MNRAS*, 307:967–976.

Ueda, J., Iono, D., Yun, M. S., Crocker, A. F., Narayanan, D., Komugi, S., Espada, D., Hatsukade, B., Kaneko, H., Matsuda, Y., Tamura, Y., Wilner, D. J., Kawabe, R., and Pan, H.-A. (2014). Cold Molecular Gas in Merger Remnants. I. Formation of Molecular Gas Disks. *ApJS*, 214:1.

Valls-Gabaud, D. and MESSIER Collaboration (2017). The MESSIER surveyor: unveiling the ultra-low surface brightness universe. In Gil de Paz, A., Knapen, J. H., and Lee, J. C., editors, *Formation and Evolution of Galaxy Outskirts*, volume 321 of *IAU Symposium*, pages 199–201.

van den Bosch, F. C. (2000). Semianalytical Models for the Formation of Disk Galaxies. I. Constraints from the Tully-Fisher Relation. *ApJ*, 530:177–192.

van der Burg, R. F. J., Hoekstra, H., Muzzin, A., Sifón, C., Viola, M., Bremer, M. N., Brough, S., Driver, S. P., Erben, T., Heymans, C., Hildebrandt, H., Holwerda, B. W., Klaes, D., Kuijken, K., McGee, S., Nakajima, R., Napolitano, N., Norberg, P., Taylor, E. N., and Valentijn, E. (2017). The abundance of ultra-diffuse galaxies from groups to clusters. UDGs are relatively more common in more massive haloes. *A&A*, 607:A79.

van Dokkum, P., Abraham, R., Brodie, J., Conroy, C., Danieli, S., Merritt, A., Mowla, L., Romanowsky, A., and Zhang, J. (2016). A High Stellar Velocity Dispersion and 100 Globular Clusters for the Ultra-diffuse Galaxy Dragonfly 44. *ApJ*, 828:L6.

van Dokkum, P. G. (2005). The Recent and Continuing Assembly of Field Elliptical Galaxies by Red Mergers. *AJ*, 130:2647–2665.

van Dokkum, P. G., Abraham, R., and Merritt, A. (2014). First Results from the Dragonfly Telephoto Array: The Apparent Lack of a Stellar Halo in the Massive Spiral Galaxy M101. *ApJ*, 782:L24.

van Dokkum, P. G., Abraham, R., Merritt, A., Zhang, J., Geha, M., and Conroy, C. (2015a). Forty-seven Milky Way-sized, Extremely Diffuse Galaxies in the Coma Cluster. *ApJ*, 798:L45.

van Dokkum, P. G., Romanowsky, A. J., Abraham, R., Brodie, J. P., Conroy, C., Geha, M., Merritt, A., Villaume, A., and Zhang, J. (2015b). Spectroscopic Confirmation of the Existence of Large, Diffuse Galaxies in the Coma Cluster. *ApJ*, 804:L26.

van Driel, W., Arnaboldi, M., Combes, F., and Sparke, L. S. (2000). A neutral hydrogen survey of polar ring galaxies. III. Nançay observations and comparison with published data. *A&AS*, 141:385–408.

van Gorkom, J. (2000). HI Images That Changed My View on the Universe. In Finley, D. G. and Goss, W. M., editors, *Radio interferometry : the saga and the science*, page 137.

van Zee, L. and Bryant, J. (1999). Neutral Gas Distribution and Kinematics of the Nearly Face-on Spiral Galaxy NGC 1232. *AJ*, 118(5):2172–2183.

Venhola, A., Peletier, R., Laurikainen, E., Salo, H., Lisker, T., Iodice, E., Capaccioli, M., Verdois Kleijn, G., Valentijn, E., Mieske, S., Hilker, M., Wittmann, C., van de Ven, G., Grado, A., Spavone, M., Cantiello, M., Napolitano, N., Paolillo, M., and Falcón-Barroso, J. (2017). The Fornax Deep Survey with VST. III. Low surface brightness dwarfs and ultra diffuse galaxies in the center of the Fornax cluster. *A&A*, 608:A142.

Walmsley, M., Ferguson, A. M. N., Mann, R. G., and Lintott, C. J. (2019). Identification of low surface brightness tidal features in galaxies using convolutional neural networks. *MNRAS*, 483:2968–2982.

Wechsler, R. H. and Tinker, J. L. (2018). The Connection Between Galaxies and Their Dark Matter Halos. *ARA&A*, 56:435–487.

Weil, M. L. and Hernquist, L. (1993). Segregation of gas and stars in shell galaxies. *ApJ*, 405:142–152.

Weinzirl, T., Jogee, S., Khochfar, S., Burkert, A., and Kormendy, J. (2009). Bulge n and B/T in High-Mass Galaxies: Constraints on the Origin of Bulges in Hierarchical Models. *ApJ*, 696:411–447.

White, S. D. M. and Rees, M. J. (1978). Core condensation in heavy halos - A two-stage theory for galaxy formation and clustering. *MNRAS*, 183:341–358.

Whitmore, B. C., Lucas, R. A., McElroy, D. B., Steiman-Cameron, T. Y., Sackett, P. D., and Olling, R. P. (1990). New observations and a photographic atlas of polar-ring galaxies. *AJ*, 100:1489–1522.

Whitmore, B. C., Schweizer, F., Leitherer, C., Borne, K., and Robert, C. (1993). Hubble Space Telescope discovery of candidate young globular clusters in the merger remnant NGC 7252. *AJ*, 106:1354–1370.

Wiklind, T., Combes, F., and Henkel, C. (1995). The molecular cloud content of early-type galaxies. V. CO in elliptical galaxies. *A&A*, 297:643.

Williams, R. E. and Christiansen, W. A. (1985). Blast wave formation of the extended stellar shells surrounding elliptical galaxies. *ApJ*, 291:80–87.

Yagi, M., Koda, J., Komiyama, Y., and Yamanoi, H. (2016). Catalog of Ultra-diffuse Galaxies in the Coma Clusters from Subaru Imaging Data. *ApJS*, 225:11.

Yang, X., Mo, H. J., van den Bosch, F. C., Zhang, Y., and Han, J. (2012). Evolution of the Galaxy-Dark Matter Connection and the Assembly of Galaxies in Dark Matter Halos. *ApJ*, 752:41.

York, D. G., Adelman, J., Anderson, Jr., J. E., Anderson, S. F., Annis, J., Bahcall, N. A., Bakken, J. A., Barkhouser, R., Bastian, S., Berman, E., Boroski, W. N., Bracker, S., Briegel, C., Briggs, J. W., Brinkmann, J., Brunner, R., Burles, S., Carey, L., Carr, M. A., Castander, F. J., Chen, B., Colestock, P. L., Connolly, A. J., Crocker, J. H., Csabai, I., Czarapata, P. C., Davis, J. E., Doi, M., Dombeck, T., Eisenstein, D., Ellman, N., Elms, B. R., Evans, M. L., Fan, X., Federwitz, G. R., Fiscelli, L., Friedman, S., Frieman, J. A., Fukugita, M., Gillespie, B., Gunn, J. E., Gurbani, V. K., de Haas, E., Haldeman, M., Harris, F. H., Hayes, J., Heckman, T. M., Hennessy, G. S., Hindsley, R. B., Holm, S., Holmgren, D. J., Huang, C.-h., Hull, C., Husby, D., Ichikawa, S.-I., Ichikawa, T., Ivezić, Ž., Kent, S., Kim, R. S. J., Kinney, E., Klaene, M., Kleinman, A. N., Kleinman, S., Knapp, G. R., Korienek, J., Kron, R. G., Kunszt, P. Z., Lamb, D. Q., Lee, B., Leger, R. F., Limmongkol, S., Lindenmeyer, C., Long, D. C., Loomis, C., Loveday, J., Lucinio, R., Lupton, R. H., MacKinnon, B., Mannery, E. J., Mantsch, P. M., Margon, B., McGehee, P., McKay, T. A., Meiksin, A., Merelli, A., Monet, D. G., Munn, J. A., Narayanan, V. K., Nash, T., Neilsen, E., Neswold, R., Newberg, H. J., Nichol, R. C., Nicinski, T., Nonino, M., Okada, N., Okamura, S., Ostriker, J. P., Owen, R., Pauls, A. G., Peoples, J., Peterson, R. L., Petravick, D., Pier, J. R., Pope, A., Pordes, R., Prosapio, A., Rechenmacher, R., Quinn, T. R., Richards, G. T., Richmond, M. W., Rivetta, C. H., Rockosi, C. M., Ruthmansdorfer, K., Sandford, D., Schlegel, D. J., Schneider, D. P., Sekiguchi, M., Sergey, G., Shimasaku, K., Siegmund, W. A., Smee, S., Smith, J. A., Snedden, S., Stone, R., Stoughton, C., Strauss, M. A., Stubbs, C., SubbaRao, M., Szalay, A. S., Szapudi, I., Szokoly, G. P., Thakar, A. R., Tremonti, C., Tucker, D. L., Uomoto, A., Vanden Berk, D., Vogeley, M. S., Waddell, P., Wang, S.-i., Watanabe, M., Weinberg, D. H., Yanny, B., Yasuda, N., and SDSS Collaboration (2000). The Sloan Digital Sky Survey: Technical Summary. *AJ*, 120:1579–1587.

Young, L. M. (2002). Molecular Gas in Elliptical Galaxies: Distribution and Kinematics. *AJ*, 124:788–810.

Young, L. M., Bureau, M., Davis, T. A., Combes, F., McDermid, R. M., Alatalo, K., Blitz, L., Bois, M., Bournaud, F., Cappellari, M., Davies, R. L., de Zeeuw, P. T., Emsellem, E., Khochfar, S., Krajnović, D., Kuntschner, H., Lablanche, P.-Y., Morganti, R., Naab, T., Oosterloo, T., Sarzi, M., Scott, N., Serra, P., and Weijmans, A.-M. (2011). The ATLAS^{3D} project - IV. The molecular gas content of early-type galaxies. *MNRAS*, 414:940–967.

Yozin, C. and Bekki, K. (2015). The quenching and survival of ultra diffuse galaxies in the Coma cluster. *MNRAS*, 452:937–943.

Zaritsky, D. (2017). Clues to the nature of ultradiffuse galaxies from estimated galaxy velocity dispersions. *MNRAS*, 464:L110–L113.

Zavala, J., Avila-Reese, V., Firmani, C., and Boylan-Kolchin, M. (2012). The growth of galactic bulges through mergers in Λ CDM haloes revisited - I. Present-day properties. *MNRAS*, 427(2):1503–1516.

Zavala, J., Avila-Reese, V., Hernández-Toledo, H., and Firmani, C. (2003). The luminous and dark matter content of disk galaxies. *A&A*, 412:633–650.

Zavala, J., Okamoto, T., and Frenk, C. S. (2008). Bulges versus discs: the evolution of angular momentum in cosmological simulations of galaxy formation. *MNRAS*, 387:364–370.

Zheng, Z., Berlind, A. A., Weinberg, D. H., Benson, A. J., Baugh, C. M., Cole, S., Davé, R., Frenk, C. S., Katz, N., and Lacey, C. G. (2005). Theoretical Models of the Halo Occupation Distribution: Separating Central and Satellite Galaxies. *ApJ*, 633:791–809.

Appendices

Appendix A

Publications

A.1 Refereed publications

- B. Mancillas, V. Ávila-Reese, Aldo Rodríguez-Puebla and D. Valls-Gabaud (2019), *The galaxy-halo connection: demography, scaling relations and radial distributions of the luminous and dark matter*, MNRAS, *to be submitted*
- E. Aquino-Ortíz, O. Valenzuela,S. F. Sánchez, H. Hernández-Toledo, V. Ávila-Reese, G. van de Ven, A. Rodríguez-Puebla, L. Zhu, B. Mancillas, M. Cano-Díaz and R. García-Benito (2018), *Kinematic scaling relations of CALIFA galaxies: A dynamical mass proxy for galaxies across the Hubble sequence*, MNRAS, 479, 2133
- B. Mancillas, P.-A. Duc, F. Combes, F. Bournaud, E. Emsellem, M. Martig, and L. Michel-Dansac (2019), *Probing the merger history of red early-type galaxies with their faint stellar substructures*, A&A, 632, A122
- B. Mancillas, F. Combes and P.-A. Duc (2019), *The molecular gas content of shell galaxies*, A&A, 630, A112
- M. I. Rodríguez, D. Valls-Gabaud, B. Mancillas, F. Combes, D. Martínez Delgado, P. Colom and J.M. Martin (2019), *On the cold gas content of ultra-diffuse galaxies*, MNRAS, *to be submitted*

A.2 Non-refereed publications

- B. Mancillas, V. Ávila-Reese, Aldo Rodríguez-Puebla and D. Valls-Gabaud (2017) *Projection Of The Stellar To Halo Mass Relation Into The Scaling Relations Of A Disc Galaxy Population*, Galaxy Evolution Across Time, Proceedings of a conference held 12-16 June, 2017 in Paris. Online at https://galaxiesinparis.sciencesconf.org/, id. 92